

THE FLORIDA STATE UNIVERSITY  
COLLEGE OF ARTS AND SCIENCES

MEASUREMENT OF POLARIZATION OBSERVABLES  
IN THE ELECTRO-EXCITATION OF THE PROTON  
TO ITS FIRST EXCITED STATE

By

RIKKI E. ROCHÉ

A Dissertation submitted to the  
Department of Physics  
in partial fulfillment of the  
requirements of the degree of  
Doctor of Philosophy

Degree Awarded:  
Summer Semester, 2003



The members of the Committee approve the dissertation of Rikki E. Roché defended on April 4, 2003.

---

Adam J. Sarty  
Professor Directing Dissertation

---

Gregory A. Riccardi  
Outside Committee Member

---

Pedro Schlottmann  
Committee Member

---

Mark Riley  
Committee Member

---

Simon Capstick  
Committee Member

The Office of Graduate Studies has verified and approved the above named committee members.





*To my grandparents:*

*Papa John and Helen  
and  
Mamaw and Pappaw*



## ACKNOWLEDGMENTS

First I would like to begin by thanking my thesis advisor, Adam Sarty, for his continuous help and support. Without his encouragement this thesis would not have been possible.

Thanks to the other members of my committee, Simon Capstick, Mark Riley, Pedro Schlottmann, and Greg Riccardi. A special thanks to Simon for the theory discussions. Also, thanks to Kirby Kemper for accommodating my special circumstances and allowing Adam to remain my official thesis advisor even though he left Florida State two years ago.

I would like to thank several other people involved in this experiment, especially Jim Kelly, Mark Jones, and Steffen Strauch. If it had not been for Jim's insistence that I write a report after every separate analysis issue, this thesis would have been much harder to write. Thanks also to Jim for reading this thesis so closely, thus allowing it to correctly reflect the actual analysis method followed. Many thanks to Mark for being the person most knowledgeable of Hall A analysis. His help has been essential for the analysis of this and many other Hall A experiments. Thank you to Steffen for writing such a useful analysis code to extract target polarization. Merci to Stéphanie Escoffier for a constant measure of the beam polarization using the Compton polarimeter, without which the response functions shown in this thesis could not have been extracted. Thanks to Dave Meekins for all his help in organizing the run plan and making sure everything that needed to be measured was measured.

Thank you to Kees de Jager, the Hall A physics staff, and the Hall A technicians especially Ed Folts (♥) and Jack Segall. Thanks to the Hall A collaboration members, especially all those who took shifts on this three month long experiment.

For the many people at both FSU (especially those who introduced me to the joys of football - Go Noles!!) and Jefferson Lab who made my time in graduate school more bearable, thank you. At FSU: Rob and Angie, Si, Adam and Nicole, Dave, Tom, Andrei, Sameer, Damon, Margie, Mike, Scott, Charlie and Carrie, Brett.... At Jefferson Lab: Olivier, Matthieu, Dan, Paul, Kevin, Julie, Mina, Kathy, Doug and Marcy, Lisa..., especially to Kathy and Lisa for being such great dog and cat sitters.

Thanks so much to my email buddies Karen, Natalie, Beth, Debi, and Chera. Their emails could always (usually) make me smile even when I was having the worst day.

I must also thank my family for being so supportive. My grandparents Helen and John Roché, and Dorothy M<sup>c</sup>Fadden who are so proud of everything I do. My parents Teresa and Jere, my brother Derek, my sister Karen, and my niece Shelby - to you all I say “no soap radio!”. Thank you so much for believing in me. I love you all!

Last, but certainly not least, I must thank the newest member of my family, as of March 1 of this year, my husband Olivier. Thank you for all the help you’ve given me in preparing this thesis, especially reading and rereading it every time I made a correction. But especially thank you for your love these past two years. I’m especially looking forward our time together now that the chaos and stress of writing a dissertation and planning a wedding are over. Notre amour est pour toujours.

## TABLE OF CONTENTS

LIST OF TABLES	xiii
LIST OF FIGURES	xv
ABSTRACT	xxi
CHAPTER 1. INTRODUCTION	1
1.1. Overview	1
1.2. Electron Scattering Formalism	5
1.3. The Differential Cross Section	7
1.4. Multipole Expansion	12
CHAPTER 2. PHYSICS MOTIVATION	17
2.1. The Standard Model	17
2.2. The $N \rightarrow \Delta(1232)$ Transition	19
2.3. Constituent Quark Model (CQM)	22
2.4. The Sato and Lee Meson-Exchange Model (SL)	26
2.5. Existing Experimental Data	27
CHAPTER 3. EXPERIMENTAL SETUP	35
3.1. Overview	35
3.2. The Continuous Electron Beam Accelerator Facility (CEBAF)	36
3.3. The Hall A Target	45
3.4. The High Resolution Spectrometers (HRS)	46
3.5. The Focal Plane Polarimeter (FPP)	53
3.6. Overview of Runplan	56
CHAPTER 4. DATA ANALYSIS	59
4.1. Overview	59
4.2. Particle Detection and Target Coordinates	61
4.3. Particle Identification (PID)	68
4.4. Extraction of Focal Plane Polarizations	72

4.5.	Extraction of Target Polarization Observables	83
4.6.	Background Subtraction	97
4.7.	Proton Form Factor Ratio	102
CHAPTER 5. RESULTS AND DISCUSSIONS		105
5.1.	Statistical Uncertainties	105
5.2.	Systematic Errors	106
5.3.	Radiative Corrections	108
5.4.	Target Polarization Results	109
5.5.	Response Function Results	110
5.6.	Comparison to Simulation and Models	110
5.7.	Conclusion	119
APPENDIX A. " $N \rightarrow \Delta$ " INTERNAL REPORT ON SPECTROMETER MISPOINTING		121
APPENDIX B. LIST OF COMPLETED RUNS FOR " $N \rightarrow \Delta$ "		137
B.1.	May 19 - June 5 Run Period	137
B.2.	June 8 - July 1 Run Period	162
B.3.	July 8 - July 9 Facility Development Time	175
B.4.	July 11 - July 31 Run Period	178
APPENDIX C. " $N \rightarrow \Delta$ " INTERNAL REPORT ON DATABASE AND $\beta$ OPTIMIZATION		193
APPENDIX D. RESULTS: TARGET POLARIZATIONS		203
D.1.	$W = 1160-1200 \text{ MeV}, Q^2 = 0.8-1.0 (\text{GeV}/c)^2$	203
D.2.	$W = 1200-1240 \text{ MeV}, Q^2 = 0.8-1.0 (\text{GeV}/c)^2$	209
D.3.	$W = 1240-1280 \text{ MeV}, Q^2 = 0.8-1.0 (\text{GeV}/c)^2$	215
D.4.	$W = 1280-1320 \text{ MeV}, Q^2 = 0.8-1.0 (\text{GeV}/c)^2$	221
D.5.	$W = 1320-1360 \text{ MeV}, Q^2 = 0.8-1.0 (\text{GeV}/c)^2$	227
D.6.	$W = 1160-1200 \text{ MeV}, Q^2 = 1.0-1.2 (\text{GeV}/c)^2$	233
D.7.	$W = 1200-1240 \text{ MeV}, Q^2 = 1.0-1.2 (\text{GeV}/c)^2$	239
D.8.	$W = 1240-1280 \text{ MeV}, Q^2 = 1.0-1.2 (\text{GeV}/c)^2$	245
D.9.	$W = 1280-1320 \text{ MeV}, Q^2 = 1.0-1.2 (\text{GeV}/c)^2$	251
D.10.	$W = 1320-1360 \text{ MeV}, Q^2 = 1.0-1.2 (\text{GeV}/c)^2$	257
APPENDIX E. RESULTS: RESPONSE FUNCTIONS		263

E.1.	$W = 1160-1200 \text{ MeV}, Q^2 = 0.8-1.0 (\text{GeV}/c)^2$	263
E.2.	$W = 1200-1240 \text{ MeV}, Q^2 = 0.8-1.0 (\text{GeV}/c)^2$	264
E.3.	$W = 1240-1280 \text{ MeV}, Q^2 = 0.8-1.0 (\text{GeV}/c)^2$	265
E.4.	$W = 1280-1320 \text{ MeV}, Q^2 = 0.8-1.0 (\text{GeV}/c)^2$	266
E.5.	$W = 1320-1360 \text{ MeV}, Q^2 = 0.8-1.0 (\text{GeV}/c)^2$	267
E.6.	$W = 1160-1200 \text{ MeV}, Q^2 = 1.0-1.2 (\text{GeV}/c)^2$	268
E.7.	$W = 1200-1240 \text{ MeV}, Q^2 = 1.0-1.2 (\text{GeV}/c)^2$	269
E.8.	$W = 1240-1280 \text{ MeV}, Q^2 = 1.0-1.2 (\text{GeV}/c)^2$	270
E.9.	$W = 1280-1320 \text{ MeV}, Q^2 = 1.0-1.2 (\text{GeV}/c)^2$	271
E.10.	$W = 1320-1360 \text{ MeV}, Q^2 = 1.0-1.2 (\text{GeV}/c)^2$	272
APPENDIX F. “ $N \rightarrow \Delta$ ” INTERNAL REPORT ON SCINTILLATOR EFFICIENCIES		273
F.1.	Electron Arm Scintillator Efficiencies	273
F.2.	Hadron Arm Scintillator Efficiencies	274
F.3.	Relative Error	275
F.4.	Results	275
BIBLIOGRAPHY		279
BIOGRAPHICAL SKETCH		283





## LIST OF TABLES

1.1	Summary of kinematics for " $N \rightarrow \Delta$ ".	3
2.1	Values of $EMR$ from measurements taken at CEA.	30
2.2	Values of $CMR$ and $EMR$ from measurements taken at DESY.	30
2.3	Values of $CMR$ and $EMR$ from measurements taken at NINA.	31
2.4	Values of $CMR$ and $EMR$ from measurements taken in Hall C of Jefferson Lab.	32
2.5	Values of $CMR$ and $EMR$ from measurements taken in Hall B of Jefferson Lab.	32
3.1	Absolute beam energy during " $N \rightarrow \Delta$ ".	38
3.2	Beam polarization measurements taken by the Møller polarimeter during " $N \rightarrow \Delta$ ".	42
3.3	Beam polarization measurements taken by the Compton polarimeter during " $N \rightarrow \Delta$ ".	44
3.4	Main design characteristics of the Hall A HRS.	48
3.5	Dimensions of the FPP straw chambers.	55
4.1	Kinematic settings for each $\cos \theta_{pq}$ region used in analysis.	60
4.2	Coefficients of the McNaughton and Hall A analyzing power parameterizations.	79
4.3	Different $^{12}\text{C}$ thicknesses in the FPP for " $N \rightarrow \Delta$ ".	82
4.4	Average false asymmetry terms.	90
4.5	Peak to background ratios for all " $N \rightarrow \Delta$ " kinematics.	99
5.1	Hall A optics resolutions at the target.	107
A.1	Survey $z_{tg}$ positions.	121

A.2	Electron arm mispointing (mm).	129
A.3	Hadron arm mispointing (mm).	130
A.4	Electron arm spectrometer $x$ -offsets (mm).	131
A.5	Electron arm spectrometer $z$ -offsets (mm).	132
A.6	Hadron arm spectrometer $x$ -offsets (mm).	133
A.7	Hadron arm spectrometer $z$ -offsets (mm).	134
A.8	Electron arm $react_z$ positions and survey $z_{tg}$ (mm).	135
A.9	Hadron arm $react_z$ positions and survey $z_{tg}$ (mm).	136
C.1	List of database and header files used in analysis of production runs.	194
F.1	Hadron arm scintillator $x$ and $y$ geometry cuts.	275
F.2	Electron arm S1 and S2 scintillator efficiencies.	276
F.3	Hadron arm S1 and S2 scintillator efficiencies.	276

## LIST OF FIGURES

1.1.1	Angular acceptance for “ $N \rightarrow \Delta$ ” with cuts of $W = 1160\text{-}1360$ MeV and $Q^2 = 0.8\text{-}1.2$ (GeV/c) <sup>2</sup> .	4
1.2.1	Leading order diagram for $p(e, e'p)\pi^0$ in the one-photon-exchange approximation.	6
1.2.2	Kinematics for the exclusive scattering “ $N \rightarrow \Delta$ ” experiment in the lab frame.	7
2.1.1	An $(e, e'p)$ scattering spectra showing three resonance regions plotted against missing mass.	19
2.2.1	Shape of particle charge density.	20
2.2.2	Pion production Feynman diagrams.	21
2.3.1	$N \rightarrow \Delta(1232)$ quadrupole transition via the one-body quadrupole operator $\hat{Q}_{[1]}$ coming from the one-quark current.	24
2.3.2	Feynman diagrams of two-body gluon and pion exchange currents.	25
2.3.3	The $N \rightarrow \Delta(1232)$ quadrupole transition via the two-body quadrupole operator $\hat{Q}_{[2]}$ originating from the two-body gluon current.	25
2.3.4	Intrinsic quadrupole deformation of the nucleon and $\Delta(1232)$ in the pion cloud model.	26
2.4.1	$Q^2$ dependence of $Im(M_{1+})$ , $Im(E_{1+})$ , and $Im(S_{1+})$ at $W = 1232$ MeV.	27
2.5.1	Polarized photon asymmetries for the $\vec{\gamma}p \rightarrow \pi^0 p$ and $\vec{\gamma}p \rightarrow \pi^+ n$ reactions plotted versus $\theta_{cm}$ .	28
2.5.2	$Q^2$ dependence of the quadrupole amplitudes, $CMR$ and $EMR$ , for $\gamma p \rightarrow \Delta(1232) \rightarrow p + \pi^0$ .	29
3.1.1	Hall A layout.	35

3.2.1	Layout of CEBAF.	36
3.2.2	Current over entire " $N \rightarrow \Delta$ " experiment, showing a world record high current with high polarization.	37
3.2.3	Setup for the Arc method of absolute electron beam energy measurement in Hall A.	39
3.2.4	The eP detector used to measure the absolute electron beam energy in Hall A.	40
3.2.5	Layout of the Møller polarimeter.	41
3.2.6	Schematic of the Compton polarimeter, showing the four dipoles of the magnetic chicane, the optical cavity, and the photon and electron detectors.	43
3.2.7	Beam polarization measurements taken by the Compton polarimeter during " $N \rightarrow \Delta$ ".	45
3.4.1	Layout of the Hall A HRS.	47
3.4.2	Side view of the HRS detector packages.	49
3.4.3	Sample coincidence time spectrum between the two HRS for $\theta_{pq} = 90^\circ$ .	50
3.4.4	Layout of the VDCs.	51
3.4.5	An example of a particle trajectory in a VDC plane.	52
3.4.6	Shower counter configuration in both HRS.	53
3.5.1	Layout of the FPP.	54
3.5.2	Six straws in two different planes of an FPP straw chamber.	55
3.5.3	Block diagram for the logic of the FPP signal.	56
4.1.1	Angular kinematic coverage and $W$ versus $Q^2$ coverage for " $N \rightarrow \Delta$ ", showing bins in $\theta_{pq}$ , $\phi_{pq}$ , $W$ , and $Q^2$ .	60
4.2.1	ADC and TDC spectra from one side of a scintillator paddle.	61
4.2.2	Drift time spectrum.	62
4.2.3	Drift cell in a VDC plane showing three tracks corresponding to three different TDC signals.	63
4.2.4	Typical VDC track crossing five drift cells in a VDC plane.	64

4.2.5	Side and top views of the VDC ( $uv$ ) and detector hut ( $xyz$ ) coordinate systems.	65
4.2.6	Transport coordinate system at the VDC (side view).	66
4.2.7	Transport coordinate system at the target.	66
4.2.8	Distributions of the proton target coordinates for $\theta_{pq} = 0^\circ$ .	68
4.3.1	$E_{miss}$ versus $p_{miss}$ spectra for $\theta_{pq} = -50^\circ$ .	69
4.3.2	Sample $\beta$ versus energy deposited in the ADC spectrum for $\theta_{pq} = -155^\circ$ .	70
4.3.3	Sample plots of target reconstruction variables for $\theta_{pq} = -135^\circ$ .	71
4.3.4	Missing mass spectrum for $\theta_{pq} = 90^\circ$ and $-90^\circ$ showing results of cuts on $tc_{cor}$ versus $react_z$ , $\beta$ versus energy deposited, and $E_{miss}$ versus $p_{miss}$ .	72
4.4.1	Illustration of the determination of a cluster in an FPP chamber.	73
4.4.2	Possible FPP tracks for two straws with drift distances $d_1$ and $d_2$ .	74
4.4.3	Cartesian angles for FPP tracks.	75
4.4.4	Spherical angles of the scattered proton in the FPP.	76
4.4.5	Principle of polarimetry: the strong interaction between the proton and carbon analyzer nucleus depends on the proton spin.	77
4.4.6	Analyzing power versus $\theta_{fpp}$ comparing the McNaughton and " $N \rightarrow \Delta$ " parameterization fits.	80
4.4.7	FPP cone test to determine if a cone of angle $\theta_{fpp}$ about the particle track is entirely within the rear chamber acceptance.	81
4.4.8	Distribution of $\theta_{fpp}$ at $\theta_{pq} = 25^\circ$ .	81
4.4.9	Secondary scattering vertex versus polar scattering angle for $\theta_{pq} = -25^\circ$ .	82
4.5.1	$\delta$ -scan of three data sets using a cut of $\theta_{fpp} = 3^\circ$ - $70^\circ$ .	85
4.5.2	Comparison of three VDC alignment methods.	86
4.5.3	$\theta_{fpp}$ -scan using cuts on the edges of the carbon blocks and the $align_{SSD}$ method.	87
4.5.4	$\delta$ -scan of $-4\% < \delta < +4\%$ using the $align_{SSD}$ method, tight cuts on carbon thickness, and $\theta_{fpp} = 5^\circ$ - $20^\circ$ .	87

4.5.5	Coverage region of elastic data for false asymmetry studies compared to “ $N \rightarrow \Delta$ ” production data coverage.	88
4.5.6	Average of the $\delta$ -scan of $-4\% < \delta < +4\%$ using the <i>align<sub>SSSD</sub></i> method, tight cuts on carbon thickness, and $< \theta_{fpp} = 5^\circ$ - $20^\circ$ .	89
4.5.7	Linear fit of $a_0$ false asymmetry term.	89
4.5.8	A simple perfect dipole approximation of the spectrometer model.	92
4.6.1	Corrected coincidence timing peaks for each “ $N \rightarrow \Delta$ ” kinematic setting.	98
4.6.2	Sample comparison of $P_t$ before and after background subtraction.	101
4.6.3	Sample comparison of helicity independent response functions before and after background subtraction.	102
4.7.1	Measurements of the electric to magnetic form factor ratio.	103
5.3.1	Feynman diagrams for internal bremsstrahlung radiative effects.	108
5.3.2	Sample comparison of Monte Carlo simulation with and without radiative corrections.	109
5.4.1	Target polarization $P_t$ for $W = 1200$ - $1240$ MeV and $Q^2 = 0.8$ - $1.0$ (GeV/c) <sup>2</sup> .	111
5.4.2	Target polarization $P_n$ for $W = 1200$ - $1240$ MeV and $Q^2 = 0.8$ - $1.0$ (GeV/c) <sup>2</sup> .	112
5.4.3	Target polarization $P_l$ for $W = 1200$ - $1240$ MeV and $Q^2 = 0.8$ - $1.0$ (GeV/c) <sup>2</sup> .	113
5.4.4	Target polarization $P'_t$ for $W = 1200$ - $1240$ MeV and $Q^2 = 0.8$ - $1.0$ (GeV/c) <sup>2</sup> .	114
5.4.5	Target polarization $P'_n$ for $W = 1200$ - $1240$ MeV and $Q^2 = 0.8$ - $1.0$ (GeV/c) <sup>2</sup> .	115
5.4.6	Target polarization $P'_l$ for $W = 1200$ - $1240$ MeV and $Q^2 = 0.8$ - $1.0$ (GeV/c) <sup>2</sup> .	116
5.5.1	Response functions for $W = 1200$ - $1240$ MeV and $Q^2 = 0.8$ - $1.0$ (GeV/c) <sup>2</sup> .	117
A.0.1	Sample $y_{tg}$ and $beam_x$ plots from run 1216.	122
A.0.2	Spectrometer mispointing.	123

A.0.3	Electron arm $x$ - and $z$ -offsets.	124
A.0.4	Hadron arm $x$ - and $z$ -offsets.	125
A.0.5	Example of a plot of $react_z$ from run 1216.	126
A.0.6	Electron and hadron arm $react_z$ positions.	127
A.0.7	Difference between electron and hadron arm $react_z$ positions.	128
C.0.1	Optimizations of hadron arm momentum versus energy deposited, hadron arm momentum versus $\beta$ , and electron arm $x_{rot}$ versus $tc_{cor}$ for runs 1223 ( $\theta_{pq} = 0^\circ$ ) and 1340 ( $\theta_{pq} = 50^\circ$ ) using database <i>db_ndelta_1</i> .	196
C.0.2	Optimizations of hadron arm momentum versus energy deposited, hadron arm momentum versus $\beta$ , and electron arm $x_{rot}$ versus $tc_{cor}$ for runs 1372 ( $\theta_{pq} = 50^\circ$ ) and 1548 ( $\theta_{pq} = 90^\circ$ ) using database <i>db_ndelta_2</i> .	197
C.0.3	Optimizations of hadron arm momentum versus energy deposited, hadron arm momentum versus $\beta$ , and electron arm $x_{rot}$ versus $tc_{cor}$ for runs 1569 ( $\theta_{pq} = 135^\circ$ ) and 2033 ( $\theta_{pq} = -155^\circ$ ) using database <i>db_ndelta_3</i> .	198
C.0.4	Optimizations of hadron arm momentum versus energy deposited, hadron arm momentum versus $\beta$ , and electron arm $x_{rot}$ versus $tc_{cor}$ for runs 2051 ( $\theta_{pq} = -135^\circ$ ) and 2675 ( $\theta_{pq} = 25^\circ$ ) using database <i>db_ndelta_4</i> .	199
C.0.5	Optimizations of hadron arm momentum versus energy deposited, hadron arm momentum versus $\beta$ , and electron arm $x_{rot}$ versus $tc_{cor}$ for runs 2846 ( $\theta_{pq} = 50^\circ$ ) and 3465 ( $\theta_{pq} = 135^\circ$ ) using database <i>db_ndelta_5</i> .	200
C.0.6	Optimizations of hadron arm momentum versus energy deposited, hadron arm momentum versus $\beta$ , and electron arm $x_{rot}$ versus $tc_{cor}$ for runs 3559 ( $\theta_{pq} = 135^\circ$ ) and 4034 ( $\theta_{pq} = 180^\circ$ ) using database <i>db_ndelta_6</i> .	201
F.4.1	Electron and hadron arm S1 and S2 scintillator efficiencies.	277





## ABSTRACT

This thesis reports results from the Thomas Jefferson National Accelerator Facility (Jefferson Lab) Hall A experiment E91-011, which measured double-polarization observables in the pion electroproduction reaction from the proton. Specifically, the experiment measured the recoil proton polarization, polarized response functions, and cross section for the  $p(\vec{e}, e'\vec{p})\pi^0$  reaction at a center-of-mass energy centered at  $W = 1232$  MeV - the peak of the  $\Delta(1232)$  resonance - and at a four-momentum transfer squared of  $Q^2 = 1.0$   $\text{GeV}^2/c^2$ . Both the recoil proton polarization and polarized response function results will be presented in this thesis.

Data were collected at Jefferson Lab, located in Newport News, Virginia during the summer of 2000. A 4.53 GeV polarized electron beam was scattered off of a cryogenic hydrogen target. The recoil proton polarization was measured in the Focal Plane Polarimeter (FPP), located in one of the two High Resolution Spectrometers (HRS) in Hall A. A maximum likelihood method was used to determine the polarized response functions directly from the measured polarizations and cross sections.

A simultaneous fit of the cross sections, the recoil proton polarizations, and angular distributions of the polarized response functions will provide a determination of individual multipole amplitudes. Some of these multipole amplitudes are related to the concept of proton deformation. Both the recoil proton polarizations and polarized response functions were compared to two phenomenological models: MAID and SAID, which have all free parameters fixed, based on fits to previous world data. The measured helicity dependent observables, which are dominated by imaginary parts of  $\Delta(1232)$ -resonance excitation multipole amplitudes, agree very well with the two models. The measured helicity independent observables, which are dominated by real parts of background multipole amplitudes, do not agree completely with either model. These helicity independent observables are being measured accurately for the first time, giving new insight to the deformation of the proton and into reaction mechanisms of pion production.



## CHAPTER 1

# INTRODUCTION

### 1.1. Overview

The quest to find the fundamental building blocks of matter and to understand how these elemental particles interact is the premise behind nuclear physics. As understanding of physical laws improves, the view on what constitutes these basic building blocks changes. For example, beginning with Rutherford's discovery of the nucleus in 1911 [1], it was assumed that the nucleus consisted of only *fundamental* particles called *protons* and *electrons*. This list of elementary particles was expanded in 1932 with the discovery of the *neutron* [2]. Experiments performed in the 1960s then discovered that protons and neutrons appear to contain smaller, point-like particles called *quarks* [3].

Today, the list of fundamental particles contains two different types of particles: *bosons* and *fermions*. Bosons are particles with integer spin, such as *photons* and *gluons*; fermions are particles with fractional spin, such as *quarks* and *leptons*. Leptons are light particles, such as electrons, that participate in electromagnetic (by exchanging photons) and weak interactions (by exchanging W and Z bosons); quarks are the basic building blocks of hadrons, such as *mesons* (e.g. pions) and *baryons* (e.g. protons and neutrons), that interact with each other through strong (by exchange of gluons) and electro-weak interactions. In their simplest form, mesons consist of a quark, anti-quark pair; baryons contain three quarks. Because the nucleus is comprised of protons and neutrons (together called *nucleons*), which in turn contain quarks, a complete understanding of the nucleus cannot be truly achieved without first understanding quarks and their interactions. However, difficulties lie in the direct observation of any properties of the quark because individual quarks cannot be isolated. For this reason, single quark characteristics can only be inferred from measurements made on groups of quarks interacting with outside forces as well as with each other.

One area of current interest to nuclear physicists is how quark interactions affect the shape of the nucleon, in particular the deviation of the proton shape from spherical. In-

formation about the shape of the nucleon can be obtained by exciting the nucleon to a higher energy state. This is analogous to experiments which excite the nucleus in order to understand the effective interactions between protons and neutrons.

A proton can be excited to its first excited state, the  $\Delta(1232)$  resonance, by a photon through an electromagnetic transition,  $\gamma + p \rightarrow \Delta(1232)$ . This transition multipole can be of three types: magnetic dipole ( $M_{1+}$ ), electric ( $E_{1+}$ ) quadrupole, or Coulomb or scalar ( $S_{1+}$ ) quadrupole.<sup>1</sup> The  $E_{1+}$  and  $S_{1+}$  multipoles are best measured as interferences with the much more dominant  $M_{1+}$ . The  $M_{1+}$  term, a magnetic dipole transition operator connecting the proton and  $\Delta(1232)$  wavefunctions by having total  $L = 0$  between the quarks in each wavefunction, is consistent with a simple spin-flip of one of the quarks inside the proton, and therefore a “spherical” proton. If the transition is made with either the electric or scalar quadrupole transition operator, some  $L > 0$  components must be included in both the proton and  $\Delta(1232)$  wavefunctions to allow the transition [4]. These resulting non-spherically symmetric spatially distributed wavefunctions are defined as “deformed”. A measurement of the  $E_{1+}$  and  $S_{1+}$  multipole terms is then an indirect measurement of the proton’s deformation. Observables dependent upon the real parts of the  $M_{1+}E_{1+}$  and  $M_{1+}S_{1+}$  multipole interferences are sensitive to these small quadrupole terms (as will be shown in Eqns. (1.4.9)-(1.4.21)). Recoil-proton polarization observables can be used to better understand the properties of nucleon resonances and the reaction mechanism for pion electroproduction, because they can access both the real and imaginary parts of the interference amplitudes.

Both recoil proton polarization and polarized response functions of the  $p(\vec{e}, e' \vec{p}) \pi^0$  reaction near the  $\Delta(1232)$  resonance, along with the differential cross section, were measured in the E91-011 (“ $N \rightarrow \Delta$ ”) experiment performed in Hall A of the Thomas Jefferson National Accelerator Facility (Jefferson Lab), located in Newport News, Virginia. This experiment ran between May 19 and August 1, 2000 using a beam energy of  $E = 4.53$  GeV, a central electron scattering angle of  $\theta_e = 14.1^\circ$ , and a central scattered electron momentum of  $k' = 3.7$  GeV/ $c$ . Data were collected for a four-momentum transfer squared centered at  $Q^2 = 1.0$  (GeV/ $c$ )<sup>2</sup>, a total center of mass (cm) energy centered at  $W = 1232$  MeV, and twelve different proton momenta and angles. Tab. 1.1 lists the nominal center of mass in-plane<sup>2</sup> ( $\theta_{pq}$ ) and out-of-plane ( $\phi_{pq}$ ) angles, in-plane laboratory angles, and central proton momenta for each kinematic setting. The total charge (beam on target or average current

<sup>1</sup>The notation for the multipole terminology will be fully clarified later in this thesis.

<sup>2</sup>Throughout this text, for convenience, the “cm” labels on  $\theta_{pq}^{cm}$  and  $\phi_{pq}^{cm}$  will be omitted, leaving simply  $\theta_{pq}$  and  $\phi_{pq}$ .

TABLE 1.1. Summary of kinematics for “ $N \rightarrow \Delta$ ”.

$\theta_{pq}$	$\phi_{pq}$	$\theta_p^{lab}$	$p_p$ (GeV/ $c$ )	charge (C)
0°		42.3°	1.378	25.9
25°	0°	38.1°	1.350	7.9
25°	180°	46.3°	1.350	4.6
50°	0°	34.3°	1.270	18.9
50°	180°	50.2°	1.270	12.9
90°	0°	29.8°	1.066	15.5
90°	180°	54.8°	1.066	20.1
135°	0°	30.8°	0.819	14.6
135°	180°	53.6°	0.819	27.6
155°	0°	34.7°	0.742	13.9
155°	180°	49.7°	0.742	13.6
180°		42.3°	0.703	5

times time) collected for each setting is also listed. Notice that all  $\phi_{pq}$  angles are either 0° or 180°; therefore in-plane. However, due to the acceptance of the Hall A spectrometers, this experiment was able to measure a considerable amount of out-of-plane data, as shown in Fig. 1.1.1.<sup>3</sup>

This thesis is separated into five chapters. The remainder of this first chapter will introduce electron scattering and how it can be used to study nucleon resonances. Also described in Chapter 1 is how the measurement of recoil proton polarizations, and polarized response functions, allow for the extraction of interference multipole amplitudes. Chapter 2 outlines the current basic knowledge about the proton and gives the motivation behind this particular experiment. The experimental equipment used by the “ $N \rightarrow \Delta$ ” experiment is discussed in Chapter 3, along with an outline of the experimental procedure. The analysis method employed for recoil proton polarization and polarized response function extraction are outlined in Chapter 4. The final chapter discusses the results of “ $N \rightarrow \Delta$ ” compared to predictions and other measurements, along with a synopsis of what analysis still needs to be completed by the E91-011 collaboration in order to extract the transition multipoles.

---

<sup>3</sup>Full, formal definitions of all kinematic quantities referred to in this paragraph will be provided later in this chapter.

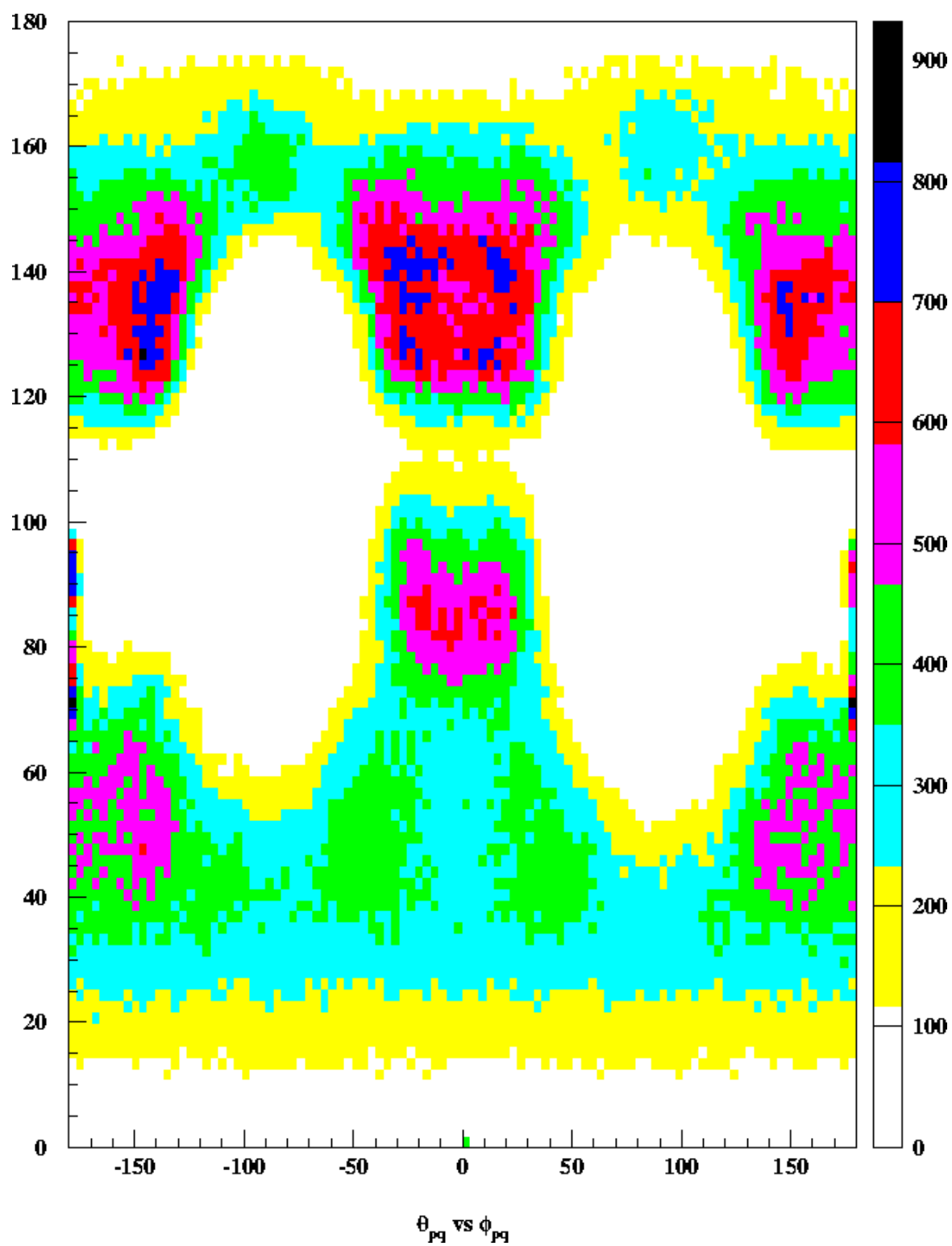


FIGURE 1.1.1. Angular acceptance for " $N \rightarrow \Delta$ " with cuts of  $W = 1160$ - $1360$  MeV and  $Q^2 = 0.8$ - $1.2$   $(\text{GeV}/c)^2$ .

## 1.2. Electron Scattering Formalism

In electron scattering an electron can exchange a virtual photon with a target nucleus thus probing the electromagnetic structure of this nucleus. This scattering is advantageous for several reasons:

- ◆ The electromagnetic coupling constant is relatively small ( $\alpha \approx e^2/(2\varepsilon_0\hbar c) = 1/137$ ), suppressing higher order perturbations. The reaction can then be described by the one photon exchange approximation, where the photon has four-momentum  $q = (\varpi, \vec{q})$ . Fig. 1.2.1 shows the lowest order Feynman diagram for  $p(e, e'p)\pi^0$  (of interest for this thesis), represented by:

$$e(k) + P(p_i) \rightarrow e(k') + P(p_p) + \pi^0(p_x), \quad (1.2.1)$$

where the initial and final electron four-momenta, and the initial and final proton momenta are  $k = (E, \vec{k})$ ,  $k' = (E', \vec{k}')$ ,  $p_i = (E_i, \vec{p}_i)$ , and  $p_p = (E_p, \vec{p}_p)$ , respectively and the pion four-momentum is  $p_x = q + p_i - p_p = (E_x, \vec{p}_x)$ . The Lorentz-invariant four-momentum transfer squared is defined as:

$$Q^2 = -q^2 = -(\varpi^2 - \vec{q}^2) \approx 4EE' \sin^2 \frac{\theta_e}{2}, \quad (1.2.2)$$

where the electron mass can be neglected if the electron is ultra-relativistic, as will be the case here. Large values of  $Q^2$  are associated with very short wavelengths. Virtual photons of these wavelengths are then able to probe the short-scale structure of the proton.

- ◆ The leptonic vertex,  $e(k) \rightarrow e(k') + \gamma^*(q)$ , is well understood in Quantum ElectroDynamics (QED), the fundamental theory of the electromagnetic interaction. Experiments are therefore able to focus on the hadronic vertex,  $\gamma^*(q) + P(p_i) \rightarrow P(p_p) + \pi^0(p_x)$  and the unknown properties of the proton structure.
- ◆ Though electrons can interact via both the weak and electromagnetic forces, the electromagnetic force is much stronger, allowing for study of the electromagnetic structure of the nucleus.

There are also disadvantages to the use of the electromagnetic probe. First, due to the small mass of the electron, radiative corrections must be accounted for. Second, because the cross section associated with electron scattering is so small, high beam intensities are required.

There are two types of electron scattering experiments: *inclusive* and *exclusive*. Inclu-

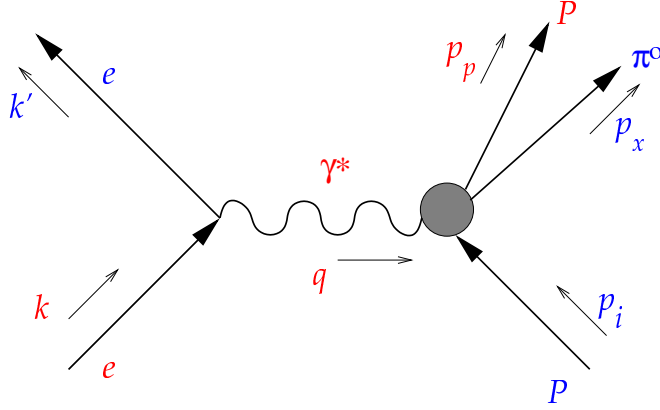


FIGURE 1.2.1. Leading order diagram for  $p(e, e'p)\pi^0$  in the one-photon-exchange approximation.

sive measurements, in which only the scattered electron is detected, limit the amount of nuclear structure information obtained because combinations of many final states are possible. Exclusive experiments, in which a recoil hadron (or photon) is detected in coincidence with the scattered electron, allow for determination of amplitudes to scatter into a specific final state, namely a proton-pion final state in this experiment.

The “ $N \rightarrow \Delta$ ” experiment reported in this thesis used exclusive electron scattering, the kinematics of which are shown in Fig. 1.2.2, in which the scattered electron was detected in coincidence with the recoil proton. Unlike the general formalism given above, here the initial proton momentum is  $p_i = 0$ . The scattering plane is defined by the incoming and scattered electrons, where  $\theta_e$  is the angle of the detected electron with respect to the incident electron beam. The reaction plane is defined by the momenta of the virtual photon  $q$  and recoil proton  $p_p$ , where the recoil proton emerges at an angle of  $\theta_{pq}$  with respect to  $q$  in the center of mass. The azimuthal angle, the angle between the scattering and reaction planes, is  $\phi_{pq}$ . The  $\pi^0$  was undetected, but its presence was verified using missing mass techniques.

Additional information about nucleon structure can be obtained when one or more of the particles is polarized. This allows the constraint of additional degrees of freedom associated with spin and/or angular momentum. The “ $N \rightarrow \Delta$ ” experiment utilized a polarized electron beam incident on a proton target. The reaction of interest was when the proton was excited to the  $\Delta(1232)$  resonance, with some of the polarization being transferred to the  $\Delta(1232)$ , and the  $\Delta(1232)$  subsequently decayed into a proton and  $\pi^0$ , with the recoil proton carrying away some polarization. The components of the recoil



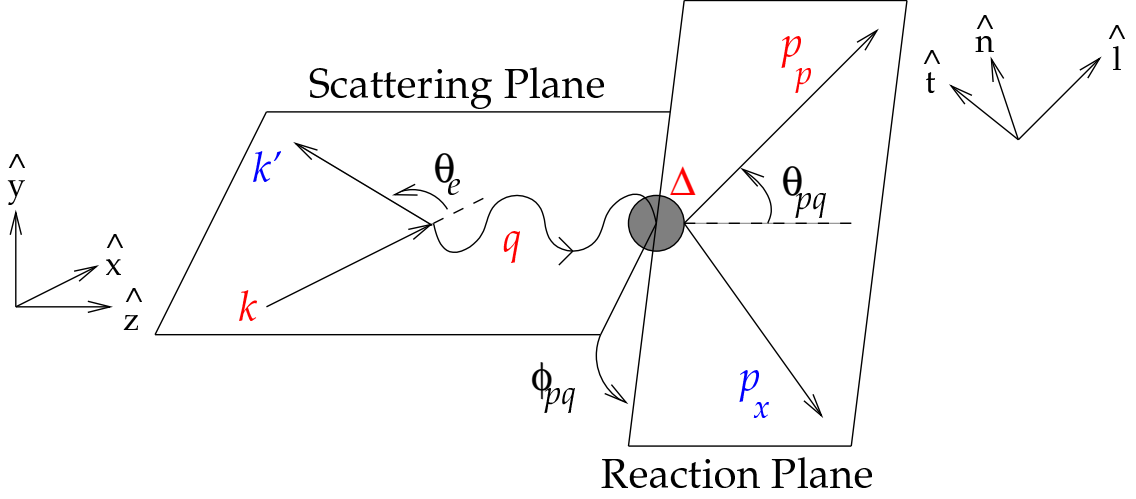


FIGURE 1.2.2. Kinematics for the exclusive scattering “ $N \rightarrow \Delta$ ” experiment in the lab frame.

proton polarization ( $\hat{s}_R$ ) at the target, shown in Fig. 1.2.2, are expressed in terms of  $\hat{n}$ ,  $\hat{l}$ , and  $\hat{t}$ , where  $\hat{n}$  is perpendicular to the reaction plane,  $\hat{l}$  is along the direction of the proton momentum, and  $\hat{t} = \hat{n} \times \hat{l}$ .

### 1.3. The Differential Cross Section

The electromagnetic structure of the nucleus can be characterized by a set of multipole matrix elements of the electromagnetic current operator. These matrix elements are directly related to the Fourier transforms of the corresponding current matrix elements involving both the initial and final nuclear states, and can be experimentally probed. The electron kinematics, along with the recoil proton momentum, can be chosen so that a particular transition between the nuclear states is investigated. For the “ $N \rightarrow \Delta$ ” experiment, these kinematics were chosen such that the transition between the proton and the  $\Delta(1232)$  was studied.

Following the conventions of Bjorken and Drell [5], the cross section in the laboratory frame for the electroproduction of polarized protons using polarized electrons on a stationary target can be written as:

$$d\sigma = \frac{2\pi m_e e^4}{E} \frac{1}{q^4} \left[ \frac{\eta_{\mu\nu} W^{\mu\nu}(\hat{s}_R)}{m_e^2} \right] \left[ \frac{m_e}{E'} \frac{d^3 k'}{(2\pi)^3} \right] \left[ \frac{m_p}{E_p} \frac{d^3 p_p}{(2\pi)^3} \right] \left[ \frac{m_x}{E_x} \frac{d^3 p_x}{(2\pi)^3} \right], \quad (1.3.1)$$

where  $m_e$ ,  $m_p$ , and  $m_x$  are the electron, proton, and pion masses, respectively,  $e$  is the electron charge,  $\eta_{\mu\nu}$  is the electron tensor,  $W^{\mu\nu}$  is the nuclear electromagnetic tensor, and  $\hat{s}_R$  is the spin vector of the ejected proton.

**1.3.1. The Electron Tensor.** The electron tensor describes the leptonic vertex. In the Extreme Relativistic Limit (ERL), this tensor can be written as a combination of a helicity-independent, symmetric, real part  $\eta_S^{\mu\nu}$  and a helicity-dependent, antisymmetric, imaginary part  $\eta_A^{\mu\nu}$  [6]:

$$\eta^{\mu\nu} = \eta_S^{\mu\nu} + \eta_A^{\mu\nu}. \quad (1.3.2)$$

These symmetric and antisymmetric pieces can in turn be characterized in terms of  $K = k + k'$ ,  $q$ , and the initial electron helicity  $h$ :

$$\eta_S^{\mu\nu} = \left[ K^\mu K^\nu + \frac{q^2}{4} \left( g^{\mu\nu} - \frac{q^\mu q^\nu}{q^2} \right) \right]. \quad (1.3.3)$$

$$\eta_A^{\mu\nu} = \frac{ih}{2} \epsilon^{\mu\nu\rho\sigma} K_\rho q_\sigma, \quad (1.3.4)$$

where the metric tensor is

$$g^{\mu\nu} = g_{\mu\nu} = \begin{pmatrix} 1 & 0 & 0 & 0 \\ 0 & -1 & 0 & 0 \\ 0 & 0 & -1 & 0 \\ 0 & 0 & 0 & -1 \end{pmatrix}, \quad (1.3.5)$$

and  $\epsilon^{\mu\nu\rho\sigma}$  is the completely antisymmetric Levi-Civita tensor as defined by Bjorken and Drell [5].

**1.3.2. The Nuclear Tensor.** The nuclear response tensor describes the hadronic vertex and contains the nuclear structure information. It can also be decomposed into symmetric and antisymmetric parts [7]:

$$W^{\mu\nu}(\hat{s}_R') = W_S^{\mu\nu}(\hat{s}_R') + W_A^{\mu\nu}(\hat{s}_R'). \quad (1.3.6)$$

When the constraints of parity invariance and current conservation are imposed, this tensor can be defined in terms of eighteen independent elements, where  $[A^\mu B^\mu]_{S,A} \equiv A^\mu B^\mu \pm A^\nu B^\mu$  [7]:

$$\begin{aligned}
W_S^{\mu\nu}(\hat{\mathbf{s}}'_R) = & (W_1 + W'_1 \hat{n} \cdot \hat{\mathbf{s}}'_R) G^{\mu\nu} + (W_2 + W'_2 \hat{n} \cdot \hat{\mathbf{s}}'_R) V_i^\mu V_i^\nu \\
& + (W_3 + W'_3 \hat{n} \cdot \hat{\mathbf{s}}'_R) V_f^\mu V_f^\nu + (W_4 + W'_4 \hat{n} \cdot \hat{\mathbf{s}}'_R) [V_i^\mu V_f^\nu]_S \\
& + \left( W_5 \hat{t} \cdot \hat{\mathbf{s}}'_R + W'_5 \hat{l} \cdot \hat{\mathbf{s}}'_R \right) [V_i^\mu \xi^\nu]_S \\
& + \left( W_6 \hat{t} \cdot \hat{\mathbf{s}}'_R + W'_6 \hat{l} \cdot \hat{\mathbf{s}}'_R \right) [V_f^\mu \xi^\nu]_S,
\end{aligned} \tag{1.3.7}$$

$$\begin{aligned}
W_A^{\mu\nu}(\hat{\mathbf{s}}'_R) = & (W_7 + W'_7 \hat{n} \cdot \hat{\mathbf{s}}'_R) [V_i^\mu V_f^\nu]_A + \left( W_8 \hat{t} \cdot \hat{\mathbf{s}}'_R + W'_8 \hat{l} \cdot \hat{\mathbf{s}}'_R \right) [\xi^\mu V_i^\nu]_A \\
& + \left( W_9 \hat{t} \cdot \hat{\mathbf{s}}'_R + W'_9 \hat{l} \cdot \hat{\mathbf{s}}'_R \right) [\xi^\mu V_f^\nu]_A,
\end{aligned} \tag{1.3.8}$$

$W_i$  and  $W'_i$  are functions of momentum-space scalars,  $\hat{\mathbf{s}}'_R$  is the direction of polarization of the recoil proton,  $\hat{n}$ ,  $\hat{t}$ , and  $\hat{l}$  are the component directions as defined in Fig. 1.2.2,

$$G^{\mu\nu} = g^{\mu\nu} - \frac{q^\mu q^\nu}{q^2}, \tag{1.3.9}$$

and  $V_i$ ,  $V_f$ ,  $\bar{V}_f$ , and  $\xi^\mu$  are a set of orthogonal, linearly independent four-vectors spanning the four-dimensional space:

$$V_i = p_i - \frac{\vec{p}_i \cdot \vec{q}}{q^2} q, \tag{1.3.10}$$

$$V_f = p_p - \frac{\vec{p}_p \cdot \vec{q}}{q^2} q, \tag{1.3.11}$$

$$\xi^\mu = \epsilon^{\mu\nu\rho\sigma} q_\nu (\bar{V}_f)_\rho (V_i)_\sigma, \tag{1.3.12}$$

and

$$\bar{V}_f = V_f - \frac{\vec{V}_f \cdot \vec{V}_i}{V_i^2} V_i. \tag{1.3.13}$$

**1.3.3. Response Functions.** The electron and nuclear tensors must now be contracted in order to calculate the cross section [7]:

$$\eta_{\mu\nu} W^{\mu\nu}(\hat{\mathbf{s}}'_R) = \eta_{\mu\nu}^S W_S^{\mu\nu}(\hat{\mathbf{s}}'_R) + \eta_{\mu\nu}^A W_A^{\mu\nu}(\hat{\mathbf{s}}'_R). \tag{1.3.14}$$

In the lab frame, after the contraction, the symmetric piece depends only on four components of the nuclear tensor:  $W_S^{00}(\hat{\mathbf{s}}'_R)$ ,  $W_S^{11}(\hat{\mathbf{s}}'_R) + W_S^{22}(\hat{\mathbf{s}}'_R)$ ,  $W_S^{11}(\hat{\mathbf{s}}'_R) - W_S^{22}(\hat{\mathbf{s}}'_R)$ , and  $W_S^{02}(\hat{\mathbf{s}}'_R) + W_S^{20}(\hat{\mathbf{s}}'_R)$ . Due to the antisymmetric nature of  $\eta_A^{\mu\nu}$ , the antisymmetric component depends solely on two components of the nuclear tensor:  $W_A^{10}(\hat{\mathbf{s}}'_R) - W_A^{01}(\hat{\mathbf{s}}'_R)$  and  $W_A^{12}(\hat{\mathbf{s}}'_R) - W_A^{21}(\hat{\mathbf{s}}'_R)$ . These relevant nuclear tensors can be expressed in terms of a set of eighteen arbitrary response functions  $R_\eta$ , dependent on  $|\vec{q}|$ ,  $|\vec{p}_p|$ ,  $\varpi$ , and  $\theta_{pq}$ , but inde-

pendent of  $\phi_{pq}$  [7]:

$$W^{00}(\hat{\mathbf{s}}'_R) = R_L + R_L^n \hat{n} \cdot \hat{\mathbf{s}}'_R, \quad (1.3.15)$$

$$W^{11}(\hat{\mathbf{s}}'_R) + W^{22}(\hat{\mathbf{s}}'_R) = R_T + R_T^n \hat{n} \cdot \hat{\mathbf{s}}'_R, \quad (1.3.16)$$

$$\begin{aligned} W^{22}(\hat{\mathbf{s}}'_R) - W^{11}(\hat{\mathbf{s}}'_R) &= (R_{TT} + R_{TT}^n \hat{n} \cdot \hat{\mathbf{s}}'_R) \cos 2\phi_{pq} \\ &\quad + \left( R_{TT}^t \hat{t} \cdot \hat{\mathbf{s}}'_R + R_{TT}^l \hat{l} \cdot \hat{\mathbf{s}}'_R \right) \sin 2\phi_{pq}, \end{aligned} \quad (1.3.17)$$

$$\begin{aligned} W^{02}(\hat{\mathbf{s}}'_R) + W^{20}(\hat{\mathbf{s}}'_R) &= (R_{LT} + R_{LT}^n \hat{n} \cdot \hat{\mathbf{s}}'_R) \sin \phi_{pq} \\ &\quad + \left( R_{LT}^t \hat{t} \cdot \hat{\mathbf{s}}'_R + R_{LT}^l \hat{l} \cdot \hat{\mathbf{s}}'_R \right) \cos \phi_{pq}, \end{aligned} \quad (1.3.18)$$

$$\begin{aligned} i [W^{10}(\hat{\mathbf{s}}'_R) - W^{01}(\hat{\mathbf{s}}'_R)] &= (R'_{LT} + R_{LT}^n \hat{n} \cdot \hat{\mathbf{s}}'_R) \cos \phi_{pq} \\ &\quad + \left( R_{LT}^t \hat{t} \cdot \hat{\mathbf{s}}'_R + R_{LT}^l \hat{l} \cdot \hat{\mathbf{s}}'_R \right) \sin \phi_{pq}, \end{aligned} \quad (1.3.19)$$

$$i [W^{12}(\hat{\mathbf{s}}'_R) - W^{21}(\hat{\mathbf{s}}'_R)] = R_{TT}^t \hat{t} \cdot \hat{\mathbf{s}}'_R + R_{TT}^l \hat{l} \cdot \hat{\mathbf{s}}'_R. \quad (1.3.20)$$

The superscripts of  $R_\eta$  denote the components of the proton polarizations as defined in Fig. 1.2.2, the subscripts  $L$ ,  $T$ ,  $LT$ , and  $TT$  refer to the longitudinal, transverse, longitudinal and in-plane transverse interference, and in-plane and orthogonal transverse interference components of the virtual photon, respectively, and the primes indicate polarizations dependent on the initial electron beam helicity.

After contracting the electron and nuclear tensors, the cross section from Eqn. (1.3.1) for the ejection of spin  $\hat{\mathbf{s}}'_R$  protons (protons with polarization components of  $\wp_n$ ,  $\wp_t$ , and  $\wp_l$ ) from scattering of electrons with helicity  $h$  on a proton (spin 1/2) target can be represented as:

$$\begin{aligned} \frac{d\sigma}{d\Omega_p} &= \frac{1}{2} \frac{p_p}{k_\gamma} \{ v_L (R_L + R_L^n \wp_n) + v_T (R_T + R_T^n \wp_n) \\ &\quad + v_{TT} [(R_{TT} + R_{TT}^n \wp_n) \cos 2\phi_{pq} + (R_{TT}^t \wp_t + R_{TT}^l \wp_l) \sin 2\phi_{pq}] \\ &\quad + v_{LT} [(R_{LT} + R_{LT}^n \wp_n) \cos \phi_{pq} + (R_{LT}^t \wp_t + R_{LT}^l \wp_l) \sin \phi_{pq}] \\ &\quad + h v'_{LT} [(R'_{LT} + R_{LT}^n \wp_n) \sin \phi_{pq} + (R_{LT}^t \wp_t + R_{LT}^l \wp_l) \cos \phi_{pq}] \\ &\quad + h v'_{TT} (R_{TT}^t \wp_t + R_{TT}^l \wp_l) \}, \end{aligned} \quad (1.3.21)$$

where  $k_\gamma = (W^2 - m_p^2)/2W$  is the laboratory energy a real photon would need to excite the same transition. The kinematic factors  $v_i$  describing the electron are defined as follows:

$$v_L = \epsilon_s, \quad (1.3.22)$$

$$v_T = 1, \quad (1.3.23)$$

$$v_{TT} = \epsilon, \quad (1.3.24)$$

$$v_{LT} = \sqrt{2\epsilon_s(1+\epsilon)}, \quad (1.3.25)$$

$$v'_{LT} = \sqrt{2\epsilon_s(1-\epsilon)}, \quad (1.3.26)$$

$$v'_{TT} = \sqrt{1-\epsilon^2}, \quad (1.3.27)$$

with  $\epsilon = [1 + 2 (\vec{q}^2/Q^2) \tan^2(\theta_e/2)]^{-1}$  being the transverse polarization of the virtual photon, and  $\epsilon_s = (Q^2/q^2)\epsilon$  the longitudinal polarization.

**1.3.4. Observables and Their Relation to Measurements in “ $N \rightarrow \Delta$ ”.** The spin dependent part of the differential cross section for pion electroproduction can be rewritten as a combination of physical observables [8]:

$$\sigma_v = \sigma_o \left[ 1 + \vec{P} \cdot \vec{\sigma} + h \left( A_h + \vec{P}' \cdot \vec{\sigma} \right) \right], \quad (1.3.28)$$

where  $\sigma_o$  is the unpolarized differential cross section,  $h$  is the longitudinal beam polarization,  $A_h$  is the beam analyzing power,  $\vec{P}$  and  $\vec{P}'$  are the helicity-independent (induced) and helicity-dependent (transferred) recoil proton polarizations, respectively, and  $\vec{\sigma}$  is the Pauli spin matrix. The net polarization of the nucleon can be expressed as a combination of the induced and transferred polarizations and the beam helicity:

$$\vec{\Pi} = \vec{P} + h\vec{P}'. \quad (1.3.29)$$

Referring to Eqn. (1.3.28), one can see that without either a polarized electron beam or a polarized recoil proton, only the unpolarized cross section  $\sigma_o$  is obtainable. However, when polarized electrons are used as a probe, it is possible to determine the analyzing power as well. If the probe is an unpolarized electron but the recoil proton is polarized, it becomes possible to measure both  $\sigma_o$  and the induced polarizations. Using both a polarized electron probe and measuring the recoil proton polarization obviously allows for the most information to be obtained:  $\sigma_o$ ,  $A_h$ , and both the induced and transferred polarizations.

The polarization observables can be decomposed into products of the kinematic factors from Eqns. (1.3.22)-(1.3.27) and the response functions from Eqns. (1.3.15)-(1.3.20) [9]:

$$\sigma_o = v_o (v_L R_L + v_T R_T + v_{TT} R_{TT} \cos 2\phi_{pq} - v_{LT} R_{LT} \cos \phi_{pq}), \quad (1.3.30)$$

$$A_h \sigma_o = v_o (-v'_{LT} R'_{LT} \sin \phi_{pq}), \quad (1.3.31)$$

$$P_n \sigma_o = v_o (v_L R_L^n + v_T R_T^n + v_{TT} R_{TT}^n \cos 2\phi_{pq} - v_{LT} R_{LT}^n \cos \phi_{pq}), \quad (1.3.32)$$

$$P_{l,t} \sigma_o = v_o \left( v_{TT} R_{TT}^{l,t} \sin 2\phi_{pq} - v_{LT} R_{LT}^{l,t} \sin \phi_{pq} \right), \quad (1.3.33)$$

$$P'_n \sigma_o = v_o (-v'_{LT} R_{LT}^m \sin \phi_{pq}), \quad (1.3.34)$$

$$P'_{l,t} \sigma_o = v_o \left( -v'_{LT} R_{LT}^{l,t} \cos \phi_{pq} + v'_{TT} R_{TT}^{l,t} \right), \quad (1.3.35)$$

where  $v_o = p_p/k_\gamma$  in the center of mass.

The “ $N \rightarrow \Delta$ ” experiment performed measurements of the electroproduction cross section and of the recoil proton polarization centered at azimuthal angles of both  $\phi_{pq} = 0^\circ$  and  $180^\circ$ ,  $Q^2 = 1.0 \text{ (GeV}/c)^2$ , and  $W = 1232 \text{ MeV}$ . These measurements, combined with the beam helicity<sup>4</sup> and the beam analyzing power, allow for the separation of all response functions listed in Eqns. (1.3.30)-(1.3.35). In the case of in-plane kinematics the terms proportional to  $\sin \phi_{pq}$  vanish. However, for the “ $N \rightarrow \Delta$ ” experiment the out-of-plane acceptance was considerable, allowing for measurement of terms containing  $\sin \phi_{pq}$  as well.

This thesis focuses on extraction of only those response functions dependent upon the measurement of the recoil proton polarization:  $R_{TT}^n, R_{LT}^n, R_{TT}^l, R_{TT}^t, R_{LT}^l, R_{LT}^t, R_{LT}^m, R_{LT}^{ll}, R_{LT}^{lt}, R_{TT}^{ll}, R_{TT}^{lt}$ , and the combination of  $v_L R_L^n + v_T R_T^n$ . For details on the cross section measurement and extraction of the remaining response functions see the thesis of Z. Chai [10].

## 1.4. Multipole Expansion

The response functions can be expanded into combinations of electromagnetic multipoles. These multipoles are more closely related to the actual physics of the observed processes. In general, an electromagnetic transition can be accomplished by any of three possible electromagnetic multipole types: magnetic ( $M$ ), electric ( $E$ ), and scalar ( $S$ ) or Coulomb ( $C$ ).

The proton is a spin 1/2 particle with positive parity ( $J^\Pi = 1/2^+$ ); the  $\Delta(1232)$  has positive parity, but is a spin 3/2 particle ( $J^\Pi = 3/2^+$ ). In the  $\Delta(1232)$  excitation process,  $\gamma^* p \rightarrow \Delta(1232)$ , spin and parity must both be conserved. For the proton to couple to a  $\Delta(1232)$ , the overall  $J^\Pi$  of the photon must be  $1^+$  or  $2^+$ , as shown:

$$\begin{aligned} J^\Pi \otimes \frac{1}{2} &= \frac{3}{2} \\ J^\Pi &= 1^+, 2^+. \end{aligned} \quad (1.4.1)$$

Since the intrinsic spin of a photon  $S^\Pi$  is  $1^-$  (being a vector particle), the coupling of the

<sup>4</sup>The beam helicity was monitored throughout the “ $N \rightarrow \Delta$ ” experiment using a Compton polarimeter.

proton with the photon's angular momentum  $l$  is written as:

$$\begin{aligned} S^\Pi \otimes l &= J^\Pi \\ 1^- \otimes l &= 1^+, 2^+. \end{aligned} \quad (1.4.2)$$

The parity due to  $l$  is given by  $\Pi = (-1)^l$ , therefore to get the needed overall + parity,  $l$  must be odd. To obtain either  $J^\Pi = 1^+$  or  $2^+$ ,  $l = 1$ .

Three possible multipole types can incite the  $N \rightarrow \Delta(1232)$  transition: magnetic, electric, and Coulomb or scalar. The parity of these multipoles are determined using the following equations [11]:

$$\Pi(MJ) = (-1)^{J+1}, \quad (1.4.3)$$

$$\Pi(EJ) = (-1)^J, \quad (1.4.4)$$

$$\Pi(CJ) = (-1)^J. \quad (1.4.5)$$

The multipoles then making the  $N \rightarrow \Delta(1232)$  transition possible are  $M1$ ,  $E2$ , and  $C2$  (in this notation of the initial reaction state).

The  $\pi N$  final state is the direct result of the  $\Delta(1232)$  decay,  $\gamma^* p \rightarrow \Delta(1232) \rightarrow \pi N$ . The total angular momentum of the final state therefore must equal that of the  $\Delta(1232)$ ,  $J_\Delta = 3/2$ . The final state total angular momentum is given by:

$$J = l \pm \frac{1}{2}, \quad (1.4.6)$$

where  $l$  is the orbital angular momentum of the system and  $1/2$  is the nucleon spin. The spin of the pion is zero and therefore does not contribute to  $J$  for this final state. In order for total angular momentum to be conserved,  $l = 1$  or  $2$ . Since both the  $\Delta(1232)$  and nucleon have positive parity as previously stated, and the pion has negative parity, parity conservation leads to:

$$\begin{aligned} \Pi(\Delta) &= \Pi(N) \cdot \Pi(\pi) \cdot (-1)^l \\ (+1) &= (+1)(-1)(-1)^l \\ &= (-1)^{l+1}, \end{aligned} \quad (1.4.7)$$

where  $l$  must be odd. Therefore  $l = 1$  is the only possibility for  $\Delta$  excitation.

The notation used to describe the multipoles in terms of the final angular momentum of the system are given by  $X_{l\pm}$  where  $X = M, E, S$  referring to the photon's multipole character and  $\pm$  indicates whether the total angular momentum ( $J$ ) of the final state was formed using the "+" or "-" sign in Eqn. (1.4.6). Using this convention, the three

multipoles contributing to the  $N \rightarrow \Delta(1232)$  transition are  $M_{1+}$ ,  $E_{1+}$ , and  $S_{1+}$ . These correspond to the notation of the virtual photon angular momentum as such:

$$\begin{aligned} M1 &\leftrightarrow M_{1+}, \\ E2 &\leftrightarrow E_{1+}, \\ C2 &\leftrightarrow S_{1+}, \end{aligned}$$

where  $L = l$  for the magnetic multipole term and  $|L - l| = 1$  for the electric and scalar multipole terms.

Finally, the response functions of Eqns. (1.3.30)-(1.3.35) can be further expressed as Legendre polynomials  $P_n(x)$  of the form:

$$R_\eta = (1 - x^2)^{\alpha_\eta/2} \sum_{n=0}^{\infty} A_{\eta n} P_n(x), \quad (1.4.8)$$

where  $x = \cos \theta_{pq}$ ,  $\alpha_\eta$  are the leading angular dependencies for the response functions  $R_\eta$ , and each of the Legendre coefficients  $A_{\eta n}$  can be further expanded in terms of pairs of real or imaginary multipole amplitudes. These full expansions in terms of the  $\theta_{pq}$  angular dependence and the bi-linear multipole amplitude combinations are given in Eqns. (1.4.9)-(1.4.21). Note that these expansions are done with the limiting assumptions that:

- (1) the  $M_{1+}$   $\Delta$ -excitation multipole is the dominant amplitude, and thus only bi-linear terms involving  $M_{1+}$  are retained (except in the case of  $R_L^n$  where no  $M_{1+}$  contribution exists); and
- (2) final-state proton-pion angular momentum is limited to  $l = 0$  (terms not due to excitation of  $\Delta$ -resonance) and  $l = 1$ , thus assuming higher partial waves have negligible contribution [9, 12, 13] (this assumption has been verified by fitting cross section angular distributions with Legendre polynomials for the expansion in proton-pion angular momentum [10, 14]).

$$R_L^n = 2 \sin \theta_{pq} \text{Im} \{ S_{1-}^* S_{0+} - 2 S_{1+}^* S_{0+} - 6 \cos \theta_{pq} S_{1-}^* S_{1+} \}, \quad (1.4.9)$$

$$R_T^n = \sin \theta_{pq} \text{Im} \{ M_{1+} E_{0+}^* + 3 \cos \theta_{pq} M_{1+} M_{1-}^* \}, \quad (1.4.10)$$

$$\begin{aligned} R_{LT}^n &= \text{Im} \{ M_{1+} S_{1-}^* - 2 M_{1+} S_{1+}^* \\ &\quad - \cos \theta_{pq} (M_{1+} S_{0+}^* - 6 \cos \theta_{pq} M_{1+} S_{1+}^*) \}, \end{aligned} \quad (1.4.11)$$

$$\begin{aligned} R_{LT}^l &= \sin \theta_{pq} \text{Im} \{ 2 M_{1+} S_{1-}^* - 4 M_{1+} S_{1+}^* \\ &\quad - 3 \cos \theta_{pq} (M_{1+} S_{0+}^* - 6 \cos \theta_{pq} M_{1+} S_{1+}^*) \}, \end{aligned} \quad (1.4.12)$$



$$R_{LT}^t = \text{Im} \left\{ 2M_{1+}S_{0+}^* + \cos \theta_{pq} [M_{1+}S_{1-}^* - 3 \cos \theta_{pq} M_{1+}S_{0+}^* - 2(7 - 9 \cos^2 \theta_{pq}) M_{1+}S_{1+}^*] \right\}, \quad (1.4.13)$$

$$R_{TT}^n = -\sin \theta_{pq} \text{Im} \left\{ 3M_{1+}E_{0+}^* + 3 \cos \theta_{pq} (M_{1+}M_{1-}^* - 4M_{1+}E_{1+}^*) \right\}, \quad (1.4.14)$$

$$R_{TT}^l = -3 \sin^2 \theta_{pq} \text{Im} \left\{ M_{1+}E_{0+}^* - 6 \cos \theta_{pq} M_{1+}E_{1+}^* \right\}, \quad (1.4.15)$$

$$R_{TT}^t = -3 \sin \theta_{pq} \text{Im} \left\{ 2M_{1+}E_{1+}^* + M_{1+}M_{1-}^* + \cos \theta_{pq} (M_{1+}E_{0+}^* - 6 \cos \theta_{pq} M_{1+}E_{1+}^*) \right\}, \quad (1.4.16)$$

$$R_{LT}^m = \text{Re} \left\{ M_{1+}S_{1-}^* - 2M_{1+}S_{1+}^* - \cos \theta_{pq} M_{1+}S_{0+}^* + 6 \cos^2 \theta_{pq} M_{1+}S_{1+}^* \right\}, \quad (1.4.17)$$

$$R_{LT}^l = \sin \theta_{pq} \text{Re} \left\{ 4M_{1+}S_{1+}^* - 2M_{1+}S_{1-}^* + 3 \cos \theta_{pq} M_{1+}S_{0+}^* - 18 \cos^2 \theta_{pq} M_{1+}S_{1+}^* \right\}, \quad (1.4.18)$$

$$R_{LT}^t = -\text{Re} \left\{ 2M_{1+}S_{0+}^* - 3 \cos^2 \theta_{pq} M_{1+}S_{0+}^* + \cos \theta_{pq} (M_{1+}S_{1-}^* - 14M_{1+}S_{1+}^*) + 18 \cos^3 \theta_{pq} M_{1+}S_{1+}^* \right\}, \quad (1.4.19)$$

$$R_{TT}^l = \cos \theta_{pq} |M_{1+}|^2 + \text{Re} \left\{ M_{1+}E_{0+}^* - 3 \cos^2 \theta_{pq} M_{1+}E_{0+}^* + 18 \cos^3 \theta_{pq} M_{1+}E_{1+}^* - \cos \theta_{pq} [12M_{1+}E_{1+}^* + 2M_{1+}M_{1-}^*] \right\}, \quad (1.4.20)$$

$$R_{TT}^t = -\sin \theta_{pq} \left\{ 2|M_{1+}|^2 - \text{Re} [6M_{1+}E_{1+}^* + M_{1+}M_{1-}^* + 3 \cos \theta_{pq} (M_{1+}E_{0+}^* - 6 \cos \theta_{pq} M_{1+}E_{1+}^*)] \right\}. \quad (1.4.21)$$

As discussed previously, due to angular momentum and parity selection rules, only the  $M_{1+}$ ,  $E_{1+}$ , and  $S_{1+}$  multipoles can excite the  $\Delta$ . All other contributing multipoles thus represent an unavoidable “background” to accessing the  $\Delta$ -excitation terms, and arise from any reaction mechanism not involving the  $\Delta$ -excitation intermediate state. These limiting assumptions in the expansion of the nuclear responses in terms of multipole amplitudes have been standard in interpreting pion electroproduction data (see discussions, for example, in Refs. [14, 15, 16, 17]).

This thesis only deals with the extraction of those response functions listed in Eqns. (1.4.9)-(1.4.21), facilitated by the measurement of polarization observables. Further analysis is underway to decompose the underlying multipoles, and will be discussed in the conclusion of Chapter 5.



## CHAPTER 2

### PHYSICS MOTIVATION

#### 2.1. The Standard Model

The *standard model* considers there to be three types of fundamental particles: leptons, quarks, and gauge particles<sup>1</sup> [18]. There are six different types of leptons: electrons, muons ( $\mu$ ), taus ( $\tau$ ), and their corresponding neutrinos ( $e$ -neutrinos,  $\mu$ -neutrinos, and  $\tau$ -neutrinos). These leptons interact via the electro-weak force by exchanging  $\gamma$ ,  $W$ , and  $Z$  gauge particles. Quarks come in six different *flavors*: up ( $u$ ), down ( $d$ ), charm ( $c$ ), strange ( $s$ ), top ( $t$ ), and bottom ( $b$ ). They interact with each other via the electro-weak and strong forces, in which gauge particles called gluons are exchanged.

Quarks form particles called hadrons which can be of two types: mesons or baryons. Mesons are bosons composed of a quark, anti-quark pair (e.g. pions). Baryons are fermions composed of three quarks (e.g. protons and neutrons). Protons ( $p$ ) and neutrons ( $n$ ) are the only stable (particles not likely to decay) particles composed of quarks. Because a single quark cannot be isolated, studies of the proton and neutron are the best way to study constituent quarks and their interactions.

A core of three *valence quarks*, along with gluons and a “sea” of quark-antiquark pairs, make up the proton and neutron. As  $Q^2 \rightarrow 0$ , hadronic properties are determined mainly by the valence quarks. The theory of Quantum ChromoDynamics (QCD) focuses on quark interactions [19]. Due to the strength of the interactions, a complete calculation in QCD of even the simplest hadronic process involves the consideration of an infinite number of Feynman diagrams and is, therefore, intractable. Consequently, approximations must be made. When hadrons are probed with very high energy projectiles, QCD with perturbative approximations makes predictions that seem to agree with observed hadronic properties [20]. Because these approximations involve perturbative expansions, however, it has been argued that they are invalid at  $Q^2$  on the order of a few  $\text{GeV}^2$  or less because the expansion parameter becomes large and the series does not converge. Sim-

---

<sup>1</sup>Gauge particles are those particles exchanged by leptons and quarks during interactions.

pler models must then be used to make inferences about low energy hadronic properties [21, 22].

**2.1.1. The Nucleon.** Heisenberg first suggested in 1932 that the proton and neutron were two states of the same particle [23]. Because they have many of the same properties, nuclear physicists still think of the proton and neutron in this way. Both have spin  $1/2$  and nearly the same mass ( $m_p = 938.3$  MeV,  $m_n = 939.6$  MeV). They differ in their electromagnetic properties: charge ( $p^+, n^0$ ) and magnetic dipole moments ( $\mu_p = 2.79$ ,  $\mu_n = -1.91$ ) [24], and therefore in their electromagnetic interactions. In their strong interactions, however, the two particles behave almost identically. The collective term for the proton and neutron is the *nucleon* ( $N$ ).

In the simplest Constituent Quark Model (CQM) (CQM - see Section 2.3) view of the nucleon, the nucleon wavefunction can be written as a linear combination of the three valence, spin  $1/2$ , quarks ( $uud$  for the proton,  $udd$  for the neutron) in  $L = 0$  ( $s$ -wave) and  $L = 2$  ( $d$ -wave) states (see, for example, [4]):

$$|N\rangle = a_s \left| S = \frac{1}{2}, L = 0 \right\rangle + a_d \left| S = \frac{3}{2}, L = 2 \right\rangle, \quad (2.1.1)$$

where the spin  $S$  and orbital angular momentum  $L$  couple to give the total angular momentum  $J = 1/2$ .<sup>2</sup>

**2.1.2. The  $\Delta(1232)$  Resonance.** The first excited state (or resonance) of the proton is the  $\Delta(1232)$ , with an invariant mass of  $W = 1232$  MeV, charge of  $+1$ , and spin of  $3/2$ . It was first observed during  $\pi N$  scattering experiments in the 1950s performed by Fermi *et al.* [25, 26]. This resonance is also composed of three valence quarks ( $uud$ ). The proton can be excited to the  $\Delta(1232)$  using an electron probe where a virtual photon interacts with the proton thereby exciting it. Like all nucleon resonances, it has a short lifetime (on the order of  $\tau = 10^{-23}$  s) [27]. Its decay channels:  $N\gamma$ ,  $n\pi^+$ , or  $p\pi^0$ , must then be studied. The  $N\gamma$  decay is the least likely with a 0.6% probability [24]. The  $n\pi^+$  and  $p\pi^0$  decays are equally probable, weighted only by the isospin.

The  $\Delta(1232)$  wavefunction can also be written as a linear combination of its three valence quarks in  $L = 0$  and  $L = 2$  states (again see, for example, [4]):

$$|\Delta(1232)\rangle = b_s \left| S = \frac{3}{2}, L = 0 \right\rangle + b_d \left| S = \frac{1}{2}, L = 2 \right\rangle \quad (2.1.2)$$

where  $S$  and  $L$  couple to give  $J = 3/2$ .

---

<sup>2</sup>The  $p$ -wave ( $L = 1$ ) state is also possible but much smaller than  $d$ -wave and therefore ignored here.

Note that because of the relatively large energy widths associated with nucleon resonance states (due to their short lifetime), in a given resonance region there are “tails” of other resonances which could contribute to scattering in that region. Other higher lying nucleon resonances close to the  $\Delta(1232)$  mass region include  $N(1440)$  (the Roper resonance),  $N(1520)$ ,  $N(1535)$ ,  $\Delta(1600)$ ,  $\Delta(1620)$ , and  $N(1680)$ . Fig. 2.1.1 is a proton scattering spectra as a function of  $W$  showing some of these resonances (figure courtesy of K. Joo).

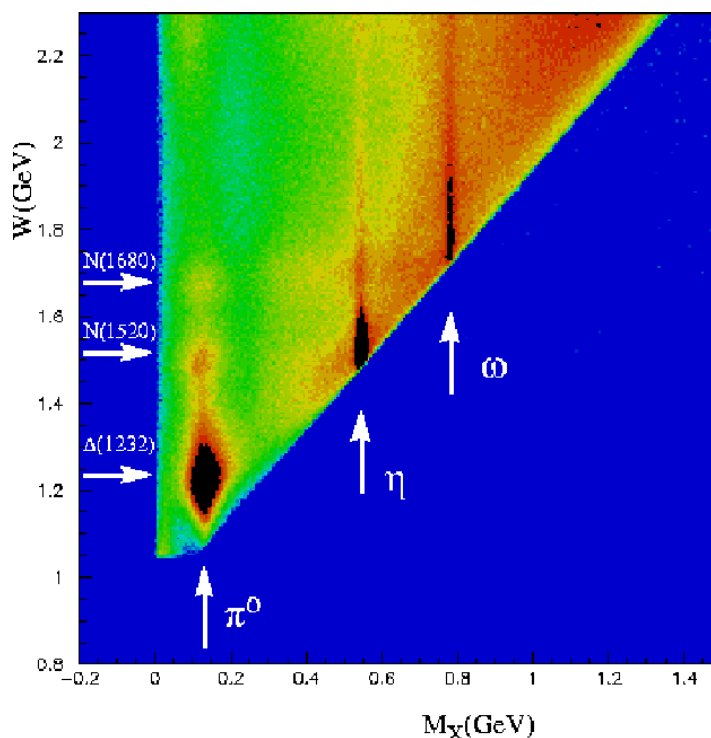


FIGURE 2.1.1. An  $(e, e'p)$  scattering spectra showing three resonance regions plotted against missing mass.

## 2.2. The $N \rightarrow \Delta(1232)$ Transition

In the simplest models of pion structure, the three quarks in the nucleon are in  $s$ -states and the charge distribution is spherically symmetric, or an electromagnetic monopole. When  $d$ -states are added into the nucleon wavefunction (as in Eqn. (2.1.1)), a quadrupole term is added to the charge distribution thereby *deforming* it. The quadrupole moment should then be a measure of the deformation of the nucleon. This quadrupole moment is

defined as:

$$Q_o = \int d^3r \rho(\vec{r}) (3z^2 - r^2), \quad (2.2.1)$$

where  $z$  is the symmetry axis of the particle and  $r$  is the equatorial axis. If the charge density is concentrated along the symmetry axis, the  $3z^2$  term dominates and  $Q_o$  is positive; the particle is prolate (cigar shaped) as in Fig. 2.2.1(a). If the charge density is concentrated along the equatorial plane, the  $r^2$  term dominates and  $Q_o$  is negative; the particle is oblate (pancake shaped) as in Fig. 2.2.1(b). For the nucleon, however, the quadrupole moment is zero due to angular momentum selection rules.<sup>3</sup> Information about nucleon deformation must consequently be obtained by electromagnetically exciting the nucleon to a higher spin state, such as a photon excitation of the proton to the  $\Delta(1232)$ .

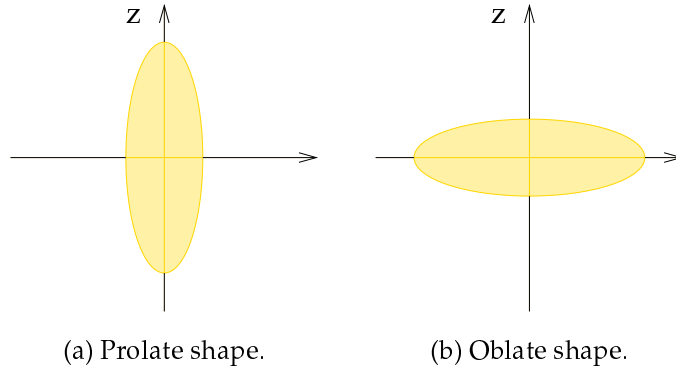


FIGURE 2.2.1. Shape of particle charge density.

**2.2.1. Pion Electroproduction.** Since the  $\Delta(1232)$  decays rather quickly, its residual decay particles,  $N\pi$ , must be studied. In addition to  $\Delta(1232)$  excitation, however, several other processes contribute to this final state, as mentioned at the end of Chapter 1. Feynman diagrams for other possible processes are shown in Fig. 2.2.2. The  $\Delta(1232)$  resonance corresponds to Fig. 2.2.2(a), while other resonance states, such as the Roper, are displayed in Fig. 2.2.2(b). Besides the resonant terms, non-resonant terms exist. For example, it is possible for the photon to interact with the proton which absorbs the photon, becomes excited (but not to a resonance state), and emits a pion to decay back into its ground

<sup>3</sup> $Q_o$  has angular momentum of 2 and positive parity, therefore:

$$\langle p | Q_o | p \rangle = \left\langle \frac{1}{2}^+ \left| 2^+ \right| \frac{1}{2}^+ \right\rangle = 0$$

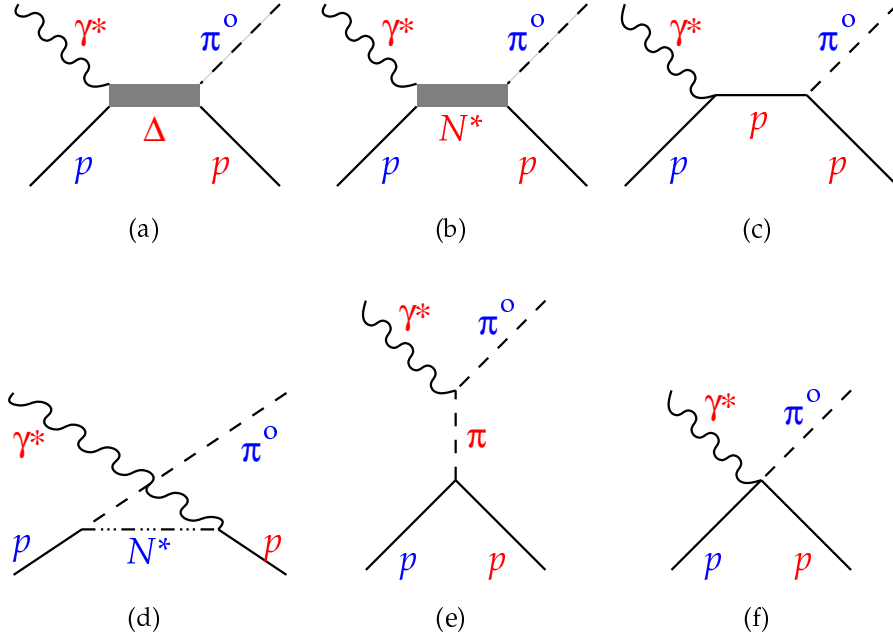


FIGURE 2.2.2. Pion production Feynman diagrams.

state energy as indicated in Fig. 2.2.2(c). The photon can also interact with a virtual meson, creating what are collectively called the Born terms exhibited in Figs. 2.2.2(d)-2.2.2(e). Other possible contributors such as the contact diagram shown in Fig. 2.2.2(f) exist. This term must be included to maintain electromagnetic gauge invariance for non-relativistic theory.

For the case of  $\Delta(1232)$  excitation, all terms other than the  $\Delta(1232)$  resonance are considered *background* terms (since the goal of this experiment was to extract information about the  $N \rightarrow \Delta(1232)$  excitation). The contribution of these background terms to the  $M_{1+}$ ,  $E_{1+}$ , and  $S_{1+}$  multipole amplitudes is mostly real, and relatively flat in  $W$ . Other possible electroproduction multipole amplitudes ( $M_{1-}$ ,  $E_{0+}$ ,  $E_{1-}$ ,  $S_{0+}$ , and  $S_{1-}$ ) are due only to the background terms. In order to extract the multipole amplitudes with some confidence, the background terms must be measured or somehow constrained.

The results of neutral pion production experiments performed in the 1960s and 1970s at the Deutsches Elektronen SYnchrotron (DESY) in Hamburg [28, 29, 30], at the electron synchrotron at the Daresbury Nuclear Physics Laboratory (NINA) [31], and at Harvard University's Cambridge Electron Accelerator (CEA) [32] revealed that the  $M_{1+}$  amplitude is dominant, with only small contributions from the  $E_{1+}$  and  $S_{1+}$  quadrupoles. This dom-

inant  $M_{1+}$  transition corresponds to a simple spin flip of one quark in the proton, an “ $L = 0$ ” (from  $L = 0$  proton to  $L = 0$   $\Delta(1232)$ ) transition, thus is sensitive to only the spherically symmetric parts of the nucleon wavefunction. Measurements of the  $E_{1+}$  and  $S_{1+}$  quadrupole amplitudes (“ $L = 2$ ” transition) then are a measure of the deformation from spherical of the nucleon. Because these amplitudes are small compared to  $M_{1+}$ , measurements must be made of observables (the polarization observables from Section 1.3.4) linearly dependent on interferences of the  $E_{1+}$  and  $S_{1+}$  quadrupoles with the  $M_{1+}$  dipole. These measurements are typically quoted as ratios of the form:

$$CMR = \frac{\text{Re}(S_{1+}^* M_{1+})}{|M_{1+}|^2}, \quad (2.2.2)$$

$$EMR = \frac{\text{Re}(E_{1+}^* M_{1+})}{|M_{1+}|^2}, \quad (2.2.3)$$

where  $CMR$  ( $EMR$ ) represents the Coulomb (Electric) quadrupole to Magnetic dipole Ratio. Some measurements of these ratios will be discussed in Section 2.5.

It is interesting to note that at very high values of  $Q^2$  for the  $\Delta(1232)$  excitation, the kinematic regime in which perturbative QCD (pQCD) calculations are possible and applicable, quark helicity conservation leads to the pQCD result that  $E_{1+} = M_{1+}$  as  $Q^2 \rightarrow \infty$  [14].

### 2.3. Constituent Quark Model (CQM)

It is believed that two different sources may be the cause of any observed quadrupole deformation in the nucleon. The first is a tensor force between valence quarks, creating  $d$ -waves in the nucleon and  $\Delta(1232)$ . Small but nonzero values of  $E_{1+}$  and  $S_{1+}$  are therefore predicted [33, 34]. The second source believed to contribute to the nucleon deformation is the presence of quark-antiquark pairs and gluons inside the nucleon, which adds additional degrees of freedom from the non-valence quarks [4]. These two contributions will be discussed in the framework of the Constituent Quark Model (CQM).

The CQM is one of the most popular low energy models for nuclear structure. It has met with some success describing experiment success and is an excellent tool for over-viewing the current understanding of the structure of the nucleon. Like the full theory of QCD, the CQM constructs baryons from three spin-1/2, positive parity quarks with mass  $m_q \approx m_N/3$ , a mass much larger than the “bare”  $m_q$  used in QCD. These heavy



constituent quarks can be surrounded by a cloud of light quark-antiquark pairs [35]. In this model, nucleons are made of only two types of quarks: the  $u$  (charge +2/3) and  $d$  (charge -1/3). In the CQM's simplest form, quarks are often treated as non-relativistic, therefore the CQM is acceptable only in the non-perturbative QCD limit (low  $Q^2$ ).

**2.3.1. The Single Quark Operator.** The color hyperfine interaction<sup>4</sup> between constituent quarks is given to lowest order in QCD by [33]:

$$H_{hyp}^{ij} = \frac{2}{3} \frac{\alpha_s}{m_i m_j} \left\{ \frac{8\pi}{3} \vec{S}_i \cdot \vec{S}_j \delta^3(\vec{r}_{ij}) + \frac{1}{r_{ij}^3} \left[ \frac{3 \vec{S}_i \cdot \vec{r}_{ij} \vec{S}_j \cdot \vec{r}_{ij}}{r_{ij}^2} - \vec{S}_i \cdot \vec{S}_j \right] \right\}, \quad (2.3.1)$$

where  $\alpha_s$  is a (strong) coupling constant,  $m_{i,j}$  is the mass of quarks  $i$  or  $j$ ,  $\vec{S}_{i,j}$  represents the quark spins, and  $\vec{r}_{ij} = \vec{r}_i - \vec{r}_j$  is the relative vector position of the two interacting quarks. The tensor part of this interaction, the second part of Eqn. (2.3.1), introduces a  $d$ -state admixture in the single-quark wavefunction. A photon can induce a quadrupole transition by lifting a single  $s$ -state quark inside the nucleon to a  $d$ -state in the  $\Delta(1232)$ , or moving a single  $d$ -state quark in the nucleon to an  $s$ -state quark in the  $\Delta(1232)$ .

The one-body quadrupole operator, summed over the three valence quarks are inside the nucleon, is written as follows [4]:

$$\hat{Q}_{[1]} = \sqrt{\frac{16\pi}{5}} \sum_{i=1}^3 e_i r_i^2 Y_2^0(\vec{r}_i) = \sum_i e_i (3z_i^2 - r_i^2), \quad (2.3.2)$$

where  $Y_2^0(\vec{r}_i)$  is a spherical harmonic of rank two and  $e_i$  is the quark charge operator. This operator needs  $d$ -waves in the nucleon or  $\Delta(1232)$  in order to make a non-zero quadrupole contribution. Sandwiching the one-body quadrupole operator between the nucleon and  $\Delta(1232)$  wavefunctions of Eqns. (2.1.1) and (2.1.2) gives a transition quadrupole moment of:

$$Q_{N \rightarrow \Delta} = -b^2 \frac{4}{\sqrt{30}} (a_s b_d - a_d b_s), \quad (2.3.3)$$

where  $b$  is a harmonic oscillator parameter describing the spatial extension of the nucleon wavefunction, and the small  $a_d b_d$  term has been neglected. Fig. 2.3.1 is a schematic of the two terms of Eqn. (2.3.3).

The  $d$ -state admixture in the single-quark excitation thus leads to nonzero  $E_{1+}$  and  $S_{1+}$  transition amplitudes. However, this single-quark excitation may not be the dominant quadrupole excitation mechanism. For the electromagnetic current to be conserved, the

<sup>4</sup>The color hyperfine interaction is the color analog of the magnetic-dipole, magnetic-dipole interaction of electromagnetism.

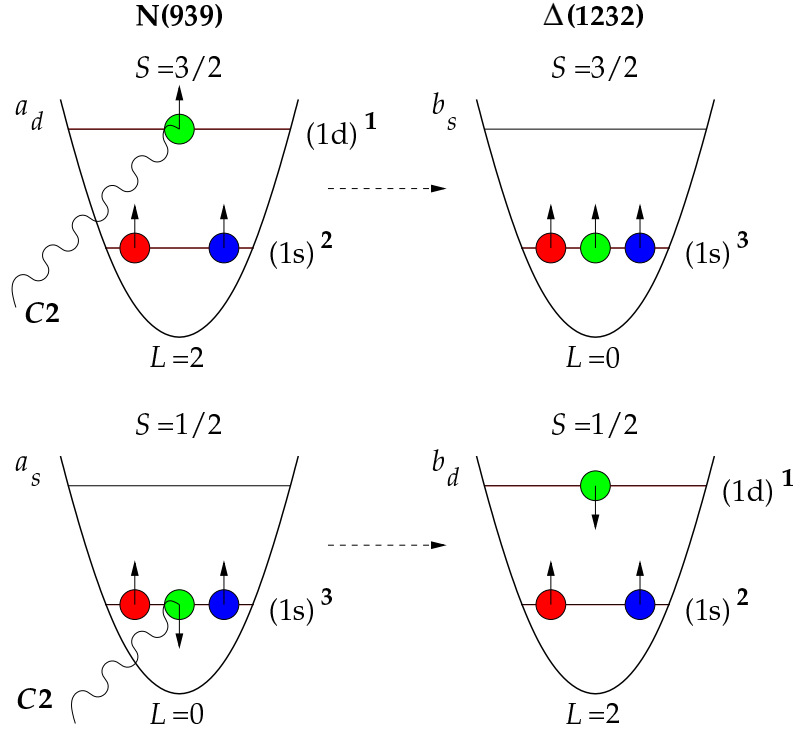


FIGURE 2.3.1.  $N \rightarrow \Delta(1232)$  quadrupole transition via the one-body quadrupole operator  $\hat{Q}_{[1]}$  coming from the one-quark current.

total electromagnetic current operator must consist of these single quark currents *and* various two-body exchange currents (see Refs. [4] and [35] for details). These two-quark currents will be discussed in the next section.

**2.3.2. The Two-Quark Operator.** It has been shown that two-body exchange currents lead to nonzero  $\Delta(1232)$  and  $N \rightarrow \Delta(1232)$  transition quadrupole moments, even if the wavefunctions have no  $d$ -state valence quark admixtures [35]. The two-body quadrupole operator, generated by the gluon and  $q\bar{q}$  pair currents shown in Fig. 2.3.2, is written as:

$$\hat{Q}_{[2]} = B \sum_{i \neq j=1}^3 e_i (3\sigma_{iz}\sigma_{jz} - \vec{\sigma}_i \cdot \vec{\sigma}_j), \quad (2.3.4)$$

where  $B$  is a constant containing the orbital and color matrix elements. This operator can simultaneously flip the spin of two quarks in the nucleon, where both the nucleon and  $\Delta(1232)$  are in the  $s$ -state ( $L = 0$ ), as illustrated in the example of Fig. 2.3.3. Even though the  $\hat{Q}_{[2]}$  quadrupole operator acts on the valence quarks, it does not describe the valence quark core deformation. Instead, it shows the the nucleon contains  $q\bar{q}$  sea quarks, the

distribution of which is not spherically symmetric.

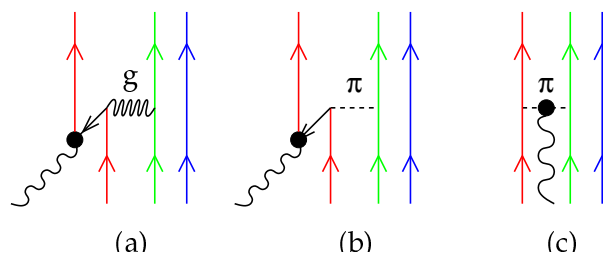


FIGURE 2.3.2. Feynman diagrams of two-body gluon and pion exchange currents.

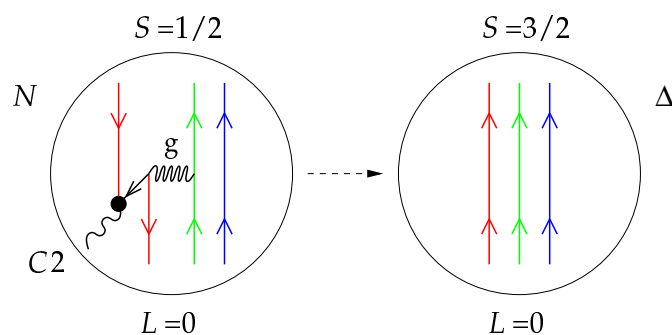


FIGURE 2.3.3. The  $N \rightarrow \Delta(1232)$  quadrupole transition via the two-body quadrupole operator  $\hat{Q}_{[2]}$  originating from the two-body gluon current.

*Pion Cloud Model.* One popular model of the two-quark currents is thus the *pion cloud model* where the valence quarks are surrounded by a deformed pion cloud [4]. This model states that all nucleon deformation comes from the pion cloud, not from the core of valence quarks. The intrinsic quadrupole deformation of the nucleon and  $\Delta(1232)$  in this pion cloud model are exhibited in Fig. 2.3.4 where the  $z$ -axis is the direction of the proton's spin. The spherical region at the origin represents the component of the wavefunctions coming from the constituent quarks themselves (the  $L = 0$  spherically symmetric state), while the non-spherical region corresponds to the component of the wavefunctions coming from the pion cloud.

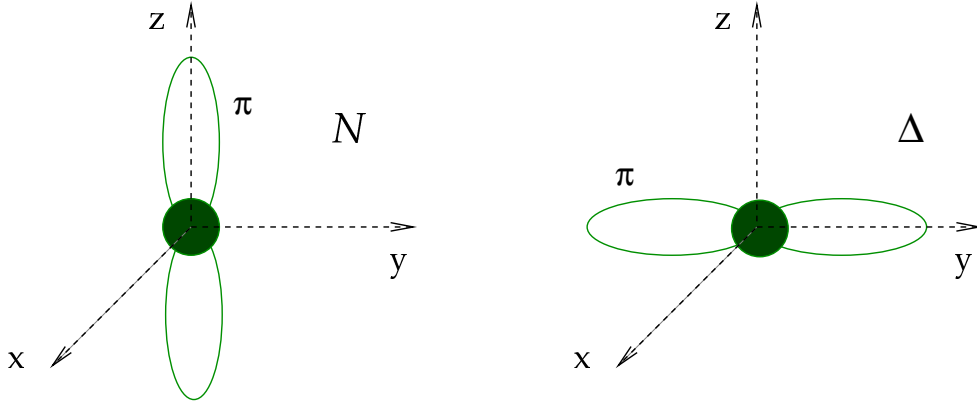


FIGURE 2.3.4. Intrinsic quadrupole deformation of the nucleon and  $\Delta(1232)$  in the pion cloud model.

#### 2.4. The Sato and Lee Meson-Exchange Model (SL)

Sato and Lee developed a meson-exchange model (SL) to help separate the reaction mechanisms from the hadron structure in the  $\gamma N \rightarrow \pi N$  (and  $\gamma N \rightarrow \pi\pi N$ ) reaction [36, 37]. This model was developed using pion photoproduction data taken at Brookhaven's Laser Electron Gamma Source (LEGS) and the MAINZ Microtron (MAMI). It uses a unitary transformation to derive an effective Hamiltonian to describe both  $\pi N$  scattering and the electroproduction of pions. The transformation is applied to a model Lagrangian with  $N$ ,  $\Delta$ ,  $\pi$ ,  $\rho$ ,  $\omega$ , and photon fields.

Sato and Lee calculated the effects of a pion cloud on pion electroproduction as a function of  $Q^2$ . These effects are shown in Fig. 2.4.1 [37]. The solid line shows their full calculation, while the dotted line represents their calculation assuming no pion cloud. The prediction is that the quadrupole amplitudes are dominated by the pion cloud at low  $Q^2$ . As  $Q^2$  increases, the effects due to the pion cloud decrease, leaving valence quark effects. The SL model is in good agreement with pion photoproduction data in the  $\Delta(1232)$  region, but not with low  $Q^2$  electroproduction data taken at Bates near the predicted peak of the pion cloud contribution [38].

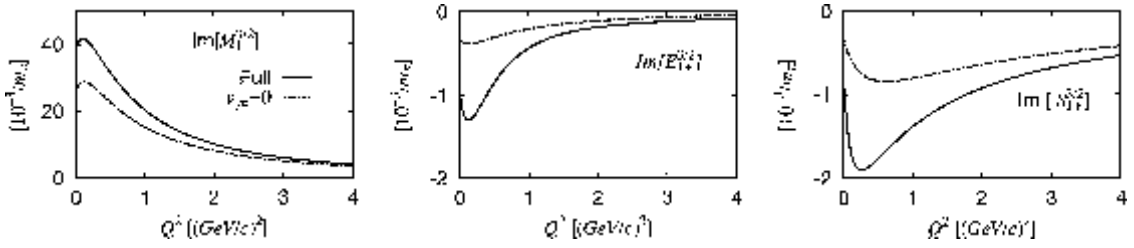


FIGURE 2.4.1.  $Q^2$  dependence of  $Im(M_{1+})$ ,  $Im(E_{1+})$ , and  $Im(S_{1+})$  at  $W = 1232$  MeV.

## 2.5. Existing Experimental Data

The  $EMR$  and  $CMR$  are typically small at low  $Q^2$ , making them difficult to measure. This is due to the fact that the background terms are of the same order of magnitude as the resonant quadrupole amplitude terms. Experiments must therefore be precise enough to separate the quadrupole signal from background contributions. The goal, then, of pion photo and electroproduction experiments is to obtain accurate data with sufficient sensitivity to not only determine the  $M_{1+}$ ,  $E_{1+}$ , and  $S_{1+}$  amplitudes, but also with sufficient coverage and sensitivity to determine (and separate) the background amplitudes which are on the same order of magnitude as  $E_{1+}$  and  $S_{1+}$ . Such experiments are being performed for a range of  $Q^2$  to provide a measure of the spatial distribution of the transition.

All analyses to date have had to rely on reaction models to extract the resonant  $M_{1+}$ ,  $E_{1+}$ , and  $S_{1+}$  amplitudes from the data, but model error can introduce much larger errors than experiment [38]. Most older data (before 1985) also have relatively large statistical uncertainties.

**2.5.1. Photon Asymmetries.** Pion photoproduction measurements made at Mainz [17] and LEGS [39],  $\vec{\gamma}p \rightarrow \pi^0 p$ ,  $\vec{\gamma}p \rightarrow \pi^+ n$ , and  $\vec{\gamma}p \rightarrow \gamma p$ , were of sufficient sensitivity to obtain both the small  $E_{1+}$  and dominant  $M_{1+}$  amplitudes. The results for the polarized photon asymmetry are shown in Fig. 2.5.1 [39]. The curves are phenomenological predictions using the Mainz Unitary Isobar Model (MAID, discussed in Section 2.5.3.1) for three different  $E_{1+}/M_{1+}$  ratios. There is good agreement between the polarized photon asymmetries for the two measurements and the model calculations, showing significant deformations of the  $N$  and  $\Delta(1232)$  ( $EMR \sim -3\%$ ). Note there remains an unresolved disagreement, however, in the unpolarized cross sections for the two measurements.

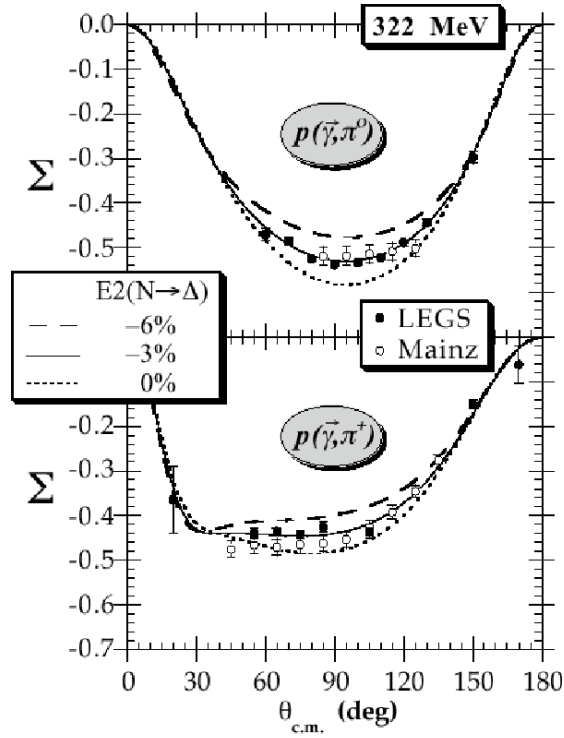


FIGURE 2.5.1. Polarized photon asymmetries for the  $\vec{\gamma}p \rightarrow \pi^0 p$  and  $\vec{\gamma}p \rightarrow \pi^+ n$  reactions plotted versus  $\theta_{cm}$ .

**2.5.2. Electric to Magnetic and Coulomb to Magnetic Multipole Ratios.** The extracted Coulomb and electric quadrupole terms for most of the available world data are shown in Fig. 2.5.2. Values and errors from the plots for each measurement can be found in the following corresponding subsection. Notice that of the more recent measurements, some are from photoproduction experiments while others are from electroproduction experiments and the bulk of the  $EMR$  and  $CMR$  values have been extracted from unpolarized cross section distributions. Because analysis of the data is complex and relies on the validity of simplifying assumptions (e.g. see Section 1.4) and/or use of a model, different measurement techniques must be compared to each other. Most of the older data has relatively large uncertainties due to this model dependence. The preliminary cross section distribution data from this “ $N \rightarrow \Delta$ ” experiment have been analyzed using the same assumptions as were used for these older data sets, and are found to be in good agreement with the older data (see PhD thesis of Z. Chai [10]). The recoil polarization measurements for “ $N \rightarrow \Delta$ ” will help fill in intermediate  $Q^2$  values (0.8-1.2 (GeV/c)<sup>2</sup>), with the combination of full angular distributions and polarization measurements greatly reducing the

reliance on models for extraction of the  $CMR$ .

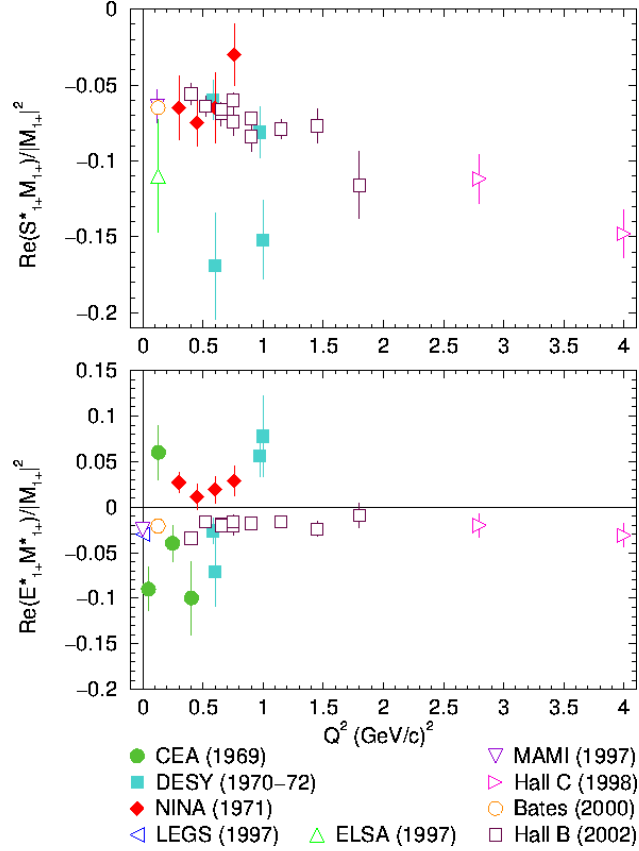


FIGURE 2.5.2.  $Q^2$  dependence of the quadrupole amplitudes,  $CMR$  and  $EMR$ , for  $\gamma p \rightarrow \Delta(1232) \rightarrow p + \pi^0$ .

2.5.2.1. *CEA*. The differential cross section for the  $p(e, e'p)\pi^0$  reaction was measured near the  $\Delta(1232)$  resonance at CEA in 1969 [32]. Data were taken at four values of  $Q^2$ : 0.05, 0.13, 0.25, and 0.40  $(\text{GeV}/c)^2$ . A multipole expansion of the cross section was done to extract the  $EMR$ , the values of which are listed in Tab. 2.1. The quoted error is both statistical and systematic. This was one of the first measurements to observe the dominance of the  $M_{1+}$  multipole, as mentioned in Section 2.2.1.

TABLE 2.1. Values of  $EMR$  from measurements taken at CEA.

$Q^2$ (GeV/c) <sup>2</sup>	$EMR$ (%)
0.0463	$-9.0 \pm 2.4_{stat+syst}$
0.130	$6 \pm 3_{stat+syst}$
0.247	$-4 \pm 2_{stat+syst}$
0.404	$-10 \pm 4_{stat+syst}$

2.5.2.2. *DESY*. Cross section measurements of the  $p(e, e'p)\pi^0$  reaction were performed at DESY in 1970 and 1972 [28, 29, 30]. These measurements were made at three values of  $Q^2$ : 0.6, 1, and 1.56<sup>5</sup> (GeV/c)<sup>2</sup>.  $CMR$  and  $EMR$  were then extracted from fits to these measured cross sections. Their values are listed in Tab. 2.2. For the first two measurements “The errors are statistical and systematic ones. An overall systematic error of about  $\pm 5\%$  should be added in addition” [29]. The final two measurements quote only statistical errors. Only the errors listed in Tab. 2.2 are shown in Fig. 2.5.2.

TABLE 2.2. Values of  $CMR$  and  $EMR$  from measurements taken at DESY.

$Q^2$ (GeV/c) <sup>2</sup>	$CMR$ (%)	$EMR$ (%)
0.60	$-16.9 \pm 3.5_{stat+syst}$	$-7.1 \pm 3.8_{stat+syst}$
1.0	$-15.2 \pm 2.6_{stat+syst}$	$7.8 \pm 4.4_{stat+syst}$
0.583	$-6.0 \pm 1.3_{stat}$	$-2.6 \pm 1.4_{stat}$
0.973	$-8.1 \pm 1.7_{stat}$	$5.6 \pm 2.2_{stat}$

2.5.2.3. *NINA*. Cross section measurements of the  $p(e, e'p)\pi^0$  reaction were performed at the 5 GeV electron synchrotron, NINA in 1971 [31]. These data were taken at four values of  $Q^2$ : 0.3, 0.45, 0.6, and 0.76 (GeV/c)<sup>2</sup>. The cross sections were analyzed in terms of a multipole expansion, thus extracting  $CMR$  and  $EMR$ . Tab. 2.3 lists these values. The errors have been “inflated by 1.42 at  $[Q^2] = 0.3$ , 1.55 at  $[Q^2] = 0.45$ , 1.41 at  $[Q^2] = 0.60$  and  $[Q^2] = 0.76$  (GeV/c)<sup>2</sup> to allow for the systematic errors in the relative sizes of the c.m. [center of mass] acceptances. We also quote ... the errors due only to the statistics of the centre-of-mass [*sic.*] bin populations including the effects of the background subtractions.” [31] From this reference it is hard for this author to determine if the errors are statistical or systematic.

<sup>5</sup>The  $Q^2=1.56$  (GeV/c)<sup>2</sup> results are not quoted in the reference, even though they were mentioned as having been measured.



TABLE 2.3. Values of  $CMR$  and  $EMR$  from measurements taken at NINA.

$Q^2$ (GeV/c) <sup>2</sup>	$CMR$ (%)	$EMR$ (%)
0.3	$-6.5 \pm 2.1_{stat+syst?}$	$2.7 \pm 1.1_{stat+syst?}$
0.45	$-7.5 \pm 1.5_{stat+syst?}$	$1.1 \pm 1.4_{stat+syst?}$
0.6	$-6.5 \pm 2.3_{stat+syst?}$	$1.9 \pm 1.5_{stat+syst?}$
0.76	$-3.0 \pm 2.0_{stat+syst}$	$2.9 \pm 1.6_{stat+syst?}$

2.5.2.4. *ELSA*. A measurement of the ratio of the out-of-plane cross sections for the  $p(e, e'\pi^0)p$  reaction at the  $\Delta(1232)$  resonance was made at Bonn's ELSA, and published in 1997 [40]. The  $CMR$  was extracted from this data at  $Q^2 = 0.127$  (GeV/c)<sup>2</sup>. The analysis neglected any background contributions, and reported a  $CMR = -11.0 \pm 3.7_{stat}\%$ . Note that this large  $CMR$  value (compared to the LEGS and MAMI  $Q^2 = 0$   $EMR$  values) coming from a "modern" experiment prompted a renewal in experimental interest (e.g. at MIT-Bates, MAMI, and Jefferson Lab). It has been suggested [15] that a sizeable contribution from the "background"  $S_{0+}$  multipole (neglected in the ELSA analysis) is responsible for the large  $CMR$  result.

2.5.2.5. *LEGS*. High precision measurements of  $p(\vec{\gamma}, \pi)$  and  $p(\vec{\gamma}, \gamma)$  cross sections and beam asymmetries were made at LEGS in 1997 [39]. These measurements were combined with measured polarization ratios to simultaneously analyze both reactions thereby greatly reducing the model dependence. The extracted  $EMR = -3.0 \pm 0.3_{stat+syst} \pm 0.2_{model}\%$ . The model error is not displayed in Fig. 2.5.2.

2.5.2.6. *MAMI*. Two separate experiments to investigate the ratio of Coulomb and electric quadrupoles to the magnetic dipole were made at MAMI. The first experiment, published in 1997, was a measurement of the differential cross section for the  $p(\vec{\gamma}, p)\pi^0$  reaction, made with good accuracy in the  $\Delta(1232)$  region [17]. From angular distributions  $EMR = -2.5 \pm 0.2_{stat} \pm 0.2_{syst}\%$  was determined. The second experiment, performed in 2001, measured the recoil proton polarization for the  $p(\vec{e}, e'\vec{p})\pi^0$  reaction in parallel kinematics at  $Q^2 = 0.121$  (GeV/c)<sup>2</sup> in the  $\Delta(1232)$  region [16]. Like the ELSA analysis, this analysis neglected the  $S_{0+}$  term. The value of  $CMR = -6.4 \pm 0.7_{stat} \pm 0.8_{syst}\%$ , was determined for  $P_x$ <sup>6</sup> measurement using the model frame work of MAID. Both the statistical and systematic errors are shown in Fig. 2.5.2.

2.5.2.7. *Hall C*. The differential cross section of the  $p(e, e'p)\pi^0$  reaction was measured in Hall C of Jefferson Lab in 1998 [41], the first experiment to measure this exclusive re-

<sup>6</sup> $P_t$  in the convention of " $N \rightarrow \Delta$ ".

action with high statistical precision in this  $Q^2$  range: 2.8 and 4.0 (GeV/c)<sup>2</sup>. Effective Lagrangian fits of the cross sections were made, formulated by Davidson, Mukhopadhyay, and Wittman [42], to extract the values of  $EMR$  and  $CMR$  which are listed in Tab. 2.4. Both the statistical and systematic errors are shown in Fig. 2.5.2.

TABLE 2.4. Values of  $CMR$  and  $EMR$  from measurements taken in Hall C of Jefferson Lab.

$Q^2$ (GeV/c) <sup>2</sup>	$CMR$ (%)	$EMR$ (%)
2.8	$-11.2 \pm 1.3_{stat} \pm 1_{syst}$	$-2.0 \pm 1.2_{stat} \pm 0.5_{syst}$
4.0	$-14.8 \pm 1.3_{stat} \pm 1_{syst}$	$-3.1 \pm 1.2_{stat} \pm 0.5_{syst}$

2.5.2.8. *Bates*. High-precision measurements of the  $p(e, e'p)\pi^0$  cross section were performed at  $Q^2 = 0.126$  (GeV/c)<sup>2</sup>, at Bates in 2000 [38]. The values  $CMR = -6.5 \pm 0.2_{stat+syst} \pm 2.5_{model}\%$  and  $EMR = 2.1 \pm 0.2_{stat+syst} \pm 2.0_{model}\%$  were then extracted by fitting these cross sections to several models. The results are very model dependent, as is apparent in quoted model error. The model errors are not plotted in Fig. 2.5.2.

TABLE 2.5. Values of  $CMR$  and  $EMR$  from measurements taken in Hall B of Jefferson Lab.

$Q^2$ (GeV/c) <sup>2</sup>	$E$ (GeV)	$CMR$ (%)	$EMR$ (%)
0.40	1.645	$-5.6 \pm 0.4_{stat} \pm 0.6_{syst}$	$-3.4 \pm 0.4_{stat} \pm 0.4_{syst}$
0.52	1.645	$-6.4 \pm 0.4_{stat} \pm 0.5_{syst}$	$-1.6 \pm 0.4_{stat} \pm 0.4_{syst}$
0.65	1.645	$-6.9 \pm 0.6_{stat} \pm 0.5_{syst}$	$-1.9 \pm 0.5_{stat} \pm 0.5_{syst}$
0.75	1.645	$-7.4 \pm 0.8_{stat} \pm 0.5_{syst}$	$-2.1 \pm 0.6_{stat} \pm 0.7_{syst}$
0.90	1.645	$-8.4 \pm 0.9_{stat} \pm 0.4_{syst}$	$-1.8 \pm 0.6_{stat} \pm 0.4_{syst}$
0.65	2.445	$-6.6 \pm 0.4_{stat} \pm 0.2_{syst}$	$-2.0 \pm 0.4_{stat} \pm 0.4_{syst}$
0.75	2.445	$-6.0 \pm 0.4_{stat} \pm 0.2_{syst}$	$-1.6 \pm 0.5_{stat} \pm 0.5_{syst}$
0.90	2.445	$-7.2 \pm 0.4_{stat} \pm 0.1_{syst}$	$-1.8 \pm 0.4_{stat} \pm 0.3_{syst}$
1.15	2.445	$-7.9 \pm 0.5_{stat} \pm 0.4_{syst}$	$-1.6 \pm 0.5_{stat} \pm 0.3_{syst}$
1.45	2.445	$-7.7 \pm 0.9_{stat} \pm 0.7_{syst}$	$-2.4 \pm 0.7_{stat} \pm 0.4_{syst}$
1.80	2.445	$-11.6 \pm 1.6_{stat} \pm 1.5_{syst}$	$-0.9 \pm 1.1_{stat} \pm 0.7_{syst}$

2.5.2.9. *Hall B*. Very recently, a large amount of experimental data has become available from measurements made in Hall B of Jefferson Lab [14], published in 2002. This experiment investigated the  $p(e, e'p)\pi^0$  cross section over a wide range of  $Q^2$  (from

0.4-1.8 (GeV/ $c$ )<sup>2</sup>,  $W$ , and beam energy  $E$ . A summary of the relevant results is listed in Tab. 2.5. Both the statistical and systematic errors are displayed in Fig. 2.5.2.

**2.5.3. Models.** All results from the current “ $N \rightarrow \Delta$ ” experiment will be compared to two phenomenological models: MAID and SAID. Both are computations using scattering amplitudes with parameterizations derived either from the Mainz Unitary Isobar Model (MAID) or a phase shift analysis of the world’s data (SAID). Both models can take any quark model prediction for the  $N \rightarrow \Delta(1232)$  transition amplitude and embed it within the reaction framework (i.e. include other multipole contributions), and provide predictions for any experimental observable.

2.5.3.1. *MAID.* The 2000 version of the MAID model will be used as a comparison to results from “ $N \rightarrow \Delta$ ” [43]. It is a model for pion photo and electroproduction containing Born terms, vector meson exchange, and nucleon resonance excitation up to the third resonance region:  $\Delta(1232)$ ,  $N(1440)$ ,  $N(1520)$ ,  $N(1535)$ ,  $N(1680)$ , and  $\Delta(1600)$ . It is unitarized using empirical  $\pi - N$  phase shifts. The resonances are parameterized in the Breit-Wigner form for all relevant multipoles. The  $Q^2$  dependence of electromagnetic resonance vertices is described with appropriate form factors in the electromagnetic helicity amplitudes. MAID gives good agreement with existing pion photo and electroproduction data on the nucleon. Because it is inherently simple, this model is well suited for predictions of the pion electroproduction data from this experiment, and further allows for future “adjustment” of multipole amplitudes to achieve the overall best agreement with all available data. This, then, provides one means for extracting the size of multipole contributions.

2.5.3.2. *SAID.* The second model used as a comparison to the “ $N \rightarrow \Delta$ ” results is called SAID [44]. It was developed by the Center for Nuclear Studies (CNS) at The George Washington University. This model uses available world data to make a phase shift analysis of the desired experimental results. SAID contains databases of both pion photo and electroproduction experiments, along with  $\pi N$  and  $NN$  scattering,  $\eta$  photoproduction, and many other types of experiments. Over 20,000 data points from  $\gamma p \rightarrow \pi^+ n$ ,  $\gamma p \rightarrow \pi^0 p$ ,  $\gamma n \rightarrow \pi^- p$ ,  $\gamma n \rightarrow \pi^0 n$ , and  $\pi^- p \rightarrow n \gamma$  measurements are used to make pion photoproduction predictions. More importantly to this thesis, the database contains on the order of 40,000 data points from pion electroproduction experiments off a proton target.



## CHAPTER 3

### EXPERIMENTAL SETUP

#### 3.1. Overview

The “ $N \rightarrow \Delta$ ” experiment was performed in Hall A of Jefferson Lab, shown schematically in Fig. 3.1.1 (taken from Ref. [45]). Nominal (central setting) kinematics were those

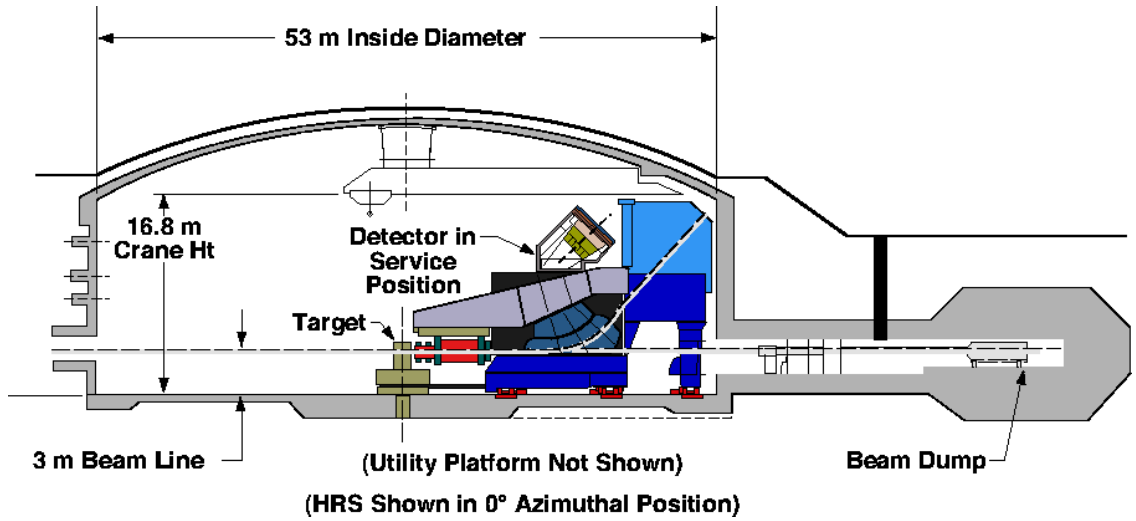


FIGURE 3.1.1. Hall A layout.

discussed in Chapter 1:  $E = 4.53$  GeV,  $\theta_e = 14.1^\circ$ ,  $k' = 3.7$  GeV/ $c$ ,  $Q^2 = 1.0$  (GeV/ $c$ )<sup>2</sup>,  $W = 1.232$  GeV, and the twelve proton spectrometer settings listed in Tab. 1.1. Longitudinally polarized electrons were obtained using a polarized source at the Continuous Electron Beam Accelerator Facility (CEBAF). The beam polarization was monitored almost continuously by either a Møller or Compton polarimeter. Once inside the experimental hall, the polarized electrons were incident on a liquid hydrogen target. Scattered electrons and recoil protons were detected in coincidence in the two Hall A High Resolution

Spectrometers (HRS). The hadron spectrometer (HRSh) contained the components of the Focal Plane Polarimeter (FPP) used to measure the polarization of the recoil protons at the focal plane. Full details on all Hall A equipment can be found in Ref. [45]. Details of the equipment specifically relevant for the “ $N \rightarrow \Delta$ ” experiment will be over-viewed in the following sections.

### 3.2. The Continuous Electron Beam Accelerator Facility (CEBAF)

The Jefferson Lab accelerator system, displayed in Fig. 3.2.1, contains a set of two linear accelerators (linacs) in a race-track shaped design recirculated by magnets in a set of recirculation arcs. The accelerator is capable of delivering a high-quality continuous

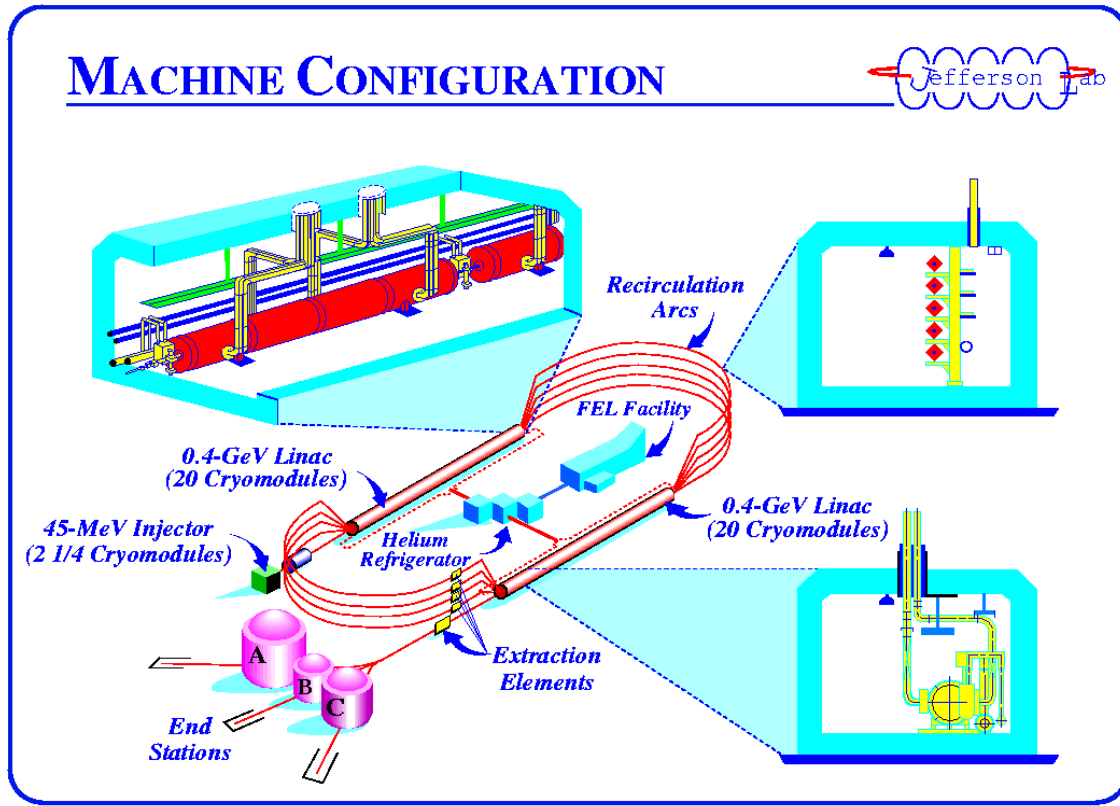


FIGURE 3.2.1. Layout of CEBAF.

(100% duty factor) electron beam, either unpolarized or polarized, to three experimental

halls, simultaneously. The maximum electron energy (at present) is 5.7 GeV, with a possible current of 70  $\mu\text{A}$  delivered to both Halls A and C concurrently or 120  $\mu\text{A}$  to either hall alone.<sup>1</sup> The beam current over “ $N \rightarrow \Delta$ ”, shown in Fig. 3.2.2, averaged approximately 45  $\mu\text{A}$ , with a **world record peak of approximately 108  $\mu\text{A}$  at high polarization!**

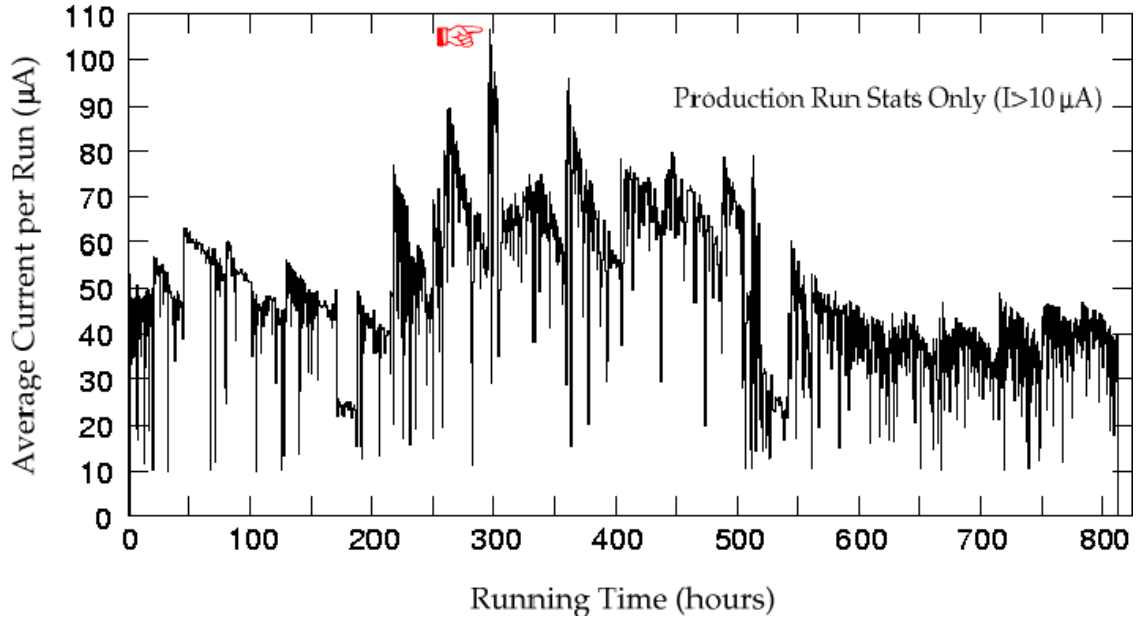


FIGURE 3.2.2. Current over entire “ $N \rightarrow \Delta$ ” experiment, showing a world record high current with high polarization.

**3.2.1. Injector and Accelerator.** The electron beam can be unpolarized or polarized with electrons originating from either a thermionic or polarized gun. The polarized gun uses a strained gallium-arsenide (GaAs) cathode, illuminated by a 1497 MHz gain-switched diode laser, operated at 780 nm. The polarization vector is determined by a Wien filter which rotates the electron’s polarization angle, taking into account spin precession in the recirculation arcs, to optimize the longitudinal polarization once the beam enters the experimental halls. By switching the circular polarization of the laser, the sign of the beam helicity is switched pseudo-randomly at a rate of 30 Hz. This is accomplished by changing the voltage on a Pockel Cell at the source.

In the injector, the electrons are accelerated through a set of cryomodules to 45 MeV, then fed into the north linac. Each linac consists of twenty super-conducting cryomodules

<sup>1</sup>Hall B requires currents only on the order of 1 nA.

where the electrons are accelerated by 0.4 GeV per linac.<sup>2</sup> After traveling through the north linac, the beam enters a recirculation arc bending its trajectory to the entrance of the south linac. The beam then enters the south linac, where it is again accelerated. Upon exiting the south linac, the beam can be either recirculated again through the linacs, or extracted into the experimental halls. The recirculation can occur up to four times (five beam passes), allowing for a beam energy of up to 5.7 GeV. Once extracted from the linacs, the beam is split at a beam switch-yard into the three experimental halls, using three independent slits to control the current for each hall.

**3.2.2. Beam Energy Measurements.** The absolute beam energy for Hall A is measured by two different methods independently: the Arc method and the eP method [46]. Tab. 3.1 gives the values measured by both methods during “ $N \rightarrow \Delta$ ”. The results for

TABLE 3.1. Absolute beam energy during “ $N \rightarrow \Delta$ ”.

Date	Arc Energy (MeV) (Uncertainty)	eP Energy (MeV) (Uncertainty)
May 23	4530.6 (0.9)	4530.3 (1.0)
June 20	4531.0 (10)	4530.0 (10)

both methods are consistent. For this analysis, the Arc results were used as the beam energy.

**3.2.2.1. Arc Energy Measurement.** The Arc method, developed by the group from Saclay (France), measures the deflection of the beam in the section of the beamline between the beam switch-yard and the hall entrance (the arc section) to determine the energy [47]. The nominal bend angle of the beam in this beamline section is  $34.3^\circ$ . Fig. 3.2.3 presents the setup used for the Arc measurement. Two measurements are made simultaneously of the magnetic field integral,  $\int \vec{B} \cdot \vec{dl}$ , in eight arc dipoles with respect to a ninth reference dipole and of the actual bend angle,  $\theta$ , of the beam in the arc based on a set of wire scanners. The electron momentum can be calculated with a relative accuracy of better than  $2 \times 10^{-4}$  using:

$$p = c \frac{\int \vec{B} \cdot \vec{dl}}{\theta}, \quad (3.2.1)$$

where  $c = 0.299792$  is the speed of light in units of GeV·rad/Tm.

<sup>2</sup>Cryomodule improvements since 2000 now allow for an acceleration of 0.58 GeV per linac.



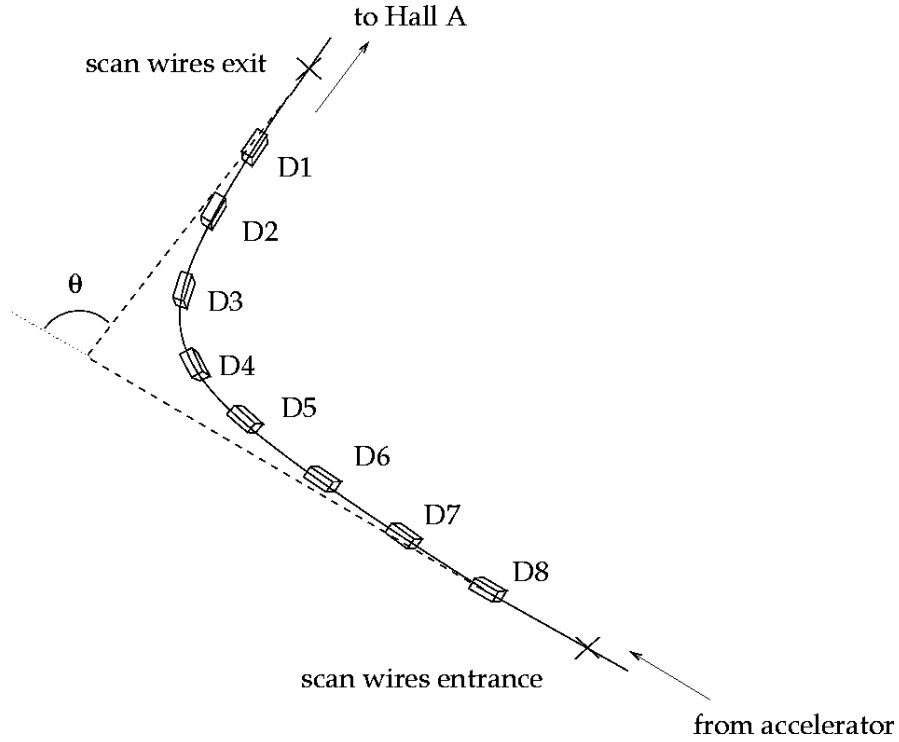


FIGURE 3.2.3. Setup for the Arc method of absolute electron beam energy measurement in Hall A.

3.2.2.2. *eP Energy Measurement.* The eP method, developed by the groups from the Blaise Pascal University in Clermont-Ferrand (France) and Saclay, uses the stand-alone device shown in Fig. 3.2.4 (taken from Ref. [45]) located along the beamline 17 m upstream of the Hall A target. Scintillators are used to trigger the system while Čerenkov detectors are used for particle identification. Two identical arms containing a proton and electron detector system made up of silicon micro-strip detectors (SSD) are placed symmetrically with respect to the beam along the vertical plane. The SSD are used to precisely measure the scattered electron and recoil proton angles,  $\theta_e$  and  $\theta_p$ , respectively, in the elastic  $^1\text{H}(e, e'p)$  reaction. These angles are measured concurrently in both arms of the detector. Uncertainties in the beam position and direction to first order are thus canceled. The incident electron energy is related to the electron and proton angles by:

$$E = M_p \frac{\cos \theta_e + \sin \theta_e / \tan \theta_p - 1}{1 - \cos \theta_p} + O\left(\frac{m_e^2}{E^2}\right). \quad (3.2.2)$$

The relative energy resolution is determined by the angular resolution of the micro-strips, and is typically better than  $2 \times 10^{-4}$ .

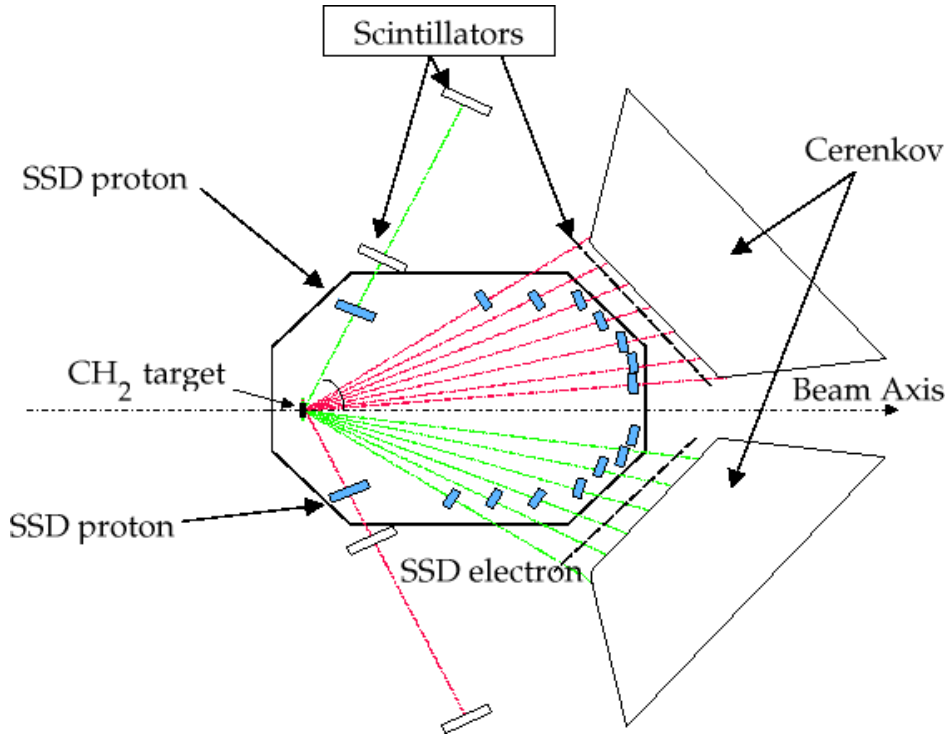
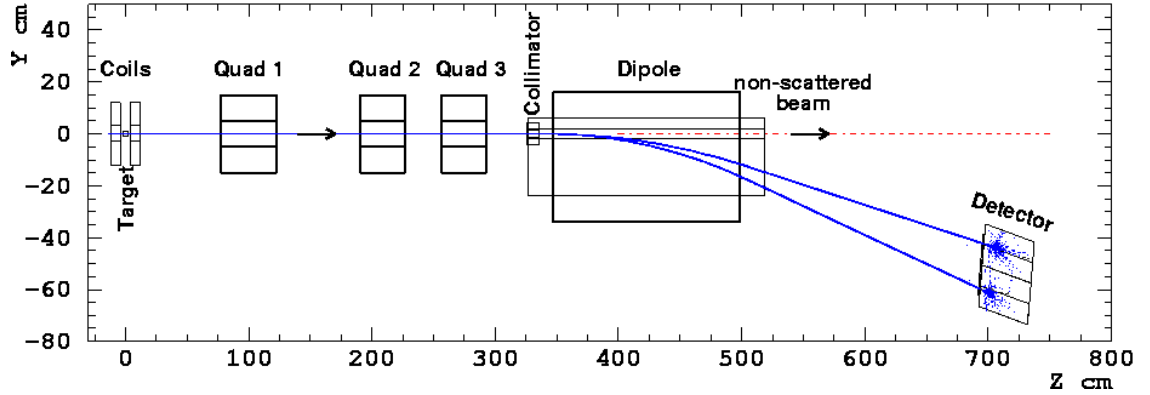


FIGURE 3.2.4. The eP detector used to measure the absolute electron beam energy in Hall A.

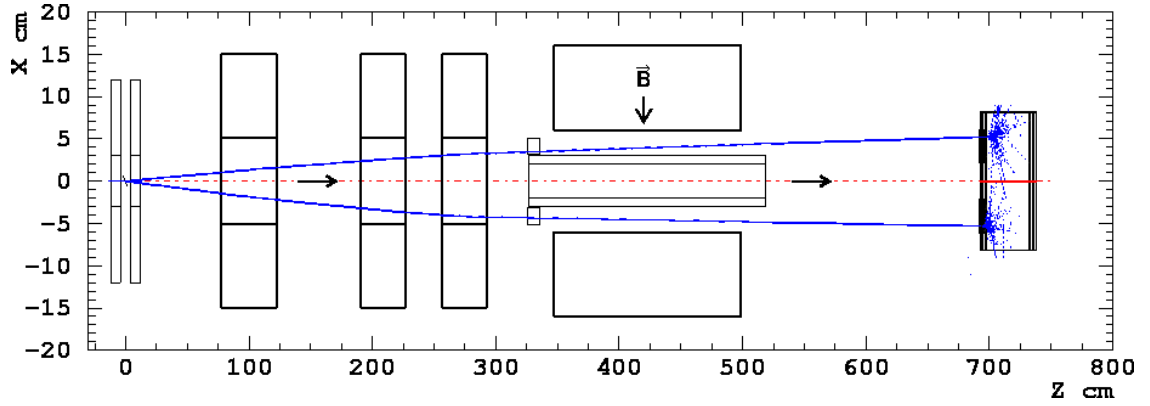
**3.2.3. Beam Polarization Measurements.** The beam helicity is a necessary piece of the differential cross section for pion electroproduction measurements, as discussed in Section 1.3.4. The Hall A beamline is equipped with two polarimeters to determine the polarization: the Møller and the Compton. Measurements made by the Møller polarimeter are invasive to the running experiment, thus for “ $N \rightarrow \Delta$ ” they were performed only as a cross check of Compton polarimeter measurements, which are not disruptive. Beam helicity measurements made by the Compton polarimeter were taken almost continuously throughout the “ $N \rightarrow \Delta$ ” experiment.

**3.2.3.1. The Møller Polarimeter.** The Møller polarimeter, exhibited in Fig. 3.2.5 (taken from Ref. [45]), was developed by the University of Kentucky and the Kharkov Institute of Physics and Technology. It uses the process of Møller scattering of polarized electrons from polarized atomic electrons in a magnetic foil:  $\vec{e}^- + \vec{e}^- \rightarrow e^- + e^-$ . The cross section for this reaction depends on the polarizations of both the beam  $\wp_e$  and the target  $\wp_{tgt}$ :

$$\sigma \propto 1 + \sum_{i=X,Y,Z} (A_{ii} \cdot \wp_{tgt\,i} \cdot \wp_{e\,i}), \quad (3.2.3)$$



(a) Side view.



(b) Top view.

FIGURE 3.2.5. Layout of the Møller polarimeter.

where  $i$  defines the projections of the polarizations and  $A_{ii}$  is the analyzing power which is dependant only on the scattering angle in the center of mass frame,  $\theta_{cm}$ .<sup>3</sup> Tab. 3.2 lists polarization measurements taken by the Møller polarimeter during " $N \rightarrow \Delta$ ". The sign difference between the July 17 measurement compared to all others is due to the following. The helicity of the beam is flipped by changing the voltage on the Pockel Cell at the source. For each event, the state of the helicity signal is recorded and can have the value -1, 0, 1, or 2: -1 (1) is when the pulse is low (high), 0 is an off period lasting about 500  $\mu\text{sec}$  between the transition from plus to minus helicity, and 2 is when the state of helicity is undetermined (rare). Ideally, -1 would correspond to a negative beam helicity and +1 a

<sup>3</sup>Maximum  $A_{ii}$  occurs at  $\theta_{cm} = 90^\circ$ .

TABLE 3.2. Beam polarization measurements taken by the Møller polarimeter during “ $N \rightarrow \Delta$ ”.

Date	Polarization (%)
May 23 18:00	$-76.6 \pm 0.2 \pm 2.4$
June 2 18:00	$-77.0 \pm 0.2 \pm 2.4$
June 9 11:00	$-75.8 \pm 0.2 \pm 2.4$
June 14 01:00	$-73.6 \pm 0.2 \pm 2.4$
June 19 22:00	$-71.7 \pm 0.2 \pm 2.4$
June 23 19:00	$-75.9 \pm 0.2 \pm 2.4$
June 26 20:00	$-75.8 \pm 0.2 \pm 2.4$
July 14 09:00	$-74.8 \pm 0.2 \pm 2.4$
July 17 18:00	$68.1 \pm 0.2 \pm 2.4$

positive beam helicity. The beam spin rotation through the accelerator is such that, in the Hall, it is rotated nearly  $180^\circ$  relative to its angle at the injector. The Møller, in the perfect case, would measure at this point a negative beam helicity. Towards the end of “ $N \rightarrow \Delta$ ” running, however, the polarized source gun had to be switched and it seems that each of the two polarized source guns have the Pockel Cell connected in such a way that the two guns use opposite sign conventions.

3.2.3.2. *The Compton Polarimeter.* The Compton polarimeter was developed jointly by Saclay, Jefferson Lab, and Clermont-Ferrand. It uses the process of Compton scattering:  $\vec{e} \vec{\gamma} \rightarrow e \gamma$ , to measure the beam polarization. This polarimeter is located just outside the entrance to the experimental hall. Its components, presented in Fig. 3.2.6 (taken from Ref. [45]), consist of a magnetic chicane, a photon source, an electromagnetic calorimeter, and an electron detector.

The polarized electron beam is deflected by the chicane and interacts with a photon beam of known circular polarization. After the interaction, the backscattered photons are detected in a calorimeter and the electrons in a Silicon Strip Detector (SSD). The interaction is described by QED, allowing for calculation of the cross section of polarized electrons scattered from polarized photons as a function of energy and scattering angle. The counting rate asymmetry is proportional to the photon and electron polarizations and the cross section asymmetry as such:

$$A_{exp} = \frac{N^+ - N^-}{N^+ + N^-} = A_c \wp_\gamma \wp_e, \quad (3.2.4)$$

where  $N^+$  and  $N^-$  are the number of photons detected for the two beam helicity states,  $A_c$

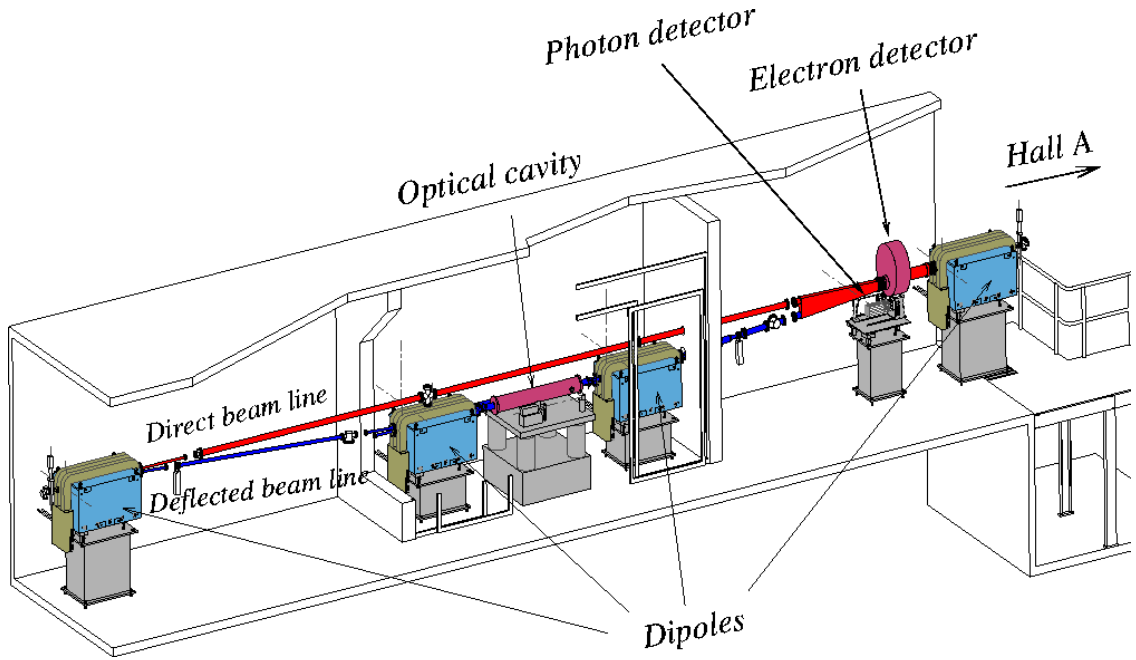


FIGURE 3.2.6. Schematic of the Compton polarimeter, showing the four dipoles of the magnetic chicane, the optical cavity, and the photon and electron detectors.

is the cross section asymmetry calculated by QED,  $\wp_\gamma$  is the (known) photon polarization, and  $\wp_e$  is the measured electron polarization. All electrons that did not interact exit the polarimeter and continue on to the Hall A target, making this an unobtrusive method.

The polarization as measured by the Compton polarimeter varied between 57% and 75% over the entire " $N \rightarrow \Delta$ " experiment and are shown in Tab. 3.3 and Fig. 3.2.7. The values in the table in parentheses correspond to periods where there was no Compton measurement; the value was deduced from close measurements when no spot move occurred. The absolute value of these measurements are plotted; the errors are the statistical and systematic errors uncorrelated run by run; the vertical dashed lines correspond to a *spot move* of the laser source or the GaAs cathode at the injector; and, the red (up to day 56) and blue points (after day 56) correspond to the two different polarized source guns (figure courtesy of S. Escoffier). Full details of the Compton polarization measurements over the entire " $N \rightarrow \Delta$ " experiment were the focus of the PhD thesis of Stéphanie Escoffier [48].

Notice that the sign of the Compton polarization values are opposite to the sign of those given by the Møller. This is simply due to the convention the two detectors use

TABLE 3.3. Beam polarization measurements taken by the Compton polarimeter during " $N \rightarrow \Delta$ ".

Date	Polarization (%)
May 22 19:30 - May 23 10:30	$73.78 \pm 0.22 \pm 1.0$
May 23 21:00 - May 24 09:30	$74.01 \pm 0.27 \pm 1.0$
May 24 11:00 - May 25 11:30	$73.68 \pm 0.19 \pm 1.0$
May 25 15:30 - May 26 03:00	$74.66 \pm 0.24 \pm 1.0$
May 27 21:30 - May 28 05:30	$(74.16 \pm 0.67 \pm 1.0)$
May 28 08:00 - May 29 04:00	$(73.81 \pm 0.38 \pm 1.0)$
May 29 06:00 - May 30 04:00	$73.81 \pm 0.38 \pm 1.0$
May 30 06:00 - May 30 14:30	$(73.81 \pm 0.38 \pm 1.0)$
May 30 14:30 - May 31 14:30	$(70.74 \pm 0.28 \pm 1.0)$
May 31 18:30 - June 1 13:30	$70.74 \pm 0.28 \pm 1.0$
June 1 17:30 - June 2 09:30	$71.19 \pm 0.28 \pm 1.0$
June 2 23:30 - June 4 00:30	$74.03 \pm 0.21 \pm 1.0$
June 4 02:30 - June 5 09:00	$74.65 \pm 0.20 \pm 1.0$
June 14 18:30 - June 18 12:30	$74.57 \pm 0.15 \pm 1.0$
June 18 12:30 - June 19 02:00	$71.12 \pm 0.28 \pm 1.0$
June 19 05:00 - June 20 05:00	$71.39 \pm 0.18 \pm 1.0$
June 20 05:00 - June 20 19:30	$68.84 \pm 0.41 \pm 1.0$
June 20 19:30 - June 22 01:30	$66.83 \pm 0.14 \pm 1.0$
June 22 03:30 - June 23 11:00	$67.30 \pm 0.16 \pm 1.0$
June 23 11:00 - June 24 07:00	$71.81 \pm 0.24 \pm 1.0$
June 24 09:30 - June 26 10:00	$71.93 \pm 0.17 \pm 1.0$
June 26 10:00 - June 29 07:30	$73.08 \pm 0.19 \pm 1.0$
June 26 11:00 - June 30 07:00	$72.90 \pm 0.30 \pm 1.0$
July 12 22:00 - July 14 19:00	$73.05 \pm 0.22 \pm 1.0$
July 14 19:00 - July 17 10:00	$-63.82 \pm 0.12 \pm 1.0$
July 17 22:00 - July 21 10:00	$-64.24 \pm 0.10 \pm 1.0$
July 21 10:00 - July 21 17:00	$-56.64 \pm 0.39 \pm 1.0$
July 21 20:00 - July 22 10:30	$-56.74 \pm 0.28 \pm 1.0$
July 22 10:30 - July 24 10:00	$-63.92 \pm 0.11 \pm 1.0$
July 24 10:00 - July 25 20:00	$-64.85 \pm 0.16 \pm 1.0$
July 25 23:30 - July 29 16:00	$-65.58 \pm 0.10 \pm 1.0$
July 29 19:30 - August 1 02:30	$-65.69 \pm 0.35 \pm 1.0$

relative to each other. The convention used in the analysis to extract the recoil proton polarizations was such that the sign of the beam for the plus helicity was taken from the Møller measurement.

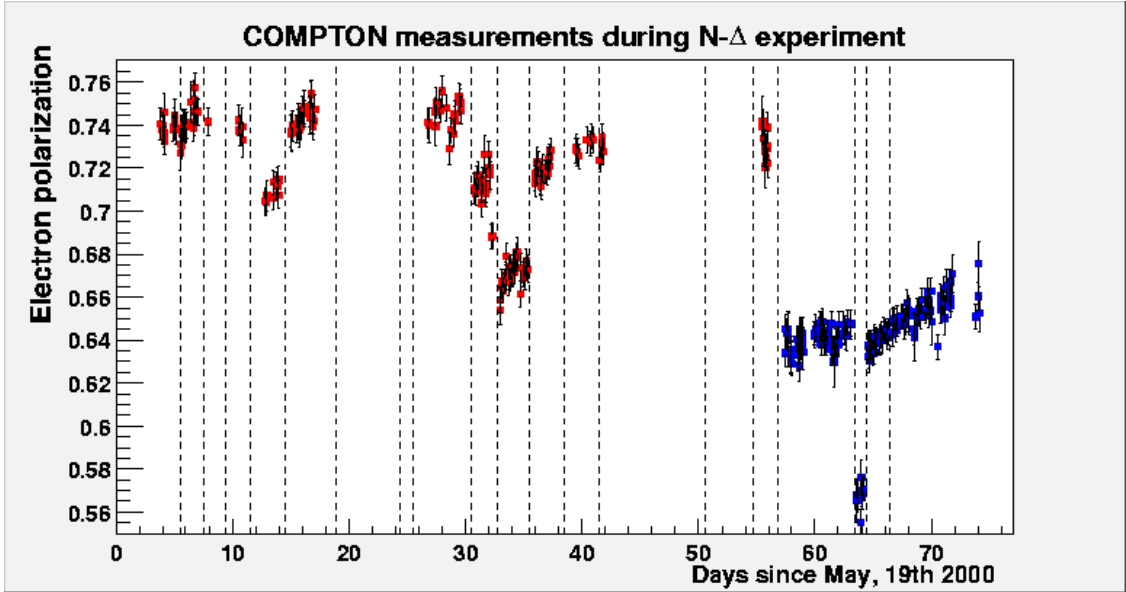


FIGURE 3.2.7. Beam polarization measurements taken by the Compton polarimeter during " $N \rightarrow \Delta$ ".

### 3.3. The Hall A Target

Once the polarized electron beam enters the experimental hall, it scatters from the standard Hall A liquid hydrogen target [49, 50]. The cryogenic target (cryotarget) system consists of a scattering vacuum chamber and a target ladder containing three cryogenic target loops.

**3.3.1. The Scattering Chamber.** The scattering chamber is separated into three sections. The base, located on the pivot of the hall, is made of stainless steel and contains several ports for vacuum pumps, visual inspection, and electrical feed-throughs. The middle section, located at beam height, is composed of aluminum with 152 mm vertical cutouts on each side of the beam covering the full angular range ( $12.5^\circ \leq \theta \leq 165^\circ$ ). These cutouts are covered with thin aluminum foils of 0.38 mm. There are also entrance and exit beam ports to insure the beam interacts only with the target. The upper section contains the cryotarget system.

**3.3.2. The Cryogenic Target (Cryotarget).** The target system is mounted inside the scattering chamber along with sub-systems for cooling, gas handling, temperature and pressure monitoring, and target control and motion. The targets are arranged in a ladder

like formation which can be controlled from the counting house to move the desired target into the beamline.

This system consists of three independent loops: a liquid hydrogen  $\text{LH}_2$  loop, a liquid deuterium  $\text{LD}_2$  loop, and a gaseous helium loop. Both the  $\text{LH}_2$  and  $\text{LD}_2$  loops contain two cylindrical aluminum target cells of 4 and 15 cm in length, with their axes along the beam direction. Each cell has a diameter of 6.35 cm, an upstream window thickness of 0.071 mm, a downstream window thickness of 0.102 mm, and a sidewall thickness of 0.178 mm. The helium loop has a single vertical cylindrical aluminum cell. Its diameter is 10.4 cm with a wall thickness of 0.33 mm.

This experiment utilized the 15 cm  $\text{LH}_2$  cell, operated at a temperature of 19 K and a pressure of 25 psi, giving a density of approximately  $0.0723 \text{ g/cm}^3$ . The target coolant (helium) was supplied by the End Station Refrigerator (ESR) at a temperature of 15 K. It was used by the target and returned at a little over 20 K. The temperature was regulated with a high-power heater to compensate for variations in the beam intensity and a feedback circuit reading the temperature from a probe.

Besides the cryotargets, there were three 'dummy' targets and five solid targets. The dummy targets were made of two thin pieces of aluminum separated by a distance of 4 cm, 10 cm, and 15 cm. They were used to mimic, and thus determine, contributions from the target windows.

Because of the small size of the beam spot, damage to the target cell at high beam current could occur. To minimize this damage, the beam is rastered. This is accomplished using dipole magnets in both the vertical and horizontal directions. The raster mode can be either amplitude modulated, producing a spherical shape in the plane transverse to the beam axis, or sinusoidal, producing a square shape. For this experiment the latter was used, where the magnet pairs were driven with a pure sine wave and a relative phase of  $90^\circ$  at frequencies that did not produce a closed Lissajous pattern. The resulting square was approximately  $4 \times 4 \text{ mm}^2$ , reducing the density fluctuation from beam heating to a fraction of a percent.

### 3.4. The High Resolution Spectrometers (HRS)

The central piece of Hall A equipment is the pair of identical  $4 \text{ GeV}/c$  HRS. Both are able to provide a momentum resolution of better than  $2 \times 10^{-4}$  and horizontal angular resolution of better than 2 mrad. Each spectrometer consists of a vertically bending



set of four super-conducting magnets in a quadrupole, quadrupole, dipole, quadrupole (QQDQ) configuration, as shown in Fig. 3.4.1. This configuration was chosen based on several considerations including: momentum resolution at the  $10^{-4}$  level in the 0.8-4.0 GeV/ $c$  momentum range, large acceptance in both angle and momentum, good position and angular resolution in the scattering plane, an extended target acceptance, and a large angular range. The  $45^\circ$  vertical bend helps to decouple, to first order, measurements of the position along the target from the momentum. The main design characteristics of the spectrometers are listed in Tab. 3.4 (taken from Ref. [45]).

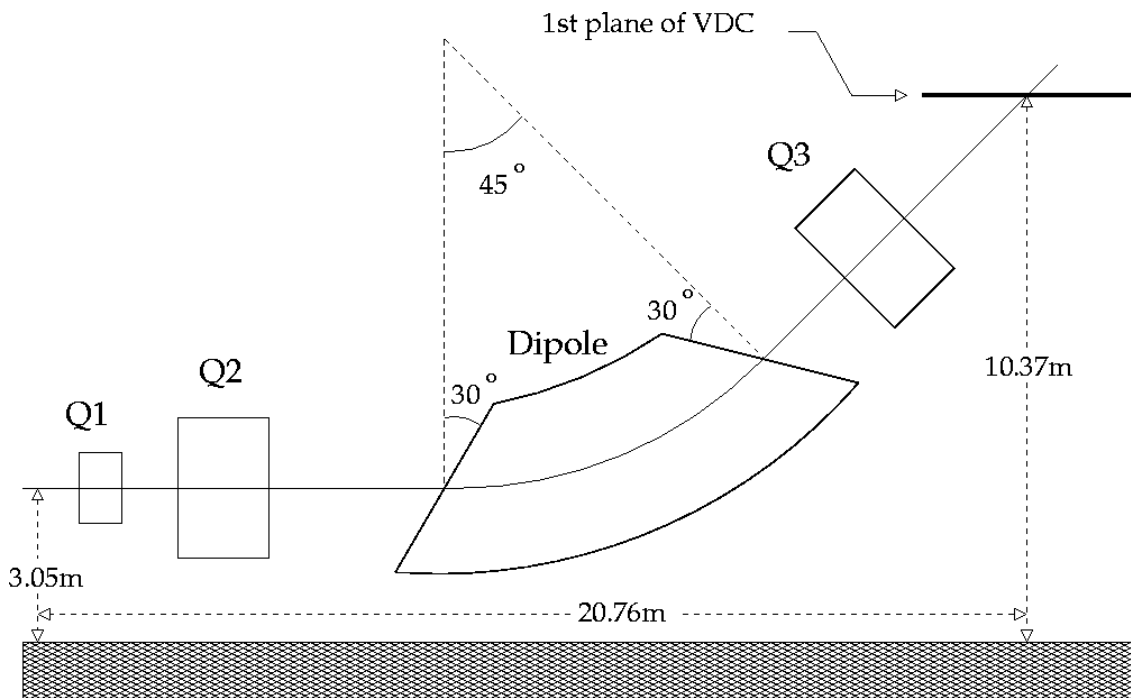


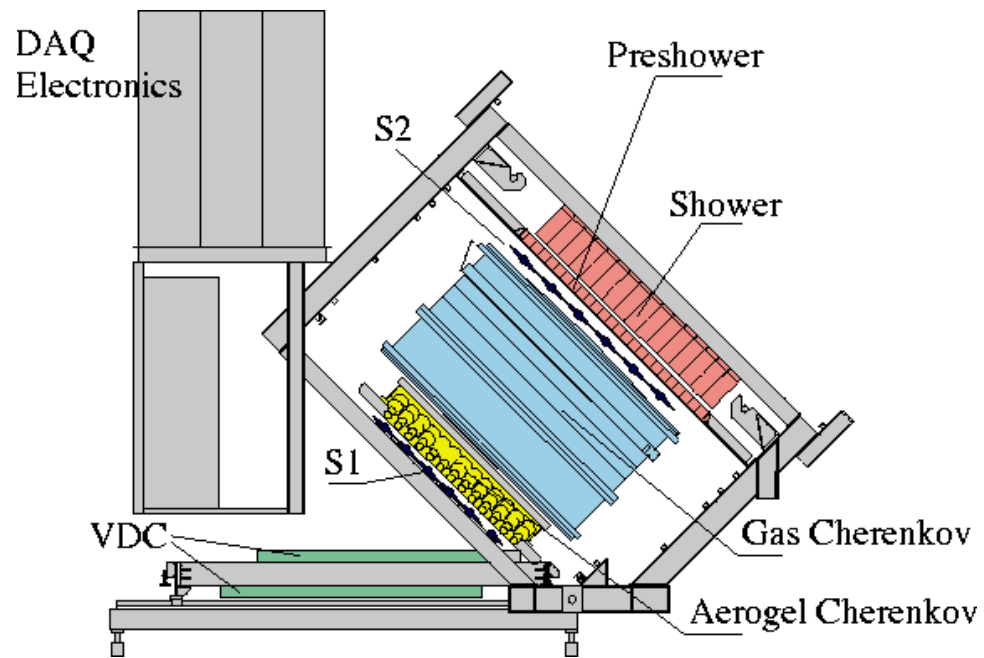
FIGURE 3.4.1. Layout of the Hall A HRS.

TABLE 3.4. Main design characteristics of the Hall A HRS.

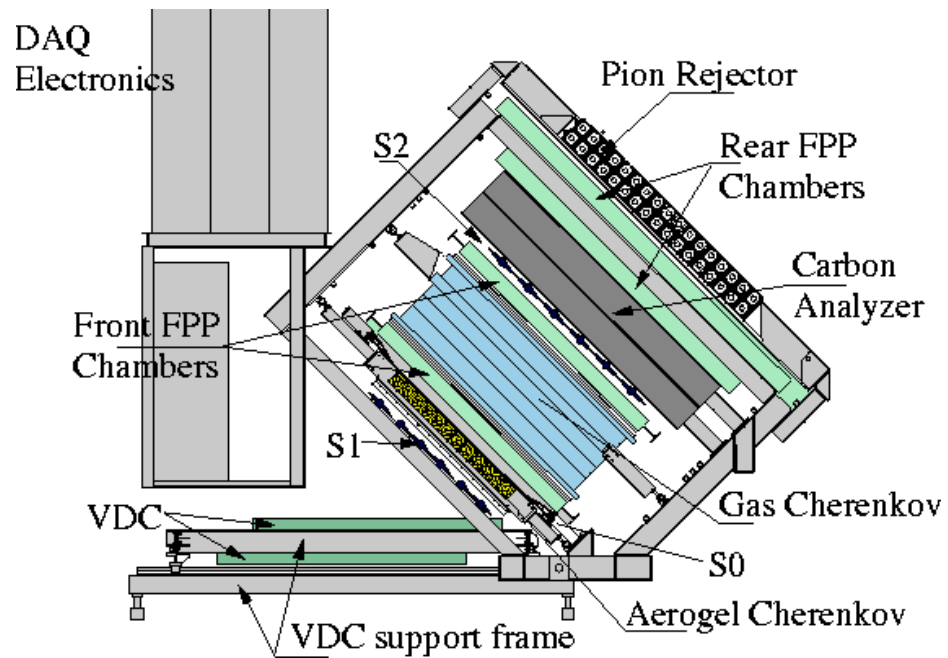
Configuration	QQDQ vertical bend
Bending Angle	45°
Optical Length	23.4 m
Momentum Range	0.3-4.0 GeV/ <i>c</i>
Momentum Acceptance	-4.5% < $\delta p/p$ < +4.5%
Dispersion at the Focus ( <i>D</i> )	12.4 m
Radial Linear Magnification ( <i>M</i> )	-2.5
<i>D/M</i>	5.0
Angular Range	12.5°-165°
Horizontal Angular Acceptance	±30 mrad
Vertical Angular Acceptance	60 mrad
Horizontal Angular Resolution	0.5 mrad
Vertical Angular Resolution	1.0 mrad
Solid Angle at $\delta p/p = 0, y_o = 0$	6 msr
Transverse Length Acceptance	±5 cm
Transverse Position Resolution	1 mm

**3.4.1. The Detector Package.** The detector packages of the two spectrometers are designed to provide a trigger to activate the data-acquisition (DAQ) system, tracking information, precise timing for time-of-flight (TOF) measurements and coincidence determination, and identification of the detected particles. Fig. 3.4.2 shows a side view of the detector packages for the two HRS (taken from Ref. [45]). The timing information and the main trigger are provided by scintillators. Particle identification (PID) is accomplished using gas and aerogel Čerenkov detectors and lead-glass shower counters. Information from the PID detectors can also be included in the trigger. Tracking information is provided by a pair of Vertical Drift Chambers (VDCs).

The main part of the detector package, the trigger scintillators and VDCs, are identical in the two HRS. The PID detector arrangement differs slightly in the two arms. The HRSh contains an additional piece of equipment essential to this experiment, the FPP used to determine the polarization of the recoil protons. The detector packages, along with all DAQ electronics are located inside a Shield Hut (SH) on top of each detector arm to protect them from background radiation present in the Hall.



(a) Electron arm detector stack.



(b) Hadron arm detector stack.

FIGURE 3.4.2. Side view of the HRS detector packages.

3.4.1.1. *Triggering.* Timing and the main trigger are provided by scintillators. In general, there are two primary scintillator planes, S1 and S2. These are separated by a distance of about 2 m. Each plane is composed of six overlapping scintillator paddles. Each paddle is attached to two Photo-Multiplier Tubes (PMTs). An additional third scintillator plane, S0, was also used during “ $N \rightarrow \Delta$ ” allowing higher trigger efficiency for the hadron. The S0 scintillator is thicker than the S1 and S2 (10 mm as opposed to 5 mm), and is viewed by two PMTs. Additional information from the gas Čerenkov can also be included in the trigger.

A coincidence between two PMTs is made for each scintillator paddle. A logical OR of these signals is made individually for the S1 and S2 planes. The main trigger for one spectrometer is formed by the logical AND of the S1 and S2 planes. The S0 and Čerenkov detectors are used to measure the trigger efficiency by requiring a hit in either the S1 or S2 plane and a hit in the third (S0 or Čerenkov) detector. A coincidence trigger (logical AND) is then made from the time overlap of the two spectrometer triggers. The various trigger signals go to the trigger supervisor module which starts the DAQ readout system. Fig. 3.4.3 shows a typical “ $N \rightarrow \Delta$ ” coincidence time spectrum between the HRS. The structure seen in the background corresponds to the RF structure of the CEBAF beam pulses.

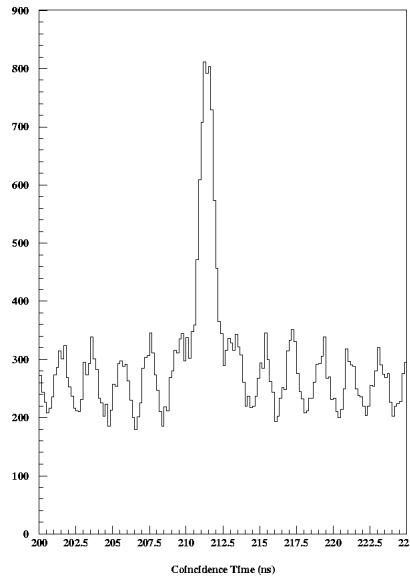
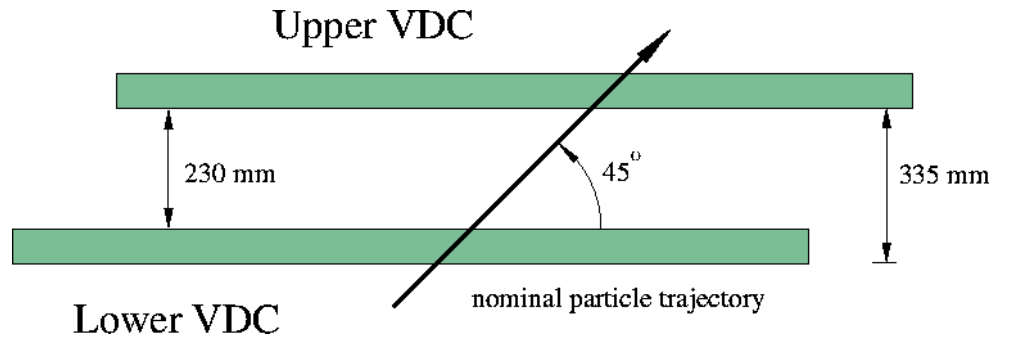
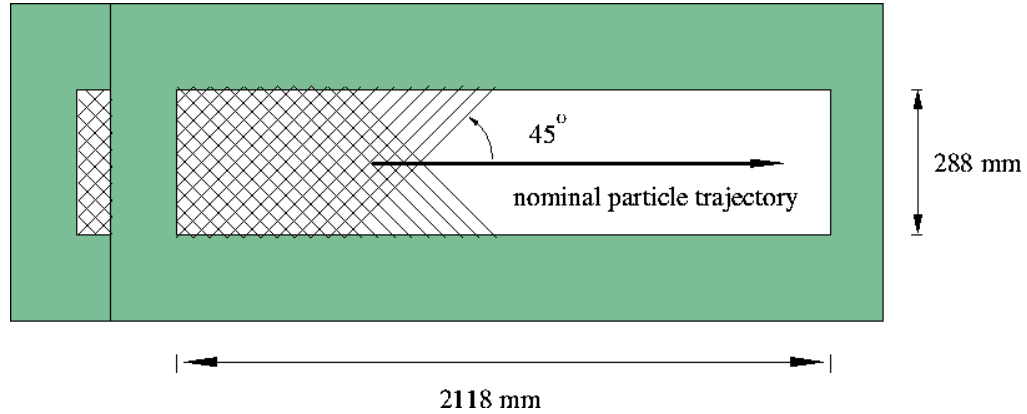


FIGURE 3.4.3. Sample coincidence time spectrum between the two HRS for  $\theta_{pq} = 90^\circ$ .

3.4.1.2. *Tracking*. Information on the track of the particle, the position and direction, is supplied by two VDCs described in detail in Refs. [51, 52]. Each chamber of the VDC is composed of two planes, each containing 368 sense wires, oriented in a  $uv$ -configuration (the wires of each plane are oriented at an angle of  $90^\circ$  with respect to each other). Each plane is oriented at an angle of  $45^\circ$  with respect to the detected particle's central trajectory (see Fig. 3.4.4, taken from Ref. [45]). The chambers are filled with a gas mixture of 62%



(a) Side view.



(b) Top view.

FIGURE 3.4.4. Layout of the VDCs.

argon (Ar) and 38% ethane. When a charged particle travels through the VDC, it ionized the Ar gas atoms, leaving behind a track of electrons and ions. The electrons drift to the sense wires where there is a field gradient of  $1/r$ . They then ionize more Ar atoms causing an avalanche. The electron avalanche is captured by the sense wires and a signal is sent

to a LeCroy amplifier-discriminator card. The logic signal output is then sent to a FastBus LeCroy Time to Digital Converter (TDC) module where the time data is put into the data stream. The drift information, combined with the drift velocity of the electrons, is used to calculate the perpendicular distance from the track to the wire that fired, as demonstrated in Fig. 3.4.5.

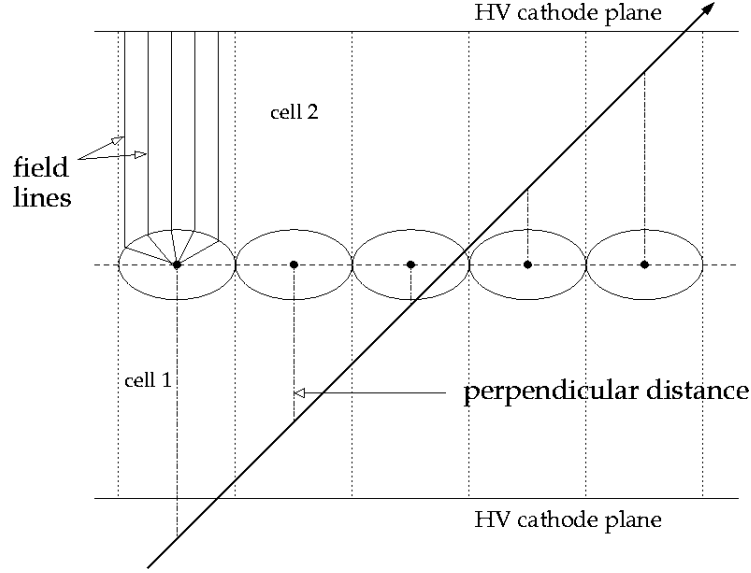
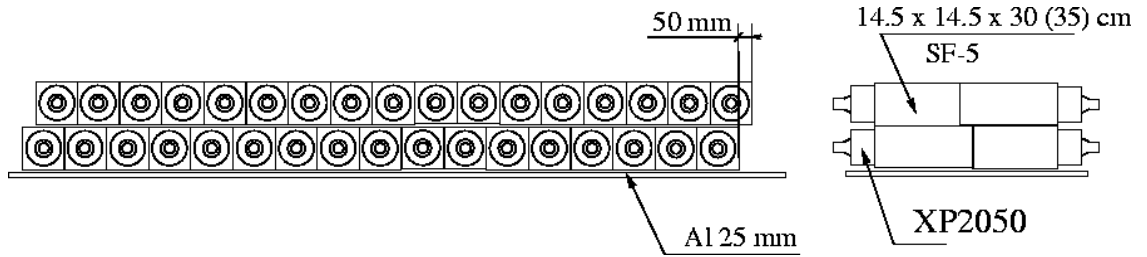


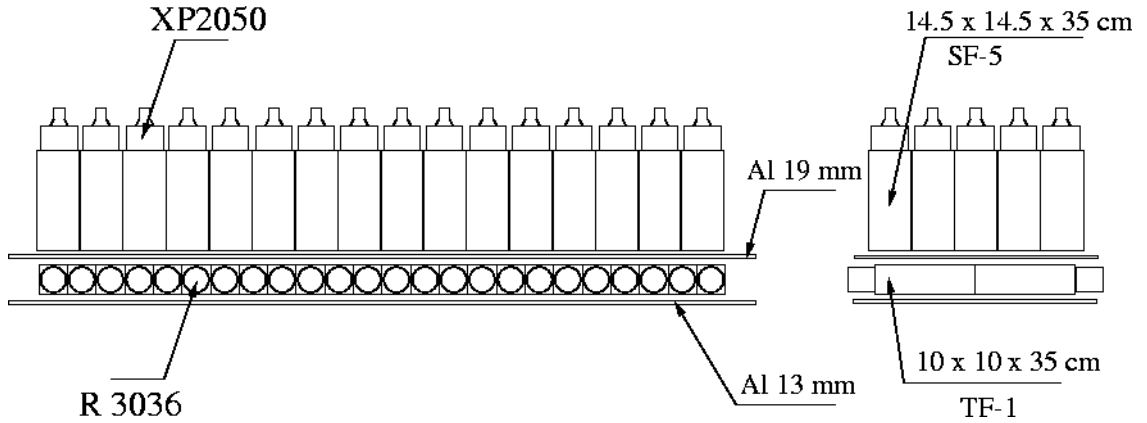
FIGURE 3.4.5. An example of a particle trajectory in a VDC plane.

3.4.1.3. *Particle Identification (PID)*. A gas Čerenkov detector is mounted between the S1 and S2 scintillator planes. This detector is filled with  $\text{CO}_2$  gas at atmospheric pressure. The pion threshold in this counter is  $4.8 \text{ GeV}/c$  allowing for identification of electrons with an efficiency of 98-99%. For more information on the gas Čerenkov detector, see Ref. [53].

Two layers of shower detectors are present in both HRS [54]. Fig. 3.4.6 (taken from Ref. [45]) shows their configuration. The combination of these shower counters and the gas Čerenkov provides a pion suppression factor of  $2 \times 10^5$  with a 99% efficiency for electrons on the HRSe. Also used during " $N \rightarrow \Delta$ " was a diffusion type aerogel Čerenkov [55]. The 9 cm thick aerogel material has a refraction index of 1.015, with a corresponding pion threshold of  $0.803 \text{ GeV}/c$ .



(a) Electron arm shower detector.



(b) Hadron arm shower detector.

FIGURE 3.4.6. Shower counter configuration in both HRS.

### 3.5. The Focal Plane Polarimeter (FPP)

The most essential piece of equipment to the running of this experiment was the FPP [56], developed jointly by Rutgers University, the College of William and Mary, the University of Georgia, and Norfolk State University. It was located at the focal plane of the hadron spectrometer where it measured the polarization of the recoil proton. Following momentum analysis and focusing in the spectrometer, the proton enters the FPP – the layout of which is presented in Fig. 3.5.1. The proton's initial trajectory is determined by a set of front straw chambers. It then undergoes a secondary scattering in an analyzer. Finally, the outgoing trajectory is determined by a set of rear straw chambers. If the protons are polarized transverse to the momentum direction, an azimuthal asymmetry results from the spin-orbit interaction with the analyzing nucleus. This asymmetry is proportional to

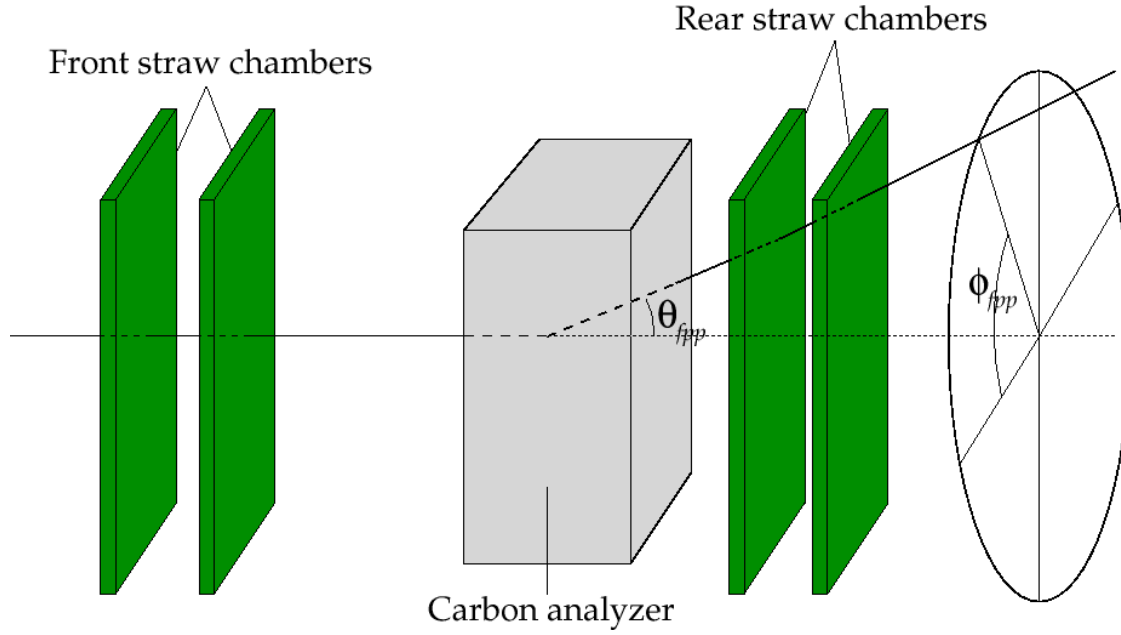


FIGURE 3.5.1. Layout of the FPP.

the proton's polarization.

For this experiment, the standard Hall A carbon (high purity graphite) analyzer was employed. Considering cost, safety, and efficiency, carbon is ideal for measuring proton polarization with a momentum up to  $2.4 \text{ GeV}/c$  [57, 58]. This analyzer consists of five carbon doors of decreasing thickness: 22.9 cm, 15.2 cm, 7.6 cm, 3.8 cm, and 1.9 cm for a maximum thickness of 51.4 cm. The thickness can be varied remotely from the counting house so that there is greater geometrical efficiency at the lower energy where the scattering distribution is less forward-peaked.

The straw chambers are a set of cylindrical tubes 1.0 cm in diameter with a thin wire running along the central axis of each straw, as shown in Fig. 3.5.2. The straws are oriented along the  $u$  and  $v$  directions, at  $45^\circ$  angles to the  $x$  and  $y$  directions. Each chamber has 3  $u$  and 3  $v$  planes<sup>4</sup> positioned normal to the spectrometer's nominal central trajectory. The dimensions of the rear straw chambers were made large enough so that the geometrical efficiency is close to 100% for events scattering at angles up to  $20^\circ$ . The dimensions of all four straw chambers are listed in Tab. 3.5.

Each straw is supplied with a mixture of 62% Ar and 38% ethane gas. The sense wire is maintained at positive high voltage relative to the straw. When a charged particle

<sup>4</sup>Chamber 3 has 2  $u$ , 2  $v$ , and 2  $x$  planes. The  $x$  planes were added to aid in the analysis of multiple tracks.



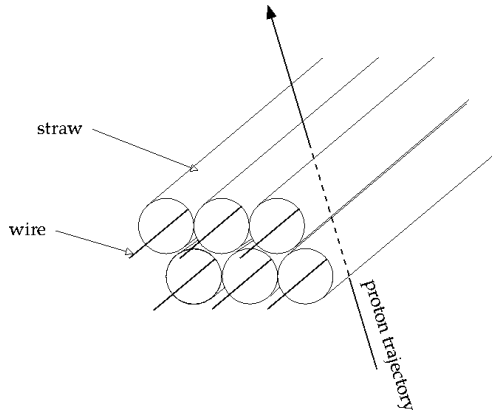


FIGURE 3.5.2. Six straws in two different planes of an FPP straw chamber.

TABLE 3.5. Dimensions of the FPP straw chambers.

Straw Chamber	1	2	3	4
Active length (cm)	209.0	209.0	267.5	292.2
Active width (cm)	60.0	60.0	122.5	140.6
Wire spacing (cm)	1.095	1.095	1.0795	1.0795

passes through the straw it ionizes the Ar gas atoms, leaving behind a track of electrons. The electrons drift towards the anode wire at a constant velocity of about  $50 \mu\text{m}/\text{sec}$ . As the electrons approach the wire with a field gradient of  $1/r$  they ionize more Ar causing an avalanche of electrons. The wires capture the avalanche and send a negative analog signal to the read out board, where it is preamplified and discriminated to give a logic pulse. Fig. 3.5.3 is the block diagram for the logic of the FPP signal.

The straw around each wire forms a physical ground causing proton tracks to leave a signal in only one wire. The signal is multiplexed into groups of eight neighboring wires to reduce the number of TDCs necessary for the FPP. For a single event it is likely that only one (or zero) wire fires for the entire group of eight, allowing each of the eight to be read by the same multiplexing chip. This chip is setup to give a logic pulse whose width depends on which wire fired. The 45 mV signal becomes 800 mV in a level shifter. The signal is then sent to the FastBus TDC module whose output is added to the data stream. This multi-hit TDC records two times: at the arrival of the leading (l.e.) and the trailing (t.e.) edges of the logic signal. Reconstruction of the difference between these two times allows for the identification of the wire that fired. The time difference between the leading

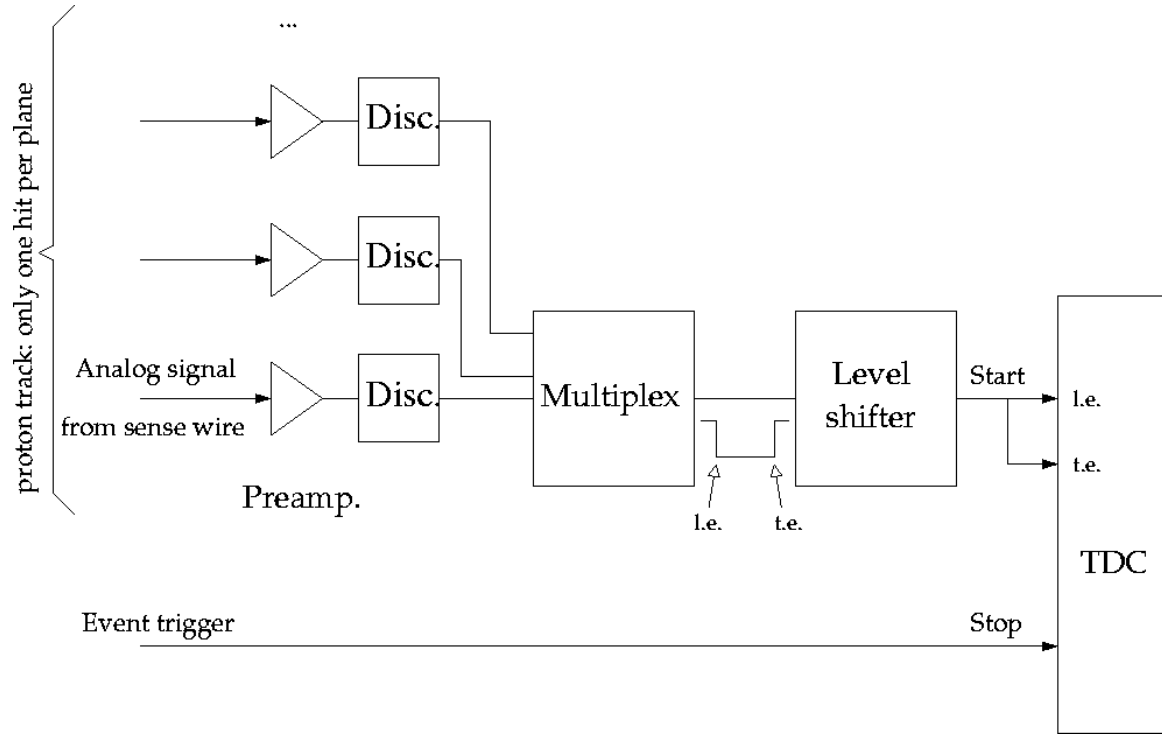


FIGURE 3.5.3. Block diagram for the logic of the FPP signal.

edge and the trigger gives the drift time.

### 3.6. Overview of Runplan

For " $N \rightarrow \Delta$ " data taking, a cycle of three types of runs were taken: a trigger efficiency run, a set of pointing reference runs, and the pion electroproduction (production) runs.

**3.6.1. Trigger Efficiency.** The trigger efficiency was checked using the maximum beam current on the  $\text{LH}_2$  target and about five minutes of data. For these runs electron arm and hadron arm triggers were taken, while coincidence triggers were prescaled away.

**3.6.2. Pointing Reference.** A set of pointing reference runs were taken using each of four targets: the carbon foil, the 4 cm dummy, the 10 cm dummy, and the 15 cm dummy. For each of these runs only  $5 \mu\text{A}$  of beam were used, without raster. Electron and hadron arm singles triggers were both taken, with coincidence triggers prescaled away. These runs were used to determine the mispointing of the spectrometers (discussed in detail in

Appendix A). The 15 cm dummy target runs were also used to determine the contribution of the target walls to the production data.

**3.6.3. Production Running.** Two sets of production runs were taken: with and without a 6 msr collimator in the nose of the spectrometer. Cross section determination needs to know exactly how many events leave the target, and how many of these events pass through the HRS. The collimator reduces the detected beam envelope, giving a better determination of the edges of the acceptance, and therefore a better cross section measurement. Once sufficient statistics were obtained for good cross section measurements, the collimator was removed. Measurements of polarization observables are not sensitive to detailed knowledge of the acceptance, since they do not depend on knowing the fraction of events leaving the target and passing through the HRS, but rely only on having as many events as possible measured. All production data was taken so that all coincidence events were recorded. Singles events from each HRS were prescaled before being recorded in order to give low dead-time. Data were taken in three different run periods: May 19 to June 5, June 8 to July 1, and July 11 to early morning August 1. Appendix B is a list of all data runs, and the type of information contained in each, taken during “ $N \rightarrow \Delta$ ”.

3.6.3.1. *Period 1: May 19 to June 5.* The first few days of the Period 1 were dedicated to:

- (1) beam energy measurements,
- (2) beam helicity measurements using the Møller polarimeter,
- (3) calibrations of the Beam Current Monitor (BCM),
- (4) target luminosity studies,
- (5) checks of the spectrometer optics using elastic scattering off of the  $\text{LH}_2$  target and a sieve slit in the nose of each spectrometer,
- (6) measurement of the analyzing power of the FPP (discussed in detail in Section 4.4.5.1), and
- (7) false asymmetry studies (discussed in detail in Section 4.5.1).

A first pass through all hadron kinematics settings shown in Tab. 1.1, except  $\theta_{pq} = 180^\circ$ <sup>5</sup>, was also made during this run period. All production data during this period were taken with the 6 msr collimator in place to allow for good cross section determination. Data from each hadron kinematic setting were taken in a cycle of:

---

<sup>5</sup> $\theta_{pq} = 180^\circ$  data was not taken until the end of the experiment to ensure that all other kinematics had sufficient statistics.

- (1) a trigger efficiency run,
- (2) pointing reference runs using the  $^{12}\text{C}$  foil target, the 4 cm dummy target, the 10 cm dummy target, and the 15 cm dummy target, and
- (3) production data.

3.6.3.2. *Period 2: June 8 to July 1.* During this second run period, a second pass of all hadron kinematics was begun – except  $\theta_{pq} = -25^\circ$ <sup>6</sup> for which enough statistics were obtained during Period 1. Trigger efficiency runs were not repeated for the second pass through a particular kinematic setting. The spectrometer mispointing measurements, however, were repeated since the mispointing changes each time the spectrometer moves. The first two or three production runs taken for each kinematic were done so with the 6 msr collimator in as a cross check of the cross section. After these first one or two runs, the 6 msr collimator was removed to allow more statistics for the extraction of polarization observables. Production measurements of  $\theta_{pq} = 0^\circ, 25^\circ, -50^\circ, -90^\circ, -135^\circ$ , and  $-155^\circ$  were completed during this period, along with some  $\vec{q}$  pointing and optics checks, and measurement of the  $^1\text{H}(e, e'p)$  elastic cross section.

3.6.3.3. *Period 3: July 11 to August 1.* The second pass through the hadron kinematics was interrupted by the 4th of July holiday and a period of facility development time (July 8 and July 9). Period 3 was then used to finish up the second pass through the production data. Spectrometer mispointing measurements were also made with each kinematic change. Production measurements of  $\theta_{pq} = 50^\circ, 90^\circ, 135^\circ$ , and  $155^\circ$  were completed during this period along. Once adequate statistics for all planned<sup>7</sup> kinematics measurements were completed, the  $\theta_{pq} = 180^\circ$  production data was taken. Some electron optics, dead-time studies, and elastic data used for false asymmetry studies were also taken during Period 3.

---

<sup>6</sup>From this point forward, kinematics with  $\phi_{pq} = 0^\circ$  will be denoted as positive  $\theta_{pq}$  while those with  $\phi_{pq} = 180^\circ$  will be denoted as negative  $\theta_{pq}$ .

<sup>7</sup> $\theta_{pq} = 180^\circ$  was unplanned. After adequate statistics for all other kinematics settings were achieved, it was decided to add this final kinematic setting.

## CHAPTER 4

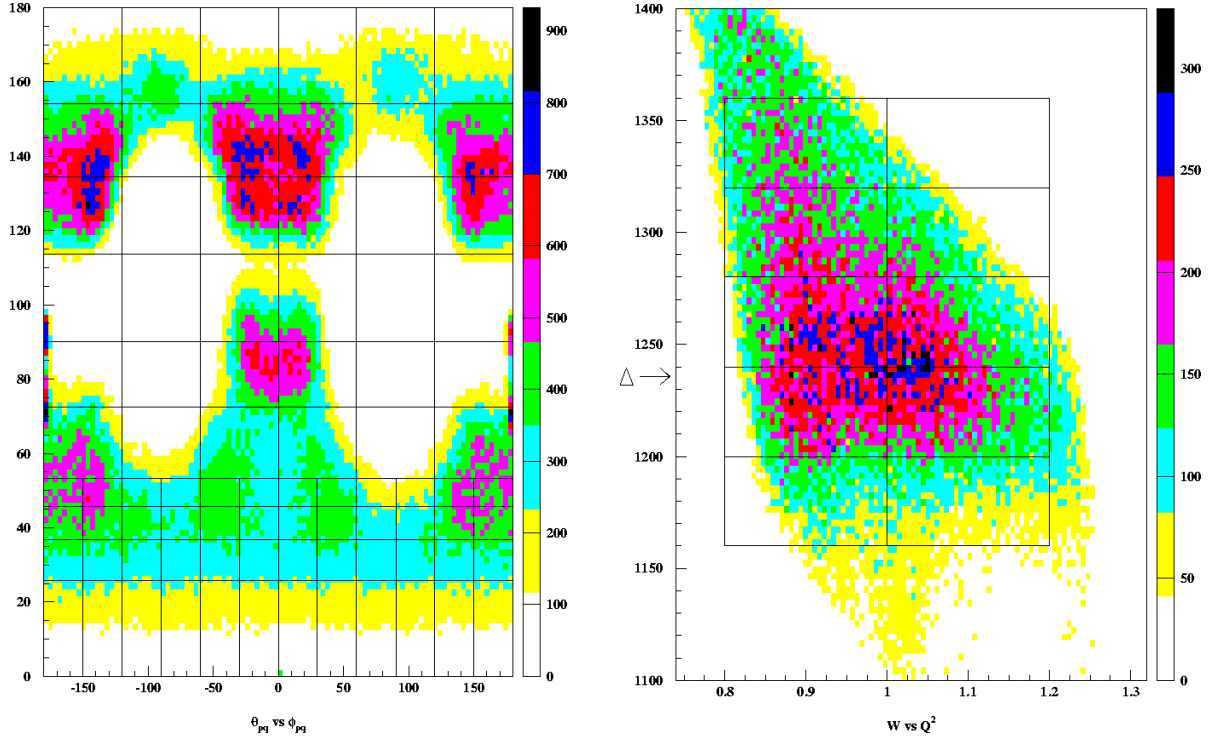
# DATA ANALYSIS

### 4.1. Overview

Scattered electrons from the  $p(\vec{e}, e'\vec{p})\pi^0$  reaction were detected in the HRSe in coincidence with recoil protons in the HRSh. This chapter will discuss the detection of these particles and how their information at the target is reconstructed, the identification of each particle, the extraction of the recoil proton polarization, and the determination of the polarized response functions.

Data were taken in a set of 12 different proton kinematic settings (those listed in Tab. 1.1). The electron kinematics were fixed at  $\theta_e = 14.1^\circ$  and  $k' = 3.7 \text{ GeV}/c$ , while the recoil proton angle in the center of mass frame (measured with respect to the central  $\vec{q}$  direction) was set to  $\theta_{pq} = 0^\circ, \pm 25^\circ, \pm 50^\circ, \pm 90^\circ, \pm 135^\circ, \pm 155^\circ$ , and  $180^\circ$  where  $+\theta_{pq}$  ( $-\theta_{pq}$ ) corresponds to  $\phi_{pq} = 0^\circ$  ( $\phi_{pq} = 180^\circ$ ). The complete angular ( $\theta_{pq}$  and  $\phi_{pq}$ ) kinematic coverage for " $N \rightarrow \Delta$ " is shown in Fig. 4.1.1(a). The  $W$  and  $Q^2$  ranges covered were also substantial, as displayed in Fig. 4.1.1(b).

The analyzed data were binned in  $\cos \theta_{pq}$  regions from -1 to 1 (in widths of 0.1 to 0.4),  $\phi_{pq}$  regions of  $30^\circ$  or  $60^\circ$  widths,  $W$  regions from 1160 to 1360 MeV (in 40 MeV widths), and  $Q^2$  regions from 0.8 to 1.2  $(\text{GeV}/c)^2$  (in 0.2  $(\text{GeV}/c)^2$  widths). This binning is indicated by the horizontal and vertical lines in Figs. 4.1.1(a) and (b). Data from several different kinematic settings overlapped for most of these regions, with the overlapping data being combined together in the analysis. Tab. 4.1 lists the individual kinematic settings contributing to each  $\cos \theta_{pq}$  region.



(a)  $\theta_{pq}$  and  $\phi_{pq}$  coverage.

(b)  $W$  and  $Q^2$  coverage.

FIGURE 4.1.1. Angular kinematic coverage and  $W$  versus  $Q^2$  coverage for “ $N \rightarrow \Delta$ ”, showing bins in  $\theta_{pq}$ ,  $\phi_{pq}$ ,  $W$ , and  $Q^2$ .

TABLE 4.1. Kinematic settings for each  $\cos \theta_{pq}$  region used in analysis.

$\cos \theta_{pq}$ Region	Kinematic Settings
-1 to -0.9	$\pm 155^\circ, 180^\circ$
-0.9 to -0.7	$\pm 135^\circ, \pm 155^\circ, 180^\circ$
-0.7 to -0.4	$\pm 135^\circ, \pm 155^\circ$
-0.4 to 0	$\pm 90^\circ, \pm 135^\circ$
0 to 0.3	$\pm 50^\circ, \pm 90^\circ$
0.3 to 0.6	$0^\circ, \pm 25^\circ, \pm 50^\circ, \pm 90^\circ$
0.6 to 0.7	$0^\circ, \pm 25^\circ, \pm 50^\circ$
0.7 to 0.8	$0^\circ, \pm 25^\circ, \pm 50^\circ$
0.8 to 0.9	$0^\circ, \pm 25^\circ, \pm 50^\circ$
0.9 to 1	$0^\circ, \pm 25^\circ, 50^\circ$

## 4.2. Particle Detection and Target Coordinates

The standard Hall A physics event analyzer is a FORTRAN-based program called ESPACE (Event Scanning Program for hall A Collaboration Experiments).<sup>1</sup> It was originally developed at Mainz and later improved at the Massachusetts Institute of Technology (MIT). It is capable of reading, decoding, and calibrating raw event data, reconstructing wire chamber tracks, computing spectrometer focal plane coordinates and target quantities, computing basic physics quantities (such as angles, four-vectors, and kinematics) defining conditional tests and making the selection of events based on these cuts, and creating histograms and event-by-event ntuples.

**4.2.1. Scintillator Analysis.** The raw data stream contains information from the Analog to Digital Converter (ADC) and Time to Digital Converter (TDC) for the PMTs at the ends of each scintillator paddle in both spectrometers. A typical signal for each is shown in Fig. 4.2.1. The pulse height of the analog signal is a measure of the amount of energy

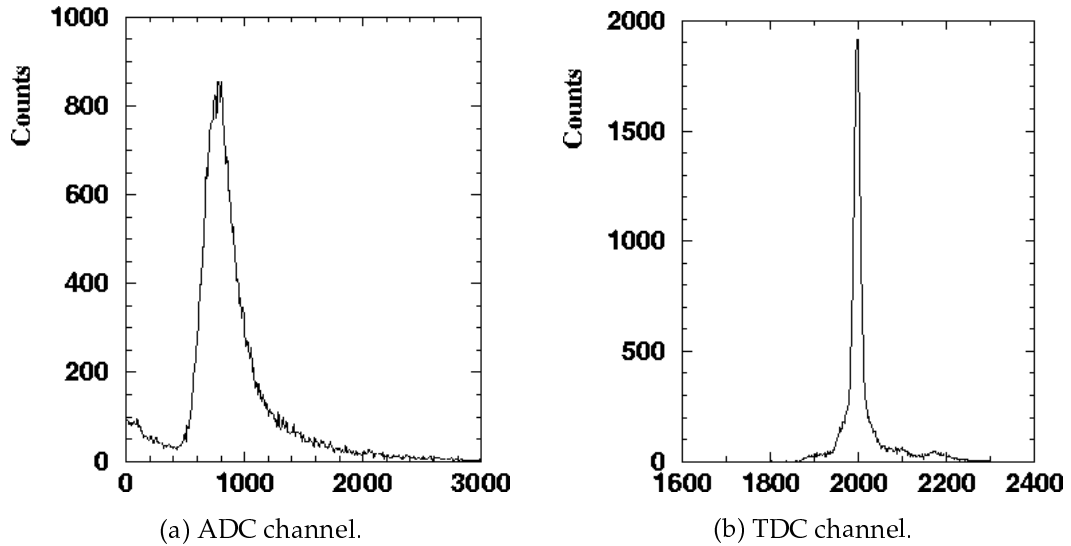


FIGURE 4.2.1. ADC and TDC spectra from one side of a scintillator paddle.

the particle loses while passing through the paddle and recorded by the ADC. A coincidence is required between the two PMTs on each side of the paddle, as well as with

<sup>1</sup>ESPACE is now being replaced by a C++ analyzer.

an additional paddle (located at a similar transverse position) of the second scintillator plane. The timing of the event is defined from the right PMT of the second plane. The trigger is defined using this timing information.

**4.2.2. Vertical Drift Chamber (VDC) Analysis.** Information about the particle trajectory at the focal plane of each spectrometer is determined by raw wire hits and drift times in the VDCs. These trajectories are transported from the focal plane to the target using known optics information about the two spectrometers. The momentum and coordinates of each particle at the target allows for the determination of the kinematics of the corresponding event.

4.2.2.1. *Converting from Drift Time to Drift Distance.* Drift time information is used to determine the perpendicular drift distance for a particular sense wire from the particle track [52]. A typical drift time spectrum is demonstrated in Fig. 4.2.2. The number of

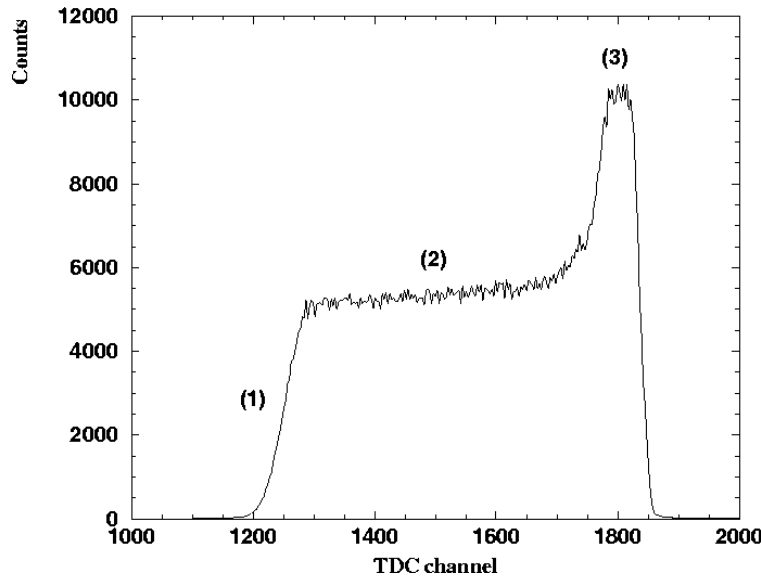


FIGURE 4.2.2. Drift time spectrum.

counts in an interval of the drift time spectrum is given by:

$$\frac{dN}{dt} = \frac{dN}{ds} \frac{ds}{dt}, \quad (4.2.1)$$

where  $s$  is the path length of the drift electron,  $ds/dt$  is the drift velocity – essentially constant except very close to the wire – and  $dN/ds$  is the effective flux through the drift line. The three regions of Fig. 4.2.2 arise due to geometric effects and correspond to the



tracks in Fig. 4.2.3. In the region closest to the cathode plane (1), the probability  $dN/ds$

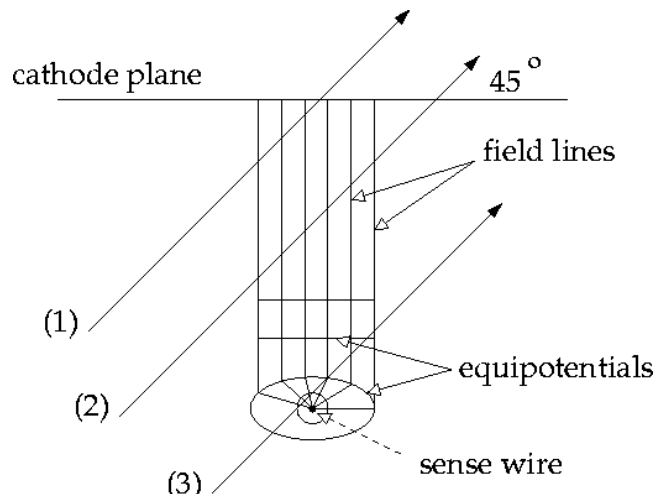


FIGURE 4.2.3. Drift cell in a VDC plane showing three tracks corresponding to three different TDC signals.

that a particle will cause the wire to fire decreases because the corresponding volume of the cell the particle travels through decreases. The plateau (2) is a region of uniform field because both  $ds/dt$  and  $dN/ds$  remain constant. The peak region (3) is the result of a combination of both a dramatic increase of  $ds/dt$  due to the avalanche effect discussed in Section 3.4.1.2 and the shape of  $dN/ds$  which goes through a peak in the quasi-radial field region next to the sense wire.

The optimal VDC track crosses five drift cells at  $45^\circ$  as exhibited in Fig. 4.2.4, making a cluster.<sup>2</sup> The shortest drift time for each cell the track passes through is determined by the arrival of the earliest electron, thus defining the *geodetic*.<sup>3</sup> The relative time  $t_0$  is calculated as such:

$$t_0 = |t_1 - t_2| - |t_4 - t_5|, \quad (4.2.2)$$

where  $t_{i=1-5}$  are the drift times of the five fired wires. A track is chosen from the cluster with the lowest  $t_0$ . The distance corresponding to the geodetic for this track is calculated for each wire using knowledge of the drift velocity. The corrected perpendicular distance is then extracted. A linear fit of these five distances is performed to get the position of the *cross-over point*, the intersection point of the track with the wire plane.

<sup>2</sup>A cluster is defined as a set of several adjacent wires firing with the possible exception of one wire.

<sup>3</sup>The geodetic is the electron path corresponding to that shortest drift time.

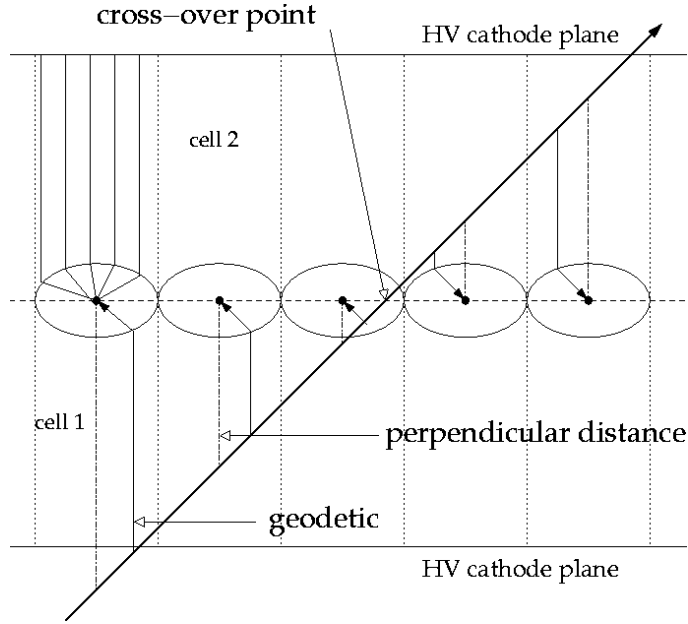


FIGURE 4.2.4. Typical VDC track crossing five drift cells in a VDC plane.

4.2.2.2. *Determination of Focal Plane Coordinates.* The position of the cross-over point is defined for each of the four VDC planes:  $u_1, u_2, v_1$ , and  $v_2$  (as shown in Fig. 4.2.5). From the four cross-over points, a particle trajectory is determined. Because of the relatively large distance between the two chambers, global angles for the two wire chambers,  $\eta_1$  and  $\eta_2$ , can be calculated:

$$\tan \eta_1 = \frac{u_2 - u_1}{d_1}, \quad (4.2.3)$$

$$\tan \eta_2 = \frac{v_2 - v_1}{d_1}, \quad (4.2.4)$$

where  $d_1 = 0.335$  m is the distance between the two  $uv$  planes. The VDC coordinate system is defined with respect to the  $u_1$  plane where  $u$  and  $v$  are defined as:

$$u = u_1, \quad (4.2.5)$$

$$v = v_1 - d_2 \tan \eta_2, \quad (4.2.6)$$

$d_2 = 0.115$  m is the distance between the  $u$  and  $v$  planes in both chambers, and  $v$  is the projected  $v_1$  position on the  $u_1$  plane.

Before they can be transported back to the target, these VDC track coordinates must be expressed in the focal plane coordinate system. First, they must be rotated to the

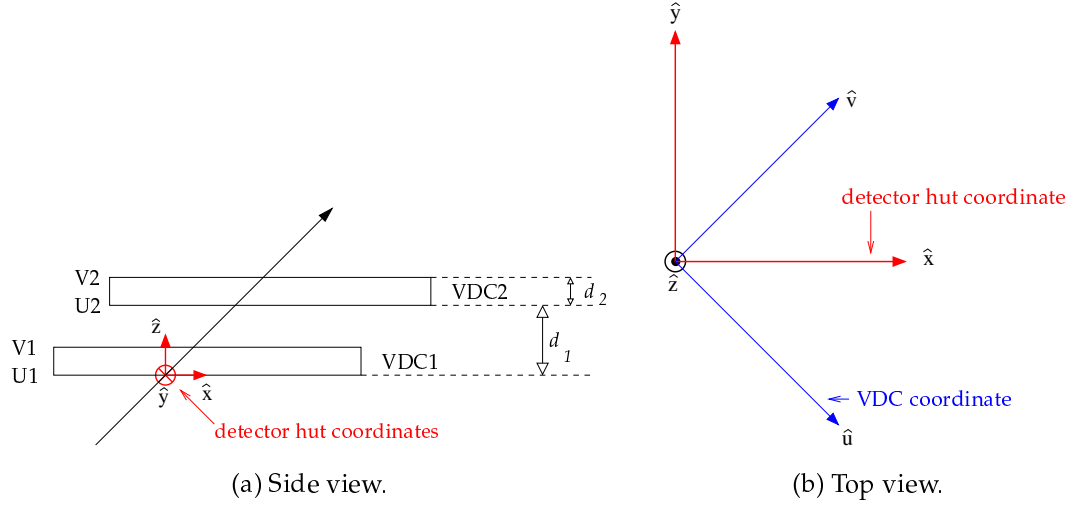


FIGURE 4.2.5. Side and top views of the VDC ( $uv$ ) and detector hut ( $xyz$ ) coordinate systems.

coordinate system of the detector hut by a  $45^\circ$  rotation about the  $z$ -axis, again referencing Fig. 4.2.5. The transformation from the VDC to the detector hut is then given by:

$$x_{det} = \frac{1}{\sqrt{2}}(u + v), \quad (4.2.7)$$

$$y_{det} = \frac{1}{\sqrt{2}}(-u + v), \quad (4.2.8)$$

$$\tan \theta_{det} = \frac{1}{\sqrt{2}}(\tan \eta_1 + \tan \eta_2), \quad (4.2.9)$$

$$\tan \phi_{det} = \frac{1}{\sqrt{2}}(-\tan \eta_1 + \tan \eta_2), \quad (4.2.10)$$

The transformation from the detector system to the spectrometer transport system is obtained by a clockwise rotation by the dipole bending angle of  $\rho_o = 45.1^\circ$  around the  $y$ -axis given by:

$$x_{trans} = x_{det} \cos \rho_o (1 + \theta_{trans} \tan \rho_o), \quad (4.2.11)$$

$$y_{trans} = y_{det} + \sin \rho_o \phi_{trans} x_{det}, \quad (4.2.12)$$

$$\theta_{trans} = \frac{\theta_{det} + \tan \rho_o}{1 - \theta_{det} \tan \rho_o}, \quad (4.2.13)$$

$$\phi_{trans} = \frac{\phi_{det}}{\cos \rho_o - \theta_{det} \sin \rho_o}. \quad (4.2.14)$$

Fig. 4.2.6 exhibits the resulting transport coordinates at the VDC.

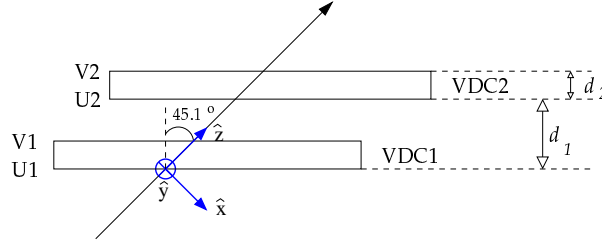


FIGURE 4.2.6. Transport coordinate system at the VDC (side view).

4.2.2.3. *Determination of Target Coordinates.* The transport coordinate system at the target is shown in Fig. 4.2.7.  $\hat{z}$  lies along the spectrometer axis,  $\hat{x}$  points vertically downward,  $\hat{y} = \hat{z} \times \hat{x}$ ,  $x_{tg}$  and  $y_{tg}$  are the vertical and horizontal positions, respectively,  $\phi_{tg}$  is the horizontal geometric angle,  $\theta_{tg}$  is the vertical geometric angle, and  $\delta$  is the relative deviation from the central momentum  $p_o$ , defined as:

$$p = p_o (1 + \delta). \quad (4.2.15)$$

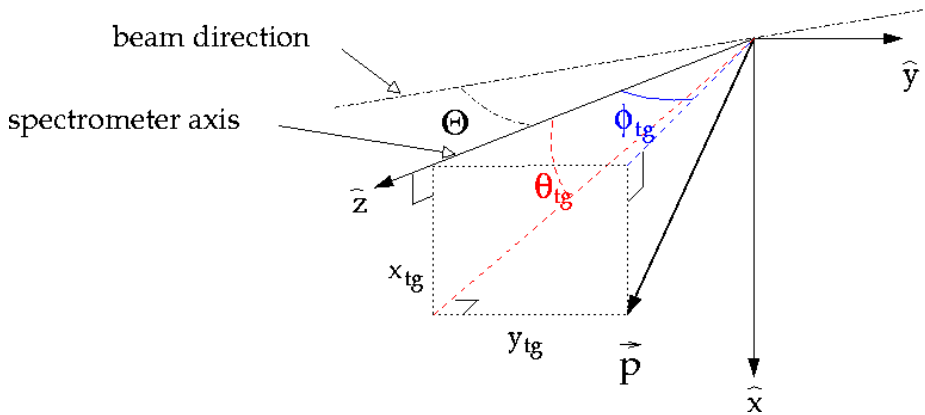


FIGURE 4.2.7. Transport coordinate system at the target.

The optics tensor of the spectrometer is now well understood. It was determined using  $(e, e')$  scattering from a thin  $^{12}\text{C}$  target and a 49 hole sieve slit positioned before the entrance to  $Q_1$ . It relates the focal plane coordinate vector  $(x_{fpp}, y_{fpp}, \theta_{fpp}, \phi_{fpp})$  to the target coordinate vector  $(y_{tg}, \theta_{tg}, \phi_{tg}, \delta)$ . The position of  $x_{tg}$  is obtained using information from

a beam position monitor located on the beam-line close to the target. The coordinates for  $\theta_{tg}$  and  $\delta$  are then corrected for the displacement in  $x_{tg}$ .

Because of various misalignments-alignments of the VDCs, the focal plane coordinate system does not necessarily coincide with the transport coordinate system. Offsets,  $Y_{000}$ ,  $T_{000}$ , and  $P_{000}$  are therefore calculated during the optimization of the optics tensor. Details on the optimization procedure for this tensor can be found in Ref. [59] and Appendix C. The transformation from the transport coordinate system to the focal plane coordinate system is made as such:

$$x_{fpp} = x_{trans}, \quad (4.2.16)$$

$$y_{fpp} = y_{trans} - Y_{000}, \quad (4.2.17)$$

$$\theta_{fpp} = \frac{\theta_{det} + T_{000}}{1 - \theta_{det} T_{000}}, \quad (4.2.18)$$

$$\phi_{fpp} = \frac{\phi_{det} - P_{000}}{\cos(\arctan T_{000}) - \theta_{det} \sin(\arctan T_{000})}. \quad (4.2.19)$$

Using a first order approximation, target quantities are related to focal plane quantities by the following matrix:

$$\begin{bmatrix} \delta \\ \theta \\ y \\ \phi \end{bmatrix}_{tg} = \begin{bmatrix} \langle \delta | x \rangle & \langle \delta | \theta \rangle & 0 & 0 \\ \langle \theta | x \rangle & \langle \theta | \theta \rangle & 0 & 0 \\ 0 & 0 & \langle y | y \rangle & \langle y | \phi \rangle \\ 0 & 0 & \langle \phi | y \rangle & \langle \phi | \phi \rangle \end{bmatrix} \begin{bmatrix} x \\ \theta \\ y \\ \phi \end{bmatrix}_{fpp}. \quad (4.2.20)$$

Null matrix elements are a result of the mid-plane symmetry of the spectrometer. A set of tensors,  $Y_{jkl}$ ,  $T_{jkl}$ ,  $P_{jkl}$ , and  $D_{jkl}$ , connects the focal plane coordinates to those of the target as follows:

$$y_{tg} = \sum Y_{jkl} \theta_{fpp}^j y_{fpp}^k \phi_{fpp}^l, \quad (4.2.21)$$

$$\theta_{tg} = \sum T_{jkl} \theta_{fpp}^j y_{fpp}^k \phi_{fpp}^l, \quad (4.2.22)$$

$$\phi_{tg} = \sum P_{jkl} \theta_{fpp}^j y_{fpp}^k \phi_{fpp}^l, \quad (4.2.23)$$

$$\delta = \sum D_{jkl} \theta_{fpp}^j y_{fpp}^k \phi_{fpp}^l, \quad (4.2.24)$$

where each tensor element is a polynomial in  $x_{fpp}$ :

$$Y_{jkl} = \sum_{i=1}^m y_{ijkl} x_{fpp}^i, \quad (4.2.25)$$

$$T_{jkl} = \sum_{i=1}^m t_{ijkl} x_{fpp}^i, \quad (4.2.26)$$

$$P_{jkl} = \sum_{i=1}^m p_{ijkl} x_{fpp}^i, \quad (4.2.27)$$

$$D_{jkl} = \sum_{i=1}^m d_{ijkl} x_{fpp}^i. \quad (4.2.28)$$

These tensor elements are obtained using a  $\chi^2$  minimization procedure. A sample of the resulting target coordinate distributions, reconstructed from the focal plane coordinates and the tensor elements defined in Eqns. (4.2.25)-(4.2.28), are shown in Fig. 4.2.8.

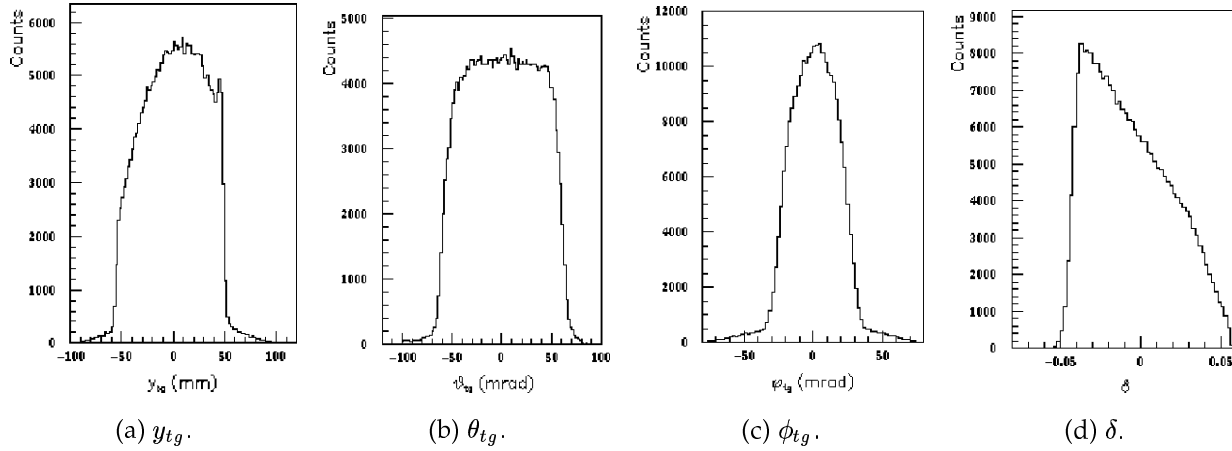


FIGURE 4.2.8. Distributions of the proton target coordinates for  $\theta_{pq} = 0^\circ$ .

### 4.3. Particle Identification (PID)

Recall that in the  $p(\vec{e}, e'\vec{p})\pi^\circ$  reaction of interest, the scattered electron is detected in the HRSe in coincidence with a proton in the HRSh. The  $\pi^\circ$ , however, remains undetected. To ensure the correct reaction is being studied, it is necessary to verify the presence of the  $\pi^\circ$ .

**4.3.1. Missing Energy and Missing Momentum.** Because the  $\pi^\circ$  is undetected, the mass missing ( $m_{miss}$ ) from the final state of the reaction should equal the mass of the

pion,  $m_\pi = 135$  MeV, where

$$m_{miss}^2 = E_{miss}^2 - p_{miss}^2, \quad (4.3.1)$$

where  $E_{miss}$  is the missing energy, and  $p_{miss}$  is the missing momentum. Information from both the electron and proton are used to reconstruct the  $E_{miss}$  and  $p_{miss}$ . A typical  $E_{miss}$  versus  $p_{miss}$  spectrum is shown in Fig. 4.3.1. Events along the diagonal represent the

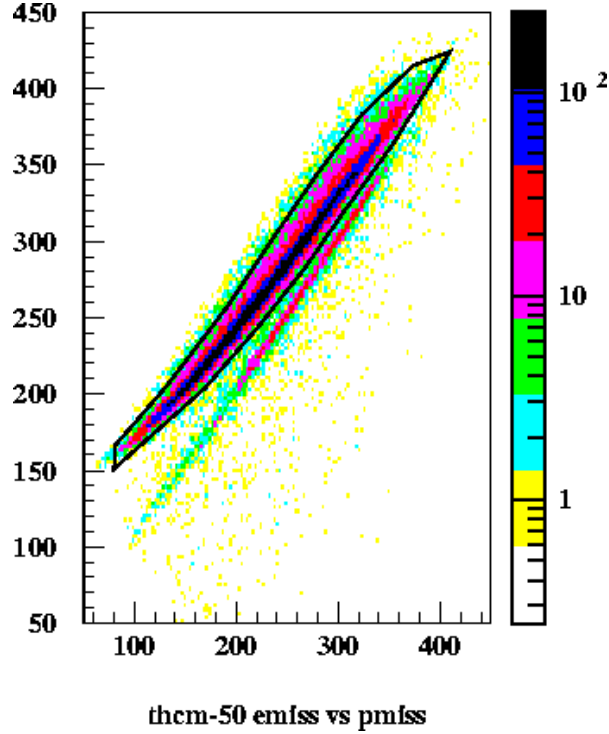


FIGURE 4.3.1.  $E_{miss}$  versus  $p_{miss}$  spectra for  $\theta_{pq} = -50^\circ$ .

presence of a photon ( $m_{miss} = 0$ ) in the final state –  $p(e, e'p)\gamma$  – originating by radiation from the scattered or incident electron after elastic scattering. The events not along this diagonal correspond to the  $\pi^0$ . A cut is placed around the  $\pi^0$  events, as demonstrated in Fig. 4.3.1. The remaining events are discarded.

**4.3.2. Velocity and Deposited Energy.** It is possible for positively charged particles aside from the desired proton (such as the  $\pi^+$  from  $\Delta(1232) \rightarrow n + \pi^+$  decay) to be detected in the HRSh. Protons and pions recoiling from the target at the same detected momentum have different velocities, with pions traveling faster, and thus also depositing different amounts of energy in the scintillators (yielding different ADC signal strengths).

In a plot of velocity versus energy deposited, the proton and  $\pi^+$  signal should be easily distinguishable. Fig. 4.3.2 shows a typical spectrum of  $\beta$  (where  $\beta = v/c$ , calculated from time of flight information), versus ADC spectrum (with ADC signal being proportional to the deposited energy). A cut is placed around the proton peak and the remainder of

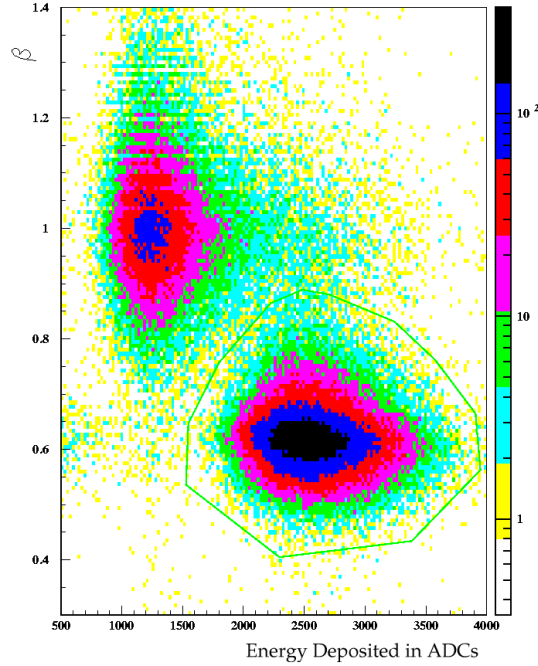


FIGURE 4.3.2. Sample  $\beta$  versus energy deposited in the ADC spectrum for  $\theta_{pq} = -155^\circ$ .

the data thrown away. One may notice that the pions seem to have a velocity greater than  $c$ . This is because  $\beta$  has been calculated from the observed momentum under the assumption that the particle has the mass of a proton, and thus “optimized” for proton detection. Details of this optimization procedure can be found in Appendix C.

**4.3.3. Target Reconstruction.** Once it has been determined that the proper reaction has been identified, it must then be ensured that the detected particles originated from a common coincidence reaction site at the target. This is done through examination of plots of the corrected coincidence time<sup>4</sup>,  $t_{cor}$ , and the position of the reaction vertex along the

<sup>4</sup>The coincidence time is corrected for differences in path length between the detected electron and proton.



direction of the beam at the target,  $react_z$ . These are shown in Figs. 4.3.3(a) and (b). Cuts are then made to ensure the detected proton and electron originated inside the target, and were detected with a short coincidence timing window.

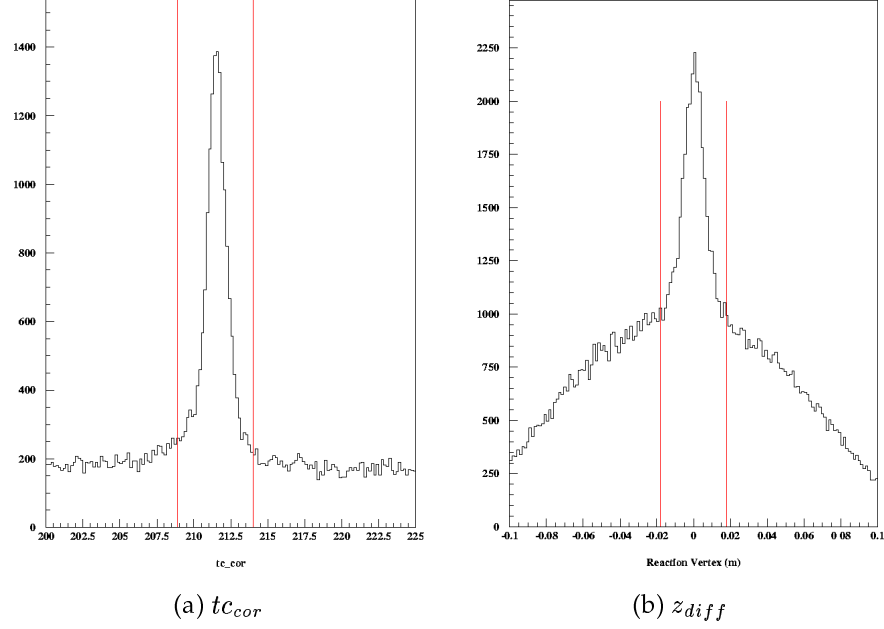


FIGURE 4.3.3. Sample plots of target reconstruction variables for  $\theta_{pq} = -135^\circ$ .

**4.3.4. Effects of Different PID Cuts.** Two typical  $m_{miss}$  spectra are shown in Fig. 4.3.4. The different curves correspond to (1) no cuts added to the data, and then with cuts defined from the various plots as just described in the three above sections: (2)  $tc_{cor}$  and  $react_z$ , (3)  $\beta$  versus deposited energy, and (3)  $E_{miss}$  versus  $p_{miss}$ . From these spectra it is obvious that the above defined PID cuts are sufficient for determining clear identification of the  $p(\vec{e}, e' \vec{p})\pi^0$  reaction.

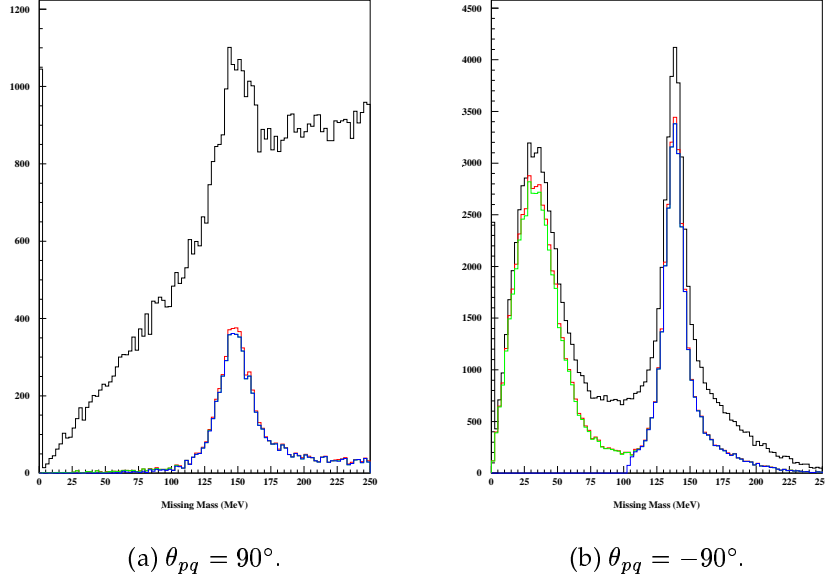


FIGURE 4.3.4. Missing mass spectrum for  $\theta_{pq} = 90^\circ$  and  $-90^\circ$  showing results of cuts on  $tc_{cor}$  versus  $react_z$ ,  $\beta$  versus energy deposited, and  $E_{miss}$  versus  $p_{miss}$ .

#### 4.4. Extraction of Focal Plane Polarizations

Once the reaction has been identified, the polarization components of the recoil proton at the focal plane can be extracted. First, the scattering angles of the proton as it traverses the carbon analyzer must be determined. This is accomplished by analysis of the information recorded from the four FPP straw chambers: identifying the wires in the FPP straw chambers that fired, calculating electron drift distances, and reconstructing the proton tracks in the front and rear chambers. These calculations are all performed within ESPACE. Detailed steps of the reconstruction of these scattering angles can be found in Refs. [56, 60], and are over-viewed in the following subsections.

**4.4.1. Demultiplexing.** As discussed in Section 3.5, the charged proton passes through straws in the FPP straw chambers, ionizing Ar gas atoms and leaving a track of electrons. These electrons drift towards the anode wire at a constant velocity, ionizing more Ar as they approach the wire, causing an avalanche of electrons. Signals from the wires are multiplexed into groups of eight by assigning a different pulse width to each straw within

the group. For analysis, the TDC signals must then be demultiplexed. The leading and trailing edges of the signal are fed into ESPACE which then calculates the time difference between them, thereby identifying the straw number that fired. ESPACE also determines the difference between the trigger signal and the leading edge, giving the drift time. An offset must be applied to the drift time to correct for various electronics delays.

**4.4.2. Drift Distance.** Once the drift time has been determined, it must be converted into drift distance. The drift distance,  $d$ , is proportional to the drift time,  $t$ , except in the region close to the anode wire. The longest drift time corresponds to the outer radius of the straw,  $r = 0.522$  cm. As the electron approaches the anode, the drift velocity increases. In this region,  $d$  is obtained from a fifth-order polynomial in  $t$ :

$$d = \sum_{n=0}^5 T(j, n)t^n, \quad (4.4.1)$$

where the coefficients  $T(j, n)$  are obtained by a fit to the integrated drift time spectra in a plane  $j$ . These coefficients are stored in a data file, which is read in by ESPACE.

**4.4.3. Track Reconstruction.** After information on the straw number and drift distance have been obtained, the proton tracks through the straw chambers can be determined. The front and rear straw chambers are analyzed separately, giving independent front (incident) and rear (scattered) tracks. In each set of chambers the  $u$  and  $v$  planes are also analyzed individually.

First, hit clusters in the  $u$  planes of each straw chamber are identified. Cluster determination is made as follows, where a cluster is defined as having at most only one hit per plane. Fig. 4.4.1 will help clarify the discussion. The three layers represent three  $u$  planes

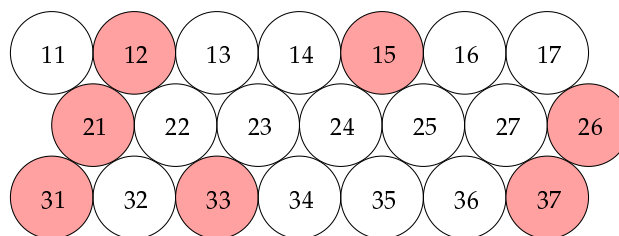


FIGURE 4.4.1. Illustration of the determination of a cluster in an FPP chamber.

in one straw chamber. The circles are cross sections of the straws and the colored straws are those that have fired. The analysis code begins by looking at  $u$ -plane 1 of the first front

straw chamber, detecting a hit in straw 12. It then looks at the straws in plane 2 adjacent to straw 12, where a hit is identified in straw 21. Straws 12 and 21 begin to form a cluster. Straws adjacent to straws 21 and 22 in plane 3 are then scanned. Hits are found in straws 31 and 33, both forming clusters with straw 12 (even though straw 22 has not fired): (12, 21, 31) and (12, 33). The code then moves back to the first plane to look for a second hit, finding that straw 15 has fired. The same procedure is followed, looking for hits in straws 24, 25, 34, 35, and 36. Since none of these straws fires, straw 15 makes a cluster of its own: (15).

After a scan of  $u$ -plane 1 is completed, the analysis code progresses to  $u$ -plane 2. Since straw 21 is already included in a cluster, it is ignored. A hit is discovered in straw 26, which forms a cluster with straw 37: (26, 37).  $u$ -plane 3 is then scanned but no hits not already included in a cluster are found. The procedure is therefore complete for this straw chamber with four identified clusters: (12, 21, 31), (12, 33), (15), and (26, 37).

The same procedure is applied to the  $u$ -planes of the second front straw chamber and the  $v$ -planes of both front straw chambers. All possible combinations of pairs of clusters in both front chambers are considered and several tracks reconstructed for each combination. These tracks pass left or right of the sense wire of every fired straw, at a distance given by the drift distance, as illustrated in Fig. 4.4.2. Straight lines are fit and a  $\chi^2$  for

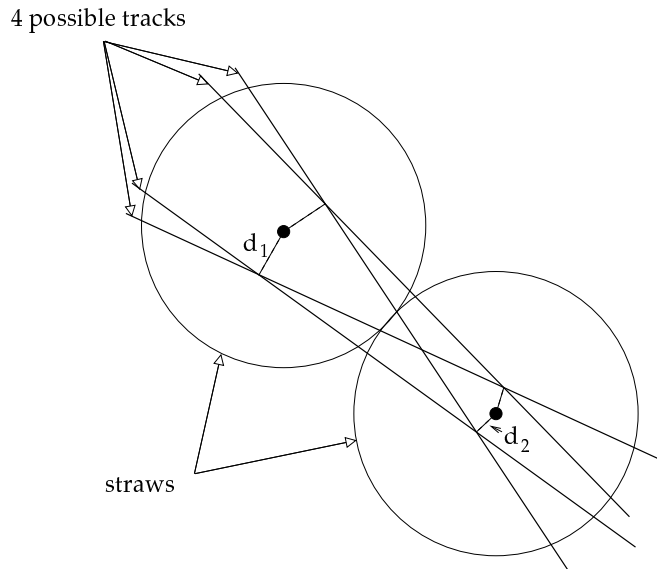


FIGURE 4.4.2. Possible FPP tracks for two straws with drift distances  $d_1$  and  $d_2$ .

each trajectory calculated. Because it is easier for a cluster with very few hits to give good  $\chi^2$ , a weight corresponding to the number of hits for the track is given to the  $\chi^2$  value. The track with the lowest  $\chi^2$  is then chosen to be the *good* track.

**4.4.4. Scattering Angle Calculation.** The Cartesian coordinates and angles for an incident track,  $\vec{I}$  are shown in Fig. 4.4.3, where  $\hat{z}$  is along the spectrometer axis at the focal plane,  $\hat{x}$  is downward perpendicular to  $\hat{z}$  in the vertical plane,  $\hat{y} = \hat{z} \times \hat{x}$ ,  $\theta_i$  is the angle between the  $z$ -axis and the projection of the track on the  $xz$ -plane,  $\phi_i$  is the angle between the  $z$ -axis and the projection of the track on the  $yz$ -plane, and  $\psi_i$  is the angle between the track and its projection on the  $yz$ -plane. The relationship between the angles can be written as:

$$\tan \psi_i = \tan \theta_i \cos \phi_i. \quad (4.4.2)$$

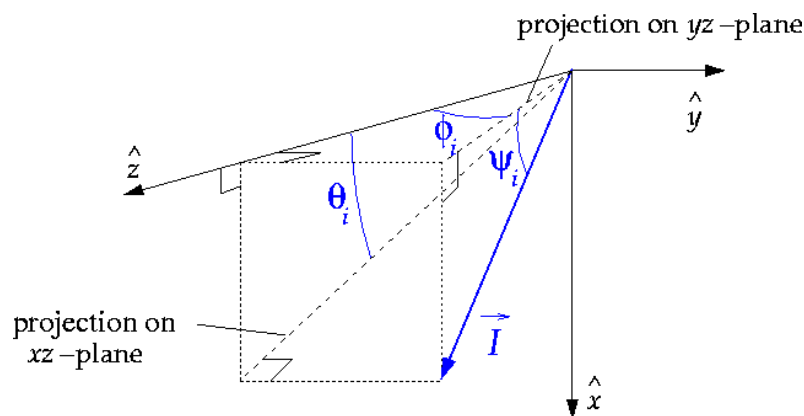


FIGURE 4.4.3. Cartesian angles for FPP tracks.

The polar and azimuthal scattering angles are determined by rotating the coordinate system event by event so that the  $z$ -axis lies along the direction of the momentum of the incident track for that event. The scattered track can also be expressed in this new coordinate system. First, the  $yz$ -plane must be rotated about the  $x$ -axis by an angle  $\phi_i$ . Then a rotation of the coordinate system by an angle  $\psi_i$  is made. The new  $z'$ -axis lies along the incident track  $\vec{I}$ . This projection is given by:

$$\begin{bmatrix} I'_x \\ I'_y \\ I'_z \end{bmatrix} = \begin{bmatrix} 0 \\ 0 \\ 1 \end{bmatrix} = \begin{bmatrix} \cos \psi_i & 0 & -\sin \psi_i \\ 0 & 1 & 0 \\ \sin \psi_i & 0 & \cos \psi_i \end{bmatrix}_1 \begin{bmatrix} 1 & 0 & 0 \\ 0 & \cos \phi_i & -\sin \phi_i \\ 0 & \sin \phi_i & \cos \phi_i \end{bmatrix}_2 \begin{bmatrix} I_x \\ I_y \\ I_z \end{bmatrix} \quad (4.4.3)$$

where matrix 1 (2) corresponds to first (second) rotation. The new projection of the scattered track  $\vec{F}$  is written similarly:

$$\begin{bmatrix} F'_x \\ F'_y \\ F'_z \end{bmatrix} = \begin{bmatrix} \cos \psi_i & 0 & -\sin \psi_i \\ 0 & 1 & 0 \\ \sin \psi_i & 0 & \cos \psi_i \end{bmatrix} \begin{bmatrix} 1 & 0 & 0 \\ 0 & \cos \phi_i & -\sin \phi_i \\ 0 & \sin \phi_i & \cos \phi_i \end{bmatrix} \begin{bmatrix} F_x \\ F_y \\ F_z \end{bmatrix}. \quad (4.4.4)$$

The polar,  $\theta_{fpp}$ , and azimuthal,  $\phi_{fpp}$ , scattering angles can now be defined as the spherical angles of the scattered track in this new coordinate system, as shown in Fig. 4.4.4, where  $\vec{F}_o$  is the projection of  $\vec{F}$  on the  $x'y'$ -plane,

$$F_o^2 = F_x'^2 + F_y'^2, \quad (4.4.5)$$

$$\theta_{fpp} = \tan^{-1} \left( \frac{F_o}{F'_z} \right), \quad (4.4.6)$$

$$\phi_{fpp} = \tan^{-1} \left( \frac{F'_x}{F'_y} \right). \quad (4.4.7)$$

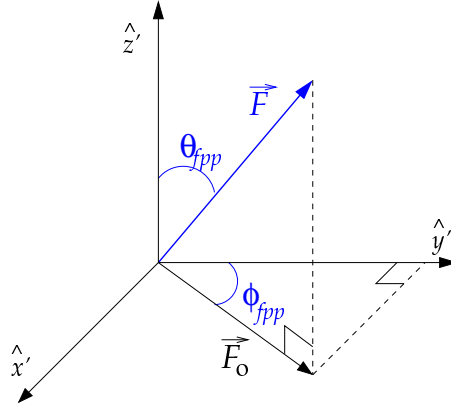
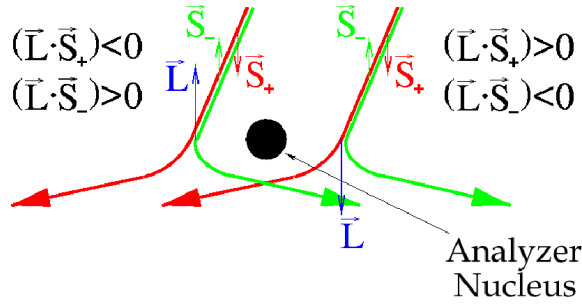


FIGURE 4.4.4. Spherical angles of the scattered proton in the FPP.

**4.4.5. Focal Plane Polarizations.** Proton polarization observables at the focal plane are determined by measuring the angular distribution of events that scatter, via the strong interaction, with the nucleus of an atom in the carbon analyzer. The strong interaction is sensitive to the direction of the spin of the incident proton through a spin-orbit coupling. Fig. 4.4.5 illustrates this principle, where vertically polarized protons interact with analyzer nuclei and scatter with left-right asymmetry. The sign of the force between the incident proton and the analyzer nucleus is determined by the sign of the scalar product



If more  $S_+$  than  $S_-$  ( $+P_x^{fpp}$ ), then more events left than right.

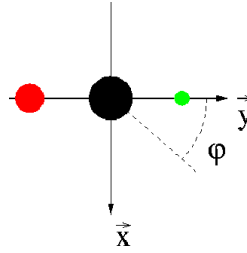


FIGURE 4.4.5. Principle of polarimetry: the strong interaction between the proton and carbon analyzer nucleus depends on the proton spin.

$\vec{L} \cdot \vec{S}$ , where  $\vec{L}$  is the orbital angular momentum of the proton with respect to the analyzer nucleus and  $\vec{S}$  is the proton's spin. As shown in Fig. 4.4.5, all spin up particles are scattered to the left while spin down particles are scattered to the right. If more spin up particles than spin down are incident on the analyzer nuclei, an asymmetry in the scattering angle will be observed. A left-right asymmetry corresponds to a vertical polarization component,  $P_x^{fpp}$ , while an up-down asymmetry corresponds to a horizontal polarization component,  $P_y^{fpp}$ .

The angular distribution for a large sample of incident protons with two polarization components can be represented by a smooth sinusoidal curve:

$$L(\theta_{fpp}, \phi_{fpp}) = \frac{1}{2\pi} [1 + A_c(\theta_{fpp}, T_p) (P_y^{fpp} \sin \phi_{fpp} - P_x^{fpp} \cos \phi_{fpp})], \quad (4.4.8)$$

where  $A_c(\theta_{fpp}, T_p)$  is the analyzing power of the  $A(p, N)X$  reaction dependant upon the polar scattering angle and kinetic energy of the proton,  $T_p$ . The analyzing power represents the strength of the spin-orbit coupling of the nuclear scattering and therefore the sensitivity of the reaction to the polarization of the incident particle.

4.4.5.1. *Analyzing Power.* Because of the limited range of energies accepted by the HRSh, one can assume that at a given  $\theta_{fpp}$ ,  $A_c$  is constant over that energy range and therefore independent of  $T_p$ .

A parameterization of the analyzing power for a large solid angle polarimeter was first outlined by Ransom *et al.* [61] in 1982. It was expanded in 1985 by McNaughton *et al.* [62] for inclusive  $p^{12}\text{C}$  scattering experiments performed at Los Alamos (LAMPF). This parameterization is divided into *low* ( $T_p \leq 450 \text{ MeV}/c$ ) and *high* ( $T_p > 450 \text{ MeV}/c$ ) energy regions, where  $T_p$  is the average proton energy at the center of the carbon analyzer. The fitting functions used for the two energy regions are given by:

$$A_c^{low} = \frac{j r}{1 + k r^2 + l r^4}, \quad (4.4.9)$$

$$A_c^{high} = \frac{j r}{1 + k r^2 + l r^4} + m \cdot p \sin(5\theta_{fpp}), \quad (4.4.10)$$

where  $r = p \sin \theta_{fpp}$ , and  $p$  is the proton momentum at the center of the carbon in units of  $\text{GeV}/c$ . The parameters  $j, k, l$ , and  $m$  are determined by an energy-dependent polynomial fit. For the low energy fit:

$$j = \sum_{n=0}^4 j_n p'^n, \quad (4.4.11)$$

$$k = \sum_{n=0}^4 k_n p'^n, \quad (4.4.12)$$

$$l = \sum_{n=0}^4 l_n p'^n, \quad (4.4.13)$$

where  $p' = p - 0.7 \text{ GeV}/c$ ; for the high energy fit:

$$j = \sum_{n=0}^3 j_n p'^n, \quad (4.4.14)$$

$$k = \sum_{n=0}^3 k_n p'^n, \quad (4.4.15)$$

$$l = \sum_{n=0}^3 l_n p'^n, \quad (4.4.16)$$

$$m = \sum_{n=0}^3 m_n p'^n, \quad (4.4.17)$$

where  $p' = p - 1.2 \text{ GeV}/c$ .



This same parameterization was used to fit elastic  $p(\vec{e}, e'\vec{p})$  data from Hall A detected with the FPP covering the entire range of proton momenta measured during “ $N \rightarrow \Delta$ ”. The procedure followed for this calibration can be found in Ref. [63]. Most of this data was taken during experiments prior to “ $N \rightarrow \Delta$ ”, with a few other points measured during “ $N \rightarrow \Delta$ ”, to fill in gaps of the “ $N \rightarrow \Delta$ ” kinematics. The coefficients determined by the Hall A elastic data are listed in Tab. 4.2, as well as the McNaughton coefficients. Fig. 4.4.6 is a plot of  $A_c$  versus  $\theta_{fpp}$  for four different proton momenta comparing the McNaughton and Hall A fits to the  $A_c$  values for the measured elastic data. The Hall A fit is used in the remainder of this analysis.

TABLE 4.2. Coefficients of the McNaughton and Hall A analyzing power parameterizations.

	Hall A (low)	McNaughton (low)	Hall A (high)	McNaughton (high)
$j_0$	4.576	5.3346	0.974	1.6575
$j_1$	-0.78	-5.5361	-2.298	1.3855
$j_2$	14.6	2.8353	43.21	9.7700
$j_3$	98.7	61.915	19.44	-149.27
$j_4$	-532	-145.54		
$k_0$	-11.9	-12.774	-26.49	-16.346
$k_1$	-131.7	-68.339	-30.29	152.53
$k_2$	1682	1333.5	1048.7	139.16
$k_3$	-5574	-3713.5	2826	-3231.1
$k_4$	6946	3738.3		
$l_0$	673	1095.3	750	1052.2
$l_1$	1866	949.50	-833	-3210.8
$l_2$	7290	-28012.0	-861	-2293.3
$l_3$	-38800	96833.0	7205	60327.0
$l_4$	-55800	-118830.0		
$m_0$			0.1402	0.13887
$m_1$			0.0414	-0.19266
$m_2$			-0.6052	-0.45643
$m_3$			0.42	8.1528
$p'$ (GeV/c)	$p$ -0.686	$p$ -0.7	$p$ -1.2831	$p$ -1.2

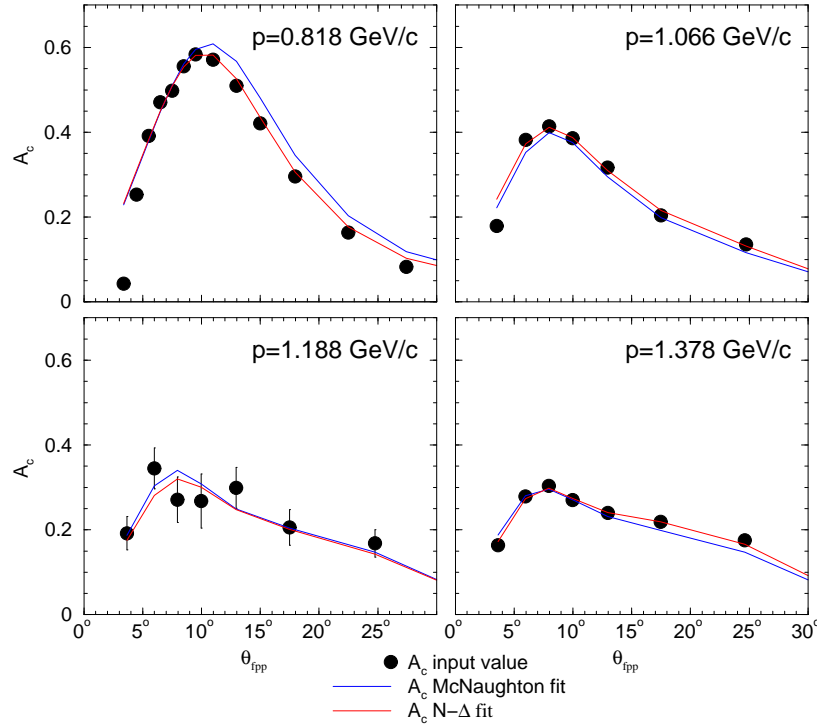


FIGURE 4.4.6. Analyzing power versus  $\theta_{fpp}$  comparing the McNaughton and “ $N \rightarrow \Delta$ ” parameterization fits.

4.4.5.2. *The Cone Test.* The rear straw chambers are of limited size, allowing for the introduction of non-physical asymmetries near the edges of the chambers. A *cone test* is applied to limit these effects. The requirement is made that a cone of angle  $\theta_{fpp}$  about the incoming track is fully within the acceptance of the rear chambers. Fig. 4.4.7 illustrates this point, where the cone for track 2 is entirely within the rear chamber acceptance while the cone for track 1 is not. Track 1 would therefore be rejected.

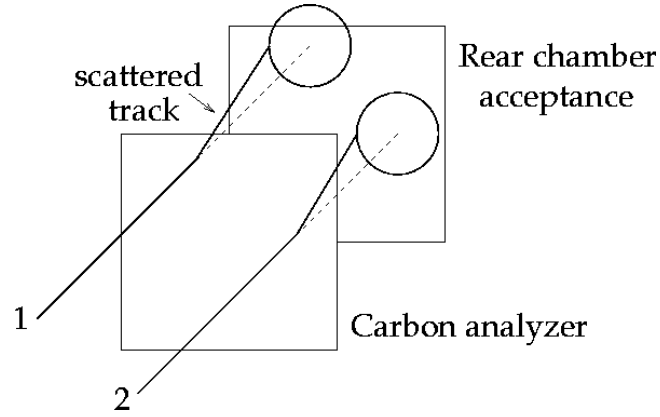


FIGURE 4.4.7. FPP cone test to determine if a cone of angle  $\theta_{fpp}$  about the particle track is entirely within the rear chamber acceptance.

4.4.5.3. *Coulomb Scattering.* Coulomb scattering involves no spin-orbit coupling and therefore has no analyzing power. This scattering is dominant at small angles ( $\theta_{fpp} < 5^\circ$ ), corresponding to the peak shown in Fig. 4.4.8. This region is therefore cut out of the data analysis.

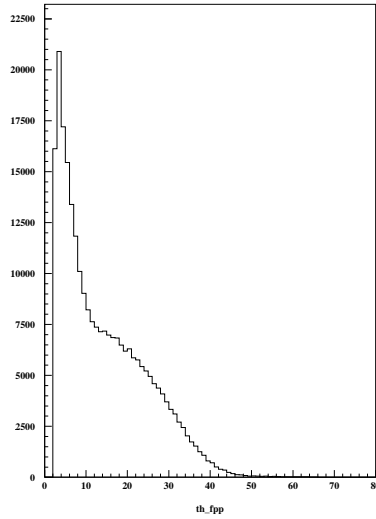


FIGURE 4.4.8. Distribution of  $\theta_{fpp}$  at  $\theta_{pq} = 25^\circ$ .

4.4.5.4. *Event Reconstruction.* Due to multiple scattering and the smearing of the particle trajectories, some scattering events reconstruct as having originated outside of the carbon analyzer. By looking at the position along the beam of the reconstructed secondary scattering vertex,  $z_{close}$ , it is possible to see these effects, as in Fig. 4.4.9. Cuts are made on

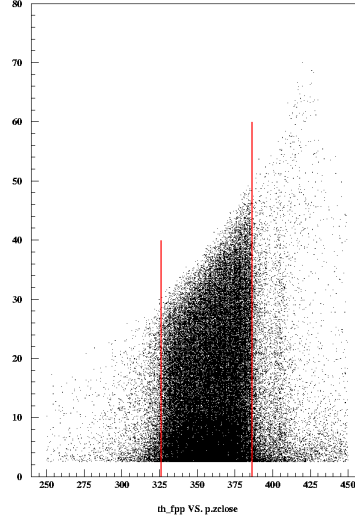


FIGURE 4.4.9. Secondary scattering vertex versus polar scattering angle for  $\theta_{pq} = -25^\circ$ .

the edges of the carbon analyzer to ensure the scattering occurred inside this region. Five different carbon thicknesses, therefore five different cuts on  $z_{close}$ , were implemented for the “ $N \rightarrow \Delta$ ” experiment, in order to keep the Coulomb scattering cone below  $5^\circ$ . The analyzer thicknesses are listed in Tab. 4.3.

TABLE 4.3. Different  $^{12}\text{C}$  thicknesses in the FPP for “ $N \rightarrow \Delta$ ”.

$\theta_{pq}$	$^{12}\text{C}$ Thickness (cm)
$0^\circ, \pm 25^\circ$	49.5
$\pm 50^\circ$	34.3
$\pm 90^\circ$	22.9
$\pm 135^\circ, \pm 155^\circ$	11.4
$180^\circ$	7.6

#### 4.5. Extraction of Target Polarization Observables

Polarization observables at the focal plane are related to those at the target by the following relationship:

$$F = S \cdot T, \quad (4.5.1)$$

where  $\vec{F} = (F_x, F_y, F_z)$  represents the focal plane polarizations;

$$\vec{T} = (T_t, T_n, T_l) = \vec{P} + hP_e \vec{P}', \quad (4.5.2)$$

represents the target polarizations with  $t$ ,  $n$ , and  $l$  defined as in Fig. 1.2.2 with  $l$  along the proton momentum,  $n$  perpendicular to the reaction plane, and  $t = n \times l$ ;  $h$  and  $P_e$  denote the sign of the helicity and magnitude of the beam polarization, respectively; and  $S$  is the spin transport matrix. The spin transport matrix is dependent on a sequence of five transformations to project the focal plane coordinates to the target and is discussed further in Section 4.5.2.4.

A maximum-likelihood method was used to extract the target polarization components from the azimuthal distribution for scattering by the FPP analyzer. This was accomplished using an analysis code, PALM (Polarization Analysis using Likelihood Method), developed by S. Strauch of George Washington University<sup>5</sup>, to determine the target polarization parameters.

In a sample of protons of focal plane polarizations  $P_x^{fpp}$  and  $P_y^{fpp}$ ,<sup>6</sup> the probability that a proton  $i$  scatters with angles  $\theta_{fpp}^i$  and  $\phi_{fpp}^i$  in the carbon analyzer is given by the angular distribution of Eqn. (4.4.8). The probability for the experimental angular distribution can then be written as the product of the individual probabilities for each proton scattered in the analyzer:

$$L = \prod_{i=1}^N \frac{1}{2\pi} (1 + \xi - \varepsilon_x \sin \phi_{fpp}^i + \varepsilon_y \cos \phi_{fpp}^i), \quad (4.5.3)$$

where  $N$  is the total number of accepted protons,  $\phi_{fpp}$  is defined as zero along the  $x$ -axis and positive  $\phi_{fpp}$  rotates towards the positive  $y$ -axis,  $\xi$  represents the false (instrumental) asymmetry (discussed further in Section 4.5.1), and the coefficients  $\varepsilon_\alpha$  are defined as:

$$\varepsilon_\alpha = A_c(\theta_{fpp}) \sum_{\beta} S_{\alpha\beta} T_\beta, \quad (4.5.4)$$

where  $\alpha \in \{x, y, z\}$  and  $\beta \in \{t, n, l\}$  represent the polarization components at the focal

<sup>5</sup>With Rutgers University at the time of code development.

<sup>6</sup>From this point forward the polarizations at the focal plane will be denoted  $P_{x,y}$  and those at the target as  $P_{n,l,t}$  thus dropping the  $fpp$  or  $tg$  superscripts.

plane and target, respectively. Because of the variation in the spin transport within the experimental acceptance, all three components of the target polarizations are accessible even though the scattering probability of each event is independent of the longitudinal polarization.

**4.5.1. Instrumental Asymmetries.** Because of its complexity and size, the Hall A FPP is not ideal. Misalignments of the FPP chambers with respect to each other<sup>7</sup> and variations in the efficiency of the chambers may introduce *instrumental (false) asymmetries*. A detailed study of the false asymmetries was performed by this author.

The false asymmetry is parameterized by four coefficients describing the functional dependence:

$$\frac{\sigma^+}{2\sigma_o^+} + \frac{\sigma^-}{2\sigma_o^-} = 1 + a_o \sin \phi_{fpp} + b_o \cos \phi_{fpp} + c_o \sin 2\phi_{fpp} + d_o \cos 2\phi_{fpp}. \quad (4.5.5)$$

By summing over the plus and minus helicity states of the incident electron beam, the results are the same as if an unpolarized beam were used. In the absence of false asymmetries, the angular distribution of elastic  $ep$  scattering with an unpolarized beam should be flat.

The false asymmetry was first examined as a function of spectrometer momentum  $\delta$  – a so-called  $\delta$ -scan. Three sets of data were examined and compared:

- (1) The radiative tail of the elastic  $H(e, e'p)$  reaction measured at the  $\theta_{pq} = -90^\circ$  “ $N \rightarrow \Delta$ ” kinematics with  $p_p = 1.066$  GeV/ $c$ , using the 7.6 and 15.2 cm carbon doors,
- (2) Five different elastic  $H(e, e'p)$  runs taken at the beginning of “ $N \rightarrow \Delta$ ” with  $p_p = 0.786, 0.803, 0.819, 0.836,$  and  $0.852$  GeV/ $c$ , using the 3.8 and 7.6 cm carbon doors,
- (3) Elastic  $H(e, e'p)$  runs taken at the end of “ $N \rightarrow \Delta$ ” with  $p_p = 1.188$  GeV/ $c$ , using the 7.6 and 15.2 cm carbon doors.

It is expected that the extracted false asymmetries for each set should be the same. The  $\delta$ -scan was accomplished by binning the momentum from  $\delta = -5\%$  to  $+5\%$  in bins of  $1\%$ .

The initial analysis was performed using *standard* (loose) cuts on the polar scattering angle and the carbon analyzer:  $3^\circ < \theta_{fpp} < 70^\circ$  and  $340 \text{ cm} < z_{close} < 390 \text{ cm}$ . An alignment method that used software to translate and rotate the chambers for alignment,  $align_{MKJ}$ ,<sup>8</sup> and where the raw track was dependant on  $x_{fpp}$ ,  $y_{fpp}$ ,  $\theta_{fpp}$ , and  $\phi_{fpp}$  was implemented. Fig. 4.5.1 shows the resulting false asymmetry  $\delta$ -scans for the three data sets. As previ-

<sup>7</sup>The FPP is also aligned to the VDCs so that the coordinate system of the FPP is the same as the transport system.

<sup>8</sup>Named for Mark K. Jones, staff scientist at Jefferson Lab.

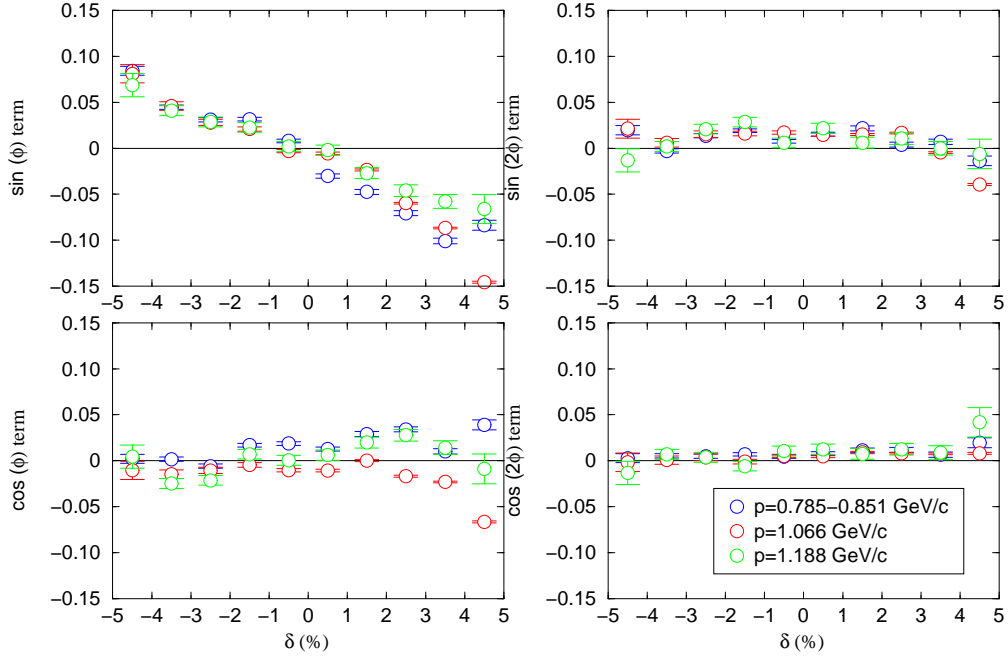


FIGURE 4.5.1.  $\delta$ -scan of three data sets using a cut of  $\theta_{fpp} = 3^\circ$ - $70^\circ$ .

ously mentioned, it is expected that all terms are zero in the absence of false asymmetries. This was not the case.

Detailed studies were then performed on the FPP chamber alignment method by S. Dieterich [64]. She compared  $align_{MKJ}$  to a second method  $align_{EB}$ <sup>9</sup> which used the front track coordinates to determine the rear track alignment and where the raw track was again dependant on  $x_{fpp}$ ,  $y_{fpp}$ ,  $\theta_{fpp}$ , and  $\phi_{fpp}$ . It was determined that both methods were capable of obtaining the precision necessary for previous Hall A experiments but neither method was adequate enough to allow for the extraction of induced polarizations which rely on the false asymmetries.

Dieterich, along with S. Strauch, developed a new alignment method  $align_{SSSD}$ . In  $align_{SSSD}$ , the front track coordinates are used to align the front chambers, rear track coordinates to align the rear chambers, and the track is dependant only upon  $x_{fpp}$  and  $y_{fpp}$  which eliminates large angle-position correlations. Fig. 4.5.2 compares  $\phi_{fpp}$  versus  $z_{close}$  for the three alignment methods. A plot such as this should show clearly the carbon analyzer region. The carbon should be “straight” in the  $z_{close}$  dimension, with sharply defined edges. Events not reconstructed inside the carbon analyzer must be rejected because they

<sup>9</sup>Named for Edward Brash of the University of Regina, Canada.

are unphysical.  $align_{EB}$  produces a non-straight carbon region;  $align_{MKJ}$  has a straight carbon region but edges which are not clearly defined;  $align_{SSD}$  reveals a sharp, straight carbon region, allowing for a clean cut on the edges of the carbon. As a result,  $align_{SSD}$  is used in the remainder of the false asymmetry analysis.

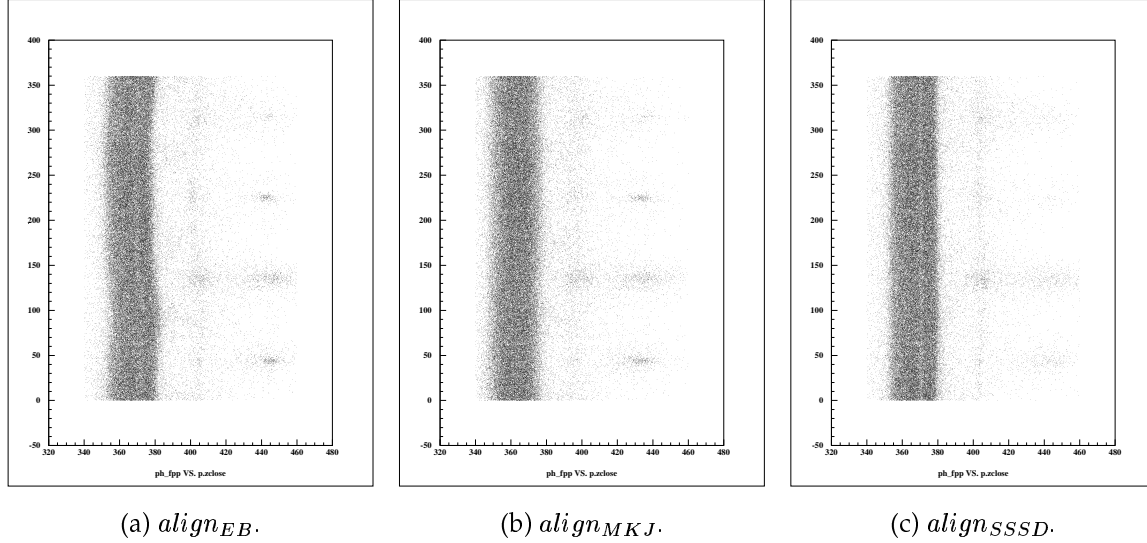


FIGURE 4.5.2. Comparison of three VDC alignment methods.

The false asymmetry was then examined as a function of  $\theta_{fpp}$ , using a  $\delta$ -range of  $-5\% < \delta < +5\%$ ,  $align_{SSD}$ , and cuts on  $z_{close}$  at the edges of the carbon analyzer. The result of this  $\theta_{fpp}$ -scan is shown in Fig. 4.5.3, where it is clear the false asymmetry changes rapidly for  $\theta_{fpp} < 5^\circ$  and  $\theta_{fpp} > 20^\circ$ . A cut is therefore made so that events in the region of  $5^\circ < \theta_{fpp} < 20^\circ$  will be included in further false asymmetry analysis. This is consistent with the known range of scattering angles with a good figure of merit,  $\sigma A_c^2$ , for the energy ranges of Jefferson Lab [45].

Due to questions about the acceptance reconstruction of the spectrometer and matrix elements outside the  $\delta$  range of  $\pm 4\%$ , another  $\delta$ -scan was performed using the above defined criteria:  $align_{SSD}$ , tight cuts on the carbon thickness in  $z_{close}$ , and  $5^\circ < \theta_{fpp} < 20^\circ$ . The results of this scan are displayed in Fig. 4.5.4.

Fig. 4.5.5 compares the  $x$  and  $y$  coverage regions of the elastic data used in the false asymmetry analysis and the  $x$  versus  $y$  coverage regions of the “ $N \rightarrow \Delta$ ” production data at the position of FPP straw chamber 3. As one can see, the false asymmetry analysis was



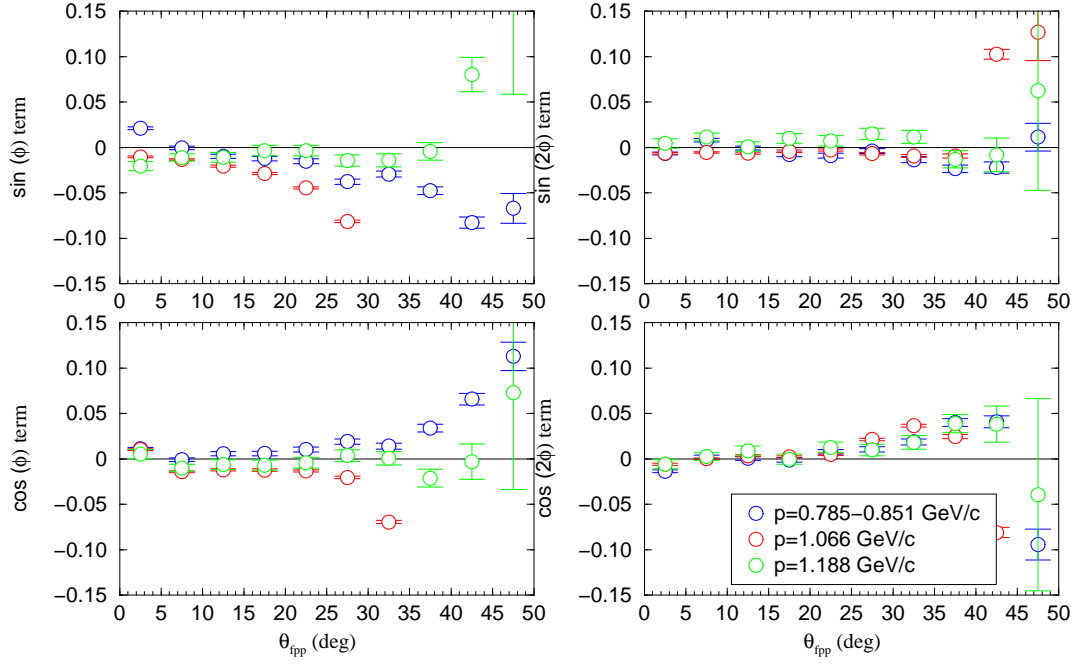


FIGURE 4.5.3.  $\theta_{fpp}$ -scan using cuts on the edges of the carbon blocks and the  $align_{SSD}$  method.

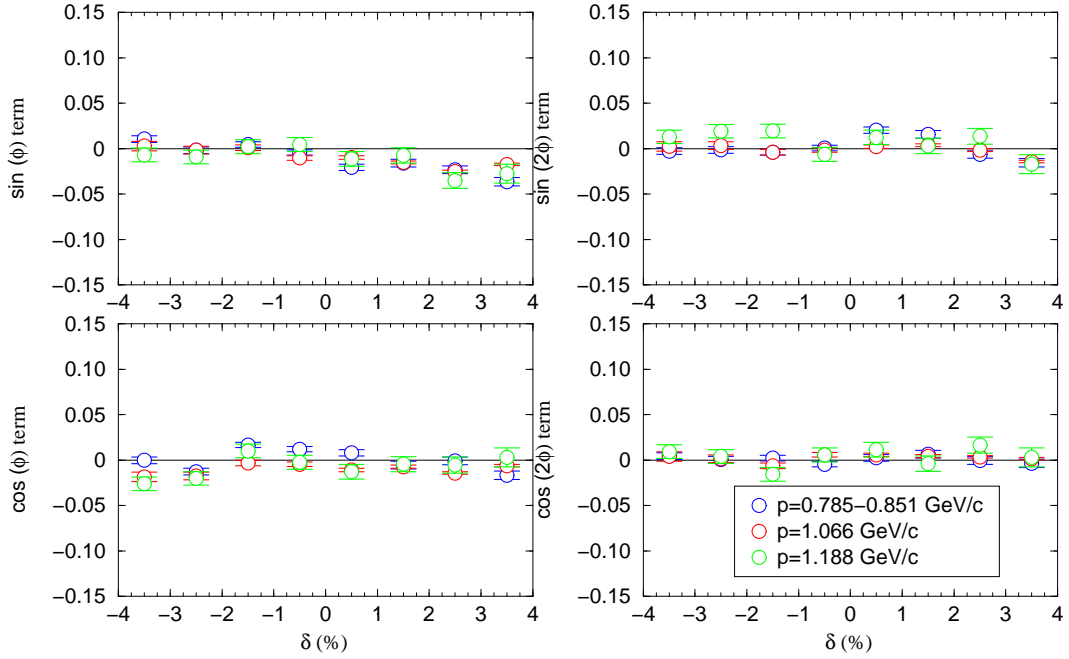


FIGURE 4.5.4.  $\delta$ -scan of  $-4\% < \delta < +4\%$  using the  $align_{SSD}$  method, tight cuts on carbon thickness, and  $\theta_{fpp} = 5^\circ$ - $20^\circ$ .

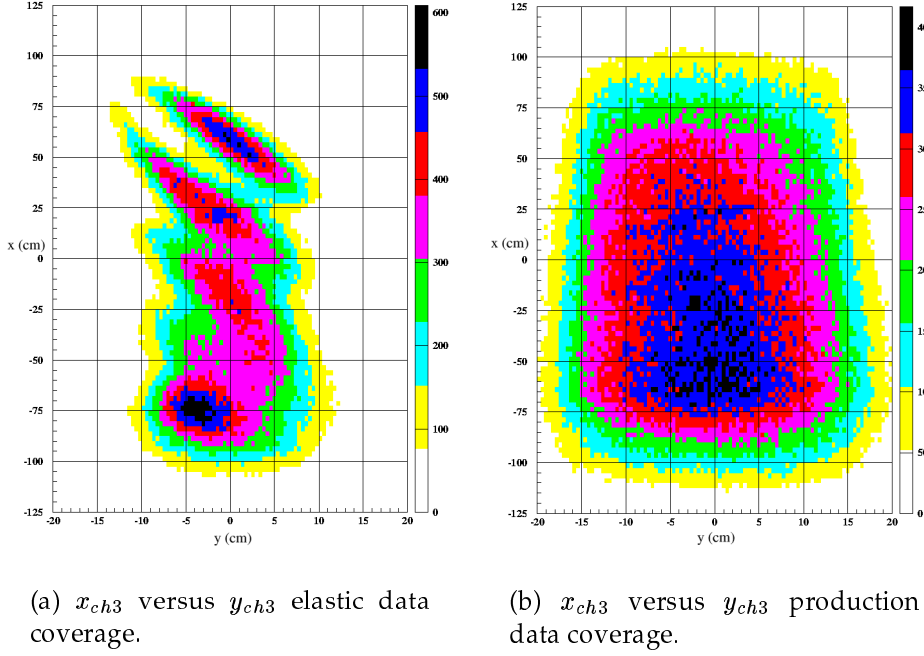


FIGURE 4.5.5. Coverage region of elastic data for false asymmetry studies compared to “ $N \rightarrow \Delta$ ” production data coverage.

performed using a substantial region of the production focal plane. It is believed therefore that the false asymmetries for the production data are well understood.

Fig. 4.5.6 is a plot of the average of the  $\delta$ -scan results from Fig. 4.5.4. The  $a_o$  and  $b_o$  terms are also compared to a monte carlo simulation. The  $a_o$  term seems to have a significant  $\delta$  dependence. A straight line fit of the  $a_o$  term was made, shown in Fig. 4.5.7. The corresponding equation is given as:

$$a_o = (-0.0045 \pm 0.0008)\delta + (-0.0104 \pm 0.0018). \quad (4.5.6)$$

This fit, along with the constant  $b_o$ ,  $c_o$ , and  $d_o$  terms, listed in Tab. 4.4, were used to account for the false asymmetries in the “ $N \rightarrow \Delta$ ” production data where the false asymmetry term of Eqn. (4.5.3) is determined by:

$$\xi = a_o \sin \phi_{fpp} + b_o \cos \phi_{fpp} + c_o \sin 2\phi_{fpp} + d_o \cos 2\phi_{fpp}. \quad (4.5.7)$$

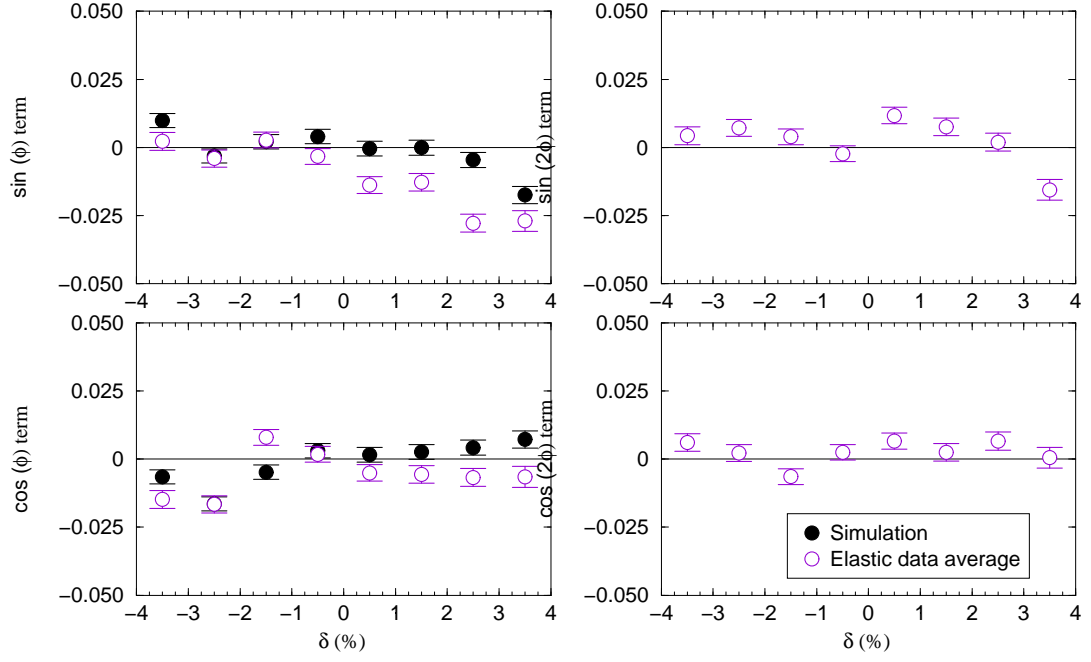


FIGURE 4.5.6. Average of the  $\delta$ -scan of  $-4\% < \delta < +4\%$  using the *align<sub>SSD</sub>* method, tight cuts on carbon thickness, and  $< \theta_{fpp} = 5^\circ$ - $20^\circ$ .

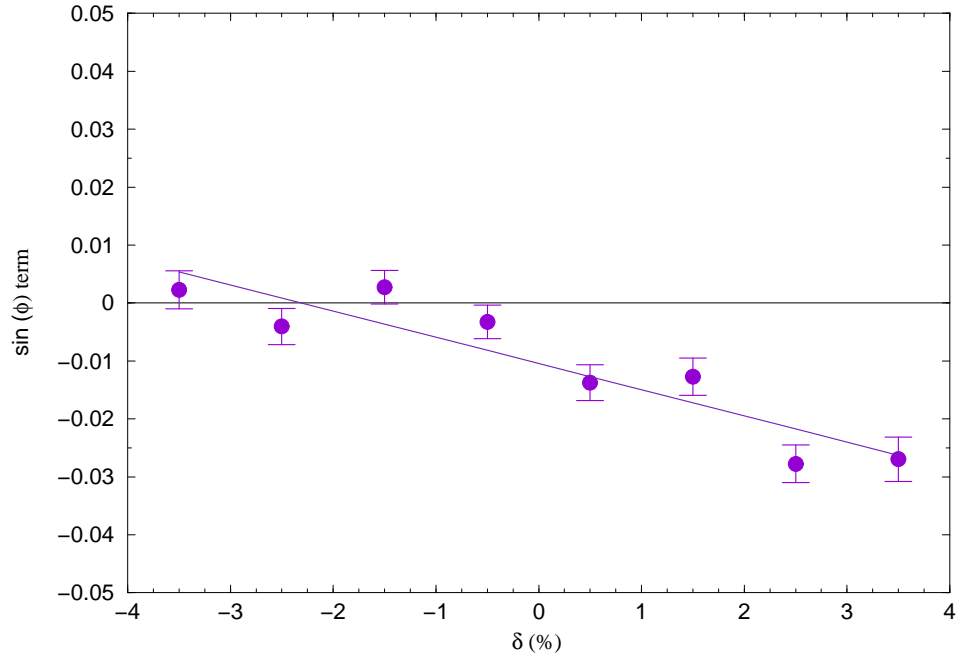


FIGURE 4.5.7. Linear fit of  $a_0$  false asymmetry term.

TABLE 4.4. Average false asymmetry terms.

False Asymmetry Term	Average Over Focal Plane
$b_o$	$-0.0057 \pm 0.0011$
$c_o$	$0.0024 \pm 0.0011$
$d_o$	$0.0025 \pm 0.0011$

**4.5.2. The Spin Transport Matrix.** The spin transport matrix is actually the result of a sequence of five transformations:

$$S = R_{fpp} C R_{spec} R_{hall} R_W, \quad (4.5.8)$$

where:

- (1)  $R_W$  first performs a Wigner rotation of the polarization vector from the center of mass to the laboratory frame,
- (2)  $R_{hall}$  performs a transformation from the laboratory frame to the hall frame,
- (3)  $R_{spec}$  performs a transformation from the hall frame to the spectrometer frame,
- (4)  $C$  transports the spin through the magnetic field of the spectrometer, and
- (5)  $R_{fpp}$  performs a transformation to the FPP coordinate system.

The resulting spin transport matrix is determined event by event in the PALM analysis code.

**4.5.2.1. Wigner Rotation.** The polarization vector must be transformed from the center of mass to the laboratory frame because the spin is defined relative to a rest frame. In both the center of mass and laboratory frames, the polarization vector is defined with  $\hat{l}$  along the direction of the proton's momentum,  $\vec{p}_{cm}$  and  $\vec{p}_{lab}$ , respectively. The rotation between the two takes the form:

$$R_W = \begin{pmatrix} \cos \chi_W & 0 & \sin \chi_W \\ 0 & 1 & 0 \\ -\sin \chi_W & 0 & \cos \chi_W \end{pmatrix} \quad (4.5.9)$$

where the Wigner-Thomas precession angle satisfies the following relationship<sup>10</sup>:

$$\chi_W = \theta_{cm} - \theta_{lab} - \theta_W \quad (4.5.10)$$

and

$$\tan \theta_{lab} = \frac{\beta_{cm} \sin \theta_{cm}}{\gamma (\beta_{cm} \cos \theta_{cm} + \beta)}, \quad (4.5.11)$$

<sup>10</sup>Recall,  $\theta_{pq} = \theta_{cm}$ .

$$\tan \theta_W = \frac{\beta \sin \theta_{cm}}{\gamma_{cm} (\beta \cos \theta_{cm} + \beta_{cm})}, \quad (4.5.12)$$

$\theta_{cm}$  and  $\theta_{lab}$  are the nucleon angle with respect to the momentum transfer  $\vec{q}$  in the center of mass and laboratory frames, respectively,  $\theta_W$  is the total rotation angle for spin,  $\beta_{cm} = p_{cm}/E_{cm}$  is the nucleon velocity in the center of mass, and  $\beta = q/(m_p + \varpi)$  is the velocity of the center of mass with respect to the laboratory. The effect of this rotation is a missing of the  $\hat{l}$  and  $\hat{t}$  components of the proton polarization.

4.5.2.2. *Transformation to the Hall Frame.* The hall reaction frame is defined with  $\hat{z}$  along the beamline,  $\hat{y}$  pointing vertically upwards, and  $\hat{x} = \hat{y} \times \hat{z}$ . The transformation from the laboratory frame to the hall frame is most easily understood if one defines the Cartesian horizontal angle  $\alpha$  in the  $xz$ -plane measured counterclockwise from  $\hat{z}$  and Cartesian vertical angle  $\beta$  with positive  $\beta$  being above the horizontal plane. The unit vectors  $\hat{q}$  and  $\hat{p}$  along the momentum transfer and nucleon momentum planes, respectively, then become:

$$\hat{q} = \begin{pmatrix} \sin \alpha_q \cos \beta_q, & \sin \beta_q, & \cos \alpha_q \cos \beta_q \end{pmatrix}, \quad (4.5.13)$$

$$\hat{p} = \begin{pmatrix} \sin \alpha_p \cos \beta_p, & \sin \beta_p, & \cos \alpha_p \cos \beta_p \end{pmatrix}, \quad (4.5.14)$$

where  $\alpha_q$  and  $\alpha_p$  are both negative because the proton spectrometer is on the right side of the beamline. The laboratory frame basis  $(\hat{S}, \hat{N}, \hat{L})$  is now defined with  $\hat{L}$  along the nucleon momentum and  $\hat{N}$  normal to the reaction plane:

$$\hat{L} = \hat{p}, \quad (4.5.15)$$

$$\hat{N} \propto \hat{q} \times \hat{p}, \quad (4.5.16)$$

$$\hat{S} = \hat{N} \times \hat{L}. \quad (4.5.17)$$

The transformation from the laboratory to the hall frame is then defined as:

$$R_{hall} = \begin{pmatrix} \hat{S} & \hat{N} & \hat{L} \end{pmatrix} \quad (4.5.18)$$

where the previously defined unit vectors are the columns of a square matrix.

4.5.2.3. *Transformation to the Spectrometer Frame.* The spectrometer frame (transport frame) is defined with  $\hat{z}$  along the central axis of the spectrometer,  $\hat{x}$  downward, and  $\hat{y} = \hat{z} \times \hat{x}$ . The transformation from the hall to the spectrometer frame is then accomplished using:

$$R_{spec} = \begin{pmatrix} 0 & -1 & 0 \\ \cos \alpha_o & 0 & -\sin \alpha_o \\ \sin \alpha_o & 0 & \cos \alpha_o \end{pmatrix} \quad (4.5.19)$$

where  $\alpha_o$  is the central angle of the spectrometer which again is negative because the hadron spectrometer is to the right of the beamline.

4.5.2.4. *Spin Transport.* The relationship between the target and focal plane polarizations is made complicated as the proton passes through the spectrometer. Due to the magnetic fields of the spectrometer magnets, the proton spin precesses around the axis of the overall magnetic field.

If the spectrometer consisted of only a single perfect dipole, exhibited in Fig. 4.5.8, the proton spin would precess around the transverse field by an angle  $\chi_o$ :

$$\chi_o = \gamma (\mu_p - 1) \rho_o, \quad (4.5.20)$$

where  $\gamma = 1/\sqrt{1 - \beta^2}$  and  $\rho_o$  is the bending angle of the trajectory.<sup>11</sup> The spin transport matrix for this pure dipole would be written as:

$$C^o = \begin{pmatrix} \cos \chi_o & 0 & -\sin \chi_o \\ 0 & 1 & 0 \\ \sin \chi_o & 0 & \cos \chi_o \end{pmatrix}. \quad (4.5.21)$$

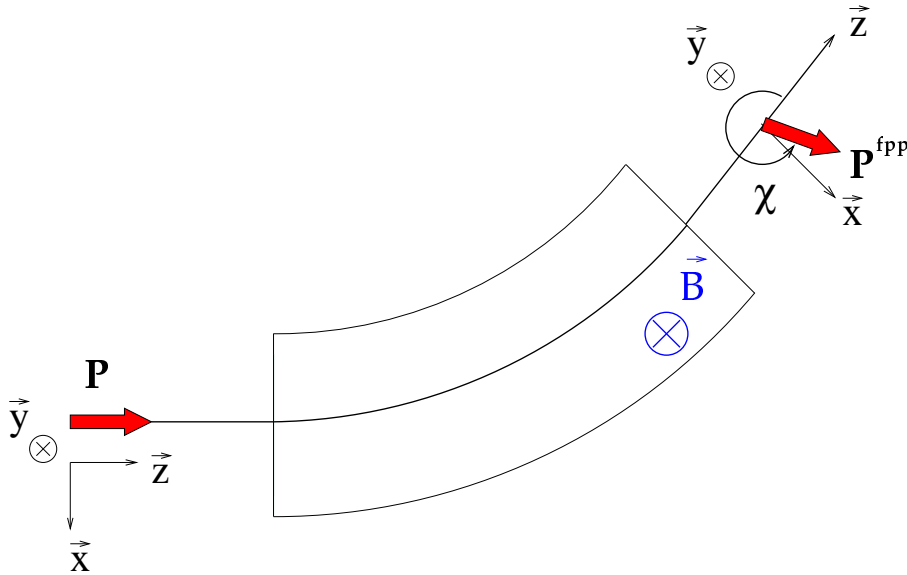


FIGURE 4.5.8. A simple perfect dipole approximation of the spectrometer model.

The actual magnetic structure of the HRS is much more complicated than this simple

<sup>11</sup>For the HRS,  $\rho_o = 45.1^\circ$ , as mentioned in Section 4.2.2.2.

dipole. First, the field inside the dipole is not uniform but distorted at the entrance and exit faces due to fringe fields. Second, there are three quadrupoles in the spectrometer system, with field components in both the  $x$  and  $y$  directions. A model of the spectrometer magnetic fields must be made using the shape of the magnetic elements and the currents in the excitation coils. This is done with the aid of a differential algebra based code created for the simulation, analysis, and design of particle optics systems, called COSY [65]. The dimensions and positions of the magnetic elements, the central momentum of the proton, and measurements of the dipole fringe fields made during the original hall commissioning are fed into COSY where the rotation matrix is computed to fifth order. The output for a given proton central momentum is a table of expansion coefficients,  $C_{ij}^{klmnp}$ , of the rotation matrix, which is then calculated event by event using each proton's position, angle, and momentum at the target in the transport frame:

$$C_{ij} = \sum_{k,l,m,n,p} C_{ij}^{klmnp} x^k \theta^l y^m \phi^n \delta^p. \quad (4.5.22)$$

4.5.2.5. *Transformation to the FPP Frame.* The proton polarization incident on the FPP analyzer must be transformed into the FPP frame. The tracks before and after scattering with the analyzer are defined in the FPP as:

$$\hat{k}_i = \begin{pmatrix} \sin \alpha_i \cos \beta_i, & \sin \beta_i, & \cos \alpha_i \cos \beta_i \end{pmatrix}, \quad (4.5.23)$$

$$\hat{k}_f = \begin{pmatrix} \sin \alpha_f \cos \beta_f, & \sin \beta_f, & \cos \alpha_f \cos \beta_f \end{pmatrix}, \quad (4.5.24)$$

where  $\alpha$  and  $\beta$  are Cartesian angles. The transformation of the incident proton from the spectrometer transport frame to the FPP frame aligned with  $\hat{k}_i$  is then given by:

$$R_{fpp} = \begin{pmatrix} \cos \alpha_i & 0 & -\sin \alpha_i \\ -\sin \alpha_i \sin \beta_i & \cos \beta_i & -\cos \alpha_i \sin \beta_i \\ \sin \alpha_i \cos \beta_i & \sin \beta_i & \cos \alpha_i \cos \beta_i \end{pmatrix}. \quad (4.5.25)$$

The polar and azimuthal scattering angles in the FPP are determined using:

$$\begin{pmatrix} \sin \theta_{fpp} \cos \phi_{fpp} \\ \sin \theta_{fpp} \sin \phi_{fpp} \\ \cos \theta_{fpp} \end{pmatrix} = R_{fpp} \hat{k}_f \quad (4.5.26)$$

so that

$$\vec{F} \cdot \hat{n}_{fpp} = F_y \cos \phi_{fpp} - F_x \sin \phi_{fpp} \quad (4.5.27)$$

where  $\hat{n}_{fpp}$  is a unit vector normal to the FPP scattering plane.

**4.5.3. Extracting Target Polarizations.** The terms of the likelihood function of Eqn. (4.5.3) can be recombined as:

$$L = \prod_{i=1}^N \frac{1}{2\pi} \left( 1 + \xi + \sum_k \lambda_{i,k} P_k + \sum_k \lambda'_{i,k} P'_k \right), \quad (4.5.28)$$

where  $\xi$  is the false asymmetry term defined in Eqn. (4.5.7),  $k \in \{t, n, l\}$  are the three polarization components at the target, and

$$\lambda_{i,1} = A_c (\theta_{fpp}^i) (S_{yt} \cos \phi_{fpp}^i - S_{xt} \sin \phi_{fpp}^i), \quad (4.5.29)$$

$$\lambda_{i,2} = A_c (\theta_{fpp}^i) (S_{yn} \cos \phi_{fpp}^i - S_{xn} \sin \phi_{fpp}^i), \quad (4.5.30)$$

$$\lambda_{i,3} = A_c (\theta_{fpp}^i) (S_{yl} \cos \phi_{fpp}^i - S_{xl} \sin \phi_{fpp}^i), \quad (4.5.31)$$

$$\lambda'_{i,1} = hP_e \lambda_{i,1}, \quad (4.5.32)$$

$$\lambda'_{i,2} = hP_e \lambda_{i,2}, \quad (4.5.33)$$

$$\lambda'_{i,3} = hP_e \lambda_{i,3}. \quad (4.5.34)$$

The idea of the maximum likelihood method is now to find the best parameters ( $P_{k=t,n,l}, P'_{k=t,n,l}$ ) to maximize this function. These parameters must satisfy the following conditions:

$$\frac{\partial L}{\partial P_k} = 0, \quad (4.5.35)$$

$$\frac{\partial L}{\partial P'_k} = 0. \quad (4.5.36)$$

However, this is a set of six non-linear equations with six unknowns where an exact solution cannot be determined. Taking the logarithm of the likelihood function to convert the product into a sum, the following equations must also be satisfied:

$$\frac{\partial \ln L}{\partial P_k} = 0, \quad (4.5.37)$$

$$\frac{\partial \ln L}{\partial P'_k} = 0, \quad (4.5.38)$$

where

$$\ln L = \sum_{i=1}^N \ln (1 + \xi + \lambda_t P_t + \lambda_n P_n + \lambda_l P_l + \lambda'_t P'_t + \lambda'_n P'_n + \lambda'_l P'_l) - \sum_{i=1}^N \ln (2\pi). \quad (4.5.39)$$

Eqns. (4.5.37)-(4.5.38) are also a set of six coupled nonlinear equations. They are linearized, as demonstrated in [66], by using the following relation:



$$\ln(1+x) = x - \frac{x^2}{2} + \sigma(x^3). \quad (4.5.40)$$

Dropping the  $\sigma(x^3)$  term and setting  $x = \xi + \lambda_t P_t + \lambda_n P_n + \lambda_l P_l + \lambda'_t P'_t + \lambda'_n P'_n + \lambda'_l P'_l$ , Eqn. (4.5.39) then becomes:

$$\begin{aligned} \ln L = & \sum_{i=1}^N [\xi + \lambda_t P_t + \lambda_n P_n + \lambda_l P_l + \lambda'_t P'_t + \lambda'_n P'_n + \lambda'_l P'_l \\ & - \frac{(\xi + \lambda_t P_t + \lambda_n P_n + \lambda_l P_l + \lambda'_t P'_t + \lambda'_n P'_n + \lambda'_l P'_l)^2}{2}] - N \ln(2\pi). \end{aligned} \quad (4.5.41)$$

The derivative of Eqn. (4.5.41) can then be taken with respect to each polarization term. For example, the derivative with respect to  $P_t$  is written as:

$$\sum [\lambda_t - \lambda_t (\xi + \lambda_t P_t + \lambda_n P_n + \lambda_l P_l + \lambda'_t P'_t + \lambda'_n P'_n + \lambda'_l P'_l)] = 0, \quad (4.5.42)$$

and therefore:

$$\sum \lambda_t (1 - \xi) = \sum (\lambda_t \lambda_t P_t + \lambda_t \lambda_n P_n + \lambda_t \lambda_l P_l + \lambda_t \lambda'_t P'_t + \lambda_t \lambda'_n P'_n + \lambda_t \lambda'_l P'_l). \quad (4.5.43)$$

If the derivative is taken with respect to each component of the polarization, the system to solve becomes:

$$\begin{bmatrix} \sum \lambda_t (1 - \xi) \\ \sum \lambda_n (1 - \xi) \\ \sum \lambda_l (1 - \xi) \\ \sum \lambda'_t (1 - \xi) \\ \sum \lambda'_n (1 - \xi) \\ \sum \lambda'_l (1 - \xi) \end{bmatrix} = \begin{bmatrix} \sum \lambda_t \lambda_t & \sum \lambda_t \lambda_n & \sum \lambda_t \lambda_l & \sum \lambda_t \lambda'_t & \sum \lambda_t \lambda'_n & \sum \lambda_t \lambda'_l \\ \sum \lambda_n \lambda_t & \sum \lambda_n \lambda_n & \sum \lambda_n \lambda_l & \sum \lambda_n \lambda'_t & \sum \lambda_n \lambda'_n & \sum \lambda_n \lambda'_l \\ \sum \lambda_l \lambda_t & \sum \lambda_l \lambda_n & \sum \lambda_l \lambda_l & \sum \lambda_l \lambda'_t & \sum \lambda_l \lambda'_n & \sum \lambda_l \lambda'_l \\ \sum \lambda'_t \lambda_t & \sum \lambda'_t \lambda_n & \sum \lambda'_t \lambda_l & \sum \lambda'_t \lambda'_t & \sum \lambda'_t \lambda'_n & \sum \lambda'_t \lambda'_l \\ \sum \lambda'_n \lambda_t & \sum \lambda'_n \lambda_n & \sum \lambda'_n \lambda_l & \sum \lambda'_n \lambda'_t & \sum \lambda'_n \lambda'_n & \sum \lambda'_n \lambda'_l \\ \sum \lambda'_l \lambda_t & \sum \lambda'_l \lambda_n & \sum \lambda'_l \lambda_l & \sum \lambda'_l \lambda'_t & \sum \lambda'_l \lambda'_n & \sum \lambda'_l \lambda'_l \end{bmatrix} \begin{bmatrix} P_t \\ P_n \\ P_l \\ P'_t \\ P'_n \\ P'_l \end{bmatrix} \quad (4.5.44)$$

where the  $\lambda$ s depend only on the spin transport matrix, analyzing power, incoming beam helicity and polarization, and scattering angles in the FPP, all which were determined during the experiment. This is exactly the set of six linear equations solved by PALM, using matrix inversion, to extract the six polarization components at the target.

**4.5.4. Response Function Extraction.** The response functions are directly related to the polarizations, as demonstrated in Eqns. (1.3.32)-(1.3.35). They can therefore also be extracted using the maximum likelihood method. The likelihood function for response function extraction can be written as:

$$L = \prod_{i=1}^N \frac{1}{2\pi} \left( 1 + \xi + \sum_k \eta_{i,k} R_k \right), \quad (4.5.45)$$

where  $R_k$  are the response functions  $R_{LT}^t, R_{TT}^t, \nu_L R_L^n + \nu_T R_T^n, R_{LT}^n, R_{TT}^n, R_{LT}^l, R_{TT}^l, R_{LT}^{tl}, R_{TT}^{tl}, R_{LT}^{ln}, R_{LT}^{ll}, R_{TT}^{ln}, R_{TT}^{ll}$ ,

$$\bar{\sigma}\eta_1 = \lambda_1 \nu_\circ \nu_{LT} \sin \phi_{pq}, \quad (4.5.46)$$

$$\bar{\sigma}\eta_2 = \lambda_1 \nu_\circ \nu_{TT} \sin 2\phi_{pq}, \quad (4.5.47)$$

$$\bar{\sigma}\eta_3 = \lambda_2 \nu_\circ, \quad (4.5.48)$$

$$\bar{\sigma}\eta_4 = \lambda_2 \nu_\circ \nu_{LT} \cos \phi_{pq}, \quad (4.5.49)$$

$$\bar{\sigma}\eta_5 = \lambda_2 \nu_\circ \nu_{TT} \cos 2\phi_{pq}, \quad (4.5.50)$$

$$\bar{\sigma}\eta_6 = \lambda_3 \nu_\circ \nu_{LT} \sin \phi_{pq}, \quad (4.5.51)$$

$$\bar{\sigma}\eta_7 = \lambda_3 \nu_\circ \nu_{TT} \sin 2\phi_{pq}, \quad (4.5.52)$$

$$\bar{\sigma}\eta_8 = \lambda'_1 \nu_\circ \nu'_{LT} \cos \phi_{pq} \quad (4.5.53)$$

$$\bar{\sigma}\eta_9 = \lambda'_1 \nu_\circ \nu'_{TT} \quad (4.5.54)$$

$$\bar{\sigma}\eta_{10} = \lambda'_2 \nu_\circ \nu'_{LT} \sin \phi_{pq} \quad (4.5.55)$$

$$\bar{\sigma}\eta_{11} = \lambda'_3 \nu_\circ \nu'_{LT} \cos \phi_{pq} \quad (4.5.56)$$

$$\bar{\sigma}\eta_{12} = \lambda'_3 \nu_\circ \nu'_{TT} \quad (4.5.57)$$

$\nu_\circ = p_p/k_\gamma$  as previously defined, and  $\nu_k$  are the kinematic factors in the “standard” convention from Eqns. (1.3.22)-(1.3.27).

The coefficients for the response functions depend on the unpolarized differential cross section,  $\bar{\sigma}$ . For each kinematic bin of this experiment, the cross sections were measured for a central  $W$ ,  $Q^2$ ,  $\theta_{pq}$ , and  $\phi_{pq}$  of the bin<sup>12</sup>. A fit to these measured cross sections was included in PALM. Each event’s measured and predicted MAID cross sections were determined at the central kinematics of the bin into which the event fell, based on the event’s  $W$ ,  $Q^2$ ,  $\theta_{pq}$ , and  $\phi_{pq}$  values. To determine the cross section used in the response function extraction for each event, the predicted MAID cross section was calculated at the event’s  $W$ ,  $Q^2$ ,  $\theta_{pq}$ , and  $\phi_{pq}$  and scaled by the ratio of the measured to predicted cross section at the central kinematics of the bin.

The response functions are then determined in a way analogous to the polarizations, where the response function parameters must satisfy a given set of conditions:

---

<sup>12</sup>These measurements were the focus of the PhD thesis of Z. Chai [10].

$$\frac{\partial \ln L}{\partial R_k} = 0, \quad (4.5.58)$$

and

$$\begin{aligned} \ln L = & \sum_{i=1}^N \ln [1 + \xi + \eta_1 R_{LT}^t + \eta_2 R_{TT}^t + \eta_3 (\nu_L R_L^n + \nu_T R_T^n) + \eta_4 R_{LT}^n + \eta_5 R_{TT}^n \\ & + \eta_6 R_{LT}^l + \eta_7 R_{TT}^l + \eta_8 R_{LT}^t + \eta_9 R_{TT}^t + \eta_{10} R_{LT}^n + \eta_{11} R_{LT}^l + \eta_{12} R_{TT}^l] \\ & - \sum_{i=1}^N \ln (2\pi). \end{aligned} \quad (4.5.59)$$

Eqn. (4.5.58) is a set of twelve coupled nonlinear equations. This likelihood function has to be linearized using the relation of Eqn. (4.5.40) and the derivative taken with respect to each response function term. The result is a solvable system of twelve equations with twelve unknowns:

$$\begin{bmatrix} \sum \eta_1 (1 - \xi) \\ \sum \eta_2 (1 - \xi) \\ \sum \eta_3 (1 - \xi) \\ \vdots \\ \sum \eta_{12} (1 - \xi) \end{bmatrix} = \begin{bmatrix} \sum \eta_1 \eta_1 & \sum \eta_1 \eta_2 & \sum \eta_1 \eta_3 & \cdots & \sum \eta_1 \eta_{12} \\ \sum \eta_2 \eta_1 & \sum \eta_2 \eta_2 & \sum \eta_2 \eta_3 & \cdots & \sum \eta_2 \eta_{12} \\ \sum \eta_3 \eta_1 & \sum \eta_3 \eta_2 & \sum \eta_3 \eta_3 & \cdots & \sum \eta_3 \eta_{12} \\ \vdots & \vdots & \vdots & \ddots & \vdots \\ \sum \eta_{12} \eta_1 & \sum \eta_{12} \eta_2 & \sum \eta_{12} \eta_3 & \cdots & \sum \eta_{12} \eta_{12} \end{bmatrix} \begin{bmatrix} R_{LT}^t \\ R_{TT}^t \\ \nu_L R_L^n + \nu_T R_T^n \\ \vdots \\ R_{TT}^l \end{bmatrix}, \quad (4.5.60)$$

where the  $\eta$ s depend on the cross section, electron kinematics, scattered proton angle in the center of mass, again all determined during “ $N \rightarrow \Delta$ ”. PALM then solves this matrix, using matrix inversion, to extract the response functions.

## 4.6. Background Subtraction

The contribution of background events to the measured polarizations and response functions had to be accounted for (subtracted away). To clarify, the background under consideration in this section refers to events generated by separate  $p(e, e')$  and  $p(e, p)$  “singles” reactions that accidentally occur within a narrow time window, thus mimicking true  $p(e, e')\pi^0$  reaction events. This background contribution was only significant for a few  $\theta_{pq}$  kinematics. Fig. 4.6.1 shows the corrected coincidence time spectra for all kinematic settings, along with the cut made on the data separating the in-time (peak) and out-of-time (background) regions. The ratio of these regions for all kinematics are listed

in Tab. 4.5.

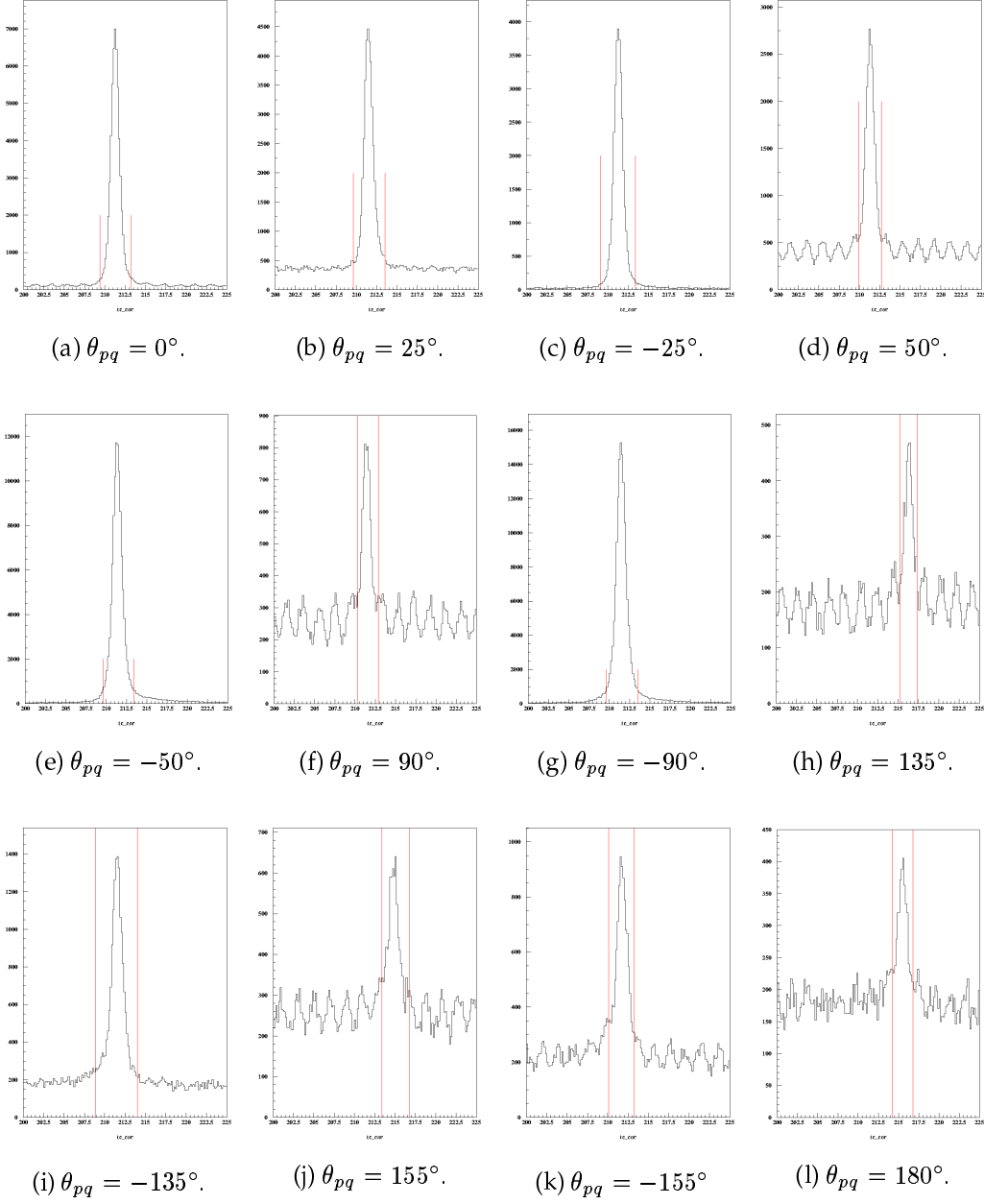


FIGURE 4.6.1. Corrected coincidence timing peaks for each “ $N \rightarrow \Delta$ ” kinematic setting.

One can see from these figures and ratios that subtraction of the background events is

TABLE 4.5. Peak to background ratios for all “ $N \rightarrow \Delta$ ” kinematics.

$\theta_{pq}$	Peak to Background Ratio	$\theta_{pq}$	Peak to Background Ratio
0°	40:1	-90°	100:1
25°	10:1	135°	2:1
-25°	100:1	-135°	7:1
50°	5:1	155°	2:1
-50°	185:1	-155°	3:1
90°	2:1	180°	2:1

only necessary for the following kinematic settings:  $90^\circ$ ,  $135^\circ$ ,  $\pm 155^\circ$ , and  $180^\circ$ . However, because certain kinematic settings overlap others in  $\cos \theta_{pq}$  (as evidenced in Tab. 4.1) and these overlapping kinematic settings are analyzed together in PALM, background subtractions have also been performed on the overlapping kinematics for the  $\cos \theta_{pq}$  regions containing these “necessary” kinematics:  $-1.0 < \cos \theta_{pq} < 0.3$ .

Background subtraction can be summarized as follows:

- (1) measurement of the polarizations for the out-of-time regions,
- (2) estimation of the number of accidentals in the in-time region, assuming the polarizations for these accidentals are the same as the out-of-time polarizations, and
- (3) subtraction of the accidental polarizations from the peak.

These steps were repeated for the response function background subtraction.

**4.6.1. Measurement of Background Polarizations.** The background contribution for each kinematic setting was determined separately. The full coincidence time window was from 200 to 225 ns. Cuts were placed around the peak in  $tc_{cor}$  to select the in-time and out-of-time regions. The polarizations and response functions for the background was determined by running PALM with a  $tc_{cor}$  cuts of 200-225 ns (the width of the full coincidence time window) and on the peak, but this time rejecting all events under the peak, therefore keeping the out-of-time background.

**4.6.2. Estimation of the Number of Accidental Events in the Peak.** The coincidence time changed from one pass through a particular kinematic setting to the next due to some changes in the timing of the DAQ logic circuit,<sup>13</sup> thereby complicating the background subtraction by involving more than one  $tc_{cor}$  cut for each kinematic setting. The different timing window widths had to then be accounted for. This was done using using the

<sup>13</sup>The aerogel Čerenkov detector was added to the trigger, causing changes in the timing of the DAQ logic circuit.

following formula:

$$Y_b^i = Y_b^i \left( \frac{w_p}{w_b} \right), \quad (4.6.1)$$

where  $i$  represents the number (first pass, second pass...) of the timing window,  $Y_b^i$  is the raw background yield (the number of events in the out-of-time region),  $w_p$  is the width of the timing peak in ns,  $w_b = 225 \text{ ns} - w_p$ , and  $Y_b^i$  is the background yield weighted by the width of the timing window. The fraction of in-time yield due to the background for each  $i$  was calculated by:

$$r_i = \frac{Y_b^i}{Y_p^i + Y_b^i}, \quad (4.6.2)$$

where  $Y_p^i$  is the yield in the peak. The total fraction of in-time yield due to background for one entire  $\theta_{pq}$  is then given by:

$$r = \frac{\sum_i r_i (Y_p^i + Y_b^i)}{Y_p + Y_b'}, \quad (4.6.3)$$

where the sum is over the number of different timing windows for the kinematic and  $Y_p$  and  $Y_b'$  are the total peak and background yield for the entire set of  $\theta_{pq}$  data.

**4.6.3. Background Correction to Polarization Observables.** The target polarization values determined by PALM were corrected for background contributions using the following formula:

$$P_{cor} = \frac{P_p - r * P_b}{1 - r}, \quad (4.6.4)$$

where  $P_p$  is the value of the polarization (either  $P_t$ ,  $P_n$ ,  $P_l$ ,  $P_t'$ ,  $P_n'$ , or  $P_l'$ ) determined by PALM for the peak region and  $P_b$  is the value of the polarization determined by PALM for the background region.

The error for this background corrected polarization is determined by:

$$\delta P_{cor}^2 = \left( \frac{1}{1 - r} \right)^2 \delta P_p^2 + \left( \frac{-r}{1 - r} \right)^2 \delta P_b^2. \quad (4.6.5)$$

Fig. 4.6.2 shows a sample comparison of the measured polarization  $P_t$  before and after the background subtraction was performed. One can see that the background correction is relatively small. This was the case for all polarization values for all kinematic regions.

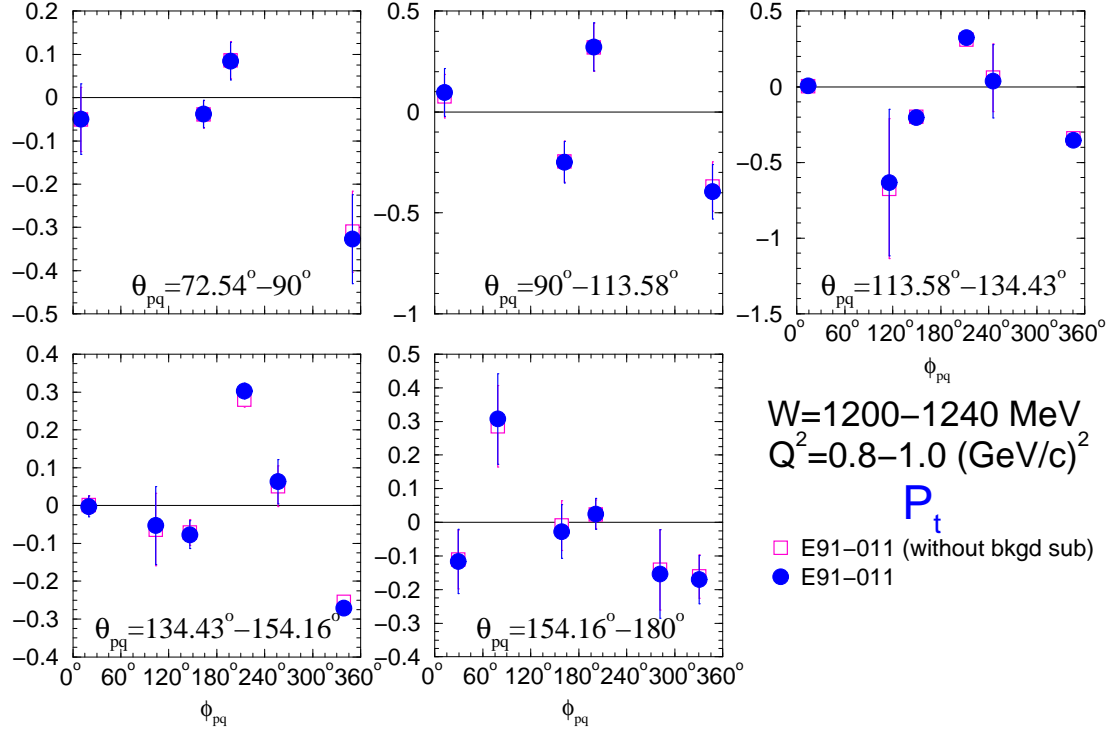


FIGURE 4.6.2. Sample comparison of  $P_t$  before and after background subtraction.

**4.6.4. Background Correction to Response Functions.** The response function values ( $R_{LT}^t, R_{TT}^t, \nu_L R_L^n + \nu_T R_T^n, R_{LT}^n, R_{TT}^n, R_{LT}^l, R_{TT}^l, R_{LT}^t, R_{TT}^t, R_{LT}^n, R_{TT}^n, R_{LT}^l, R_{TT}^l$ ) determined by PALM were corrected for background in much the same way:

$$R_{cor} = R_p - r * R_b, \quad (4.6.6)$$

where  $R_p$  is the response function determined by PALM for the peak and  $R_b$  is the response function value for the background. The error was determined using:

$$\delta R_{cor}^2 = \delta R_p^2 + (-r)^2 \delta R_b^2. \quad (4.6.7)$$

Fig. 4.6.3 shows a sample comparison of the measured helicity dependent response functions before and after the background subtraction.<sup>14</sup> The background correction is also small for all response functions.

<sup>14</sup>Recall: Background subtraction for  $\theta_{pq}$  points lower than  $62^\circ$  was not necessary.

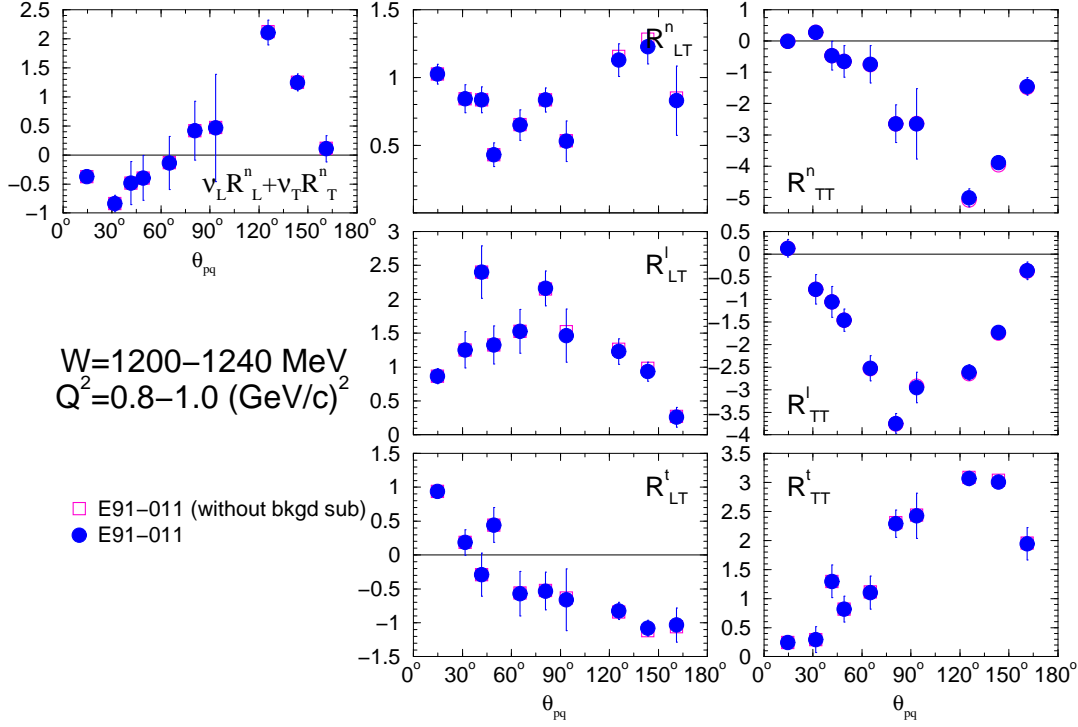


FIGURE 4.6.3. Sample comparison of helicity independent response functions before and after background subtraction.

#### 4.7. Proton Form Factor Ratio

Using elastic calibration data from this experiment it was possible to extract the ratio of the electric ( $G_E$ ) to magnetic ( $G_M$ ) form factors. These form factors are used as a measure of the charge and magnetization distribution inside the nucleon. They describe the internal structure responsible for the difference between electromagnetic electron scattering off of the nucleon to electron scattering off of point-like particles.

Polarimetry is a useful tool for measuring the ratio of electric to magnetic form factors for the nucleon. The form factor ratio is given by:

$$\frac{G_E}{G_M} = -\frac{hP_n}{hP_l} \frac{E + E'}{2m} \tan \frac{\theta_e}{2}. \quad (4.7.1)$$

(The polarization terms  $P_n$  and  $P_l$  are the same as those extracted as described in Section 4.5.3.) The first recoil polarization measurements of the ratio of the electric to magnetic form factors, performed at Bates at  $Q^2 = 0.38$  and  $0.5$   $(\text{GeV}/c)^2$  [67, 68], helped



prove the feasibility of the recoil polarization technique. Jefferson Lab, with its high luminosity and polarized beam, have now allowed for precise measurements of this ratio at  $Q^2$  up to  $5.6 \text{ (GeV/c)}^2$ . Calibration data from “ $N \rightarrow \Delta$ ” have also allowed for the extraction of this ratio. Fig. 4.7.1 is a plot of the current world data on the ratio of  $\mu_p G_{Ep}/G_{Mp}$  (where  $\mu_p$  is the proton’s magnetic moment and  $G_{Ep}$  and  $G_{Mp}$  are the electric and magnetic form factors of the proton) along with the “ $N \rightarrow \Delta$ ” data point, showing only statistical errors. Along with the polarization measurements [67, 68, 69, 70, 71, 63]

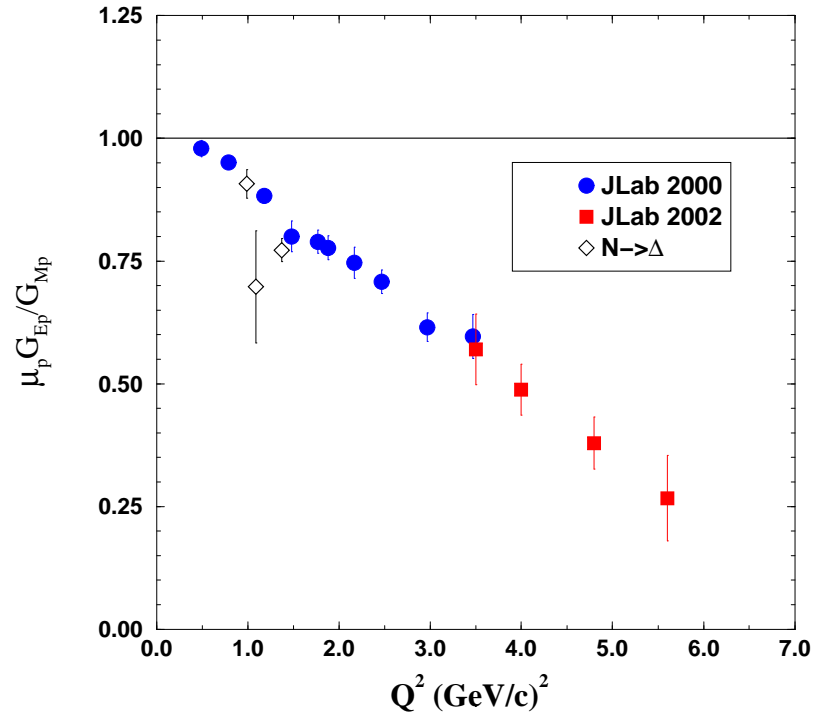


FIGURE 4.7.1. Measurements of the electric to magnetic form factor ratio.

discussed above, data from cross section measurements using Rosenbluth separation, are also shown [72, 73, 74, 75, 76]. Because these calibration measurements agree with  $\mu_p G_{Ep}/G_{Mp}$  also taken in Hall A, there is confidence in the ability to deal with the spin precession and extraction of the polarization observables.



## CHAPTER 5

### RESULTS AND DISCUSSIONS

This chapter discusses the results of the analyses described in Chapter 4. The statistical and systematic errors will also be discussed along with radiative effects on polarization observables and response functions. The experimental results will be compared with other data and theoretical predictions. The remainder of analysis issues needed for extraction of the multipoles will also be outlined.

#### 5.1. Statistical Uncertainties

The statistical uncertainties on the target polarizations and response functions are the result of the propagation of the uncertainty of the amplitude of the asymmetries at the focal plane  $A_c(\theta_{fpp}) P_x^{fpp}$  and  $A_c(\theta_{fpp}) P_y^{fpp}$ . These asymmetries are directly proportional to the square root of the number of events  $n$  that contribute to the amplitude, events for which a track can be reconstructed and that have scattered in the carbon analyzer via the strong interaction:

$$\Delta [A_c(\theta_{fpp}) P_x^{fpp}] = \Delta [A_c(\theta_{fpp}) P_y^{fpp}] = \sqrt{\frac{2}{n}}. \quad (5.1.1)$$

This number reflects the overall efficiency of the polarimeter. Inefficiencies may be due to the inefficiencies of some straws in the straw chambers or the lack of detection of neutrons ejected from the carbon nucleus when struck by the incoming proton. For a given scattering angle  $\theta_{fpp}$ , the efficiency of the FPP can be defined as:

$$\varepsilon(\theta_{fpp}) = \frac{n_{eff}(\theta_{fpp})}{n_o}, \quad (5.1.2)$$

where  $n_o$  is the number of protons entering the FPP and  $n_{eff}(\theta_{fpp})$  is the number of outgoing proton tracks with a polar angle  $\theta_{fpp}$  that pass the cone test (discussed in Section 4.4.5.2). The number of events which participate in the measurement of the asymmetry is then given by:

$$n_{eff}(\theta_{fpp}) = n_o \varepsilon(\theta_{eff}) . \quad (5.1.3)$$

However, only those events that interact with the carbon analyzer via the strong interaction contribute to the actual asymmetry. Furthermore, the sensitivity of these events to the spin-orbit coupling varies depending on scattering angle. The number of measured events  $n_{eff}(\theta_{fpp})$  must therefore be multiplied by  $A_c^2(\theta_{fpp})$  to give the number of events contributing to the asymmetry at an angle of  $\theta_{fpp}$ :

$$n(\theta_{fpp}) = n_o \varepsilon(\theta_{fpp}) A_c^2(\theta_{fpp}) . \quad (5.1.4)$$

The total number of events then contributing to the asymmetry - and thus to the focal plane polarization measurement and its associated uncertainty as given in Eqn. (5.1.1) - is found by integrating Eqn. (5.1.4) over  $\theta_{fpp}$ :

$$n = n_o \int_{\theta_{min}}^{\theta_{max}} \varepsilon(\theta_{fpp}) A_c^2(\theta_{fpp}) d\theta_{fpp} . \quad (5.1.5)$$

## 5.2. Systematic Errors

Systematic errors for the “ $N \rightarrow \Delta$ ” experiment have yet to be studied in detail. It is of importance to note, however, that for measurements of recoil polarization systematic errors are much smaller than statistical errors and therefore should have little effect on the accuracy of the results presented here. Errors associated with the uncertainty in beam energy and proton momentum are negligible. The overall error on the beam polarization, approximately 1.3%<sup>1</sup>, contributes directly to the overall systematic error on the extracted helicity-dependent polarizations.

The largest source of systematic errors in this experiment is in the spin precession as the proton travels through the magnetic field of the spectrometer. The precession is described by the rotation matrix relating the polarizations at the target to the polarizations at the focal plane, as outlined in Section 4.5.2:

$$\begin{bmatrix} P_x^{fpp} \\ P_y^{fpp} \end{bmatrix} = \begin{bmatrix} S_{xt} & S_{xn} & S_{xl} \\ S_{yt} & S_{yn} & S_{yl} \end{bmatrix} \begin{bmatrix} P_t \\ P_n \\ P_l \end{bmatrix} . \quad (5.2.1)$$

The angle, position, and momentum of the proton at the target are used in calculating the

<sup>1</sup>For details on this uncertainty see Ref. [48].

spin matrix elements event by event; the spectrometer optics are then very important. The Hall A spectrometer optics were studied extensively by N. Liyanage [59]. The resulting resolutions are listed in Tab. 5.1. To first order, the spin matrix can be approximated so that Eqn. (5.2.1) can be rewritten as:

$$\begin{bmatrix} P_x^{fpp} \\ P_y^{fpp} \end{bmatrix} = \begin{bmatrix} \cos \chi_o & 0 & \sin \chi_o \\ 0 & 1 & 0 \end{bmatrix} \begin{bmatrix} P_t \\ P_n \\ P_l \end{bmatrix}, \quad (5.2.2)$$

where the precession angle is  $\chi_o = (\mu_p - 1) \theta_{bend}$ . In order for the precession angle to be determined precisely, the bending angle must be reconstructed accurately. The uncertainty on the bending angle is approximately 3 mrad, corresponding to a deviation of  $1.6^\circ$  in precession angle [69].

TABLE 5.1. Hall A optics resolutions at the target.

value	resolution
in-plane angular resolution	2 mrad
out-of-plane angular resolution	6 mrad
transverse position resolution	4.0 mm
momentum resolution	$2.5 \times 10^{-4}$

The accuracy of the determination of the proton polarization at the focal plane depends on the accuracy to which the scattering angle in the FPP is known. The rear straw chambers of the FPP are 30 cm apart with a resolution of 0.3 mm. The resolution of the FPP straw chambers is then

$$\frac{0.3 \times 10^{-3} \text{ m}}{0.3 \text{ m}} = 10^{-3} \text{ rad} = 1 \text{ mrad} \quad (5.2.3)$$

in both the polar ( $\theta_{fpp}$ ) and azimuthal ( $\phi_{fpp}$ ) scattering angles. The effect on focal plane polarizations due to this resolution has not yet been calculated for this experiment, but studies for other polarization experiments performed using the Hall A FPP show the effect to be small - much smaller than statistics (for example, see [63]).

### 5.3. Radiative Corrections

There are three basic types of radiative effects: internal bremsstrahlung, external bremsstrahlung, and Landau straggling. Internal bremsstrahlung occurs when the electron interacts with the Coulomb field of the target nucleus involved in the  $e(e'p)$  reaction by radiating real and/or virtual photons along with the virtual photon being exchanged with the target. External bremsstrahlung occurs when the electron interacts with the Coulomb field of a nucleus not involved in the  $e(e'p)$  reaction. Landau straggling occurs when the electron and proton lose energy due to ionization. Fig. 5.3.1 shows the diagrams for internal bremsstrahlung effects.

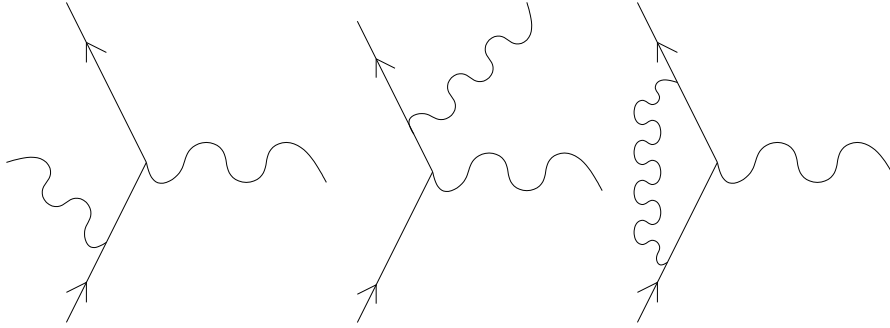


FIGURE 5.3.1. Feynman diagrams for internal bremsstrahlung radiative effects.

For the measurement of polarization observables, the number of events that fall outside a particular kinematic range does not need to be accounted for when making radiative corrections to data within that particular range. The issue, instead, is in determining how the radiation shifts the actual interaction kinematics to the kinematics observed by the spectrometer measurement (which are “post radiation” kinematics) (see, for example, discussions in Ref. [77]). The shift depends on two factors: the width of the kinematic cut made and the derivatives of the observables on the kinematic factors. If an observable is strongly dependent on the kinematics of the interaction, a small shift in the kinematics could lead to a large shift in the observable.

As of yet, radiative corrections have not been applied to the polarization observables and response functions. However, initial studies have been made to investigate the shift in the observables, and thus the overall size of effects from radiation on these observables,

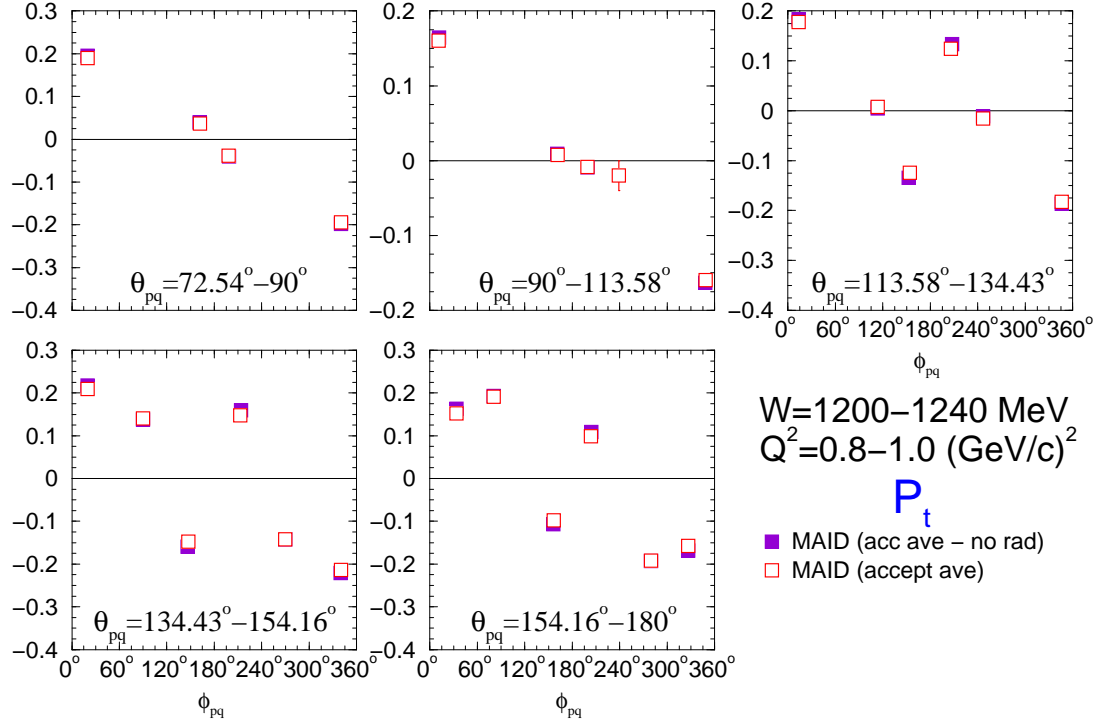


FIGURE 5.3.2. Sample comparison of Monte Carlo simulation with and without radiative corrections.

has been investigated using MCEEP simulations. Results of this investigation are shown in Fig. 5.3.2 where a sample of the  $P_t$  polarization term for  $W = 1200\text{--}1240$  MeV and  $Q^2 = 0.8\text{--}1.0$  (GeV/c)<sup>2</sup> is shown. MCEEP was run with both radiative effects turned on (corresponding to the red squares) and turned off (the purple circles). From this sample plot, it seems that radiative effects are very small, if not negligible, in this analysis. Before publication these effects will be studied in more detail for all observables, and a correction made to the results if necessary.

#### 5.4. Target Polarization Results

Recall that bins in  $W$  were made for values from 1160 to 1360 MeV in widths of 40 MeV, and in  $Q^2$  from 0.8 to 1.2 (GeV/c)<sup>2</sup> in widths of 0.2 (GeV/c)<sup>2</sup>, as shown in Fig. 4.1.1(b). The three induced ( $P_t$ ,  $P_n$ , and  $P_l$ , defined in Eqns. (1.3.32)-(1.3.33)) target polarizations, along with the three transferred ( $hP'_t$ ,  $hP'_n$ , and  $hP'_l$  defined in Eqns. (1.3.34)-(1.3.35)) target polarizations, where to extract  $P'_t$ ,  $P'_n$ , and  $P'_l$  one must divide by the beam helicity  $h$ , for

the  $W$  bin including the  $\Delta(1232)$  resonance ( $1200 \text{ MeV} < W < 1240 \text{ MeV}$ ) and the  $Q^2$  bin of  $0.8 (\text{GeV}/c)^2 < Q^2 < 1.0 (\text{GeV}/c)^2$  are shown in Figs. 5.4.1-5.4.6. Polarizations for all  $W$  and  $Q^2$  bins can be found in Appendix D.

Recall that each polarization is binned in  $\cos \theta_{pq}$  regions from -1 to 1 (in widths of 0.1 to 0.4), as shown in Fig. 4.1.1, corresponding to the ten different panels for each polarization. The solid circles are the measured polarization values placed at the average  $\phi_{pq}$  value for each  $\phi_{pq}$  bin. The open squares correspond to the acceptance averaged MAID model (using MCEEP) predictions. MCEEP will be discussed in Section 5.6.1. The solid and dashed lines corresponds to the MAID and SAID predictions, respectively. These polarization observables are all sensitive to the interference of non-resonant and non-dominant resonant amplitudes with the dominant  $M_{1+}$  amplitude, as discussed in Chapter 1 (see again Eqns. (1.3.32)-(1.3.35) and (1.4.9)-(1.4.21)).

## 5.5. Response Function Results

The eight induced response functions ( $\nu_L R_L^n + \nu_T R_T^n$ ,  $R_{LT}^n$ ,  $R_{LT}^l$ ,  $R_{LT}^t$ ,  $R_{TT}^n$ ,  $R_{TT}^l$ ,  $R_{TT}^t$  defined in Eqns. (1.4.9)-(1.4.16)), along with the five transferred response functions ( $R_{LT}^n$ ,  $R_{LT}^l$ ,  $R_{LT}^t$ ,  $R_{TT}^n$ ,  $R_{TT}^t$  defined in Eqns. (1.4.17)-(1.4.21)), for the  $1200 \text{ MeV} < W < 1240 \text{ MeV}$  and  $0.8 (\text{GeV}/c)^2 < Q^2 < 1.0 (\text{GeV}/c)^2$  bins are shown in Figs. 5.5.1(a) and (b). Response functions for each bin in  $W$  and  $Q^2$  can be found in Appendix E. The solid circles are the extracted response function values placed at the average  $\theta_{pq}$  value for each  $\theta_{pq}$  bin, the open squares correspond to the acceptance averaged MAID predictions (using MCEEP), and the solid and dashed lines corresponds to the MAID and SAID predictions, respectively.

## 5.6. Comparison to Simulation and Models

**5.6.1. Simulation: MCEEP Acceptance Averaging.** Because it is insufficient to simply compare theoretical values evaluated at nominal kinematics, or point acceptance, with experimental observables measured and averaged over a finite acceptance, a Monte Carlo routine - MCEEP (Monte Carlo for  $(\underline{e}, \underline{e}'p)$ ) developed by P. E. Ulmer [78] - was used to average a theoretical model (MAID) over an experimental acceptance determined by the acceptance of the spectrometer.



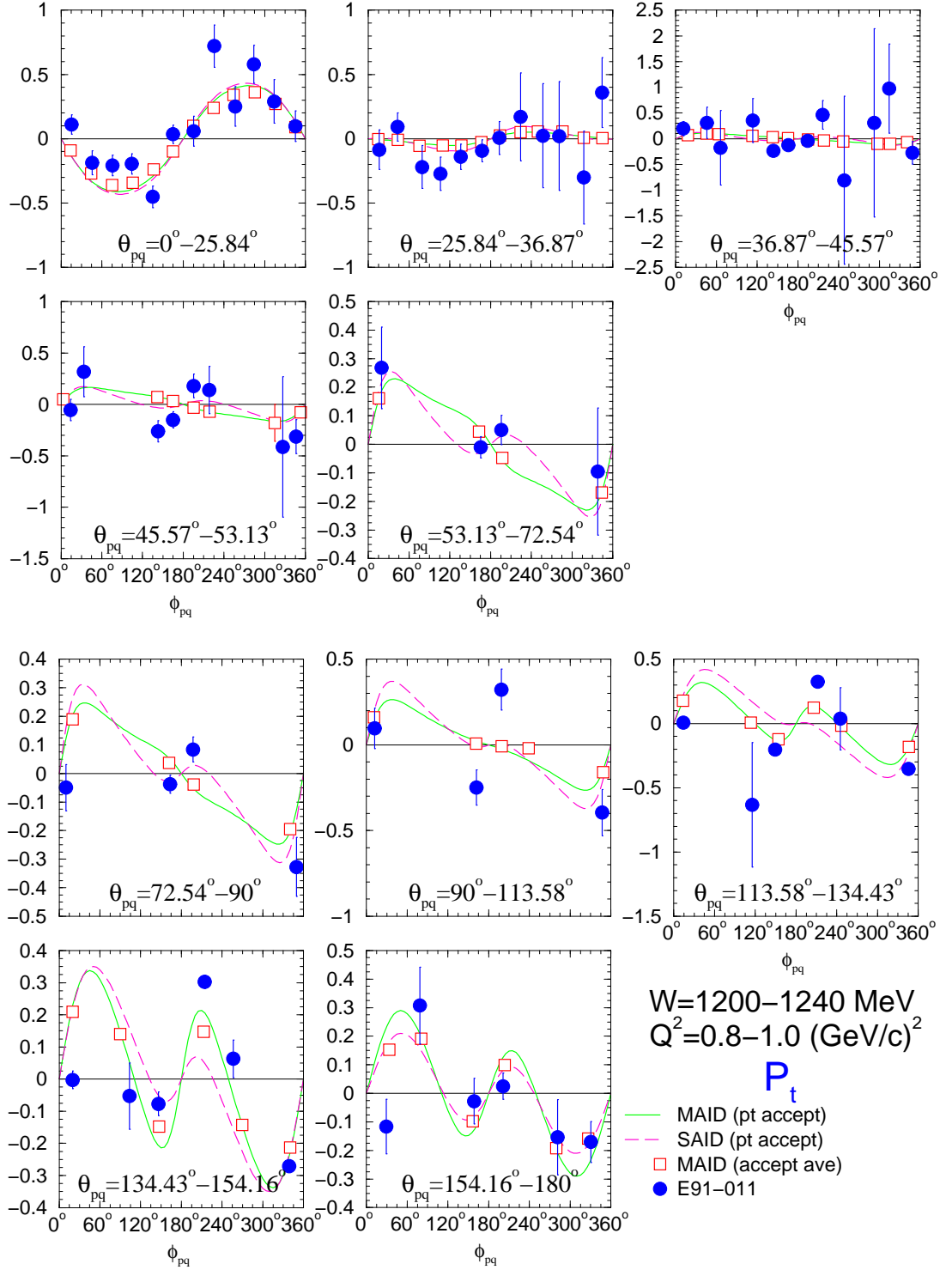


FIGURE 5.4.1. Target polarization  $P_t$  for  $W = 1200-1240$  MeV and  $Q^2 = 0.8-1.0$  (GeV/c) $^2$ .

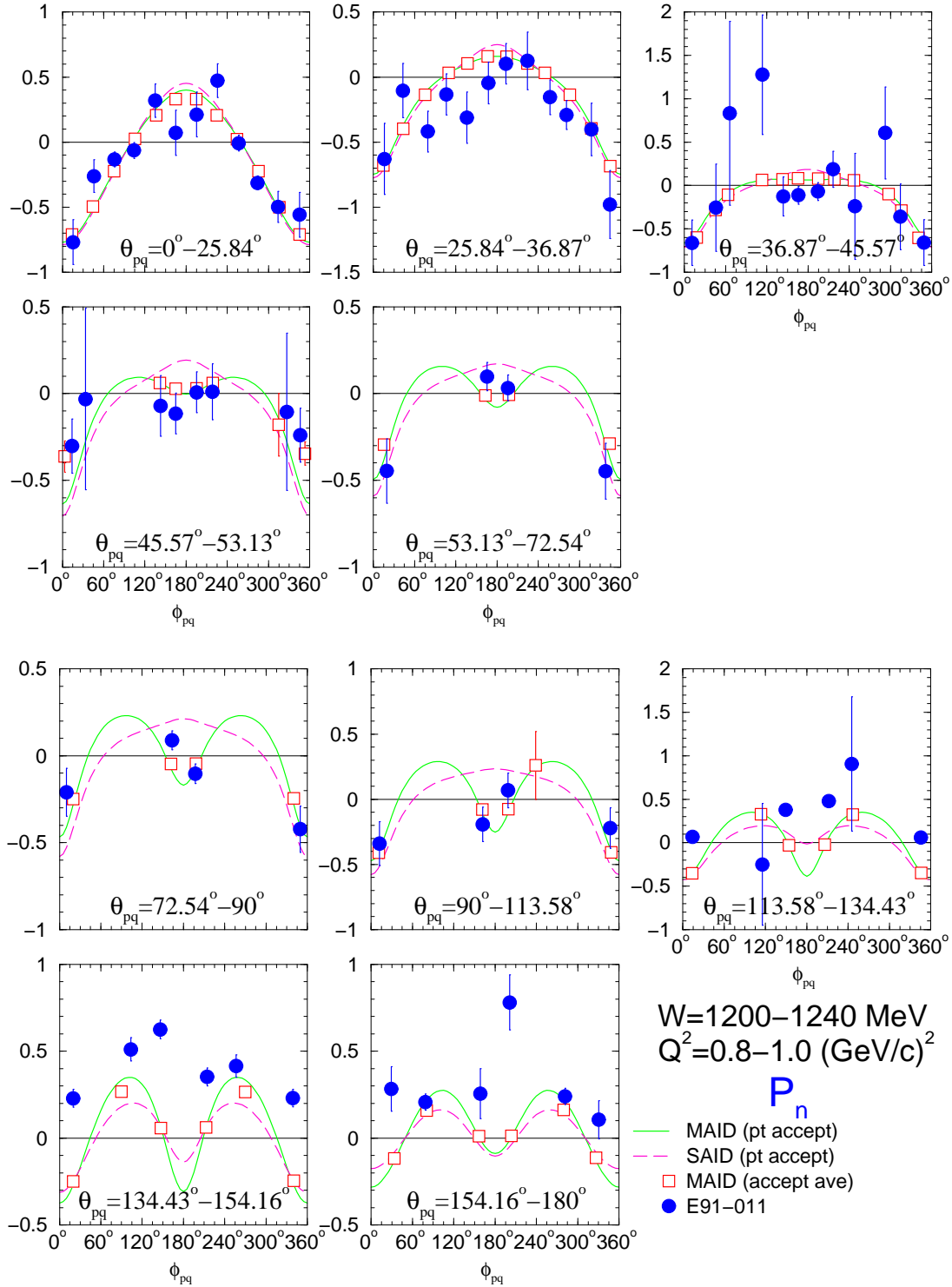


FIGURE 5.4.2. Target polarization  $P_n$  for  $W = 1200\text{--}1240 \text{ MeV}$  and  $Q^2 = 0.8\text{--}1.0 \text{ (GeV/c)}^2$ .

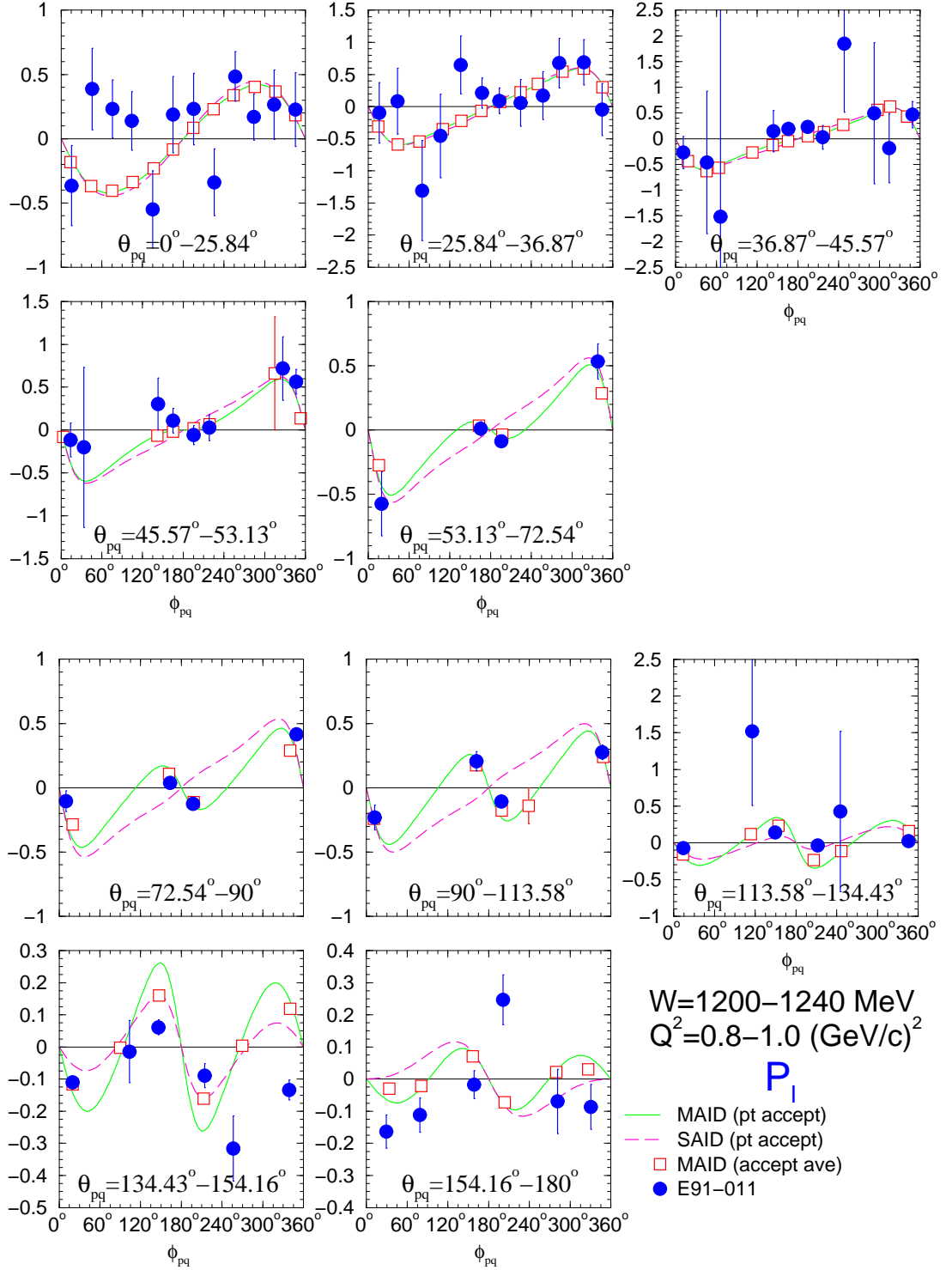


FIGURE 5.4.3. Target polarization  $P_l$  for  $W = 1200-1240$  MeV and  $Q^2 = 0.8-1.0$  (GeV/c) $^2$ .

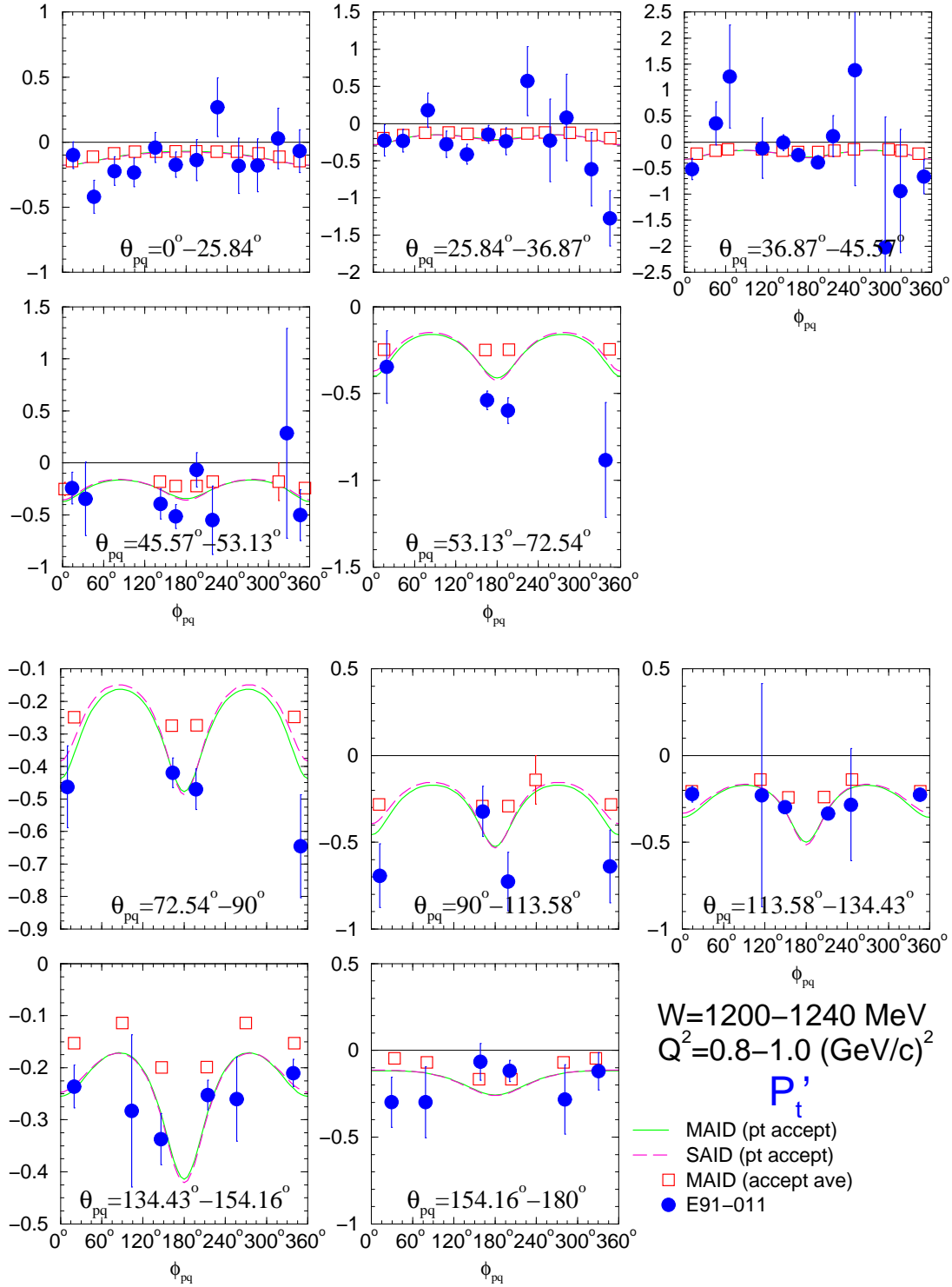


FIGURE 5.4.4. Target polarization  $P'_t$  for  $W = 1200-1240$  MeV and  $Q^2 = 0.8-1.0$  (GeV/c) $^2$ .

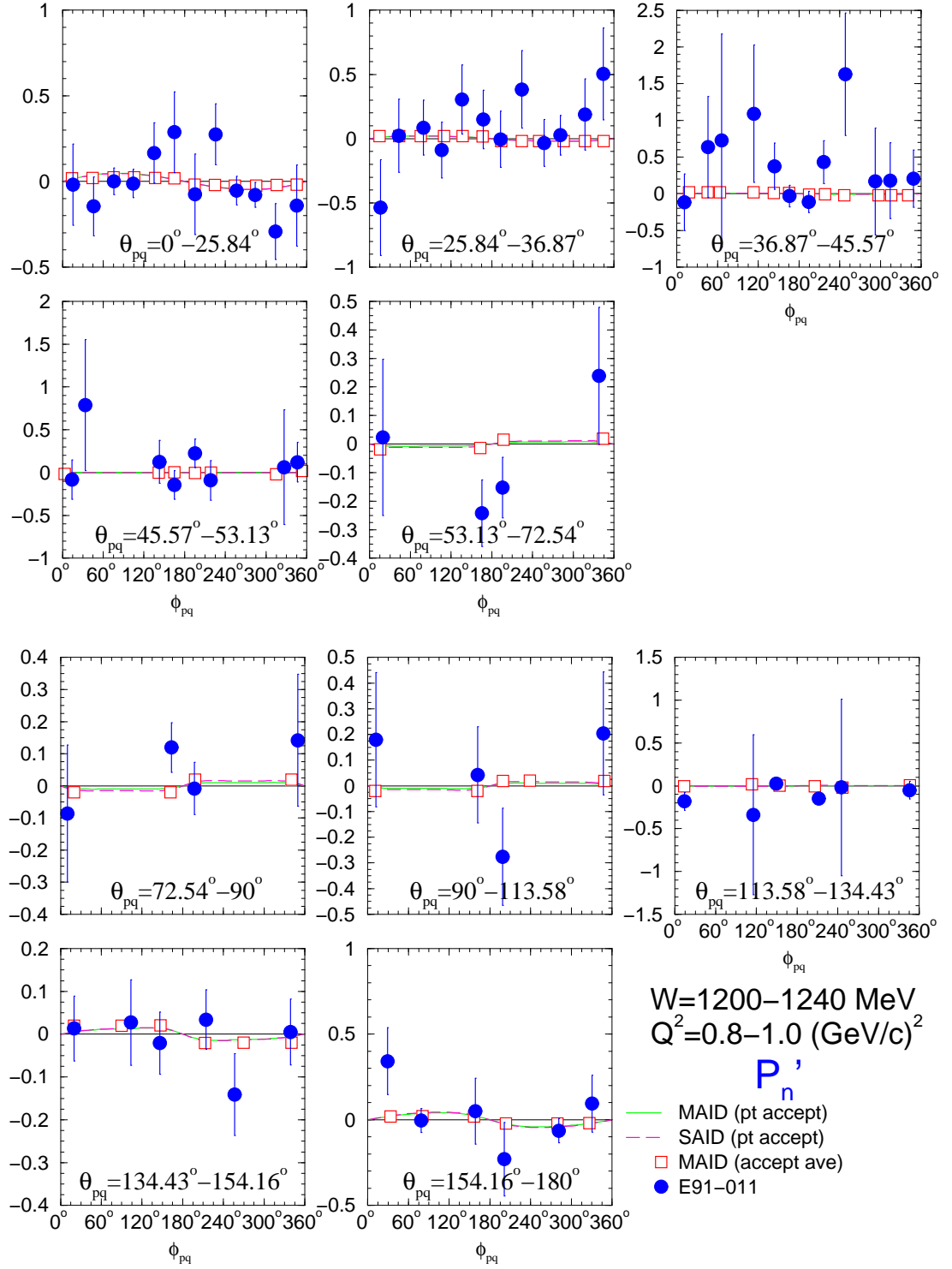


FIGURE 5.4.5. Target polarization  $P'_n$  for  $W = 1200-1240$  MeV and  $Q^2 = 0.8-1.0$  (GeV/c) $^2$ .

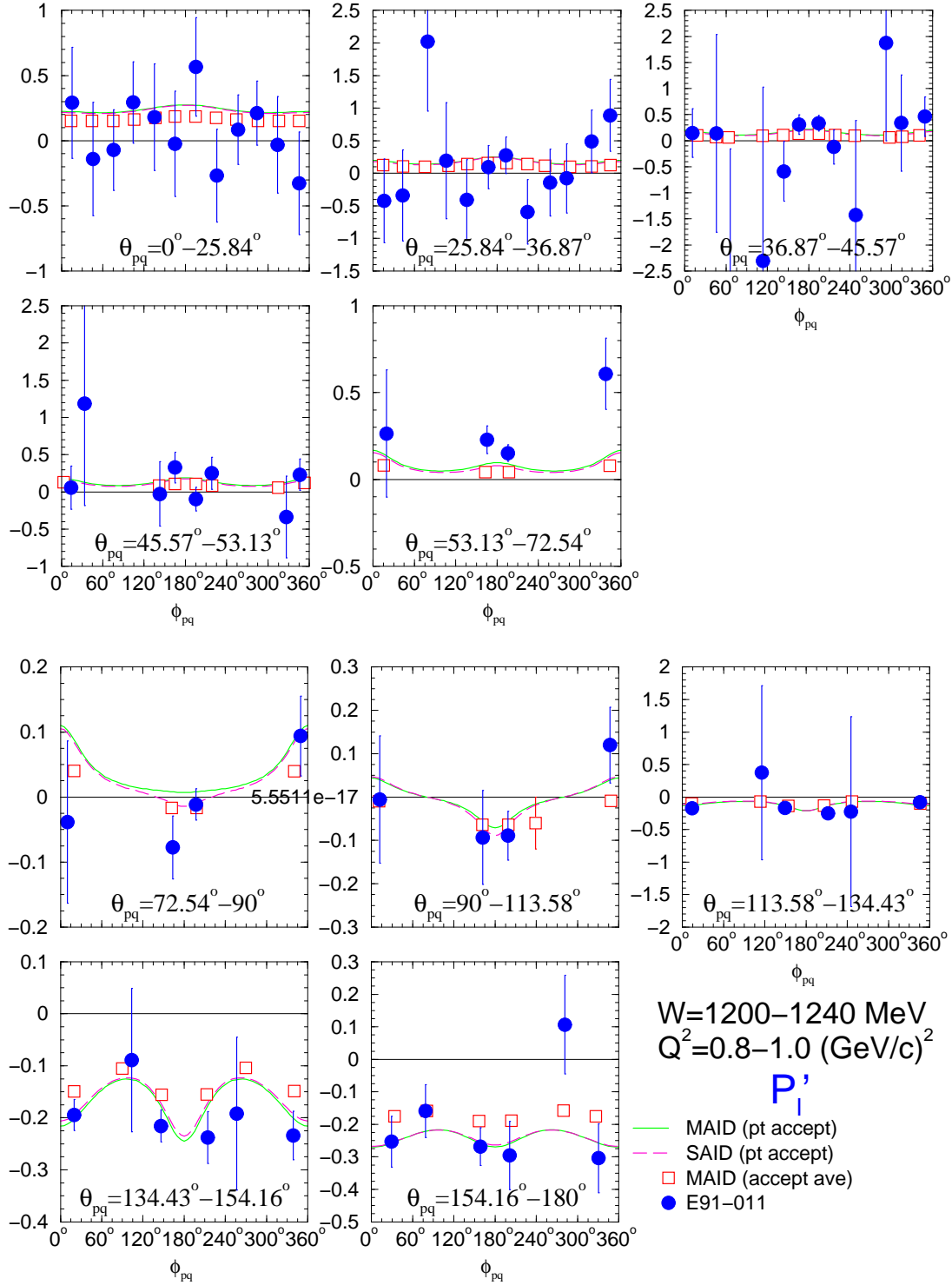
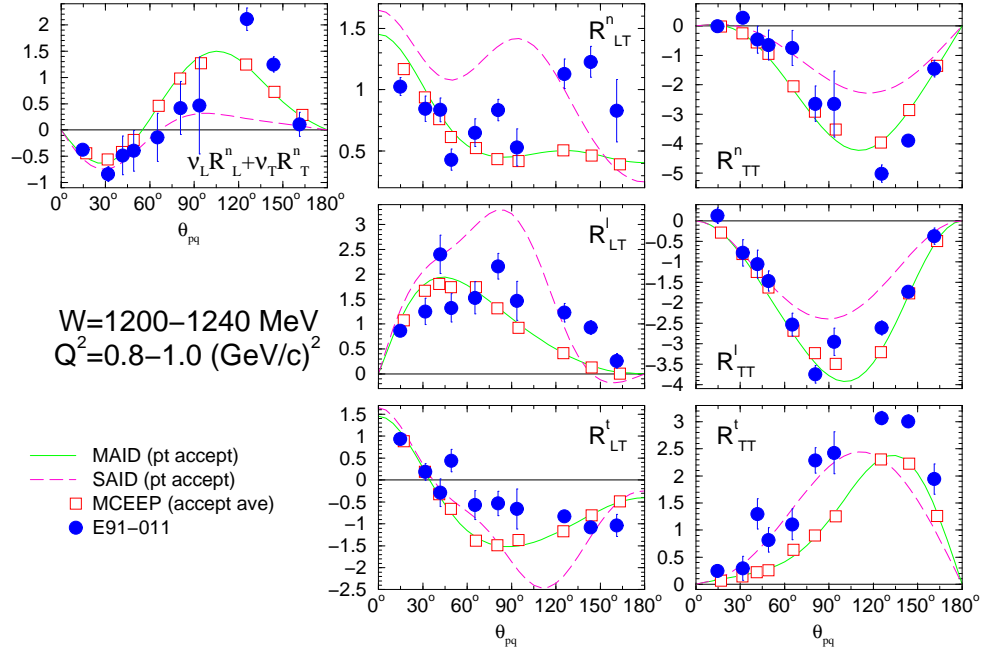
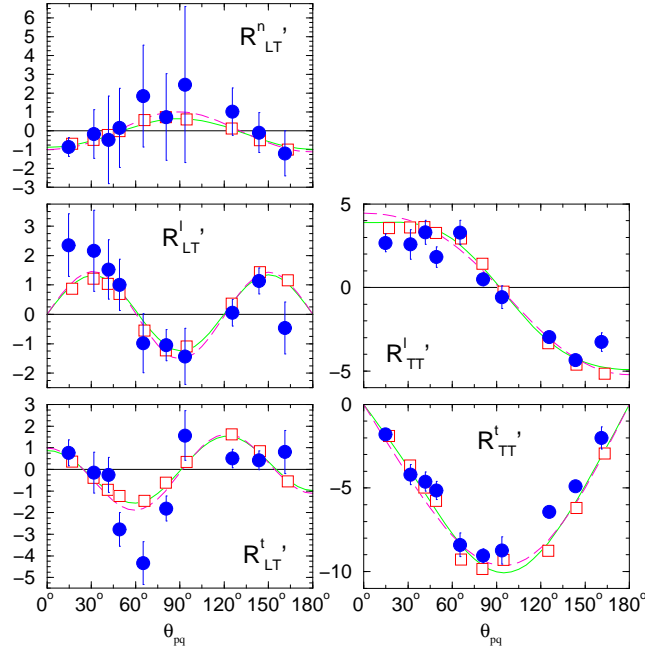


FIGURE 5.4.6. Target polarization  $P'_l$  for  $W = 1200-1240 \text{ MeV}$  and  $Q^2 = 0.8-1.0 \text{ (GeV/c)}^2$ .



(a) Helicity independent (induced) response functions.



(b) Helicity dependent (transferred) response functions.

FIGURE 5.5.1. Response functions for  $W = 1200-1240 \text{ MeV}$  and  $Q^2 = 0.8-1.0 \text{ (GeV/c)}^2$ .

MCEEP uses a uniform random sampling method to populate the experimental acceptance. Weights corresponding to the relevant observables (cross section, polarization, response function, etc.) are computed according to a certain user selected physics model, MAID in the case of this analysis. The reaction vertex (beam-target interaction point) is chosen at random to be somewhere inside the target volume. Then, an event is chosen by randomly selecting, somewhere in the experimental acceptance, a momentum, and in-plane and out-of-plane angles for both the scattered electron and recoil proton. As a result recoil polarization observables can be simulated, as well as cross sections. MCEEP uses a COSY spin matrix file to account for spin precession of the proton's polarization through the spectrometer (as discussed earlier in Section 4.5.2.4).

The MCEEP simulation also allows for calculation and inclusion of the radiative effects discussed in Section 5.3. This allows the most direct comparison of the MAID predictions with the measured data, since the data have also (naturally) experienced radiative effects. All MCEEP simulation results displayed in Figs. 5.4.1-5.5.1 have *included* these radiative effects.

Since MAID was used as the input cross section for the MCEEP simulation, the MCEEP results in Figs. 5.4.1-5.5.1 would fall along the line corresponding to the MAID “nominal kinematics” predictions, if the effects of acceptance averaging (and radiative effects) were small. It is seen from these figures that this is indeed mostly the case. There are discrepancies, however, between a few MCEEP helicity dependent polarizations and the nominal MAID prediction. There is some evidence that the discrepancies may arise because data from several different kinematic settings of the spectrometers are combined together for each single data point shown. This issue is currently under investigation, and can be resolved with more extensive study of the simulation results. If “acceptance effects” still remain after final study, “correction factors” will be applied to those few polarizations where discrepancies remain between MCEEP acceptance averaged and nominal predictions, in order to allow simple and direct comparison to “nominal kinematics” theory predictions.

**5.6.2. Models: MAID and SAID.** The helicity dependent observables ( $hP'_t, hP'_n, hP'_l, R'^n_{LT}, R'^l_{LT}, R'^t_{LT}, R'^l_{TT},$  and  $R'^t_{TT}$ ) are highly dominated by the imaginary parts of the  $M_{1+}, E_{1+},$  and  $S_{1+}$  amplitudes, which correspond to the  $\Delta$ -resonance excitation amplitudes (this can be inferred from Eqns. (1.4.9)-(1.4.21)). The fact that the two model predictions (MAID and SAID) for these helicity dependent observables are in very good agreement with each other (seen in Figs. 5.4.2, 5.4.4, 5.4.6, and 5.5.1(b)) is an indication that these multipoles are predicted to be nearly identical in the two model frameworks. The fact



that this data now also demonstrates good agreement with both of these models for all of the helicity dependent observables is a further confirmation that these  $\Delta$ -excitation amplitudes appear to be well-understood (at least, well constrained and described by both MAID and SAID).

On the other hand, the helicity independent observables ( $P_t, P_n, P_l, R_L^n, R_T^n, R_{LT}^n, R_{LT}^l, R_{TT}^n, R_{TT}^l, R_{TT}^t$ ) are driven by the real parts of the non-dominant multipoles - corresponding to the non-resonant amplitudes. These multipoles are clearly not well understood currently, as evidenced by the differences in predictions for these observables between MAID and SAID (see Figs. 5.4.1, 5.4.3, 5.4.5, and 5.5.1(a)). Further, the fact that this data shows marked deviation from either prediction for most of these observables confirms that modification to many of the multipole amplitudes will be required. The results from this analysis will be added to both the MAID and SAID databases in order to yield a better understanding of these non-resonant amplitudes.

## 5.7. Conclusion

Induced and transferred polarization observables and thirteen response functions for the  $p(\vec{e}, e'\vec{p})\pi^0$  reaction have been measured at a  $Q^2 = 1.0 \text{ (GeV}/c)^2$  and centered at the peak of the  $\Delta(1232)$  resonance. Twelve different kinematic settings were combined to give substantial coverage in both  $\theta_{pq}$  and  $\phi_{pq}$ . Both the polarizations and response functions were compared to two phenomenological models: MAID and SAID, based on previous world data. From these results, it is obvious that neither model is sufficient to completely describe the deformation of the proton structure since neither accurately reflects the non-resonant multipole amplitudes.

Further analysis is now underway to perform a full multipole expansion of the response functions. This analysis uses all polarization and response function data discussed in this thesis, along with all cross section data from the same experiment to simultaneously fit the angular distributions of all response functions. As a result, all corresponding individual multipole amplitudes will be extracted.



## APPENDIX A

### " $N \rightarrow \Delta$ " INTERNAL REPORT ON SPECTROMETER MISPOINTING

The determination of the mispointing of the Hall A High Resolution Spectrometers, both electron (HRSe) and hadron (HRSh), is accomplished using two different methods: (1) using a carbon pointing run and (2) using a script, called LVDT, to determine the offsets from the EPICS data in the CODA file.

For the carbon pointing runs the spectrometer mispointing was found using Eqn. (A.0.1):

$$p = -y_{tg} - z_{tg} \sin \theta + beam_x \cos \theta, \quad (\text{A.0.1})$$

where  $y_{tg}$  is the non-dispersive position at the scattering point of the target,  $z_{tg}$  is the position at the scattering point in the target along the beam (this value comes from a survey of the target and is shown in Tab. A.1),  $beam_x$  is the beam position at  $z = 0$  derived

TABLE A.1. Survey  $z_{tg}$  positions.

survey date	$z_{tg}$ (mm)	run numbers
May 16, 2000	$1.01 \pm 0.5$	1025-1340
May 26, 2000	$0.46 \pm 0.5$	1346-2688
June 30, 2000	$1.14 \pm 0.5$	2720-4040

from the bpm positions, and  $\theta$  is the spectrometer angle. For the HRSe  $\theta$  is entered as a positive value while HRSh angles are entered as negative values. Values for  $y_{tg}$  and  $beam_x$  were determined from histogram fits using some initial  $x$  and  $z$  offset values in the ESPACE header file. Examples of the  $y_{tg}$  and  $beam_x$  fits are shown in Figs. A.0.1(a) and (b). The mispointing for each spectrometer arm is then calculated using Eqn. (A.0.1), the  $y_{tg}$  value found from the paw fit, the  $z_{tg}$  survey position shown in Tab. A.1, the  $beam_x$  position found from the paw fit, and the spectrometer angle. From the mispointing and spectrometer angle, the spectrometer offsets in the  $x$  and  $z$  directions are determined by:

$$x = p \cos \theta \quad (\text{A.0.2})$$

$$z = -p \sin \theta. \quad (\text{A.0.3})$$

The carbon mispointing and offset values found were then compared to values found from running the LVDT. This script takes the spectrometer angle floor mark and vernier, combined with the CODA data file and determines the spectrometer mispointing and offsets.

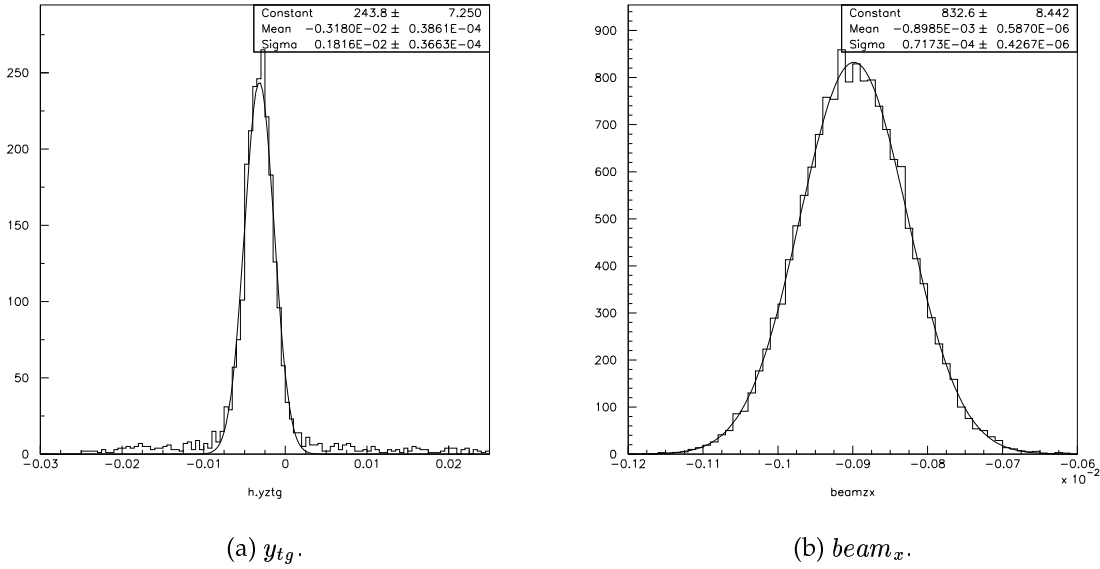
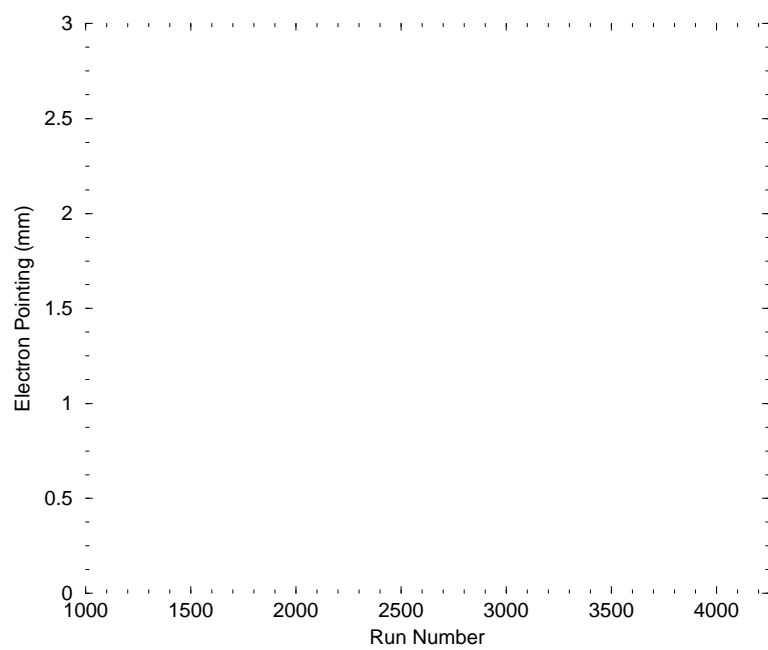
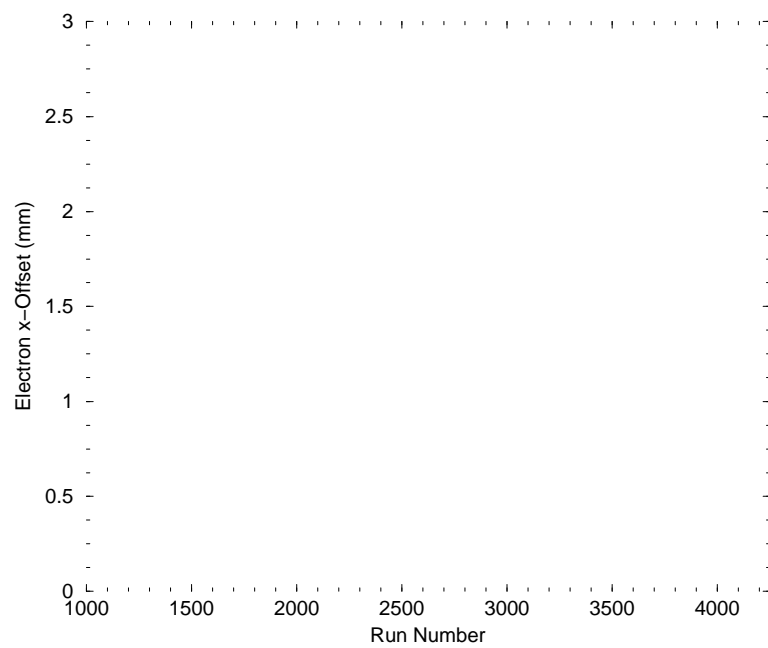


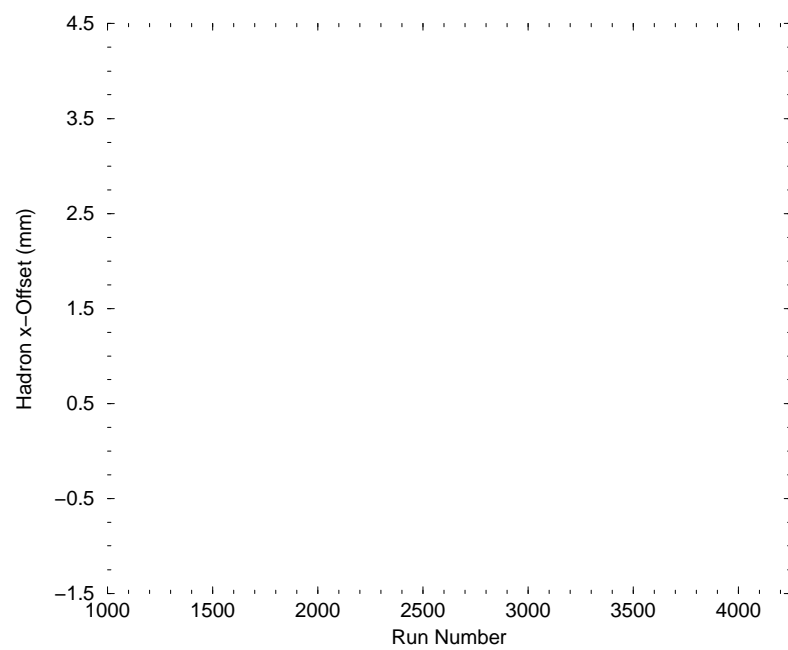
FIGURE A.0.1. Sample  $y_{tg}$  and  $beam_x$  plots from run 1216.

Comparisons of the mispointing and spectrometer  $x$  and  $z$  offsets for each spectrometer are shown in the following figures: Figs. A.0.2(a) and (b) show the electron and hadron arm spectrometer mispointing; Figs. A.0.3(a) and (b), and A.0.4(a) and (b) show the electron  $x$ - and  $z$ -offsets, and hadron  $x$ - and  $z$ -offsets, respectively, where the shaded regions represent offsets determined by spectrometer surveys. As you can see, both the mispointing values and the spectrometer offsets for the carbon pointing method, the LVDT method, and the surveys for the HRSe agree very well, but not so for the HRSh.

To determine which set of detector offsets, those found using the carbon pointing method versus those found from the LVDT calculation, should be used in the ESPACE header files for further analysis, ESPACE was rerun for each set of offsets. The  $react_z$  variable, the  $z$ -coordinate of the reaction point in the target, was determined by a histogram fit. An example of this  $react_z$  variable determination is shown in Fig. A.0.5. This







$react_z$  should be the same as the survey value for  $z_{tg}$ . Figs. A.0.6(a) and (b) show the  $react_z$  determined using the offsets found for both methods. The shaded region again represents the survey results and the associated errors. In both of these figures, it seems the spectrometer offsets found using the carbon pointing runs reproduces the  $z_{tg}$  position much better than the spectrometer offsets found using the LVDT script. Fig. A.0.7 shows the differences between the  $react_z$  position found in the electron and hadron arm analyses. You can see from this plot that the carbon pointing method gives consistent results for  $react_z$  from both spectrometer arms, while not so for the LVDT method. Run number 1760 was used to optimize the HRSe detector offsets used in the analysis database while run 2722 was used to optimize the offsets for the HRSh. The spectrometer offsets found using the carbon pointing method should therefore be used in further “ $N \rightarrow \Delta$ ” analysis.

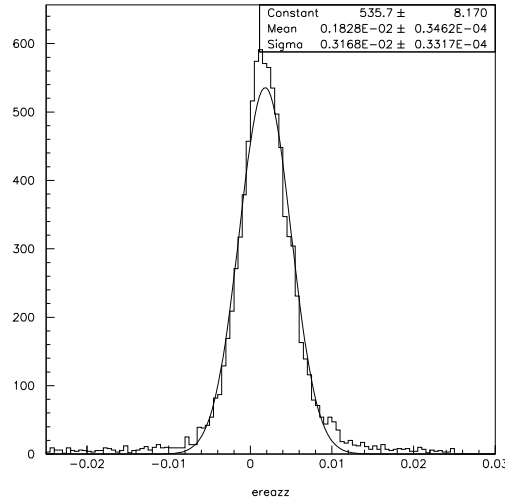
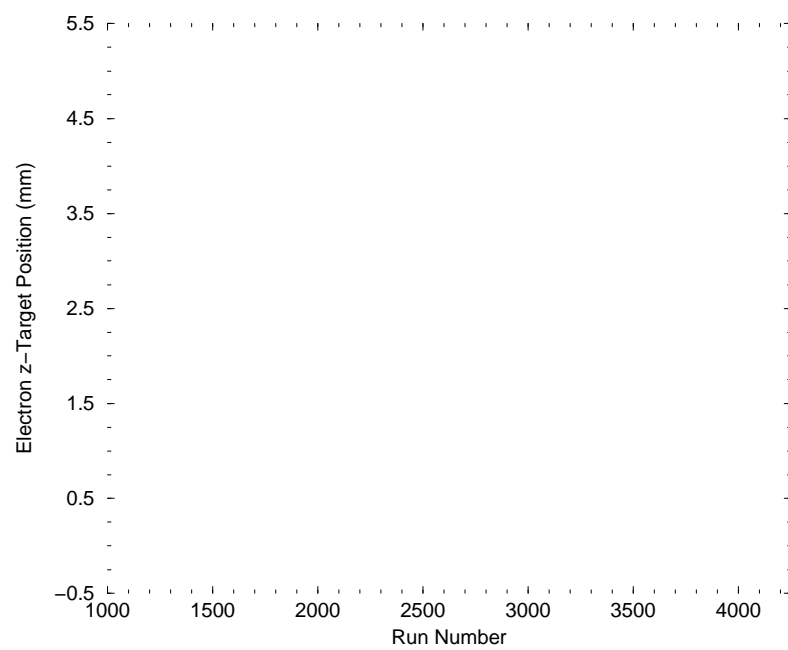


FIGURE A.0.5. Example of a plot of  $react_z$  from run 1216.

Tabs. A.2 and A.3 list the values for the electron and hadron arm mispointing for the carbon pointing method, the LVDT method, and the survey values. Tabs. A.4, A.5, A.6, and A.7 give the  $x$ - and  $z$ -offsets for the HRSe and HRSh, respectively. Tabs. A.8 and A.9 list the  $react_z$  position determined by both the carbon pointing and LVDT methods compared to survey.





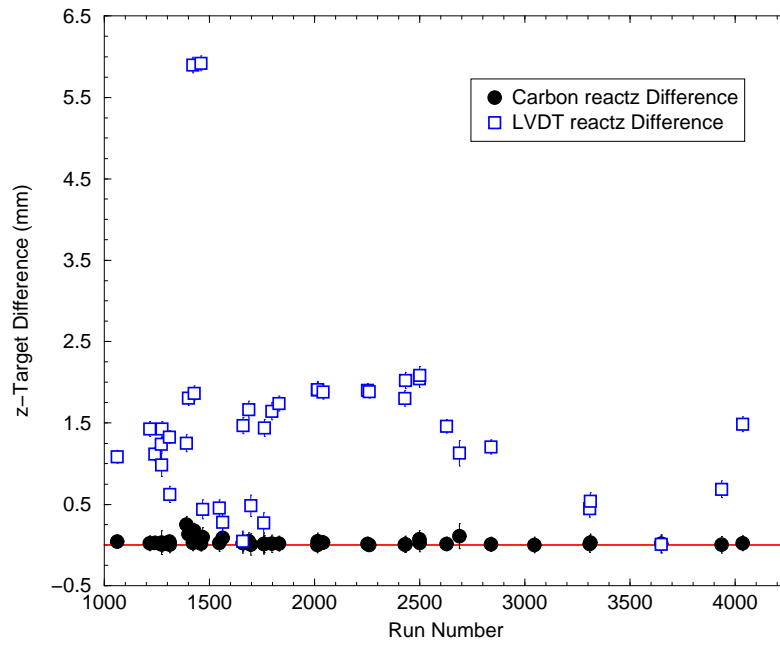


FIGURE A.0.7. Difference between electron and hadron arm  $react_z$  positions.

TABLE A.2. Electron arm mispointing (mm).

$\theta_{cm}$	run	carbon	LVDI	survey	$\theta_{cm}$	run	carbon	LVDI	survey
-	1061	2.281 $\pm$ 0.155	2.32	2.44 $\pm$ 0.50	-155°	1796	1.300 $\pm$ 0.122	1.18	1.19 $\pm$ 0.50
0°	1216	1.318 $\pm$ 0.122	1.22	-	-155°	1831	1.213 $\pm$ 0.122	1.11	1.19 $\pm$ 0.50
25°	1240	1.282 $\pm$ 0.122	1.19	-	-155°	2012	1.285 $\pm$ 0.122	1.15	1.19 $\pm$ 0.50
25°	1271	1.312 $\pm$ 0.122	1.20	-	-155°	2014	1.307 $\pm$ 0.122	1.15	1.19 $\pm$ 0.50
-25°	1273	1.300 $\pm$ 0.123	1.22	-	-135°	2041	1.296 $\pm$ 0.122	1.16	1.19 $\pm$ 0.50
-25°	1274	1.315 $\pm$ 0.122	1.22	-	-135°	2252	1.269 $\pm$ 0.122	1.18	1.19 $\pm$ 0.50
-25°	1310	1.327 $\pm$ 0.122	1.22	-	-90°	2260	1.263 $\pm$ 0.122	1.16	1.19 $\pm$ 0.50
50°	1311	1.267 $\pm$ 0.123	1.18	-	-90°	2429	1.252 $\pm$ 0.122	1.16	1.19 $\pm$ 0.50
50°	1390	1.160 $\pm$ 0.167	1.11	1.19 $\pm$ 0.50	-50°	2432	1.255 $\pm$ 0.122	1.15	1.19 $\pm$ 0.50
-50°	1399	1.182 $\pm$ 0.139	1.15	1.19 $\pm$ 0.50	-50°	2498	1.294 $\pm$ 0.122	1.16	1.19 $\pm$ 0.50
-50°	1420	1.254 $\pm$ 0.122	0.21	1.19 $\pm$ 0.50	0°	2500	1.277 $\pm$ 0.122	1.13	1.19 $\pm$ 0.50
-90°	1427	1.239 $\pm$ 0.146	1.17	1.19 $\pm$ 0.50	25°	2628	1.199 $\pm$ 0.122	1.13	1.19 $\pm$ 0.50
-90°	1459	1.283 $\pm$ 0.122	0.21	1.19 $\pm$ 0.50	-	2688	2.028 $\pm$ 0.156	2.02	1.91 $\pm$ 0.50
90°	1467	1.195 $\pm$ 0.144	1.09	1.19 $\pm$ 0.50	-	2722	-	1.77	-
90°	1547	1.203 $\pm$ 0.122	1.10	1.19 $\pm$ 0.50	50°	2838	0.660 $\pm$ 0.122	0.74	0.87 $\pm$ 0.50
135°	1562	1.204 $\pm$ 0.123	1.10	1.19 $\pm$ 0.50	90°	3046	0.665 $\pm$ 0.122	-	0.87 $\pm$ 0.50
135°	1658	1.240 $\pm$ 0.122	1.11	1.19 $\pm$ 0.50	135°	3308	0.618 $\pm$ 0.122	0.82	0.87 $\pm$ 0.50
-135°	1660	1.282 $\pm$ 0.122	1.18	1.19 $\pm$ 0.50	135°	3311	0.587 $\pm$ 0.122	0.82	0.87 $\pm$ 0.50
-135°	1687	1.294 $\pm$ 0.122	1.18	1.19 $\pm$ 0.50	155°	3648	0.653 $\pm$ 0.122	0.84	0.87 $\pm$ 0.50
155°	1696	1.237 $\pm$ 0.122	1.13	1.19 $\pm$ 0.50	180°	3936	0.701 $\pm$ 0.122	0.85	0.87 $\pm$ 0.50
155°	1758	1.237 $\pm$ 0.122	1.13	1.19 $\pm$ 0.50	-	4035	0.770 $\pm$ 0.122	0.89	0.87 $\pm$ 0.50
-155°	1761	1.282 $\pm$ 0.122	1.18	1.19 $\pm$ 0.50					

TABLE A.3. Hadron arm mispointing (mm).

$\theta_{cm}$	run	carbon	LVDt	survey	$\theta_{cm}$	run	carbon	LVDt	survey
-	1061	0.365 $\pm$ 0.368	1.22	1.09 $\pm$ 0.50	-155°	1796	0.052 $\pm$ 0.385	0.91	0.82 $\pm$ 0.50
0°	1216	-3.183 $\pm$ 0.339	-2.53	-	-155°	1831	-0.090 $\pm$ 0.383	0.93	0.82 $\pm$ 0.50
25°	1240	-3.442 $\pm$ 0.310	-3.00	-	-155°	2012	-0.146 $\pm$ 0.383	0.86	0.82 $\pm$ 0.50
25°	1271	-3.468 $\pm$ 0.309	-2.99	-	-155°	2014	-0.075 $\pm$ 0.383	0.87	0.82 $\pm$ 0.50
-25°	1273	0.466 $\pm$ 0.365	0.90	-	-135°	2041	-1.062 $\pm$ 0.404	0.00	-
-25°	1274	0.336 $\pm$ 0.364	1.08	-	-135°	2252	-1.195 $\pm$ 0.404	0.03	-
-25°	1310	0.428 $\pm$ 0.363	1.10	-	-90°	2260	-0.997 $\pm$ 0.410	0.21	-
50°	1311	-3.563 $\pm$ 0.282	-3.43	-	-90°	2429	-0.891 $\pm$ 0.410	0.25	-
50°	1390	-3.845 $\pm$ 0.285	-3.41	-	-50°	2432	-3.676 $\pm$ 0.386	-2.45	-
-50°	1399	-0.683 $\pm$ 0.386	0.48	-	-50°	2498	-3.655 $\pm$ 0.387	-2.54	-
-50°	1420	-0.680 $\pm$ 0.387	1.50	-	0°	2500	-3.879 $\pm$ 0.340	-2.91	-
-90°	1427	-0.358 $\pm$ 0.410	0.78	-	25°	2628	-3.812 $\pm$ 0.310	-3.09	-
-90°	1459	-0.355 $\pm$ 0.411	0.82	-	-	2688	-2.907 $\pm$ 0.373	0.48	0.34 $\pm$ 0.50
90°	1467	-3.666 $\pm$ 0.251	-3.71	-	-	2722	-1.194 $\pm$ 0.143	-1.26	-1.15 $\pm$ 0.50
90°	1547	-3.692 $\pm$ 0.250	-3.69	-	50°	2838	-4.813 $\pm$ 0.283	-3.95	-
135°	1562	-2.902 $\pm$ 0.258	-3.03	-	90°	3046	-4.179 $\pm$ 0.249	-3.90	-
135°	1658	-2.856 $\pm$ 0.259	-3.12	-	135°	3308	-3.271 $\pm$ 0.258	-3.06	-
-135°	1660	-0.403 $\pm$ 0.406	0.49	-	135°	3311	-3.262 $\pm$ 0.258	-3.05	-
-135°	1687	-0.439 $\pm$ 0.405	0.55	-	155°	3648	-0.120 $\pm$ 0.285	0.32	-
155°	1696	-3.418 $\pm$ 0.289	-3.38	-	180°	3936	-0.611 $\pm$ 0.339	0.28	-
155°	1758	-3.303 $\pm$ 0.289	-3.40	-	-	4035	-1.000 $\pm$ 0.408	0.62	0.90 $\pm$ 0.50
-155°	1761	0.027 $\pm$ 0.384	0.81	0.82 $\pm$ 0.50					

TABLE A.4. Electron arm spectrometer  $x$ -offsets (mm).

$\theta_{cm}$	run	carbon $x$	LVDT $x$	survey $x$	$\theta_{cm}$	run	carbon $x$	LVDT $x$	survey $x$
-	1061	2.17±0.15	2.207	2.32±0.48	-155°	1796	1.26±0.12	1.143	1.15±0.49
0°	1216	1.28±0.12	1.180	-	-155°	1831	1.18±0.12	1.081	1.15±0.49
25°	1240	1.24±0.12	1.156	-	-155°	2012	1.25±0.12	1.112	1.15±0.49
25°	1271	1.27±0.12	1.162	-	-155°	2014	1.27±0.12	1.111	1.15±0.49
-25°	1273	1.26±0.12	1.185	-	-135°	2041	1.26±0.12	1.123	1.15±0.49
-25°	1274	1.28±0.12	1.185	-	-135°	2252	1.23±0.12	1.140	1.15±0.49
-25°	1310	1.29±0.12	1.188	-	-90°	2260	1.22±0.12	1.125	1.15±0.49
50°	1311	1.23±0.12	1.142	-	-90°	2429	1.21±0.12	1.122	1.15±0.49
50°	1390	1.13±0.16	1.079	1.15±0.49	-50°	2432	1.22±0.12	1.118	1.15±0.49
-50°	1399	1.15±0.14	1.114	1.15±0.49	-50°	2498	1.25±0.12	1.126	1.15±0.49
-50°	1420	1.22±0.12	0.201	1.15±0.49	0°	2500	1.24±0.12	1.097	1.15±0.49
-90°	1427	1.20±0.14	1.132	1.15±0.49	25°	2628	1.16±0.12	1.095	1.15±0.49
-90°	1459	1.24±0.12	0.208	1.15±0.49	-	2688	1.93±0.15	1.922	1.82±0.48
90°	1467	1.16±0.14	1.059	1.15±0.49	-	2722	-	0.965	-
90°	1547	1.17±0.12	1.070	1.15±0.49	50°	2838	0.640±0.118	0.720	0.84±0.49
135°	1562	1.17±0.12	1.068	1.15±0.49	90°	3046	0.645±0.119	-	0.84±0.49
135°	1658	1.20±0.12	1.073	1.15±0.49	135°	3308	0.599±0.118	0.798	0.84±0.49
-135°	1660	1.24±0.12	1.144	1.15±0.49	135°	3311	0.569±0.118	0.798	0.84±0.49
-135°	1687	1.26±0.12	1.147	1.15±0.49	155°	3648	0.633±0.118	0.810	0.84±0.49
155°	1696	1.20±0.12	1.099	1.15±0.49	180°	3936	0.680±0.118	0.828	0.84±0.49
155°	1758	1.20±0.12	1.101	1.15±0.49	-	4035	0.747±0.118	0.868	0.84±0.49
-155°	1761	1.24±0.12	1.141	1.15±0.49					

TABLE A.5. Electron arm spectrometer  $z$ -offsets (mm).

$\theta_{cm}$	run	carbon $z$	LVD $\Gamma$ $z$	survey $z$	$\theta_{cm}$	run	carbon $z$	LVD $\Gamma$ $z$	survey $z$
-	1061	-0.707 $\pm$ 0.048	-0.721	-0.76 $\pm$ 0.16	-155°	1796	-0.316 $\pm$ 0.030	-0.287	-0.29 $\pm$ 0.12
0°	1216	-0.321 $\pm$ 0.030	-0.296	-	-155°	1831	-0.295 $\pm$ 0.030	-0.271	-0.29 $\pm$ 0.12
25°	1240	-0.312 $\pm$ 0.030	-0.721	-	-155°	2012	-0.312 $\pm$ 0.030	-0.279	-0.29 $\pm$ 0.12
25°	1271	-0.319 $\pm$ 0.030	-0.292	-	-155°	2014	-0.318 $\pm$ 0.030	-0.279	-0.29 $\pm$ 0.12
-25°	1273	-0.316 $\pm$ 0.030	-0.298	-	-135°	2041	-0.315 $\pm$ 0.030	-0.282	-0.29 $\pm$ 0.12
-25°	1274	-0.320 $\pm$ 0.030	-0.298	-	-135°	2252	-0.309 $\pm$ 0.030	-0.286	-0.29 $\pm$ 0.12
-25°	1310	-0.323 $\pm$ 0.030	-0.298	-	-90°	2260	-0.307 $\pm$ 0.030	-0.283	-0.29 $\pm$ 0.12
50°	1311	-0.308 $\pm$ 0.030	-0.287	-	-90°	2429	-0.304 $\pm$ 0.030	-0.282	-0.29 $\pm$ 0.12
50°	1390	-0.282 $\pm$ 0.041	-0.271	-0.29 $\pm$ 0.12	-50°	2432	-0.305 $\pm$ 0.030	-0.281	-0.29 $\pm$ 0.12
-50°	1399	-0.287 $\pm$ 0.034	-0.280	-0.29 $\pm$ 0.12	-50°	2498	-0.315 $\pm$ 0.030	-0.283	-0.29 $\pm$ 0.12
-50°	1420	-0.305 $\pm$ 0.030	-0.050	-0.29 $\pm$ 0.12	0°	2500	-0.311 $\pm$ 0.030	-0.276	-0.29 $\pm$ 0.12
-90°	1427	-0.301 $\pm$ 0.036	-0.284	-0.29 $\pm$ 0.12	25°	2628	-0.292 $\pm$ 0.030	-0.275	-0.29 $\pm$ 0.12
-90°	1459	-0.312 $\pm$ 0.030	-0.052	-0.29 $\pm$ 0.12	-	2688	-0.629 $\pm$ 0.048	-0.628	-0.59 $\pm$ 0.16
90°	1467	-0.291 $\pm$ 0.035	-0.266	-0.29 $\pm$ 0.12	-	2722	-	-1.478	-
90°	1547	-0.293 $\pm$ 0.030	-0.269	-0.29 $\pm$ 0.12	50°	2838	-0.161 $\pm$ 0.030	-0.181	-0.21 $\pm$ 0.12
135°	1562	-0.293 $\pm$ 0.030	-0.268	-0.29 $\pm$ 0.12	90°	3046	-0.162 $\pm$ 0.030	-	-0.21 $\pm$ 0.12
135°	1658	-0.302 $\pm$ 0.030	-0.270	-0.29 $\pm$ 0.12	135°	3308	-0.150 $\pm$ 0.030	-0.200	-0.21 $\pm$ 0.12
-135°	1660	-0.312 $\pm$ 0.030	-0.287	-0.29 $\pm$ 0.12	135°	3311	-0.143 $\pm$ 0.030	-0.200	-0.21 $\pm$ 0.12
-135°	1687	-0.315 $\pm$ 0.030	-0.288	-0.29 $\pm$ 0.12	155°	3648	-0.159 $\pm$ 0.030	-0.203	-0.21 $\pm$ 0.12
155°	1696	-0.301 $\pm$ 0.030	-0.276	-0.29 $\pm$ 0.12	180°	3936	-0.171 $\pm$ 0.030	-0.208	-0.21 $\pm$ 0.12
155°	1758	-0.301 $\pm$ 0.030	-0.276	-0.29 $\pm$ 0.12	-	4035	-0.187 $\pm$ 0.030	-0.218	-0.21 $\pm$ 0.12
-155°	1761	-0.312 $\pm$ 0.030	-0.287	-0.29 $\pm$ 0.12					

TABLE A.6. Hadron arm spectrometer  $x$ -offsets (mm).

$\theta_{cm}$	run	carbon $x$	LVD T $x$	survey $x$	$\theta_{cm}$	run	carbon $x$	LVD T $x$	survey $x$
-	1061	-0.248 $\pm$ 0.250	-0.829	-0.74 $\pm$ 0.34	-155°	1796	-0.033 $\pm$ 0.249	-0.589	-0.53 $\pm$ 0.32
0°	1216	2.35 $\pm$ 0.25	1.868	-	-155°	1831	0.058 $\pm$ 0.247	-0.601	-0.53 $\pm$ 0.32
25°	1240	2.71 $\pm$ 0.24	2.364	-	-155°	2012	0.094 $\pm$ 0.248	-0.558	-0.53 $\pm$ 0.32
25°	1271	2.73 $\pm$ 0.24	2.356	-	-155°	2014	0.049 $\pm$ 0.248	-0.564	-0.53 $\pm$ 0.32
-25°	1273	-0.322 $\pm$ 0.252	-0.618	-	-135°	2041	0.630 $\pm$ 0.240	0.002	-
-25°	1274	-0.232 $\pm$ 0.252	-0.748	-	-135°	2252	0.708 $\pm$ 0.239	-0.019	-
-25°	1310	-0.296 $\pm$ 0.250	-0.761	-	-90°	2260	0.575 $\pm$ 0.237	-0.120	-
50°	1311	2.94 $\pm$ 0.23	2.835	-	-90°	2429	0.514 $\pm$ 0.236	-0.145	-
50°	1390	3.18 $\pm$ 0.24	2.818	-	-50°	2432	2.35 $\pm$ 0.25	1.572	-
-50°	1399	0.438 $\pm$ 0.247	-0.306	-	-50°	2498	2.34 $\pm$ 0.25	1.629	-
-50°	1420	0.436 $\pm$ 0.248	-0.319	-	0°	2500	2.87 $\pm$ 0.25	2.152	-
-90°	1427	0.206 $\pm$ 0.236	-0.449	-	25°	2628	3.00 $\pm$ 0.24	2.432	-
-90°	1459	0.204 $\pm$ 0.237	-0.475	-	-	2688	0.198 $\pm$ 0.254	-0.326	-0.23 $\pm$ 0.34
90°	1467	3.18 $\pm$ 0.22	3.222	-	-	2722	1.15 $\pm$ 0.14	1.208	1.11 $\pm$ 0.48
90°	1547	3.20 $\pm$ 0.22	3.201	-	50°	2838	3.98 $\pm$ 0.23	3.262	-
135°	1562	2.49 $\pm$ 0.22	2.603	-	90°	3046	3.63 $\pm$ 0.22	3.382	-
135°	1658	2.45 $\pm$ 0.22	2.681	-	135°	3308	2.81 $\pm$ 0.22	2.626	-
-135°	1660	0.239 $\pm$ 0.241	-0.288	-	135°	3311	2.80 $\pm$ 0.22	2.616	-
-135°	1687	0.260 $\pm$ 0.240	-0.325	-	155°	3648	0.099 $\pm$ 0.235	-0.265	-
155°	1696	2.81 $\pm$ 0.24	2.779	-	180°	3936	0.452 $\pm$ 0.251	-0.210	-
155°	1758	2.71 $\pm$ 0.24	2.797	-	-	4035	0.585 $\pm$ 0.239	-0.361	-0.53 $\pm$ 0.29
-155°	1761	-0.018 $\pm$ 0.248	-0.521	-0.53 $\pm$ 0.32					

TABLE A.7. Hadron arm spectrometer  $z$ -offsets (mm).

$\theta_{cm}$	run	carbon $z$	LVD $\Gamma$ $z$	survey $z$	$\theta_{cm}$	run	carbon $z$	LVD $\Gamma$ $z$	survey $z$
-	1061	-0.267 $\pm$ 0.269	-0.892	-0.80 $\pm$ 0.37	-155°	1796	-0.039 $\pm$ 0.293	-0.695	-0.63 $\pm$ 0.38
0°	1216	2.14 $\pm$ 0.23	1.700	-	-155°	1831	0.069 $\pm$ 0.292	-0.710	-0.63 $\pm$ 0.38
25°	1240	2.12 $\pm$ 0.19	1.854	-	-155°	2012	0.111 $\pm$ 0.292	-0.659	-0.63 $\pm$ 0.38
25°	1271	2.14 $\pm$ 0.19	1.847	-	-155°	2014	0.006 $\pm$ 0.292	-0.666	-0.63 $\pm$ 0.38
-25°	1273	-0.337 $\pm$ 0.264	-0.648	-	-135°	2041	0.855 $\pm$ 0.325	0.003	-
-25°	1274	-0.243 $\pm$ 0.263	-0.783	-	-135°	2252	0.962 $\pm$ 0.325	-0.026	-
-25°	1310	-0.310 $\pm$ 0.262	-0.797	-	-90°	2260	0.815 $\pm$ 0.335	-0.170	-
50°	1311	2.01 $\pm$ 0.16	1.932	-	-90°	2429	0.728 $\pm$ 0.335	-0.205	-
50°	1390	2.17 $\pm$ 0.16	1.902	-	-50°	2432	2.82 $\pm$ 0.30	1.884	-
-50°	1399	0.525 $\pm$ 0.296	-0.367	-	-50°	2498	2.81 $\pm$ 0.30	1.954	-
-50°	1420	0.522 $\pm$ 0.297	-0.382	-	0°	2500	2.61 $\pm$ 0.23	1.957	-
-90°	1427	0.292 $\pm$ 0.335	-0.636	-	25°	2628	2.35 $\pm$ 0.19	1.907	-
-90°	1459	0.290 $\pm$ 0.336	-0.673	-	-	2688	0.213 $\pm$ 0.273	-0.351	-0.25 $\pm$ 0.37
90°	1467	1.82 $\pm$ 0.13	1.845	-	-	2722	0.329 $\pm$ 0.039	0.346	0.32 $\pm$ 0.14
90°	1547	1.84 $\pm$ 0.12	1.833	-	50°	2838	2.71 $\pm$ 0.16	2.223	-
135°	1562	1.49 $\pm$ 0.13	1.551	-	90°	3046	2.08 $\pm$ 0.12	1.937	-
135°	1658	1.46 $\pm$ 0.13	1.598	-	135°	3308	1.68 $\pm$ 0.13	1.565	-
-135°	1660	0.325 $\pm$ 0.327	-0.392	-	135°	3311	1.67 $\pm$ 0.13	1.559	-
-135°	1687	0.353 $\pm$ 0.326	-0.441	-	155°	3648	0.068 $\pm$ 0.162	-0.184	-
155°	1696	1.95 $\pm$ 0.17	1.925	-	180°	3936	0.411 $\pm$ 0.228	-0.191	-
155°	1758	1.88 $\pm$ 0.16	1.938	-	-	4035	0.811 $\pm$ 0.331	-0.500	-0.73 $\pm$ 0.41
-155°	1761	-0.021 $\pm$ 0.293	-0.616	-0.63 $\pm$ 0.38					



TABLE A.8. Electron arm  $react_z$  positions and survey  $z_{tg}$  (mm).

$\theta_{cm}$	run	carbon	LVDT	$z_{tg}$	$\theta_{cm}$	run	carbon	LVDT	$z_{tg}$
-	1061	1.001 $\pm$ 0.032	0.876 $\pm$ 0.032	1.01 $\pm$ 0.50	-155°	1796	0.447 $\pm$ 0.043	0.958 $\pm$ 0.043	0.46 $\pm$ 0.50
0°	1216	1.006 $\pm$ 0.035	1.436 $\pm$ 0.035	1.01 $\pm$ 0.50	-155°	1831	0.433 $\pm$ 0.050	0.857 $\pm$ 0.049	0.46 $\pm$ 0.50
25°	1240	1.036 $\pm$ 0.040	1.409 $\pm$ 0.040	1.01 $\pm$ 0.50	-155°	2012	0.460 $\pm$ 0.045	1.039 $\pm$ 0.045	0.46 $\pm$ 0.50
25°	1271	0.994 $\pm$ 0.050	1.470 $\pm$ 0.050	1.01 $\pm$ 0.50	-155°	2014	0.456 $\pm$ 0.055	1.128 $\pm$ 0.054	0.46 $\pm$ 0.50
-25°	1273	1.020 $\pm$ 0.076	1.351 $\pm$ 0.076	1.01 $\pm$ 0.50	-135°	2041	0.432 $\pm$ 0.045	1.034 $\pm$ 0.045	0.46 $\pm$ 0.50
-25°	1274	1.003 $\pm$ 0.033	1.405 $\pm$ 0.033	1.01 $\pm$ 0.50	-135°	2252	0.456 $\pm$ 0.043	0.845 $\pm$ 0.043	0.46 $\pm$ 0.50
-25°	1310	0.957 $\pm$ 0.040	1.398 $\pm$ 0.040	1.01 $\pm$ 0.50	-90°	2260	0.471 $\pm$ 0.034	0.881 $\pm$ 0.034	0.46 $\pm$ 0.50
50°	1311	0.992 $\pm$ 0.065	1.384 $\pm$ 0.065	1.01 $\pm$ 0.50	-90°	2429	0.457 $\pm$ 0.055	0.846 $\pm$ 0.055	0.46 $\pm$ 0.50
50°	1390	0.555 $\pm$ 0.052	0.770 $\pm$ 0.052	0.46 $\pm$ 0.50	-50°	2432	0.444 $\pm$ 0.049	0.875 $\pm$ 0.049	0.46 $\pm$ 0.50
-50°	1399	0.561 $\pm$ 0.054	0.720 $\pm$ 0.054	0.46 $\pm$ 0.50	-50°	2498	0.486 $\pm$ 0.040	1.023 $\pm$ 0.040	0.46 $\pm$ 0.50
-50°	1420	0.429 $\pm$ 0.034	4.830 $\pm$ 0.034	0.46 $\pm$ 0.50	0°	2500	0.427 $\pm$ 0.041	1.064 $\pm$ 0.041	0.46 $\pm$ 0.50
-90°	1427	0.588 $\pm$ 0.052	0.889 $\pm$ 0.052	0.46 $\pm$ 0.50	25°	2628	0.439 $\pm$ 0.034	0.714 $\pm$ 0.034	0.46 $\pm$ 0.50
-90°	1459	0.468 $\pm$ 0.036	4.939 $\pm$ 0.036	0.46 $\pm$ 0.50	-	2688	0.441 $\pm$ 0.052	0.453 $\pm$ 0.052	0.46 $\pm$ 0.50
90°	1467	0.489 $\pm$ 0.065	0.917 $\pm$ 0.065	0.46 $\pm$ 0.50	-	2722	-	-	1.14 $\pm$ 0.50
90°	1547	0.455 $\pm$ 0.044	0.879 $\pm$ 0.044	0.46 $\pm$ 0.50	50°	2838	1.127 $\pm$ 0.039	0.785 $\pm$ 0.039	1.14 $\pm$ 0.50
135°	1562	0.434 $\pm$ 0.062	0.878 $\pm$ 0.062	0.46 $\pm$ 0.50	90°	3046	1.138 $\pm$ 0.054	-	1.14 $\pm$ 0.50
135°	1658	0.478 $\pm$ 0.056	1.031 $\pm$ 0.055	0.46 $\pm$ 0.50	135°	3308	1.106 $\pm$ 0.046	0.267 $\pm$ 0.046	1.14 $\pm$ 0.50
-135°	1660	0.445 $\pm$ 0.040	0.859 $\pm$ 0.040	0.46 $\pm$ 0.50	135°	3311	1.152 $\pm$ 0.047	0.160 $\pm$ 0.047	1.14 $\pm$ 0.50
-135°	1687	0.403 $\pm$ 0.051	0.897 $\pm$ 0.051	0.46 $\pm$ 0.50	155°	3648	1.114 $\pm$ 0.042	0.352 $\pm$ 0.042	1.14 $\pm$ 0.50
155°	1696	0.460 $\pm$ 0.045	0.888 $\pm$ 0.045	0.46 $\pm$ 0.50	180°	3936	1.150 $\pm$ 0.045	0.509 $\pm$ 0.044	1.14 $\pm$ 0.50
155°	1758	0.456 $\pm$ 0.043	0.873 $\pm$ 0.043	0.46 $\pm$ 0.50	-	4035	1.147 $\pm$ 0.038	0.616 $\pm$ 0.038	1.14 $\pm$ 0.50
-155°	1761	0.459 $\pm$ 0.044	0.891 $\pm$ 0.044	0.46 $\pm$ 0.50					

TABLE A.9. Hadron arm  $react_z$  positions and survey  $z_{tg}$  (mm).

$\theta_{cm}$	run	carbon	LVDI	$z_{tg}$	$\theta_{cm}$	run	carbon	LVDI	$z_{tg}$
-	1061	0.958±0.046	-0.210±0.046	1.01±0.50	-155°	1796	0.465±0.063	-0.686±0.064	0.46±0.50
0°	1216	0.984±0.057	0.010±0.057	1.01±0.50	-155°	1831	0.453±0.041	-0.883±0.041	0.46±0.50
25°	1240	1.007±0.041	0.291±0.041	1.01±0.50	-155°	2012	0.457±0.050	-0.869±0.050	0.46±0.50
25°	1271	1.006±0.034	0.232±0.034	1.01±0.50	-155°	2014	0.408±0.043	-0.782±0.043	0.46±0.50
-25°	1273	0.989±0.069	0.364±0.069	1.01±0.50	-135°	2041	0.464±0.041	-0.846±0.041	0.46±0.50
-25°	1274	1.012±0.060	-0.021±0.060	1.01±0.50	-135°	2252	0.471±0.039	-1.056±0.039	0.46±0.50
-25°	1310	1.001±0.036	0.070±0.037	1.01±0.50	-90°	2260	0.471±0.045	-1.004±0.045	0.46±0.50
50°	1311	0.998±0.035	0.759±0.035	1.01±0.50	-90°	2429	0.452±0.040	-0.955±0.041	0.46±0.50
50°	1390	0.304±0.051	-0.482±0.051	0.46±0.50	-50°	2432	0.435±0.051	-1.146±0.051	0.46±0.50
-50°	1399	0.424±0.039	-1.089±0.039	0.46±0.50	-50°	2498	0.413±0.064	-1.021±0.065	0.46±0.50
-50°	1420	0.457±0.062	-1.070±0.062	0.46±0.50	0°	2500	0.400±0.066	-1.021±0.067	0.46±0.50
-90°	1427	0.412±0.040	-0.976±0.040	0.46±0.50	25°	2628	0.426±0.049	-0.747±0.049	0.46±0.50
-90°	1459	0.449±0.056	-0.980±0.056	0.46±0.50	-	2688	0.330±0.101	-0.677±0.102	0.46±0.50
90°	1467	0.390±0.051	0.479±0.051	0.46±0.50	-	2722	0.987±0.129	1.086±0.111	1.14±0.50
90°	1547	0.429±0.058	0.424±0.058	0.46±0.50	50°	2838	1.139±0.048	-0.420±0.048	1.14±0.50
135°	1562	0.344±0.064	0.595±0.064	0.46±0.50	90°	3046	1.135±0.042	0.556±0.042	1.14±0.50
135°	1658	0.452±0.070	0.982±0.070	0.46±0.50	135°	3308	1.119±0.056	0.714±0.056	1.14±0.50
-135°	1660	0.474±0.059	-0.609±0.060	0.46±0.50	135°	3311	1.118±0.055	0.700±0.055	1.14±0.50
-135°	1687	0.453±0.052	-0.768±0.052	0.46±0.50	155°	3648	1.131±0.068	0.342±0.067	1.14±0.50
155°	1696	0.451±0.088	0.405±0.088	0.46±0.50	180°	3936	1.145±0.059	-0.177±0.058	1.14±0.50
155°	1758	0.442±0.081	0.598±0.081	0.46±0.50	-	4035	1.124±0.053	-0.870±0.054	1.14±0.50
-155°	1761	0.472±0.061	-0.550±0.061	0.46±0.50					

## APPENDIX B

### LIST OF COMPLETED RUNS FOR “ $N \rightarrow \Delta$ ”

#### B.1. May 19 - June 5 Run Period

run	comment
1019-1024	harp

##### B.1.1. Hadron Arm Optics Check<sup>1</sup>.

run	prescales	$p_h$	$\theta_h$	$p_e$	$\theta_e$	target	h/e coll	comment
1025	1,1,1,1, $\infty$	1.7820	47.087	3.6597	18.065	12C	6/sv	wrong e Q2
1026						4dum		wrong e Q2
1027						15dum		wrong e Q2
1028						10dum		wrong e Q2
1029						12C	6/6	wrong e Q2
1030						15dum		wrong e Q2
1031						10dum		wrong e Q2
1032						4dum		wrong e Q2
1033		0.0000				LH2	sv/sv	rast 0.5*0.5 hrsh fld chng redo hrse opt
1034		0.5222				12C		no rast
1035-1036		0.0000				4dum		
1037						4dum		rast 0.5*0.5

<sup>1</sup>Throughout this appendix,  $\infty$  represents 65535 - the highest used prescale setting in Hall A; 6 = 6 collimator, op = op collimator, sv = sv slit collimator; 4dum = 4 cm dummy target, 10dum = 10 cm dummy target, 15dum = 15 cm dummy, LH2 = 15 cm LH2 target.

run	prescales	$p_h$	$\theta_h$	$p_e$	$\theta_e$	target	h/e coll	comment
1038	1,1,1,1, $\infty$	1.0383	47.087	3.6597	18.065	15dum	sv/sv	
1039	1,1,1k,1k, $\infty$	1.1033						
1040		1.3228				10dum		
1041		1.4475					sv/6	no rast
1042		1.4709				15dum		
1043		1.5043				4dum		
1044		1.5190				12C		
1045								harp 875
1046								harp 876
1047								harp 878
1048								harp 879
1049								harp 880
1050								harp 881
1051								harp 882
1052								harp 883
1053								harp 884
1054								harp 885

### B.1.2. $Q^2 = 1.64 \text{ GeV}^2$ .

B.1.2.1. *Spectrometer  $q$ -Pointing Check,  $Q^2 = 1.64 \text{ GeV}^2$ .*

run	prescales	$p_h$	$\theta_h$	$p_e$	$\theta_e$	target	h/e coll	comment
1055	10,10,160,1k,1	1.5521	47.087	3.6597	18.065	LH2	6/sv	spot 2*4
1056	1k,80,100,40,1						6/6	
1057	1,80,1,40,1					10dum		rast off
1058						15dum		
1059								junk
1060						4dum		rast off
1061						12C		

B.1.2.2. *Hydrogen Elastic  $\delta$ -Scan in the HRSE,  $Q^2 = 1.64 \text{ GeV}^2$ .*

run	prescales	$p_h$	$\theta_h$	$p_e$	$\theta_e$	target	h/e coll	comment
1062	10,80,1,40,1	1.5521	47.087	3.8064	18.06	LH2	6/6	junk
1063								delta +4%
1064							6/op	
1065							6/sv	wrong ps
1066	10,80,10,40,1			3.7332				delta +2%
1067	$\infty, \infty, \infty, \infty, 1$							only T5s
1068-1069								junk
1070							6/6	
1071							6/op	
1072				3.8064			6/sv	delta +4%
1073				3.660				delta 0%
1074							6/6	
1075							6/op	
1076	2,1,1,1,1					12C		singles
1077	1,1,1,1,1	1.5521	47.087	3.660	18.06	4dum	6/op	singles
1078						15dum		singles
1079						10dum		singles
1080	$\infty, \infty, \infty, \infty, 1$			3.5868		LH2		delta -2%
1081							6/6	
1082							6/sv	
1083				3.5136				delta -4%
1084							6/6	
1085							6/op	

**B.1.3. BCM Callibration.**

run	prescales	$p_h$	$\theta_h$	$p_e$	$\theta_e$	target	h/e coll
1086	$\infty, \infty, \infty, \infty, 1$	1.4150	47.087	3.8039	18.069	LH2	6/6

**B.1.4.  $Q^2 = 1.37 \text{ GeV}^2$ .**B.1.4.1. *Pointing Reference Measurement,  $Q^2 = 1.37 \text{ GeV}^2$ .*

run	prescales	$p_h$	$\theta_h$	$p_e$	$\theta_e$	target	h/e coll
1087	$\infty, \infty, \infty, \infty, 1$	1.3780	50.326	3.8067	16.149	12C	6/6
1088						4dum	
1089						15dum	
1090	1,1,1,1,1					15dum	

B.1.4.2. *Hydrogen Elastic Check,  $Q^2 = 1.37 \text{ GeV}^2$ .*

run	prescales	$p_h$	$\theta_h$	$p_e$	$\theta_e$	target	h/e coll	comment
1091	1k,70,150,20,1	1.3780	50.326	3.8067	16.149	LH2	6/6	
1092							6/op	
1093							6/sv	
1094-1095								junk
1096								harp 887

B.1.4.3. *Target Luminosity Current Scan,  $Q^2 = 1.37 \text{ GeV}^2$ .*

run	prescales	$p_h$	$\theta_h$	$p_e$	$\theta_e$	target	h/e coll	current	comment
1097	1,1,1,1,1	1.3780	50.326	3.8067	16.149	LH2	6/6	0.9582	fst fdbk off
1098								0.9867	fst fdbk on
1099						12C		1.0436	
1100								0.8961	
1101								2.3558	
1102						LH2		2.4688	
1103	4,1,1,1,1							4.3960	
1104								4.4001	
1105								4.8509	
1106	10,10,4,10,1							8.4060	
1107	20,20,8,20,1							19.2013	

<sup>2</sup>Note for Run 1119: The target was moved to LH2 at about event 150,000.

run	prescales	$p_h$	$\theta_h$	$p_e$	$\theta_e$	target	h/e coll	current	comment
1108	30,30,16,30,1	1.3780	50.326	3.8067	16.149	LH2	6/6	27.7506	
1109	45,45,24,45,1							31.9160	
1110	55,55,32,55,1							50.7433	
1111	4,4,1,4,1							49.8218	wrong ps
1112	50,50,24,50,1							43.8214	
1113						12C		48.5898	
1114	1,10,1,10,1							45.9860	
1115								33.7819	40 $\mu A$
1116	1,10,1,10,1							23.2026	30 $\mu A$
1117								16.8305	20 $\mu A$
1118								9.1746	10 $\mu A$
1119								2.6923	5 $\mu A$

B.1.4.4. *Trigger Efficiency Check,  $Q^2 = 1.37 \text{ GeV}^2$ .*

run	prescales	$p_h$	$\theta_h$	$p_e$	$\theta_e$	target	h/e coll	current	comment
1120	1,1,1,1,10k	1.3780	50.326	3.8067	16.149	LH2	6/6	4.8632	
1121	20,20,20,-,10k							43.4292	wrong ps4
1122	20,20,20,20,10k							46.2890	
1123	10,10,10,10,10k							44.2627	
1124	40,40,40,40,1							48.0819	
1125	400,400,40,40,2							48.0175	adjust ps
1126									junk

B.1.4.5. *Target Luminosity Rast Scan,  $Q^2 = 1.37 \text{ GeV}^2$ .*

run	prescales	$p_h$	$\theta_h$	$p_e$	$\theta_e$	target	h/e coll	comment
1127	500,500,500,500,1	1.3780	50.326	3.8067	16.149	LH2	6/6	rast 4*4, harp 888
1128								rast 3*3, harp 889
1129								rast 2*2, harp 890
1130								rast 1*1, harp 891
1131	20,5,10,5,1					12C		rast 1*1, harp 892
1132								rast 2*2, harp 893
1133								rast 3*3, harp 894
1134								rast 4*4, harp 895

**B.1.5.  $Q^2 = 1.88 \text{ GeV}^2$ .**

B.1.5.1. *Pointing Reference Measurement,  $Q^2 = 1.88 \text{ GeV}^2$ .*

run	prescales	$p_h$	$\theta_h$	$p_e$	$\theta_e$	target	h/e coll
1135	1,1,1,1,1	1.6981	44.609	3.5330	19.689	12C	6/6
1136						4dum	
1137						15dum	
1138						10dum	

B.1.5.2. *Hydrogen Elastic Check,  $Q^2 = 1.88 \text{ GeV}^2$ .*

run	prescales	$p_h$	$\theta_h$	$p_e$	$\theta_e$	target	h/e coll
1139	50,10,20,7,1	1.6981	44.609	3.5330	19.689	LH2	6/6
1140							6/op
1141							6/sv



**B.1.6.  $Q^2 = 2.65 \text{ GeV}^2$ .****B.1.6.1. *Hydrogen Elastic,  $Q^2 = 2.65 \text{ GeV}^2$ .***

run	prescales	$p_h$	$\theta_h$	$p_e$	$\theta_e$	target	h/e coll	comment
1142	50,10,20,7,1	2.1568	37.726	3.1217	24.966	LH2	6/6	junk
1143								

**B.1.6.2. *Pointing Reference Measurement,  $Q^2 = 2.65 \text{ GeV}^2$ .***

run	prescales	$p_h$	$\theta_h$	$p_e$	$\theta_e$	target	h/e coll
1144	1,1,1,1,1	2.1568	37.726	3.1217	24.966	10dum	6/6
1145						15dum	
1146						4dum	
1147						12C	

**B.1.7.  $Q^2 = 3.48 \text{ GeV}^2$ .****B.1.7.1. *Pointing Reference Measurement,  $Q^2 = 3.48 \text{ GeV}^2$ .***

run	prescales	$p_h$	$\theta_h$	$p_e$	$\theta_e$	target	h/e coll
1148	1,1,1,1,1	2.6283	31.739	2.6830	30.966	12C	6/6
1149						4dum	
1150						15dum	
1151						10dum	

**B.1.7.2. *Hydrogen Elastic,  $Q^2 = 3.48 \text{ GeV}^2$ .***

run	prescales	$p_h$	$\theta_h$	$p_e$	$\theta_e$	target	h/e coll
1152	10,10,10,10,1	2.6283	31.739	2.6830	30.966	LH2	6/6

**B.1.8.  $Q^2 = 4.13 \text{ GeV}^2$ .**B.1.8.1. *Hydrogen Elastic,  $Q^2 = 4.13 \text{ GeV}^2$ .*

run	prescales	$p_h$	$\theta_h$	$p_e$	$\theta_e$	target	h/e coll
1153	10,10,10,10,1	2.9708	31.740	2.3583	30.966	LH2	6/6

B.1.8.2. *Pointing Reference Measurement,  $Q^2 = 4.13 \text{ GeV}^2$ .*

run	prescales	$p_h$	$\theta_h$	$p_e$	$\theta_e$	target	h/e coll
1154	1,1,1,1,1	2.9708	27.831	2.3583	35.967	12C	6/6
1155						4dum	
1156						15dum	
1157						10dum	

**B.1.9. BCM Calibrations.**

run	prescales	$p_h$	$\theta_h$	$p_e$	$\theta_e$	target	h/e coll
1158	1,1,1,1,1	0.000	27.831	3.5625	35.97	LH2	6/6
1159		2.6854	27.799	3.8067			

B.1.9.1. *Sieve Slit Run on  $^{12}\text{C}$ .*

run	prescales	$p_h$	$\theta_h$	$p_e$	$\theta_e$	target	h/e coll
1160	1,1,1,1,1	2.4929	50.322	3.8067	16.154	12C	6/sv

**B.1.10. FPP Straight Throughs.**

run	prescales	$p_h$	$\theta_h$	$p_e$	$\theta_e$	target	h/e coll
1161	$\infty, \infty, 1, \infty, 1$	1.3780	50.322	3.8067	16.154	LH2	6/sv

B.1.10.1. *False Asymmetry and  $A_c$  for  $p_h = 1.378 \text{ GeV}$ .*

run	prescales	$p_h$	$\theta_h$	$p_e$	$\theta_e$	target	h/e coll	comment
1162-1174	22k,1400,5400,400,1	1.3780	50.322	3.8067	16.154	LH2	op/6	
1175		0.000						
1176								junk
1177-1204		1.3780						

B.1.10.2. *Pointing Reference Measurement.*

run	prescales	$p_h$	$\theta_h$	$p_e$	$\theta_e$	target	h/e coll	comment
1205-1206	1,1400,1,400,1	1.3780	50.322	3.8067	16.154	10dum	op/6	
1207						15dum		
1208						4dum		
1209						12C		
1210								harp 898

**B.1.11. Transitional Kinematics Setting: Hadron Arm at H Elastic  $1.37 \text{ GeV}^2$  Setting, Electron Arm at " $N \rightarrow \Delta$ "  $\theta_{pq} = 0^\circ$  Setting.**

run	prescales	$p_h$	$\theta_h$	$p_e$	$\theta_e$	target	h/e coll	comment
1211	1,1,1,1,1	1.3780	50.322	3.6683	14.075	12C	6/6	pointing ref
1212	10,1,1,1,1					4dum		pointing ref
1213						15dum		pointing ref
1214						10dum		pointing ref
1215	300, $\infty$ , 10, $\infty$ ,1					LH2		real measmt for rate-lum bootstrap

**B.1.12.  $\theta_{pq} = 0^\circ$ .**

B.1.12.1. *Pointing Reference,  $\theta_{pq} = 0^\circ$ .*

run	prescales	$p_h$	$\theta_h$	$p_e$	$\theta_e$	target	h/e coll
1216	1,1,1,1,1	1.3780	42.303	3.6683	14.075	12C	6/6
1217	10,1,1,1,1					4dum	
1218						15dum	
1219						10dum	

B.1.12.2. *Trigger Efficiency Studies,  $\theta_{pq} = 0^\circ$ .*

run	prescales	$p_h$	$\theta_h$	$p_e$	$\theta_e$	target	h/e coll
1220	1,1,1,1, $\infty$	1.3780	42.303	3.6683	14.075	LH2	6/6
1221-1222	10,1,1,1, $\infty$						

B.1.12.3. *Production Point,  $\theta_{pq} = 0^\circ$ .*

prod	run	prescales	$p_h$	$\theta_h$	$p_e$	$\theta_e$	target	h/e coll	comment
✓	1223	$\infty, 3k, 9k, 500, 1$	1.3780	42.303	3.6683	14.075	LH2	6/6	
	1224								cosmics
✓	1225								
✓	1226								bpm ioc off
✓	1227-1238								
	1239								cosmics

**B.1.13.**  $\theta_{pq} = 25^\circ$ ,  $\phi_{pq} = 0^\circ$ .

B.1.13.1. *Pointing Reference*,  $\theta_{pq} = 25^\circ$ ,  $\phi_{pq} = 0^\circ$ .

run	prescales	$p_h$	$\theta_h$	$p_e$	$\theta_e$	target	h/e coll	comment
1240	2,3k,1,500,1	1.3501	38.117	3.6683	14.075	12C	6/6	rast off
1241								
1242						15dum		
1243	4, 3k,1,500,1							
1244						10dum		
1245	8,3k,2,500,1					4dum		

B.1.13.2. *Efficiency Studies*,  $\theta_{pq} = 25^\circ$ ,  $\phi_{pq} = 0^\circ$ .

run	prescales	$p_h$	$\theta_h$	$p_e$	$\theta_e$	target	h/e coll	comment
1246	$\infty$ ,3k,9k,500,1	1.3501	38.117	3.6683	14.075	LH2	6/6	6" door out
1247-1248	65,30,30,5, $\infty$							
1249	65,3,30,1, $\infty$							

B.1.13.3. *Production Point*,  $\theta_{pq} = 25^\circ$ ,  $\phi_{pq} = 0^\circ$ .

prod	run	prescales	$p_h$	$\theta_h$	$p_e$	$\theta_e$	target	h/e coll
✓	1250-1268	$\infty$ ,3k,9k,500,1	1.3501	38.117	3.6683	14.075	LH2	6/6

B.1.13.4. *Pointing Reference*,  $\theta_{pq} = 25^\circ$ ,  $\phi_{pq} = 0^\circ$ .

run	prescales	$p_h$	$\theta_h$	$p_e$	$\theta_e$	target	h/e coll	comment
1269	8,3k,2,500,1	1.3501	38.117	3.6683	14.075	10dum	6/6	
1270						15dum		
1271						12C		rast off
1272						4dum		

**B.1.14.**  $\theta_{pq} = 25^\circ$ ,  $\phi_{pq} = 180^\circ$ .

B.1.14.1. *Pointing Reference*,  $\theta_{pq} = 25^\circ$ ,  $\phi_{pq} = 180^\circ$ .

run	prescales	$p_h$	$\theta_h$	$p_e$	$\theta_e$	target	h/e coll	comment
1273	8,3k,2,500,1	1.3501	46.330	3.6683	14.075	12C	6/6	rast off, short run
1274	1,3k,1,500,1							
1275	2,3k,1,500,1					4dum		
1276						15dum		
1277						10dum		

B.1.14.2. *Production Point*,  $\theta_{pq} = 25^\circ$ ,  $\phi_{pq} = 180^\circ$ .

prod	run	prescales	$p_h$	$\theta_h$	$p_e$	$\theta_e$	target	h/e coll	comment
✓	1278	2k,3k,100,500,1	1.3501	46.330	3.6683	14.075	LH2	6/6	ck rast/rts
✓	1279								
✓	1280-1293	$\infty$ ,3k,4500,500,1							
	1294								junk
✓	1295-1296								
	1297								junk
✓	1298-1303								

B.1.14.3. *Move Position at Target  $\pm 2\text{mm}$  Horizontal.*

run	prescales	$p_h$	$\theta_h$	$p_e$	$\theta_e$	target	h/e coll	comment
1304	$\infty$ ,3k,4500,500,1	1.3501	46.330	3.6683	14.075	LH2	6/6	x=+2mm
1305								x=-2mm

B.1.14.4. *Pointing Reference*,  $\theta_{pq} = 25^\circ$ ,  $\phi_{pq} = 180^\circ$ .

run	prescales	$p_h$	$\theta_h$	$p_e$	$\theta_e$	target	h/e coll	comment
1306	5,3k,1,500,1	1.3501	46.330	3.6683	14.075	10dum	6/6	
1307						15dum		
1308						4dum		
1309						12C		rast on
1310								rast off

**B.1.15.**  $\theta_{pq} = 50^\circ$ ,  $\phi_{pq} = 0^\circ$ .

B.1.15.1. *Pointing Reference*,  $\theta_{pq} = 50^\circ$ ,  $\phi_{pq} = 0^\circ$ .

run	prescales	$p_h$	$\theta_h$	$p_e$	$\theta_e$	target	h/e coll	comment
1311	5,3k,1,500,1	1.2700	34.285	3.6683	14.075	12C	6/6	rast off
1312								rast on
1313						4dum		
1314	3,3k,3,500,1					15dum		
1315						10dum		

B.1.15.2. *Production Point*,  $\theta_{pq} = 50^\circ$ ,  $\phi_{pq} = 0^\circ$ .

prod	run	prescales	$p_h$	$\theta_h$	$p_e$	$\theta_e$	target	h/e coll	comment
	1316-1321	15k,3k,9k,500,1	1.2700	34.29	3.6683	14.075	LH2	6/6	junk
✓	1322-1323								

B.1.15.3. *Trigger Efficiency*,  $\theta_{pq} = 50^\circ$ ,  $\phi_{pq} = 0^\circ$ .

run	prescales	$p_h$	$\theta_h$	$p_e$	$\theta_e$	target	h/e coll
1324	200,20,200,10, $\infty$	1.2700	34.29	3.6683	14.075	LH2	6/6

B.1.15.4. *Continue Production Point*,  $\theta_{pq} = 50^\circ$ ,  $\phi_{pq} = 0^\circ$ .

prod	run	prescales	$p_h$	$\theta_h$	$p_e$	$\theta_e$	target	h/e coll	comment
✓	1325-1326	15k,3k,9k,500,1	1.2700	34.29	3.6683	14.075	LH2	6/6	
✓	1327								roc14 crash
✓	1328-1340								
	1341								harp 907
	1342-1343								target shift

### B.1.16. Checks After Target Fix.

run	prescales	$p_h$	$\theta_h$	$p_e$	$\theta_e$	target	h/e coll	comment
1344	1,1,1,1, $\infty$	1.5520	34.286	3.6600	18.067	12C	6/6	junk
1345								harp 909
1346								singles
1347						15dum		singles
1348						10dum		singles
1349						4dum		singles
1350			47.090					singles
1351						15dum		singles
1352						10dum		singles
1353-1354	$\infty, \infty, \infty, \infty, 1$					LH2		coin
1355							6/sv	coin
1356								junk
1357	$\infty, \infty, \infty, \infty, 1$							coin
1358	1,1,1,1, $\infty$					12C	6/6	singles
1359								junk
1360	50,10,1,10, $\infty$				14.074			singles
1361	1,10,1,10, $\infty$					4dum		singles
1362-1363	10,10,1,10, $\infty$					LH2		singles
1364								harp 910
1365								junk
1366	1,1,1,1, $\infty$	1.2700	34.285			12C		singles



run	prescales	$p_h$	$\theta_h$	$p_e$	$\theta_e$	target	h/e coll	comment
1367	1,1,1,1, $\infty$	1.2700	34.285	3.6600	14.074	4dum	6/6	singles
1368						15dum		singles
1369						10dum		singles
1370	200,20,200,10, $\infty$					LH2		high ps
1371	20,2,20,1, $\infty$							high ps

**B.1.17. Continue  $\theta_{pq} = 50^\circ$ ,  $\phi_{pq} = 0^\circ$ .**

B.1.17.1. *Continue Production Point*,  $\theta_{pq} = 50^\circ$ ,  $\phi_{pq} = 0^\circ$ .

prod	run	prescales	$p_h$	$\theta_h$	$p_e$	$\theta_e$	target	h/e coll	comment
✓	1372-1386	15k,3k,9k,500,1	1.2700	34.285	3.6600	14.074	LH2	6/6	
	1387-1388								junk
	1389								harp 911

B.1.17.2. *Pointing Reference*,  $\theta_{pq} = 50^\circ$ ,  $\phi_{pq} = 0^\circ$ .

run	prescales	$p_h$	$\theta_h$	$p_e$	$\theta_e$	target	h/e coll	comment
1390	2,1,2,1,1	1.2700	34.285	3.6600	14.074	12C	6/6	rast on
1391	10,1,10,1,1					15dum		
1392	7,1,7,1,1					4dum		
1393	10,1,10,1,1					10dum		

**B.1.18.**  $\theta_{pq} = 50^\circ$ ,  $\phi_{pq} = 180^\circ$ .

B.1.18.1. *Pointing Reference*,  $\theta_{pq} = 50^\circ$ ,  $\phi_{pq} = 180^\circ$ .

run	prescales	$p_h$	$\theta_h$	$p_e$	$\theta_e$	target	h/e coll	comment
1394	10,1,10,1,1	1.2700	50.160	3.6600	14.074	10dum	6/6	
1395	15,1,1,1,1							
1396						15dum		
1397						4dum		
1398						12C		rast on
1399	5,1,1,1,1							rast on

B.1.18.2. *Trigger Efficiency*,  $\theta_{pq} = 50^\circ$ ,  $\phi_{pq} = 180^\circ$ .

run	prescales	$p_h$	$\theta_h$	$p_e$	$\theta_e$	target	h/e coll
1400	1,1,1,1, $\infty$	1.2700	50.160	3.6600	14.074	LH2	6/6

B.1.18.3. *Production Point*,  $\theta_{pq} = 50^\circ$ ,  $\phi_{pq} = 180^\circ$ .

prod	run	prescales	$p_h$	$\theta_h$	$p_e$	$\theta_e$	target	h/e coll	comment
✓	1401-1404	8k,800,400,40,1	1.2700	50.160	3.6600	14.074	LH2	6/6	
	1405								harp 912
✓	1406-1418								
	1419								harp 915

B.1.18.4. *Pointing Reference*,  $\theta_{pq} = 50^\circ$ ,  $\phi_{pq} = 180^\circ$ .

run	prescales	$p_h$	$\theta_h$	$p_e$	$\theta_e$	target	h/e coll	comment
1420	1,1,1,1,1	1.2700	50.160	3.6600	14.074	12C	6/6	rast off
1421	5,1,1,1,1					4dum		
1422	10,1,1,1,1					15dum		
1423						10dum		

**B.1.19.**  $\theta_{pq} = 90^\circ$ ,  $\phi_{pq} = 180^\circ$ .

B.1.19.1. *Pointing Reference*,  $\theta_{pq} = 90^\circ$ ,  $\phi_{pq} = 180^\circ$ .

run	prescale	$p_h$	$\theta_h$	$p_e$	$\theta_e$	target	h/e coll	comment
1424	10,10,2,5,1	1.0660	54.783	3.6600	14.074	10dum	6/6	
1425						15dum		
1426						4dum		
1427	3,1,1,1,1					12C		rast on

B.1.19.2. *Trigger Efficiency*,  $\theta_{pq} = 90^\circ$ ,  $\phi_{pq} = 180^\circ$ .

run	prescales	$p_h$	$\theta_h$	$p_e$	$\theta_e$	target	h/e coll
1428	1,1,1,1, $\infty$	1.0660	54.783	3.6600	14.074	LH2	6/6

B.1.19.3. *Production Point*,  $\theta_{pq} = 90^\circ$ ,  $\phi_{pq} = 180^\circ$ .

prod	run	prescales	$p_h$	$\theta_h$	$p_e$	$\theta_e$	target	h/e coll	comment
✓	1429-1440	6k,500, 500,40,1	1.0660	54.783	3.6600	14.074	LH2	6/6	
	1441								harp 916-917
✓	1442-1456								
	1457								junk
	1458								harp 918

B.1.19.4. *Pointing Reference*,  $\theta_{pq} = 90^\circ$ ,  $\phi_{pq} = 180^\circ$ .

run	prescales	$p_h$	$\theta_h$	$p_e$	$\theta_e$	target	h/e coll
1459	1,1,1,1,1	1.0660	54.783	3.6600	14.074	12C	6/6
1460	3,10,1,10,1					4dum	
1461						15dum	
1462	600,30,40,10,1						
1463	8,10,2,10,1					10dum	

**B.1.20.**  $\theta_{pq} = 90^\circ$ ,  $\phi_{pq} = 0^\circ$ .

B.1.20.1. *Pointing Reference*,  $\theta_{pq} = 90^\circ$ ,  $\phi_{pq} = 0^\circ$ .

run	prescales	$p_h$	$\theta_h$	$p_e$	$\theta_e$	target	h/e coll	comment
1464	10,30,40,50,1	1.0660	29.811	3.6600	14.074	10dum	6/6	
1465						15dum		
1466						4dum		
1467	4,10,4,10,1					12C		rast on

B.1.20.2. *Production Point*,  $\theta_{pq} = 90^\circ$ ,  $\phi_{pq} = 0^\circ$ .

prod	run	prescales	$p_h$	$\theta_h$	$p_e$	$\theta_e$	target	h/e coll	comment
✓	1468-1469	6500,500,20k,45,1	1.0660	29.811	3.6600	14.074	LH2	6/6	
✓	1470	6500,500,20k,450,1							
✓	1471								15 $\mu A$

B.1.20.3. *Trigger Efficiency*,  $\theta_{pq} = 90^\circ$ ,  $\phi_{pq} = 0^\circ$ .

run	prescale	$p_h$	$\theta_h$	$p_e$	$\theta_e$	target	h/e coll
1472	20,2,20,1, $\infty$	1.0660	29.811	3.6600	14.074	LH2	6/6

B.1.20.4. *Continue Production Point*,  $\theta_{pq} = 90^\circ$ ,  $\phi_{pq} = 0^\circ$ .

prod	run	prescales	$p_h$	$\theta_h$	$p_e$	$\theta_e$	target	h/e coll	comment
✓	1473-1477	6500,500, 20k,450,1	1.0660	29.811	3.6600	14.074	LH2	6/6	
	1478-1479								cosmics
	1480								junk
	1481								cosmics
	1482								pedastals
	1483								junk
	1484								harp 920
	1485								junk

prod	run	prescales	$p_h$	$\theta_h$	$p_e$	$\theta_e$	target	h/e coll	comment
✓	1486-1511	6500,500, 20k,450,1	1.0660	29.811	3.6600	14.074	LH2	6/6	
	1512-1517								junk
	1518-1519						12C		rast ck
✓	1520-1529						LH2		
	1530								junk
✓	1531								5 $\mu A$
	1532-1533								cosmics
	1534-1537								trig tests hrsh 2 pks
	1538								junk
	1539-1543								trig tests hrsh 2 pks

B.1.20.5. *Pointing Reference*,  $\theta_{pq} = 90^\circ$ ,  $\phi_{pq} = 0^\circ$ .

run	prescales	$p_h$	$\theta_h$	$p_e$	$\theta_e$	target	h/e coll	comment
1544	10,30,40,50,1	1.0660	29.811	3.6600	14.074	10dum	6/6	
1545	10,30,20,50,1					15dum		
1546						4dum		
1547						12C		rast off

B.1.20.6. *Trigger Efficiency*,  $\theta_{pq} = 90^\circ$ ,  $\phi_{pq} = 0^\circ$ .

run	prescales	$p_h$	$\theta_h$	$p_e$	$\theta_e$	target	h/e coll	comment
1548	6500,500,20k,450,1	1.0660	29.811	3.6600	14.074	LH2	6/6	trig reloaded
1549-1561								cosmics - fix trig prob

**B.1.21.**  $\theta_{pq} = 135^\circ$ ,  $\phi_{pq} = 0^\circ$ .

B.1.21.1. *Pointing Reference*,  $\theta_{pq} = 135^\circ$ ,  $\phi_{pq} = 0^\circ$ .

run	prescales	$p_h$	$\theta_h$	$p_e$	$\theta_e$	target	h/e coll	comment
1562	1,500,1,450,1	0.8188	30.806	3.6600	14.074	12C	6/6	50 $\mu A$
1563								junk
1564								harp
1565						4dum		5 $\mu A$
1566						15dum		5 $\mu A$
1567						10dum		5 $\mu A$

B.1.21.2. *Trigger Efficiency*,  $\theta_{pq} = 135^\circ$ ,  $\phi_{pq} = 0^\circ$ .

run	prescales	$p_h$	$\theta_h$	$p_e$	$\theta_e$	target	h/e coll	comment
1568	1,1,1,1,20k	0.8188	30.806	3.6600	14.074	LH2	6/6	50 $\mu A$

B.1.21.3. *Production Point*,  $\theta_{pq} = 135^\circ$ ,  $\phi_{pq} = 0^\circ$ .

prod	run	prescale	$p_h$	$\theta_h$	$p_e$	$\theta_e$	target	h/e coll	comment
✓	1569	6500,500, 20k,450,1	0.8188	30.806	3.6600	14.07	LH2	6/6	50 $\mu A$
✓	1570								
✓	1571								bad fpp multiplex
✓	1572-1577								fpp okay
✓	1578-1581	6500,500, 20k,450,2							
✓	1582-1585	6500,500, 20k,450,1							
✓	1586								high dt
✓	1587-1590								
✓	1591-1593								high dt

prod	run	prescale	$p_h$	$\theta_h$	$p_e$	$\theta_e$	target	h/e coll	comment
✓	1594-1602	6500,600, 20k,500,1	0.8188	30.806	3.6600	14.07	LH2	6/6	
	1603								junk
✓	1604-1616								
✓	1617								high dt
✓	1618		0.8188	30.806	3.6600	14.07	LH2	6/6	
	1619-1620								junk
✓	1621-1639								
✓	1640								high dt
✓	1641-1644								
✓	1645								high dt
✓	1646								
✓	1647								high dt
✓	1648-1654								

B.1.21.4. *Pointing Reference*,  $\theta_{pq} = 135^\circ$ ,  $\phi_{pq} = 0^\circ$ .

run	prescales	$p_h$	$\theta_h$	$p_e$	$\theta_e$	target	h/e coll	comment
1655	1,500,1,450,1	0.8188	30.806	3.6600	14.074	10dum	6/6	
1656						15dum		
1657						4dum		
1658	1, 1, 2, 1, 1					12C		
1659								harp 922

**B.1.22.**  $\theta_{pq} = 135^\circ$ ,  $\phi_{pq} = 180^\circ$ .

B.1.22.1. *Pointing Reference*,  $\theta_{pq} = 135^\circ$ ,  $\phi_{pq} = 180^\circ$ .

run	prescales	$p_h$	$\theta_h$	$p_e$	$\theta_e$	target	h/e coll	comment
1660	1,1,2,1,1	0.8188	53.635	3.6600	14.074	12C	6/6	
1661	1,500,1,450,1					4dum		
1662						15dum		
1663						10dum		high dt
1664-1665								

B.1.22.2. *Trigger Efficiency*,  $\theta_{pq} = 135^\circ$ ,  $\phi_{pq} = 180^\circ$ .

run	prescales	$p_h$	$\theta_h$	$p_e$	$\theta_e$	target	h/e coll
1667	1,500,1,450,1	0.8188	53.635	3.6600	14.074	LH2	6/6
1668	1,1,1,1, $\infty$						

B.1.22.3. *Production Point*,  $\theta_{pq} = 135^\circ$ ,  $\phi_{pq} = 180^\circ$ .

prod	run	prescales	$p_h$	$\theta_h$	$p_e$	$\theta_e$	target	h/e coll
✓	1669-1683	5k,500,1400,100,1	0.8188	53.635	3.6600	14.074	LH2	6/6

B.1.22.4. *Pointing Reference*,  $\theta_{pq} = 135^\circ$ ,  $\phi_{pq} = 180^\circ$ .

run	prescales	$p_h$	$\theta_h$	$p_e$	$\theta_e$	target	h/e coll	comment
1684	4,1,4,1,1	0.8188	53.635	3.6600	14.074	10dum	6/6	
1685						15dum		
1686						4dum		
1687						12C		
1688								harp 923
1689-1692								timing tests
1693-1694								cosmics



**B.1.23.**  $\theta_{pq} = 155^\circ$ ,  $\phi_{pq} = 0^\circ$ .

B.1.23.1. *Pointing Reference*,  $\theta_{pq} = 155^\circ$ ,  $\phi_{pq} = 0^\circ$ .

run	prescales	$p_h$	$\theta_h$	$p_e$	$\theta_e$	target	h/e coll	comment
1695	1,1,4,1,1	0.7418	34.731	3.6600	14.074	12C	6/6	rast on
1696								rast off
1697						4dum		
1698						15dum		
1699						10dum		

B.1.23.2. *Trigger Efficiency*,  $\theta_{pq} = 155^\circ$ ,  $\phi_{pq} = 0^\circ$ .

run	prescales	$p_h$	$\theta_h$	$p_e$	$\theta_e$	target	h/e coll	comment
1700	1,1,1,1,1	0.7418	34.731	3.6600	14.074	LH2	6/6	5 $\mu A$

B.1.23.3. *Production Point*,  $\theta_{pq} = 155^\circ$ ,  $\phi_{pq} = 0^\circ$ .

prod	run	prescales	$p_h$	$\theta_h$	$p_e$	$\theta_e$	target	h/e coll	comment
✓	1701	5k,500, 1400,100,1	0.7418	34.731	3.6600	14.074	LH2	6/6	50 $\mu A$
✓	1702	5k,500, 14k,500,1							
✓	1703-1732								25 $\mu A$ S/N okay
✓	1733								50 $\mu A$
✓	1734-1752	10k,1k, 30k,1k,1							50 $\mu A$

B.1.23.4. *Pointing Reference,  $\theta_{pq} = 155^\circ$ ,  $\phi_{pq} = 0^\circ$ .*

run	prescales	$p_h$	$\theta_h$	$p_e$	$\theta_e$	target	h/e coll	comment
1753	0,20,40,20,1	0.7418	34.731	3.6600	14.07	10dum	6/6	5 $\mu A$ , rast off
1754								junk
1755	5,20,20,20,1					15dum		5 $\mu A$ , rast off
1756						4dum		5 $\mu A$ , rast off
1757								junk
1758	1,20,4,20,1					12C		5 $\mu A$ , rast off
1759								harp 924
1760							6/sv	changing hrsh angle

**B.1.24.  $\theta_{pq} = 155^\circ$ ,  $\phi_{pq} = 180^\circ$ .**

B.1.24.1. *Pointing Reference,  $\theta_{pq} = 155^\circ$ ,  $\phi_{pq} = 180^\circ$ .*

run	prescales	$p_h$	$\theta_h$	$p_e$	$\theta_e$	target	h/e coll	comment
1761	3,20,5,20,1	0.7418	49.720	3.6600	14.074	12C	6/6	20 $\mu A$ , rast off
1762	1,20,2,20,1					4dum		5 $\mu A$ , rast off
1763						15dum		5 $\mu A$ , rast off
1764						10dum		5 $\mu A$ , rast off

B.1.24.2. *Production Point,  $\theta_{pq} = 155^\circ$ ,  $\phi_{pq} = 180^\circ$ .*

prod	run	prescales	$p_h$	$\theta_h$	$p_e$	$\theta_e$	target	h/e coll	comment
✓	1765-1766	6700,1400, 5450,400,1	0.7418	49.720	3.6600	14.074	LH2	6/6	
	1767								junk
✓	1768								
✓	1769-1775	6700,1400, 2k,400,1							
	1776								harp 925
✓	1777-1778								

prod	run	prescales	$p_h$	$\theta_h$	$p_e$	$\theta_e$	target	h/e coll	comment
✓	1779	6700,1400, 2k,400,1	0.7418	49.720	3.6600	14.074	LH2	6/6	roc14 crash
✓	1780-1785								
✓	1786								short run
✓	1787-1795								

B.1.24.3. *Pointing Reference,  $\theta_{pq} = 155^\circ$ ,  $\phi_{pq} = 180^\circ$ .*

run	prescale	$p_h$	$\theta_h$	$p_e$	$\theta_e$	target	h/e coll	comment
1796	2, $\infty$ ,4, $\infty$ ,1	0.7418	49.720	3.6600	14.074	12C	6/6	5 $\mu A$ , rast off
1797						4dum		5 $\mu A$ , rast off
1798	4, $\infty$ ,2, $\infty$ ,1					15dum		5 $\mu A$ , rast off
1799	4, $\infty$ ,8, $\infty$ ,1					10dum		5 $\mu A$ , rast off, fast feedback off
1800								5 $\mu A$ , rast off
1801								harp 926

B.1.24.4. *Continue Production Point,  $\theta_{pq} = 155^\circ$ ,  $\phi_{pq} = 180^\circ$ .*

prod	run	prescales	$p_h$	$\theta_h$	$p_e$	$\theta_e$	target	h/e coll	comment
✓	1802	6700,1400, 2k,400,1	0.7418	49.720	3.6600	14.074	LH2	6/6	roc14 crash
✓	1803-1805								

## B.2. June 8 - July 1 Run Period

run	comment
1823-1829	cosmics
1830	harp 927

**B.2.1.**  $\theta_{pq} = 155^\circ$ ,  $\phi_{pq} = 180^\circ$ .

B.2.1.1. *Pointing Reference*,  $\theta_{pq} = 155^\circ$ ,  $\phi_{pq} = 180^\circ$ .

run	prescales	$p_h$	$\theta_h$	$p_e$	$\theta_e$	target	h/e coll	comment
1831	2, $\infty$ ,2, $\infty$ , $\infty$	0.7418	49.721	3.6600	14.074	12C	6/6	h scint pad s1-6 in wrong position
1832						4dum		
1833						15dum		
1834						10dum		
1835-1836						LH2		rast checks

B.2.1.2. *Luminosity Scan*<sup>3</sup>.

run	prescales	$p_h$	$\theta_h$	$p_e$	$\theta_e$	target	h/e coll	comment
1837	30, $\infty$ , $\infty$ , $\infty$ , $\infty$	0.7418	49.721	3.6600	14.074	LH2	6/6	20 $\mu A$
1838								40 $\mu A$
1839	60, $\infty$ , $\infty$ , $\infty$ , $\infty$							40 $\mu A$
1840-1841	90, $\infty$ , $\infty$ , $\infty$ , $\infty$							60 $\mu A$
1842	100, $\infty$ , $\infty$ , $\infty$ , $\infty$							70 $\mu A$
1843-1844	115, $\infty$ , $\infty$ , $\infty$ , $\infty$							80 $\mu A$

<sup>3</sup>Hadron scintillator paddle s1-6 in wrong position.

B.2.1.3. *Production Point*,  $\theta_{pq} = 155^\circ$ ,  $\phi_{pq} = 180^\circ$ .

prod	run	prescales	$p_h$	$\theta_h$	$p_e$	$\theta_e$	target	h/e coll	comment
	1845-1851	11200,1100, 8800,240,1	0.7418	49.721	3.6600	14.08	LH2	6/6	junk
✓	1852								unstbl bm
✓	1853								
✓	1854-1855			49.720				op/op	
✓	1856-1861	13k,1300, 14k,240,1							
✓	1862								e Q3 qnch
✓	1863-1866								
✓	1867								e Q3 qnch
✓	1868-1872								
✓	1873								e Q3 qnch
✓	1874-1875								
✓	1876								rf prob, unstbl bm
✓	1877								
✓	1878								rf prob
✓	1879-1890								
✓	1891								e Q3 qnch
✓	1892-1894								
✓	1895								e Q3 qnch
✓	1896-1915								
	1916-1917								junk
✓	1918								high dt
✓	1919								
✓	1920								unstbl bm
✓	1921-1922								
✓	1923-1924								unstbl bm
✓	1925-1928								
✓	1929								unstbl bm

prod	run	prescales	$p_h$	$\theta_h$	$p_e$	$\theta_e$	target	h/e coll	comment
✓	1930	13k,1300, 14k,240,1	0.7418	49.720	3.6600	14.08	LH2	op/op	
✓	1931								high dt
✓	1932								
✓	1933								e Q3 qnch
✓	1934-1944								
✓	1945								e Q3 qnch
✓	1946-1950								
✓	1951								e Q3 qnch
✓	1952								
✓	1953								e Q3 qnch
✓	1954								
✓	1955-1956								e Q3 qnch
	1957								junk
✓	1958-1960								
✓	1961-1962								e Q3 qnch
✓	1963-1975								
✓	1976-1977								high dt
✓	1978-1987								
✓	1988								e Q3 qnch
	1989								junk
✓	1990-1991					14.079			
✓	1992								e Q3 qnch
	1993								junk
✓	1994								
✓	1995-1996								e Q3 qnch
✓	1997-2000								
✓	2001								e Q3 qnch
✓	2002-2003								fast fbk off
✓	2004-2011								

B.2.1.4. *Pointing Reference*,  $\theta_{pq} = 155^\circ$ ,  $\phi_{pq} = 180^\circ$ .

run	prescales	$p_h$	$\theta_h$	$p_e$	$\theta_e$	target	h/e coll	comment
2012	2,1300,4,240,1	0.7418	49.720	3.6600	14.079	12C	op/op	5 $\mu A$ , rast off
2013								harp 929
2014	1,1300,1,240,1							5 $\mu A$ , rast off
2015						4dum		5 $\mu A$ , rast off
2016						10dum		5 $\mu A$ , rast off

B.2.1.5. *Continue Production Point*,  $\theta_{pq} = 155^\circ$ ,  $\phi_{pq} = 180^\circ$ .

prod	run	prescales	$p_h$	$\theta_h$	$p_e$	$\theta_e$	target	h/e coll	comment
✓	2017-2020	13k,1300, 14k,240,1	0.7418	49.720	3.6600	14.079	LH2	op/op	
✓	2021								e Q3 qnch
✓	2022-2032								
✓	2033								e Q3 qnch

B.2.2.  $\theta_{pq} = 135^\circ$ ,  $\phi_{pq} = 180^\circ$ .

run	comment
2037	harp 930

B.2.2.1. *Pointing Reference*,  $\theta_{pq} = 135^\circ$ ,  $\phi_{pq} = 180^\circ$ .

run	prescales	$p_h$	$\theta_h$	$p_e$	$\theta_e$	target	h/e coll	comment
2034-2039	1,1300,1,200,1	0.8188	-	3.6600	14.079	15dum	op/op	junk
2040			53.640					correct $\theta_h$
2041						12C		
2042						4dum		
2043						10dum		

B.2.2.2. *Trigger Efficiency*,  $\theta_{pq} = 135^\circ$ ,  $\phi_{pq} = 180^\circ$ .

run	prescales	$p_h$	$\theta_h$	$p_e$	$\theta_e$	target	h/e coll	comment
2044	1,1,1,200, $\infty$	0.8188	53.640	3.6600	14.074	LH2	6/6	junk
2045								$5 \mu A$

B.2.2.3. *Production Point*,  $\theta_{pq} = 135^\circ$ ,  $\phi_{pq} = 180^\circ$ .

prod	run	prescales	$p_h$	$\theta_h$	$p_e$	$\theta_e$	target	h/e coll	comment
	2046-2050	13k,1400, 3800,15,1	0.8188	53.640	3.6600	14.079	LH2	op/op	junk
✓	2051-2058								
✓	2059								ffbk off
✓	2060-2067								
✓	2068								adaq prob
✓	2069-2098								
✓	2099-2100								unstbl bm
✓	2101-2112								
	2113								junk
✓	2114-2123								
✓	2124								roc14 prob
✓	2125-2128								
✓	2129	13k,1400, 3800,1k,1							new t4 defn
✓	2130-2140								
✓	2141								unstbl bm
	2142								junk
✓	2143-2148								
✓	2149								roc14 crash
	2150								junk
✓	2151-2163								
✓	2164-2165								$50 \mu A$ , RF prob



prod	run	prescales	$p_h$	$\theta_h$	$p_e$	$\theta_e$	target	h/e coll	comment
✓	2166-2167	13k,1400, 3800,1k,1	0.8188	53.640	3.6600	14.079	LH2	op/op	60 $\mu A$
✓	2168-2171								
✓	2172								h Q1 trip
✓	2173-2192								
✓	2193								
✓	2194	1,1400,1, $\infty$ ,1							
	2195								cosmics
✓	2196								
✓	2197-2210	13k,1400, 3800,1k,1							
	2211-2212								cosmics
✓	2213	1,1,1,1000,1							
✓	2214-2216	13k,1400, 3800,1k,1							
✓	2217								tgt ioc crash
✓	2218-2236								
✓	2237								unstbl bm
✓	2238-2247								

B.2.2.4. *Pointing Reference*,  $\theta_{pq} = 135^\circ$ ,  $\phi_{pq} = 180^\circ$ .

run	prescales	$p_h$	$\theta_h$	$p_e$	$\theta_e$	target	h/e coll	comment
2248	3,1400,3,1k,1	0.8188	53.640	3.6600	14.074	10dum	6/6	junk
2249								
2250						15dum		
2251						4dum		
2252						12C		
2253-2254								junk
2255								harp 933
2256								harp 934

run	prescales	$p_h$	$\theta_h$	$p_e$	$\theta_e$	target	h/e coll	comment
2257-2258	3,1400,3,1k,1	0.8188	53.640	3.6600	14.074	12C	6/6	junk
2259								harp 937

### B.2.3. $\theta_{pq} = 90^\circ$ , $\phi_{pq} = 180^\circ$ .

B.2.3.1. *Pointing Reference*,  $\theta_{pq} = 90^\circ$ ,  $\phi_{pq} = 180^\circ$ .

run	prescales	$p_h$	$\theta_h$	$p_e$	$\theta_e$	target	h/e coll	comment
2260	3,1400,3,1k,1	1.0660	54.785	3.6600	14.074	12C	6/6	
2261						4dum		
2262						15dum		
2263						10dum		
2264-2270								junk

B.2.3.2. *Trigger Efficiency Check*,  $\theta_{pq} = 90^\circ$ ,  $\phi_{pq} = 180^\circ$ .

run	prescales	$p_h$	$\theta_h$	$p_e$	$\theta_e$	target	h/e coll
2271	1,1,1,1, $\infty$	1.0660	54.785	3.6600	14.074	LH2	6/6

B.2.3.3. *Production Point*,  $\theta_{pq} = 90^\circ$ ,  $\phi_{pq} = 180^\circ$ .

prod	run	prescales	$p_h$	$\theta_h$	$p_e$	$\theta_e$	target	h/e coll	comment
✓	2272-2273	13k,1400, 3800,1k,1	1.0660	54.785	3.6600	14.08	LH2	6/6	
✓	2274-2292							op/op	
	2293-2294						10cm dm		unknown
	2295						LH2		junk
✓	2296	1,1400, 3800,1k,1							high dt
	2297								junk
✓	2298	13k,1400, 3800,1k,1							high dt

prod	run	prescales	$p_h$	$\theta_h$	$p_e$	$\theta_e$	target	h/e coll	comment
✓	2299-2305	13k,1400, 3800,1k,1	1.0660	54.785	3.6600	14.08	LH2	op/op	
✓	2306-2316	6k,500, 500,1500,1							
✓	2317								unstbl
									beam
✓	2318-2335								
	2336						empty		trig tests
	2337-2344								cosmics
	2345-2346								junk
	2347								harp 942
✓	2348-2349	1800,200, 200,200,1					LH2		
✓	2350								unstbl beam
✓	2351								roc1-3 crash
✓	2352-2363	18k,2k, 2k,4k,1							
✓	2364								
✓	2365-2366								
✓	2367								unstbl beam
✓	2368-2373								
✓	2374								roc14 crash
✓	2375-2393								
	2394-2397								junk
✓	2398-2414								
✓	2415-2423	9k,1k, 1k,2k,1							
✓	2424							6/op	5 $\mu A$
✓	2425	9,1,1,20,1							5 $\mu A$

B.2.3.4. *Pointing Reference*,  $\theta_{pq} = 90^\circ$ ,  $\phi_{pq} = 180^\circ$ .

run	prescales	$p_h$	$\theta_h$	$p_e$	$\theta_e$	target	h/e coll	comment
2426	3,1,1,10,1	1.0660	54.785	3.6600	14.074	10dum	6/6	
2427						15dum		
2428						4dum		
2429						12C		
2430								harp 943

**B.2.4.**  $\theta_{pq} = 50^\circ$ ,  $\phi_{pq} = 180^\circ$ .

B.2.4.1. *Pointing Reference*,  $\theta_{pq} = 50^\circ$ ,  $\phi_{pq} = 180^\circ$ .

run	prescales	$p_h$	$\theta_h$	$p_e$	$\theta_e$	target	h/e coll	comment
2431	3,1,1,10,1	1.2700	50.178	3.6600	14.074	12C	6/6	junk
2432								
2433						4dum		
2434						15dum		
2435						10dum		
2436								junk

B.2.4.2. *Trigger Efficiency Check*,  $\theta_{pq} = 50^\circ$ ,  $\phi_{pq} = 180^\circ$ .

run	prescales	$p_h$	$\theta_h$	$p_e$	$\theta_e$	target	h/e coll
2437	1,1,1,1, $\infty$	1.2700	50.178	3.6600	14.074	LH2	6/6

B.2.4.3. *Production Point*,  $\theta_{pq} = 50^\circ$ ,  $\phi_{pq} = 180^\circ$ .

prod	run	prescales	$p_h$	$\theta_h$	$p_e$	$\theta_e$	target	h/e coll	comment
✓	2438-2439	5k,40, 20,1500,1	1.2700	50.18	3.6600	14.08	LH2	6/6	

prod	run	prescales	$p_h$	$\theta_h$	$p_e$	$\theta_e$	target	h/e coll	comment
✓	2440-2441	5k,40, 20,1500,1	1.2700	50.18	3.6600	14.08	LH2	op/op	
✓	2442	5k,600, 400,1500,1							coda crash
	2443								junk
✓	2444-2453								
✓	2454								tgt ioc rbt
✓	2455-2456								
✓	2457								unstbl bm
✓	2458-2466								
✓	2467								roc14 crash
✓	2468-2474								
✓	2475								unstbl bm
✓	2476								
✓	2477-2478								unstbl bm
✓	2479								
✓	2480								unstbl bm
✓	2481-2492								

B.2.4.4. *Pointing Reference*,  $\theta_{pq} = 50^\circ$ ,  $\phi_{pq} = 180^\circ$ .

run	prescales	$p_h$	$\theta_h$	$p_e$	$\theta_e$	target	h/e coll	comment
2493	3,50,1,200,1	1.2700	50.179	3.6600	14.079	10dum	op/op	junk
2494								
2495						15dum		
2496								junk
2497						4dum		
2498	1,50,1,200,1					12C		
2499								harp 944

**B.2.5.  $\theta_{pq} = 0^\circ$ .**

B.2.5.1. *Pointing Reference,  $\theta_{pq} = 0^\circ$ .*

run	prescales	$p_h$	$\theta_h$	$p_e$	$\theta_e$	target	h/e coll
2500	1,50,1,200,1	1.3782	42.305	3.6600	14.079	12C	op/op
2501						4dum	
2502						15dum	
2503						10dum	

B.2.5.2. *Trigger Efficiency,  $\theta_{pq} = 0^\circ$ .*

run	prescales	$p_h$	$\theta_h$	$p_e$	$\theta_e$	target	h/e coll
2504	1,1,1,1,10k	1.3782	42.305	3.6600	14.079	LH2	6/6

B.2.5.3. *Production Point,  $\theta_{pq} = 0^\circ$ .*

prod	run	prescales	$p_h$	$\theta_h$	$p_e$	$\theta_e$	target	h/e coll	comment
✓	2505-2506	5k,500, 800,1800,1	1.3782	42.305	3.6600	14.079	LH2	6/6	
✓	2507-2537							op/op	
	2538-2546								cosmics
	2547								junk
	2548								harp 945
	2549-2564								junk
✓	2565-2566								
✓	2567							6/op	roc14 crash
	2568								junk
✓	2569-2584								
✓	2585								high dt
✓	2586-2590								
✓	2591								high dt
✓	2592-2597								
	2598-2599								junk

prod	run	prescales	$p_h$	$\theta_h$	$p_e$	$\theta_e$	target	h/e coll	comment
✓	2600-2613	5k,500, 800,1800,1	1.3782	42.305	3.6600	14.079	LH2	6/op	
	2614-2616								junk
✓	2617								ET server down
✓	2618-2625								
	2626-2627								junk

**B.2.6.**  $\theta_{pq} = 25^\circ$ ,  $\phi_{pq} = 0^\circ$ .

B.2.6.1. *Pointing Reference*,  $\theta_{pq} = 25^\circ$ ,  $\phi_{pq} = 0^\circ$ .

run	prescales	$p_h$	$\theta_h$	$p_e$	$\theta_e$	target	h/e coll	comment
2628	1,500,1,1800,1	1.3501	38.117	3.6600	14.074	12C	6/6	harp 948
2629						4dum		
2630						15dum		
2631						10 cm dum		

B.2.6.2. *Trigger Efficiency*,  $\theta_{pq} = 25^\circ$ ,  $\phi_{pq} = 0^\circ$ .

run	prescales	$p_h$	$\theta_h$	$p_e$	$\theta_e$	target	h/e coll	comment
2632	1,1,1,1, $\infty$	1.3501	38.114	3.6600	14.074	LH2	6/6	5 $\mu A$
2633								10 $\mu A$

B.2.6.3. *Production Point*,  $\theta_{pq} = 25^\circ$ ,  $\phi_{pq} = 0^\circ$ .

prod	run	prescales	$p_h$	$\theta_h$	$p_e$	$\theta_e$	target	h/e coll	comment
✓	2634	6k,250, 2500,2500,1	1.3501	38.114	3.6600	14.08	LH2	6/6	
✓	2635	5k,500,2k,2k,1							
✓	2636							op/op	

prod	run	prescales	$p_h$	$\theta_h$	$p_e$	$\theta_e$	target	h/e coll	comment
✓	2637	6k,600, 2400,2400,1	1.3501	38.114	3.6600	14.08	LH2	op/op	
✓	2638-2640	7k,700, 3k,2400,1							
✓	2641								roc14 crash
✓	2642								tgt ioc reboot
✓	2643-2663								
	2664								junk
✓	2665-2675								

### B.2.7. Spectrometer q-Pointing and Optics Checks.

#### B.2.7.1. Singles Data.

run	prescales	$p_h$	$\theta_h$	$p_e$	$\theta_e$	target	h/e coll	comment
2676	23,∞,80,∞,1k	1.3501	38.114	3.6600	18.070	LH2	op/op	unstable beam
2677								

#### B.2.7.2. Electron Optics & Hadron q-Pointing.

run	prescales	$p_h$	$\theta_h$	$p_e$	$\theta_e$	target	h/e coll	comment
2678	23,∞,80,∞,10k	1.552	47.09	3.8064	18.07	LH2	op/sv	e q3 trip
2679								delta -4%
2680				3.7332				delta -2%
2681	1,∞,∞,∞,1			3.6600			6/sv	delta 0%, h $\vec{q}$ pointing



### B.2.7.3. Coincidence Elastic Cross Section.

run	prescales	$p_h$	$\theta_h$	$p_e$	$\theta_e$	target	h/e coll	comment
2682	3, $\infty$ ,3, $\infty$ ,1	1.5520	47.090	3.6600	18.070	LH2	6/6	high dt
2683	10, $\infty$ ,3, $\infty$ ,1							high dt
2684	20, $\infty$ ,6, $\infty$ ,2							optics, q pointing

### B.2.7.4. Quasielastic $^{12}\text{C}$ Run.

run	prescales	$p_h$	$\theta_h$	$p_e$	$\theta_e$	target	h/e coll	comment
2685	200, $\infty$ ,200, $\infty$ ,1	1.5520	47.090	3.6600	18.070	12C	6/6	quasielastic

### B.2.7.5. Single Arm Optics.

run	prescales	$p_h$	$\theta_h$	$p_e$	$\theta_e$	target	h/e coll	comment
2686	1, $\infty$ , $\infty$ , $\infty$ ,1	1.5520	47.090	3.5868	18.070	LH2	6/sv	delta 2%
2687				3.5135				delta 4%

### B.2.7.6. More Coincidence Elastic Cross Section.

run	prescales	$p_h$	$\theta_h$	$p_e$	$\theta_e$	target	h/e coll	comment
2688	1, $\infty$ ,1, $\infty$ ,1	1.5520	47.090	3.5136	18.070	12C	6/6	no rast

## B.3. July 8 - July 9 Facility Development Time

### B.3.1. HRSh Detector Offsets<sup>4</sup>.

#### B.3.1.1. Delta Scan.

run	prescales	$p_h$	$\theta_h$	$p_e$	$\theta_e$	target	h/e coll	comment
2720	2,1,10,100,1,20	2.9940	16.006	1.1000	56.846	12C	sv/6	electron hv off

<sup>4</sup>All runs with spectrometers in reverse polarity.

run	prescales	$p_h$	$\theta_h$	$p_e$	$\theta_e$	target	h/e coll	comment
2721	2,1,10,100,1,20	2.9450	16.006	1.1000	56.846	12C	sv/6	electron hv off
2722	2,1,1,100,1,20							electron hv off

### B.3.1.2. Target Scan.

run	prescales	$p_h$	$\theta_h$	$p_e$	$\theta_e$	target	h/e coll
2723	2,1,1,100,1,20	2.9450	16.006	1.1000	56.846	15dum	6/6
2724						4dum	
2725						10dum	

## B.3.2. (e,e'p) Measurements.

### B.3.2.1. First Point<sup>5</sup>.

run	prescales	$p_h$	$\theta_h$	$p_e$	$\theta_e$	target	h/e coll	comment
2726	300,5,50,1k,1,20	2.9940	16.006	0.9860	56.846	10dum	6/6	junk
2727								
2728	0,1,8,130,1,20					12C		
2729						4LH2	sv/6	
2730							6/6	
2731-2732								junk
2733	500,8,1k,2k,1,20					LH2		

<sup>5</sup>Here 4LH2 = 4 cm LH2 target.

### B.3.2.2. Second Point.

run	prescales	$p_h$	$\theta_h$	$p_e$	$\theta_e$	target	h/e coll	comment
2734	500,8,1k,2k,1,20	2.8020	19.997	1.2385	50.668	LH2	6/6	junk
2735								
2736								junk
2737	150,4,40,500,1,20					10dum		
2738						12C		
2739								junk

### B.3.2.3. Third Point.

run	prescales	$p_h$	$\theta_h$	$p_e$	$\theta_e$	target	h/e coll	comment
2740	1,4,1,500,1,20	2.0772	34.621	2.0765	34.610	12C	6/6	junk
2741								fst fdbk off
2742-2754								junk
2755						LH2		4x1 rast

### B.3.2.4. Fourth Point.

run	prescales	$p_h$	$\theta_h$	$p_e$	$\theta_e$	target	h/e coll	comment
2756	1,4,1,500,1,20	1.8452	40.000	2.2387	30.625	12C	6/6	junk
2757								wrong $p_e$ , should be 2.3287
2758						LH2		wrong $p_e$ , should be 2.3287

### B.3.2.5. Fifth Point.

run	prescales	$p_h$	$\theta_h$	$p_e$	$\theta_e$	target	h/e coll	comment
2759	1,4,1,500,1,20	1.4852	50.021	2.7129	24.770	12C	6/6	
2760								junk
2761						LH2		

## B.4. July 11 - July 31 Run Period

**B.4.1.**  $\theta_{pq} = 50^\circ$ ,  $\phi_{pq} = 0^\circ$ .

B.4.1.1. *Pointing Reference*,  $\theta_{pq} = 50^\circ$ ,  $\phi_{pq} = 0^\circ$ .

run	prescales	$p_h$	$\theta_h$	$p_e$	$\theta_e$	target	h/e coll	comment
2837	1,100,1, $\infty$ ,1, $\infty$	1.2700	34.289	3.6600	14.079	12C	6/6	harp 955
2838								
2839						4dum		
2840						15dum		
2841						10dum		

B.4.1.2. *Trigger Efficiency*,  $\theta_{pq} = 50^\circ$ ,  $\phi_{pq} = 0^\circ$ .

run	prescales	$p_h$	$\theta_h$	$p_e$	$\theta_e$	target	h/e coll
2842	1,1,1,1, $\infty$ , $\infty$	1.2700	34.289	3.6600	14.079	LH2	6/6

B.4.1.3. *Production Point*,  $\theta_{pq} = 50^\circ$ ,  $\phi_{pq} = 0^\circ$ .

prod	run	prescales	$p_h$	$\theta_h$	$p_e$	$\theta_e$	target	h/e coll	comment
✓	2843	2k,50,2k, 100,1, $\infty$	1.2700	34.289	3.6600	14.08	LH2	6/6	adjusting rast
✓	2844								coda prob
✓	2845								5-40 $\mu A$
✓	2846-2847								
	2848								junk
✓	2849							op/op	fast fdbk off unstbl bm
✓	2850								fast fdbk off
	2851-2852								junk
✓	2853-2855								
✓	2856								unstbl bm
✓	2857-2858								

prod	run	prescales	$p_h$	$\theta_h$	$p_e$	$\theta_e$	target	h/e coll	comment
✓	2859	2k,50,2k, 100,1, $\infty$	1.2700	34.289	3.6600	14.08	LH2	op/op	aero in trig
✓	2860	2k,50,2k, 100,1,2k							unstbl bm
✓	2861								
✓	2862								unstbl bm
✓	2863-2864								
✓	2865								coda crash
✓	2866								31 $\mu A$
✓	2867								high dt
✓	2868								
✓	2869								no aero in trig
✓	2870-2872								
✓	2873-2884	758,50,897, 308,1,2k							
	2885								junk
✓	2886								
	2887								junk
	2888-2896								cosmics
	2897								junk
	2898								harp 956
✓	2899	758,42,884, 314,1, $\infty$							new inject gun
✓	2900-2901	10k,1k,13k, 4k,1, $\infty$							
✓	2902-2903								unstbl bm
✓	2904-2906								
✓	2907								file split
✓	2908-2912								
✓	2913-2914								file split
✓	2915-2922								

prod	run	prescales	$p_h$	$\theta_h$	$p_e$	$\theta_e$	target	h/e coll	comment
✓	2923-2924	10k,1k,7k, 4k,1,6k	1.2700	34.289	3.6600	14.08	LH2	op/op	no aero in trig
✓	2925								normal trig
✓	2926-2933	10k,1k,13k, 4k,1, $\infty$							
	2934								junk
✓	2935-2939								
✓	2940								h dep ch asy 1.0%
✓	2941								h dep ch asy -1.2%
✓	2942								h dep ch asy 0.9%
✓	2943								h dep ch asy 0.5%
	2944								junk
✓	2945								h dep ch asy 0.23%
✓	2946								h dep ch asy 0.14%
	2947								junk
✓	2948								h dep ch asy 4.6e-4
	2949								junk
✓	2950-2953								
✓	2954								bpm prob
✓	2955-2960								
	2961								junk
✓	2962-2971								
✓	2972								high dt
✓	2973-2974								
✓	2976-2991								
✓	2992								coda crash

prod	run	prescales	$p_h$	$\theta_h$	$p_e$	$\theta_e$	target	h/e coll	comment
✓	2993-3018	10k,1k,13k, 4k,1, $\infty$	1.2700	34.289	3.6600	14.08	LH2	op/op	
✓	3019								high dt
✓	3020-3030								
	3031								junk
✓	3032								fast fdbk off
✓	3033-3037								

**B.4.2.**  $\theta_{pq} = 90^\circ$ ,  $\phi_{pq} = 0^\circ$ .

run	comment
3038	cosmics
3039	junk
3040	harp 958 (bpm x=0, y=0)
3041	harp 959 (bpm x=-1, y=-1)
3042-3043	junk
3044	harp 960 (bpm x=-1, y=+1) & harp 961 (bpm x=+1, y=+1)
3045	harp 962 (x=+1, y=-1)

B.4.2.1. *Pointing Reference*,  $\theta_{pq} = 90^\circ$ ,  $\phi_{pq} = 0^\circ$ .

run	prescales	$p_h$	$\theta_h$	$p_e$	$\theta_e$	target	h/e coll	comment
3046	1,10k,1,20k,1, $\infty$	1.0660	29.812	3.6600	14.078	12C	6/6	5 $\mu A$ , rast off
3047						4dum		"
3048						15dum		"
3049						10dum		"

B.4.2.2. *Trigger Efficiency*,  $\theta_{pq} = 90^\circ$ ,  $\phi_{pq} = 0^\circ$ .

run	prescales	$p_h$	$\theta_h$	$p_e$	$\theta_e$	target	h/e coll	comment
3050	1,1,1,1, $\infty$ , $\infty$	1.0660	29.812	3.6600	14.078	LH2	6/6	aerogel in trigger

B.4.2.3. *Production Point*,  $\theta_{pq} = 90^\circ$ ,  $\phi_{pq} = 0^\circ$ .

prod	run	prescales	$p_h$	$\theta_h$	$p_e$	$\theta_e$	target	h/e coll	comment
✓	3051	4k,100,7k, 2300,1, $\infty$	1.0660	29.812	3.6600	14.078	LH2	6/6	aero in trig high dt
✓	3052	4k,200,7k, 2300,1,10200							
✓	3053							op/op	
✓	3054-3102	4500,400,9k, 2500,1,14k							
✓	3103								old trig
✓	3105-3141								aero in trig
✓	3142	4500,400,100, 2500,1,14k							old trig
✓	3143-3154	4500,400,9k, 2500,1,14k							aero in trig
	3155								junk
✓	3156								
✓	3157								e scint HV adjust prior
✓	3158								
✓	3159								unstbl bm roc15 reset
✓	3160-3179								
✓	3180	4500,400,9k, 2500,1,1400							coda prob
✓	3181-3208								



prod	run	prescales	$p_h$	$\theta_h$	$p_e$	$\theta_e$	target	h/e coll	comment
✓	3209	4500,400,9k, 2500,1,1400	1.0660	29.812	3.6600	14.078	LH2	op/op	26 $\mu A$ , dt check
✓	3210-3223								
✓	3224								10.8 $\mu A$ , dt check
	3225								junk
✓	3226-3234								
	3235								junk
✓	3236-3238	4500,400,9k, 2500,1,14k							
✓	3239								no end run
✓	3240-3263								
	3264-3266								cosmics
	3267-3268								pulser
	3269-3296								cosmics
✓	3297								5 $\mu A$
✓	3298								10 $\mu A$
✓	3299								21 $\mu A$
✓	3300								47 $\mu A$
✓	3301-3306								
	3307								junk

**B.4.3.**  $\theta_{pq} = 135^\circ$ ,  $\phi_{pq} = 0^\circ$ .

B.4.3.1. *Pointing Reference*,  $\theta_{pq} = 135^\circ$ ,  $\phi_{pq} = 0^\circ$ .

run	prescales	$p_h$	$\theta_h$	$p_e$	$\theta_e$	target	h/e coll	comment
3308	1,4k,2,12500,1,14k	0.8188	30.806	3.6600	14.074	12C	6/6	harp 963
3309-3310								junk
3311								harp 964-965
3312-3313						4dum		
3314-3315						15dum		

run	prescales	$p_h$	$\theta_h$	$p_e$	$\theta_e$	target	h/e coll	comment
3316	1,4k,2,12500,1,14k	0.8188	30.806	3.6600	14.074	10dum	6/6	

B.4.3.2. *Trigger Efficiency*,  $\theta_{pq} = 135^\circ$ ,  $\phi_{pq} = 0^\circ$ .

run	prescales	$p_h$	$\theta_h$	$p_e$	$\theta_e$	target	h/e coll
3317	1,1,1,1, $\infty$ ,1	0.8188	30.806	3.6600	14.074	LH2	??/6

B.4.3.3. *Production Point*,  $\theta_{pq} = 135^\circ$ ,  $\phi_{pq} = 0^\circ$ .

prod	run	prescales	$p_h$	$\theta_h$	$p_e$	$\theta_e$	target	h/e coll	comment
✓	3318	4k,50, $\infty$ , 2800,1,15k	0.8188	30.806	3.6600	14.074	LH2	6/6	5 $\mu A$
✓	3319								10 $\mu A$
✓	3320								20 $\mu A$
✓	3321								40 $\mu A$
✓	3322	4k,200,10k, 2800,1,15k				14.079		op/op	48 $\mu A$ , file split
✓	3323								
✓	3324-3328	4385,334, 12931,2677, 1,20664							
✓	3329								25 $\mu A$ , eff. test
✓	3330								44 $\mu A$
✓	3331								
✓	3332								file split 2x
✓	3333								file split
✓	3334								
✓	3335								high dt
	3336								junk
✓	3337-3372								

prod	run	prescales	$p_h$	$\theta_h$	$p_e$	$\theta_e$	target	h/e coll	comment
✓	3373	4385,334, 12931,2677, 1,20664	0.8188	30.806	3.6600	14.079	LH2	op/op	file split
✓	3374-3411								
✓	3417								roc14 crash
✓	3418-3419								old trig
	3420								junk
✓	3421								
✓	3422								high dt
✓	3424-3465								
✓	3466								high dt
	3467-3492								junk
	3493-3495								cosmics
✓	3496-3509	4407,297, 13322,2718, 1,21190							diff T0
✓	3510								high dt, diff TO
✓	3512								file split, diff TO
✓	3513-3517								diff T0, tdc prob
	3518-3526								cosmics
✓	3527								spot check, fst fdbk off
✓	3528-3534								
✓	3535								coda crash
✓	3536-3549								
✓	3550-3551								fst fdbk off
✓	3552								
	3553								junk
✓	3554-3555								
✓	3556								unstbl bm

prod	run	prescales	$p_h$	$\theta_h$	$p_e$	$\theta_e$	target	h/e coll	comment
✓	3557-3558	4407,297, 13322,2718, 1,21190	0.8188	30.806	3.6600	14.079	LH2	op/op	
✓	3559								tdc fixed
✓	3560								high dt
✓	3561-3563								
✓	3564								high dt
	3565								junk
✓	3566-3578								
✓	3579								high dt
	3580-3581								junk
✓	3582-3622								
✓	3623								$2 \mu A$
✓	3624-3633								

#### B.4.4. Electron Arm Optics.

run	prescales	$p_h$	$\theta_h$	$p_e$	$\theta_e$	target	h/e coll
3634	1, $\infty$ , $\infty$ , $\infty$ , $\infty$ , $\infty$	0.8188	30.806	3.6600	14.075	LH2	op/sv
3635		0.7919					??/sv
3636		0.7499	34.703				6/sv
3637		0.7485					
3638		0.7477					
3639		0.7408					
3640		0.7418					op/sv

**B.4.5.  $\theta_{pq} = 155^\circ$ ,  $\phi_{pq} = 0^\circ$ .**

**B.4.5.1. *Pointing Reference*,  $\theta_{pq} = 155^\circ$ ,  $\phi_{pq} = 0^\circ$ .**

run	prescales	$p_h$	$\theta_h$	$p_e$	$\theta_e$	target	h/e coll	comment
3641	1, $\infty$ ,1, $\infty$ , $\infty$ , $\infty$	0.7418	34.709	3.6600	14.074	10dum	6/6	
3642								harp 966
3643	3, $\infty$ ,10, $\infty$ , $\infty$ , $\infty$	0.7418	34.709	3.6600	14.074	10dum	6/6	harp 967
3644	2, $\infty$ ,8, $\infty$ , $\infty$ , $\infty$							
3645						15dum		
3646						4dum		
3647	1, $\infty$ ,4, $\infty$ , $\infty$ , $\infty$							
3648						12C		

**B.4.5.2. *Trigger Efficiency*,  $\theta_{pq} = 155^\circ$ ,  $\phi_{pq} = 0^\circ$ .**

run	prescales	$p_h$	$\theta_h$	$p_e$	$\theta_e$	target	h/e coll
3649-3650	1,1,1,1, $\infty$ ,1	0.7418	34.703	3.6600	14.074	LH2	6/6

**B.4.5.3. *Production Point*,  $\theta_{pq} = 155^\circ$ ,  $\phi_{pq} = 0^\circ$ .**

prod	run	prescales	$p_h$	$\theta_h$	$p_e$	$\theta_e$	target	h/e coll	comment
✓	3651	4407,297, 13322,2718, 1,21190	0.7418	34.703	3.6600	14.074	LH2	6/6	
✓	3652-3669					14.079		op/op	
✓	3670								roc14 crash
✓	3671								no bpm info
✓	3672-3677								
✓	3678								unstbl bm
✓	3679								unstbl bm
✓	3680								unstbl bm
✓	3681								
✓	3682								unstbl bm

prod	run	prescales	$p_h$	$\theta_h$	$p_e$	$\theta_e$	target	h/e coll	comment
✓	3683	4407,297, 13322,2718, 1,21190	0.7418	34.703	3.6600	14.079	LH2	op/op	some pulsed
✓	3684-3695								
✓	3696								er back up
	3697								junk
✓	3698-3704								
✓	3705								er back up
	3706-3707								junk
✓	3708-3726								
✓	3727-3762	5234,394, 14661,2845, 1,21040							5 $\mu A$
✓	3763								5 $\mu A$
✓	3764								10 $\mu A$
✓	3765								20 $\mu A$
✓	3766-3767								40 $\mu A$
✓	3768-3775								
✓	3776								high dt
	3777								junk
✓	3778-3785								
✓	3786								unstbl bm
✓	3787-3798								
✓	3799								unstbl bm
✓	3800								
✓	3801								unstbl bm
✓	3802-3833								
	3834								junk
✓	3835-3840								
✓	3841								70 % dt
✓	3842-3858								
✓	3859								high dt
✓	3860-3893								

prod	run	prescales	$p_h$	$\theta_h$	$p_e$	$\theta_e$	target	h/e coll	comment
✓	3894	5234,394, 14661,2845, 1,21040	0.7418	34.703	3.6600	14.079	LH2	op/op	daq prob
	3895								junk
✓	3896-3925								
✓	3926-3927								old trig

#### B.4.6. Deadtime Study.

run	prescales	$p_h$	$\theta_h$	$p_e$	$\theta_e$	target	h/e coll	comment
3928-3929	7500,50,44k, 5200,1,21040	0.7031	27	3.6600	14.079	LH2	op/ op	old trig, rast off, had strobe 820 kHz
3930			21					old trig, had strobe 1 MHz
3931								junk
3932								old trig, had strobe 1 MHz
3933-3934	7500,500,50k, 6k,3,21040							old trig, had strobe 1 MHz

#### B.4.7. $\theta_{pq} = 180^\circ$ .

##### B.4.7.1. Pointing Reference, $\theta_{pq} = 180^\circ$ .

run	prescales	$p_h$	$\theta_h$	$p_e$	$\theta_e$	target	h/e coll	comment
3935	1,500,3,6k,1,21040	0.7031	42.282	3.6600	14.079	12C	op/op	junk
3936								rast off
3937						4dum		harp 971
3938								harp 972
3939						15dum		
3940						10dum		

B.4.7.2. *Trigger Efficiency,  $\theta_{pq} = 180^\circ$ .*

run	prescales	$p_h$	$\theta_h$	$p_e$	$\theta_e$	target	h/e coll	comment
3941	1,1,1,1, $\infty$ ,21040	0.7031	42.282	3.6600	14.079	LH2	op/op	aero in trig

B.4.7.3. *Production Point,  $\theta_{pq} = 180^\circ$ .*

prod	run	prescales	$p_h$	$\theta_h$	$p_e$	$\theta_e$	target	h/e coll	comment
✓	3942	7500,50, 20k,3k, 1,21040	0.7031	42.282	3.6600	14.079	LH2	op/op	aero in trig
✓	3943	7500,500, 20k,3k, 1,21040							
✓	3944-3945	6968,488, 18592,3078, 1,21040							
✓	3946-3949								old trig
✓	3950								aero in trig, 42 $\mu A$
✓	3951								30 $\mu A$
✓	3952								20 $\mu A$
✓	3953								10 $\mu A$
✓	3954								5 $\mu A$
✓	3955								41 $\mu A$
✓	3956-3958					14.074		6/6	
✓	3959-3961								old trig
✓	3962								unstbl bm
✓	3963-3964								
✓	3965								unstbl bm
✓	3966								
✓	3967-3968					14.079		op/op	aero in trig



prod	run	prescales	$p_h$	$\theta_h$	$p_e$	$\theta_e$	target	h/e coll	comment
✓	3969-3970	6968,4888, 18592,3078, 1,19900							
✓	3971-3997	4912,337, 9979,2042, 1,13163							
✓	3998								roc14 crash
✓	3999-4000								
✓	4005								coda prob
✓	4006-4013								
✓	4014								stk trace err
✓	4015								
✓	4016								high dt
✓	4017-4021								
✓	4022								unstbl bm
✓	4023-4028								
✓	4029								unstbl bm
✓	4030-4034								

#### B.4.8. Elastic (e'p).

run	prescales	$p_h$	$\theta_h$	$p_e$	$\theta_e$	target	h/e coll	comment
4035	1, $\infty$ ,1, $\infty$ ,1, $\infty$	1.1880	54.201	3.9540	14.077	12C	6/6	10 $\mu A$
4036	2000,50,200,600,1, $\infty$					LH2		high dt
4037								e Q2 fault
4038-4039	1866,54,141,498,1, $\infty$							
4040								e Q2 fault



## APPENDIX C

### " $N \rightarrow \Delta$ " INTERNAL REPORT ON DATABASE AND $\beta$ OPTIMIZATION

A finalized list of the specific header files and databases used in the analysis of the production data for the " $N \rightarrow \Delta$ " experiment are found in Tab. C.1. The use of different databases arise due to different optimizations, as will be discussed further in this appendix. Different header files must be used for each kinematic setting because these headers depend on the proton kinematics (which change from kinematic setting to kinematic setting). The same header file cannot be used from one pass through a kinematic setting to another pass through the same setting because the mispointing of the spectrometer changes whenever the spectrometer is moved (see Appendix A), and this mispointing is included in the header file.

Each header file contains information pertaining to the particular spectrometer setting such as the magnetic fields of the dipoles, the spectrometer angles, and the spectrometer offsets. The spectrometer angles were determined using the relations:

$$\theta_{spec} = \theta_{fm} - \frac{p_{carbon}}{8458 \text{ mm}} \left( \frac{57.296^\circ}{\text{rad}} \right), \quad (\text{C.0.1})$$

$$\theta_{fm} = \theta_{LVDT} + \frac{p_{LVDT}}{8458 \text{ mm}} \left( \frac{57.296^\circ}{\text{rad}} \right), \quad (\text{C.0.2})$$

where  $\theta_{spec}$  is the spectrometer angle needed for the header file,  $\theta_{fm}$  is the angle between the front jack of the spectrometer and the target,  $\theta_{LVDT}$  is the spectrometer angle determined by the LVDT code,  $p_{carbon}$  and  $p_{LVDT}$  are carbon and LVDT mispointing values found in Tabs. A.2 and A.3, and 8458 mm is the distance from the front jack of the spectrometer to the target. The electron and hadron spectrometer  $x$ - and  $z$ -offsets used in the header files can be found in Tabs. A.4, A.5, A.6, and A.7. The values used for both the electron and hadron  $y$ -offsets are those determined by the LVDT code. The header files also contain information specific to the target used, but for all production running this target was liquid  $^1\text{H}$  and thus, this information is the same for all of the header files listed in Tab. C.1.

TABLE C.1. List of database and header files used in analysis of production runs.

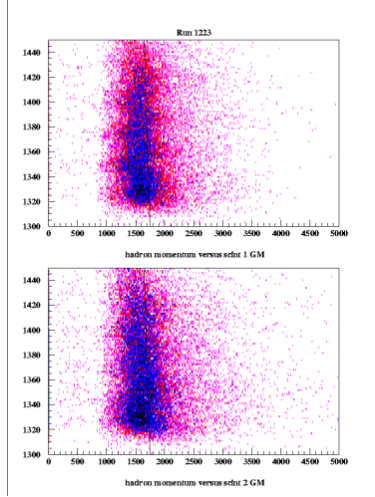
$\theta_{pq}$	runs	database	header
0°	1220-1238	<i>db_ndelta_1</i>	<i>hdr_ndelta_thcm0_1</i>
25°	1246-1268	⋮	<i>hdr_ndelta_thcm25_1</i>
-25°	1278-1305	⋮	<i>hdr_ndelta_thcm-25_1</i>
50°	1322-1340	⋮	<i>hdr_ndelta_thcm50_1</i>
⋮	1372-1386	<i>db_ndelta_2</i>	<i>hdr_ndelta_thcm50_2</i>
-50°	1400-1418	⋮	<i>hdr_ndelta_thcm-50_1</i>
-90°	1428-1456	⋮	<i>hdr_ndelta_thcm-90_1</i>
90°	1468-1531, 1548	⋮	<i>hdr_ndelta_thcm90_1</i>
135°	1568-1654	<i>db_ndelta_3</i>	<i>hdr_ndelta_thcm135_1</i>
-135°	1667-1683	⋮	<i>hdr_ndelta_thcm-135_1</i>
155°	1700-1752	⋮	<i>hdr_ndelta_thcm155_1</i>
-155°	1765-1795, 1802-1805	⋮	<i>hdr_ndelta_thcm-155_1</i>
⋮	1837-2011, 2017-2033	⋮	<i>hdr_ndelta_thcm-155_2</i>
-135°	2045-2247	<i>db_ndelta_4</i>	<i>hdr_ndelta_thcm-135_2</i>
-90°	2271-2425	⋮	<i>hdr_ndelta_thcm-90_2</i>
-50°	2437-2492	⋮	<i>hdr_ndelta_thcm-50_2</i>
0°	2504-2625	⋮	<i>hdr_ndelta_thcm0_2</i>
25°	2632-2675	⋮	<i>hdr_ndelta_thcm25_2</i>
50°	2842-3037	<i>db_ndelta_5</i>	<i>hdr_ndelta_thcm50_3</i>
90°	3050-3306	⋮	<i>hdr_ndelta_thcm90_2</i>
135°	3317-3512	⋮	<i>hdr_ndelta_thcm135_2</i>
⋮	3559-3633	<i>db_ndelta_6</i>	⋮
155°	3649-3927	⋮	<i>hdr_ndelta_thcm155_2</i>
180°	3941-4034	⋮	<i>hdr_ndelta_thcm180_1</i>

The six finalized databases originated as two databases, *db\_ndelta\_period1* and *db\_ndelta\_period2*. The *db\_ndelta\_period1* database was the original database used for the first run periods, May 19 - June 30, 2000 and contained optimized beta, optimized scintillator ADCs, optimized scintillator VDCs, and the correct coefficients for the BPMs as

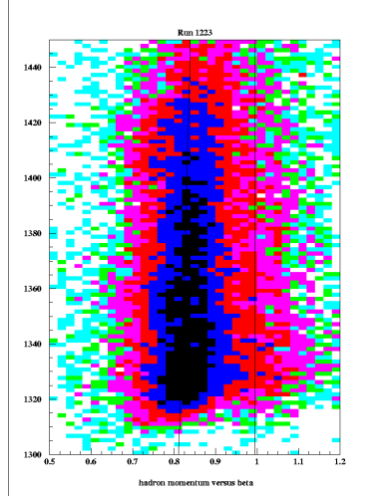
determined by Z. Chai. It also contained the electron  $\theta$ ,  $\phi$ ,  $y_{tg}$ ,  $y000$ ,  $t000$ , and  $p000$  as optimized by N. Liyanage. He began with the VDC 3.5 GeV database; optimized the  $t000$ ,  $y000$ , and  $p000$  using run number 1760; then optimized  $\theta$  and  $\phi$  using  $^1\text{H}$  and sieve slit data using a reduced number of elements in  $\theta$ ; and optimized the  $y030$  element. There are no  $t000$  or  $y000$  terms for electron optics in this database. This optimization was then improved upon by Z. Chai. The hadron and electron arm  $\delta$ 's were optimized by the author of this thesis and E. Penel, respectively, using the December 1999  $^{12}\text{C}$  elastic data. The hadron arm  $\theta$  and  $\phi$  were optimized by Z. Chai using the December 1999 845 MeV data, while he optimized the hadron arm  $y_{tg}$ ,  $y000$ ,  $p000$ , and  $t000$  using the 700 MeV and 1.0 GeV  $\delta$  pointing data. The differences between  $db\_ndelta\_1$ ,  $db\_ndelta\_2$ ,  $db\_ndelta\_3$ , and  $db\_ndelta\_4$  arise in the optimization of the scintillator ADC geometric means (proportional to the amount of energy deposited in the ADC). This deposited energy was optimized over four different sets of runs; runs 1220-1340 resulting in  $db\_ndelta\_1$ , runs 1372-1548 resulting in  $db\_ndelta\_2$ , runs 1568-2033 resulting in  $db\_ndelta\_3$ , runs 2045-2675 resulting in  $db\_ndelta\_4$ . Each of these four databases are the same except for this deposited energy optimization. Detailed descriptions of optimization techniques can be found in Ref. [59].

The  $db\_ndelta\_period2$  database was the original database to be used for the final run period, July 11 - July 31. The differences between  $db\_ndelta\_5$  and  $db\_ndelta\_6$  are limited to optimization of hadron arm deposited energy and the hadron arm  $\beta$ .

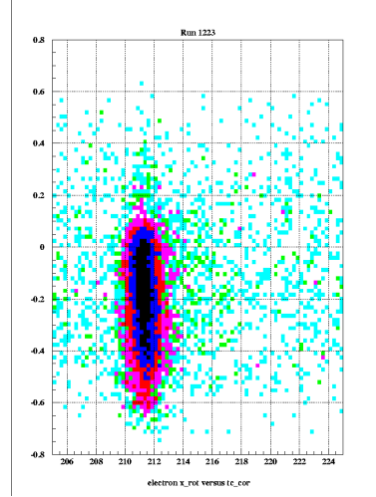
The optimizations of the hadron arm deposited energy, hadron arm  $\beta$ , and time offsets were performed by N. Liyanage and this author. Figs. C.0.1-C.0.6 show the hadron arm deposited energy optimizations, hadron arm  $\beta$  optimizations, and electron arm  $t_{cor}$  optimizations (shown compared to  $x_{rot}$ , the dispersive position of the particle track in the u1 scintillator plane).



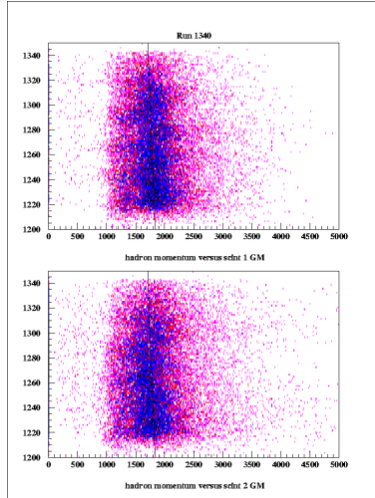
(a)  $p_p$  versus deposited energy for run 1223.



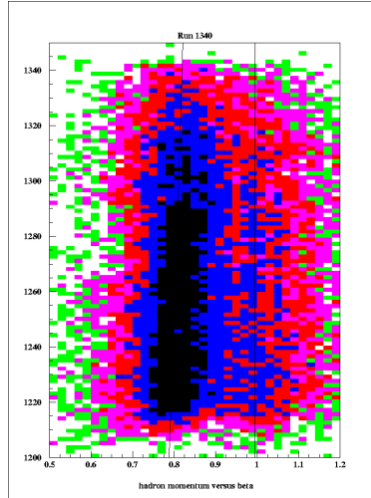
(b)  $p_p$  versus  $\beta$  for run 1223.



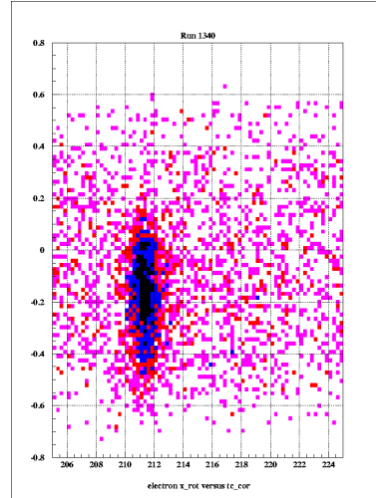
(c) Electron  $x_{rot}$  versus  $tc_{cor}$  for run 1223.



(d)  $p_p$  versus deposited energy for run 1340.

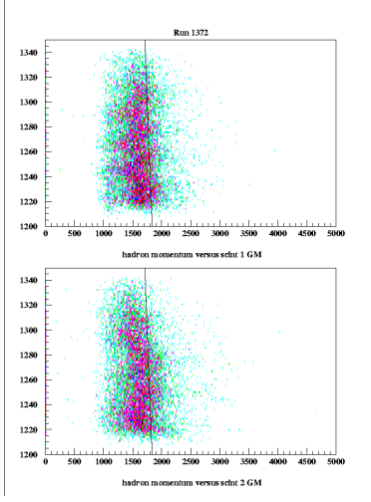


(e)  $p_p$  versus  $\beta$  for run 1340.

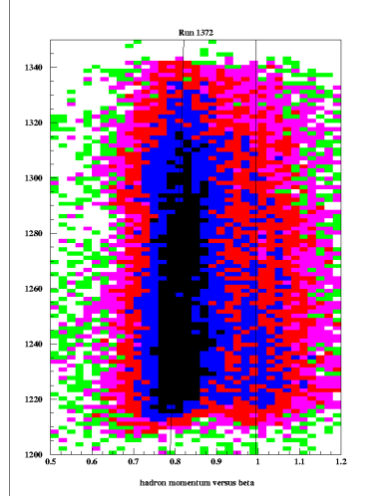


(f) Electron  $x_{rot}$  versus  $tc_{cor}$  for run 1340.

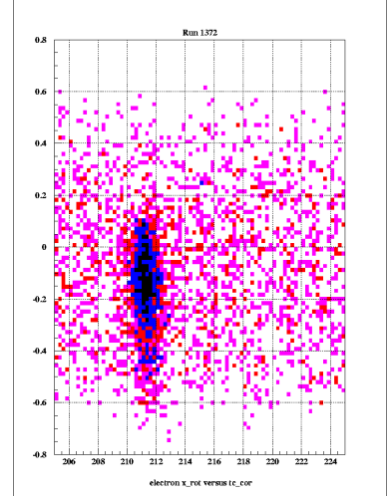
FIGURE C.0.1. Optimizations of hadron arm momentum versus energy deposited, hadron arm momentum versus  $\beta$ , and electron arm  $x_{rot}$  versus  $tc_{cor}$  for runs 1223 ( $\theta_{pq} = 0^\circ$ ) and 1340 ( $\theta_{pq} = 50^\circ$ ) using database *db\_ndelta\_1*.



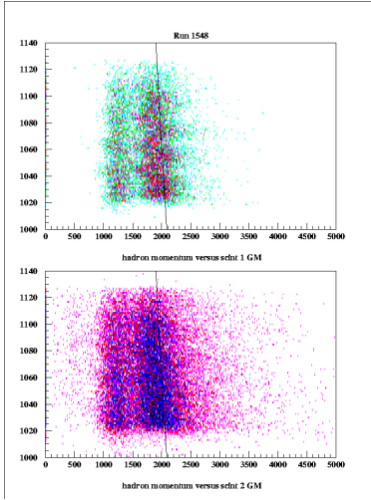
(a)  $p_p$  versus deposited energy for run 1372.



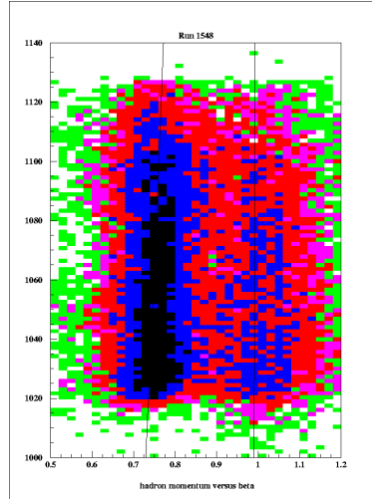
(b)  $p_p$  versus  $\beta$  for run 1372.



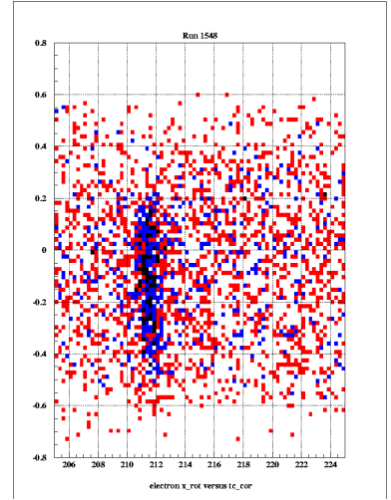
(c) Electron  $x_{rot}$  versus  $tc_{cor}$  for run 1372.



(d)  $p_p$  versus deposited energy for run 1548.

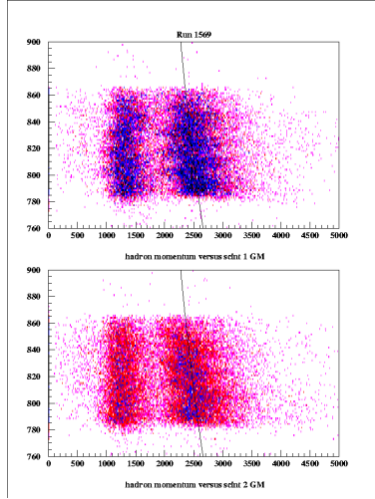


(e)  $p_p$  versus  $\beta$  for run 1548.

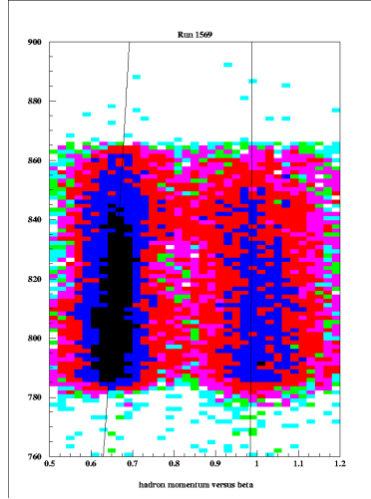


(f) Electron  $x_{rot}$  versus  $tc_{cor}$  for run 1548.

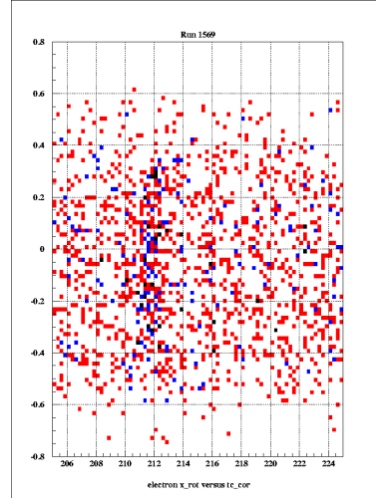
FIGURE C.0.2. Optimizations of hadron arm momentum versus energy deposited, hadron arm momentum versus  $\beta$ , and electron arm  $x_{rot}$  versus  $tc_{cor}$  for runs 1372 ( $\theta_{pq} = 50^\circ$ ) and 1548 ( $\theta_{pq} = 90^\circ$ ) using database *db\_ndelta\_2*.



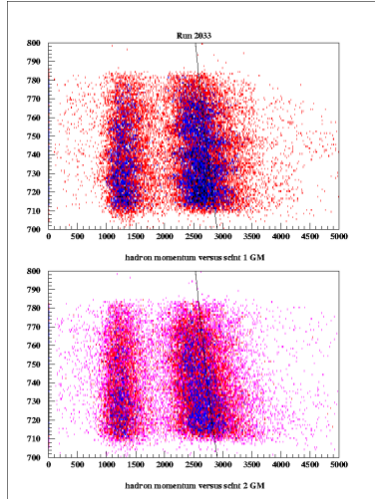
(a)  $p_p$  versus deposited energy for run 1569.



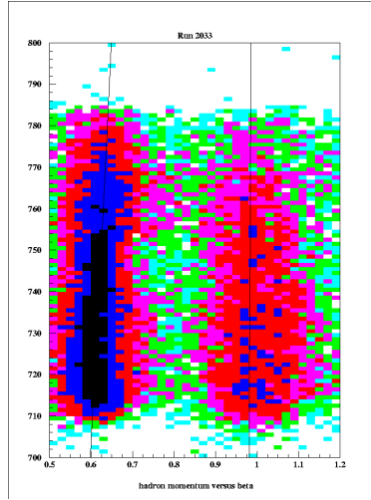
(b)  $p_p$  versus  $\beta$  for run 1569.



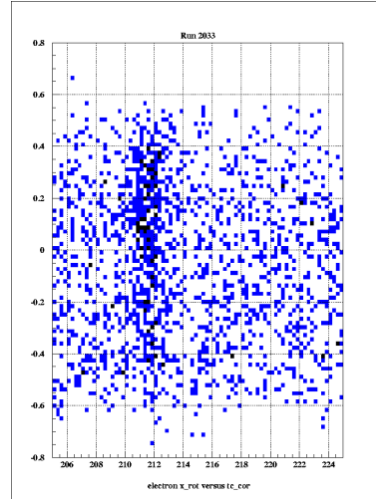
(c) Electron  $x_{rot}$  versus  $tc_{cor}$  for run 1569.



(d)  $p_p$  versus deposited energy for run 2033.



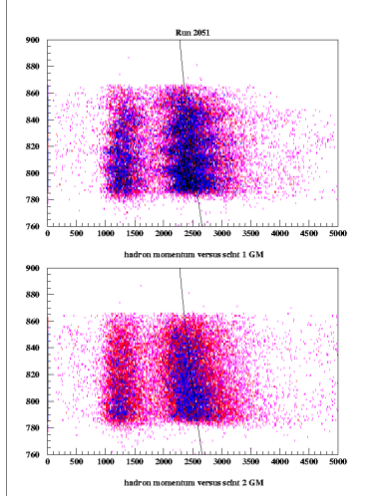
(e)  $p_p$  versus  $\beta$  for run 2033.



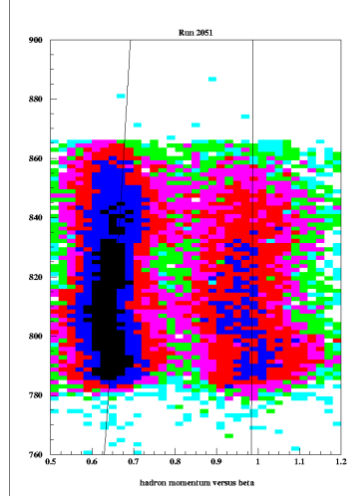
(f) Electron  $x_{rot}$  versus  $tc_{cor}$  for run 2033.

FIGURE C.0.3. Optimizations of hadron arm momentum versus energy deposited, hadron arm momentum versus  $\beta$ , and electron arm  $x_{rot}$  versus  $tc_{cor}$  for runs 1569 ( $\theta_{pq} = 135^\circ$ ) and 2033 ( $\theta_{pq} = -155^\circ$ ) using database *db\_ndelta\_3*.

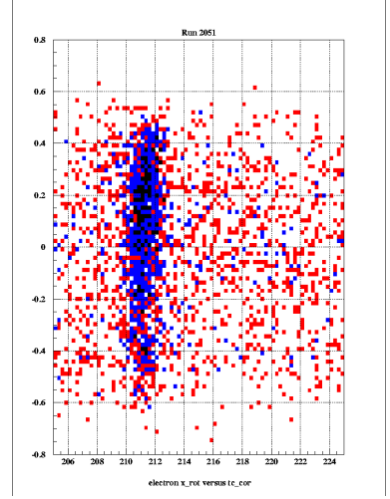




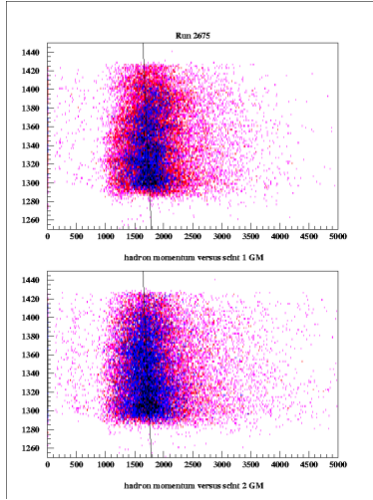
(a)  $p_p$  versus deposited energy for run 2051.



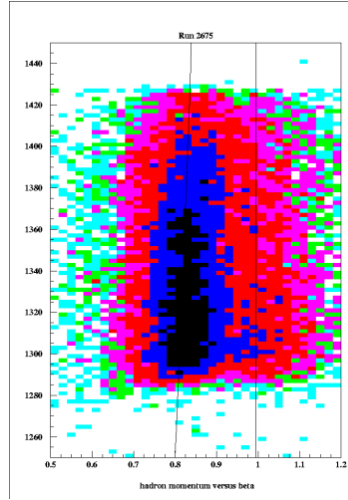
(b)  $p_p$  versus  $\beta$  for run 2051.



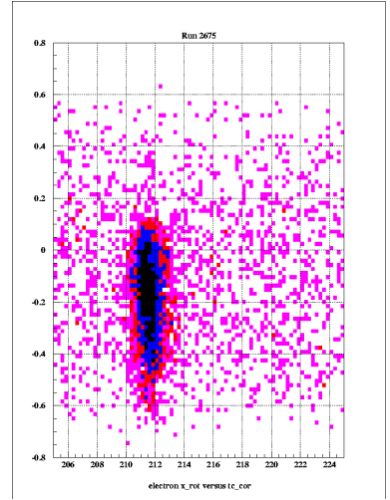
(c) Electron  $x_{rot}$  versus  $tc_{cor}$  for run 2051.



(d)  $p_p$  versus deposited energy for run 2675.

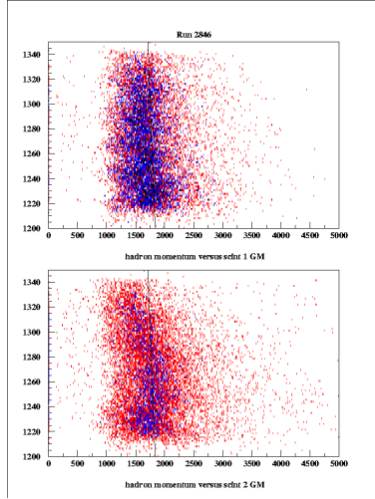


(e)  $p_p$  versus  $\beta$  for run 2675.

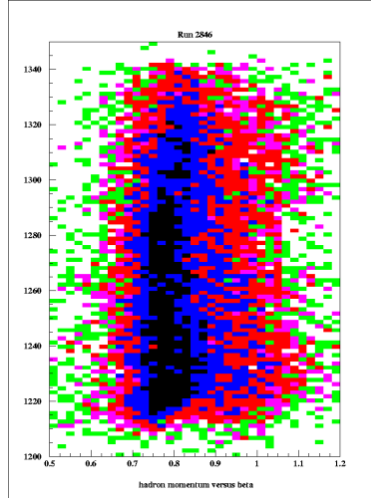


(f) Electron  $x_{rot}$  versus  $tc_{cor}$  for run 2675.

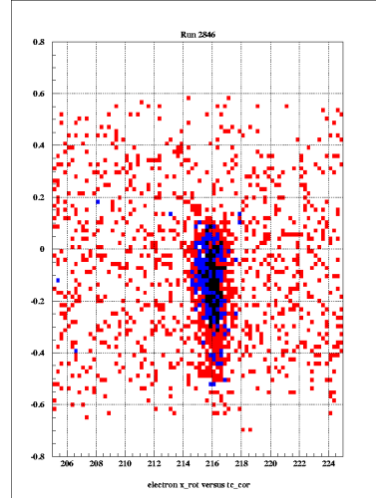
FIGURE C.0.4. Optimizations of hadron arm momentum versus energy deposited, hadron arm momentum versus  $\beta$ , and electron arm  $x_{rot}$  versus  $tc_{cor}$  for runs 2051 ( $\theta_{pq} = -135^\circ$ ) and 2675 ( $\theta_{pq} = 25^\circ$ ) using database *db\_ndelta\_4*.



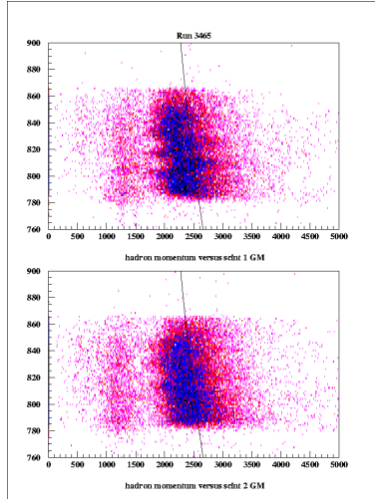
(a)  $p_p$  versus deposited energy for run 2846.



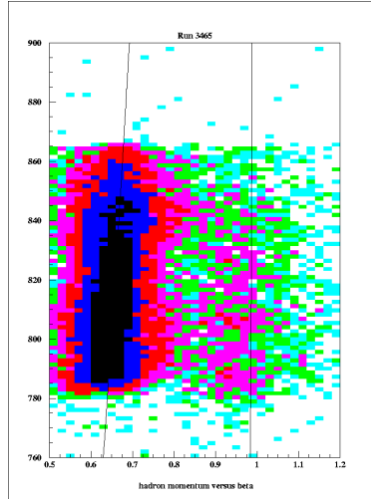
(b)  $p_p$  versus  $\beta$  for run 2846.



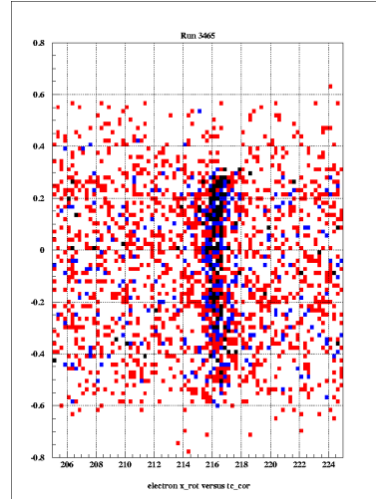
(c) Electron  $x_{rot}$  versus  $tc_{cor}$  for run 2846.



(d)  $p_p$  versus deposited energy for run 3465.

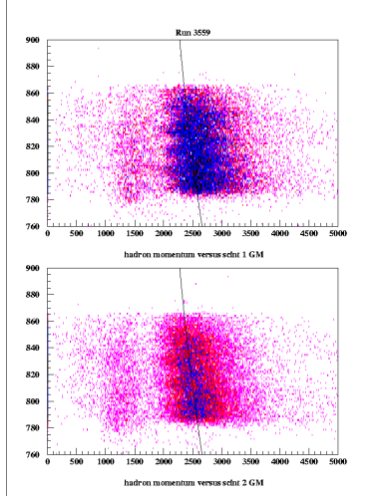


(e)  $p_p$  versus  $\beta$  for run 3465.

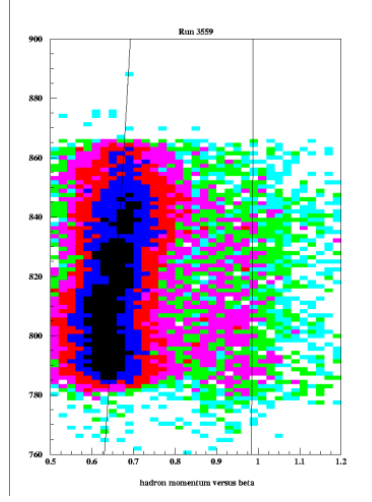


(f) Electron  $x_{rot}$  versus  $tc_{cor}$  run 3465.

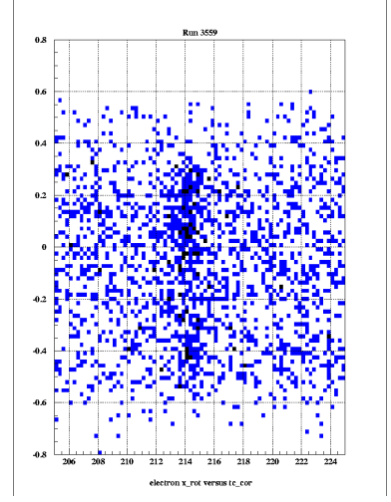
FIGURE C.0.5. Optimizations of hadron arm momentum versus energy deposited, hadron arm momentum versus  $\beta$ , and electron arm  $x_{rot}$  versus  $tc_{cor}$  for runs 2846 ( $\theta_{pq} = 50^\circ$ ) and 3465 ( $\theta_{pq} = 135^\circ$ ) using database *db\_delta\_5*.



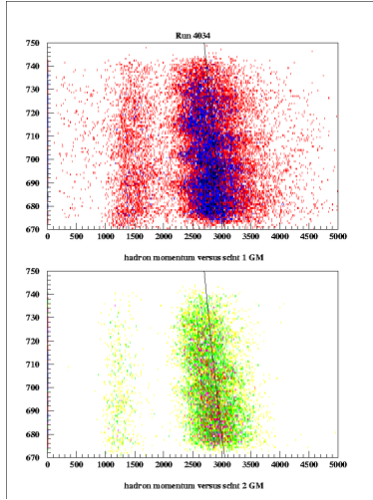
(a)  $p_p$  versus deposited energy for run 3559.



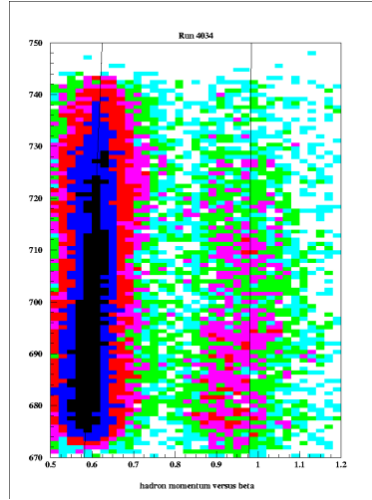
(b)  $p_p$  versus  $\beta$  for run 3559.



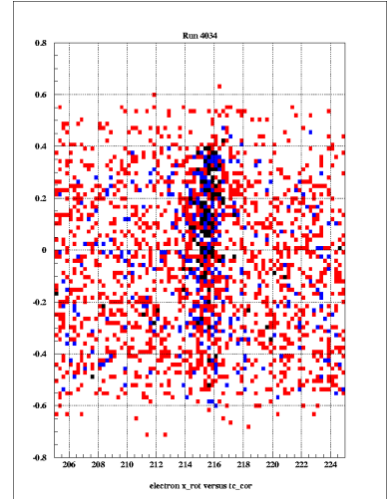
(c) Electron  $x_{rot}$  versus  $tc_{cor}$  for run 3559.



(d)  $p_p$  versus deposited energy for run 4034.



(e)  $p_p$  versus  $\beta$  for run 4034.



(f) Electron  $x_{rot}$  versus  $tc_{cor}$  for run 4034.

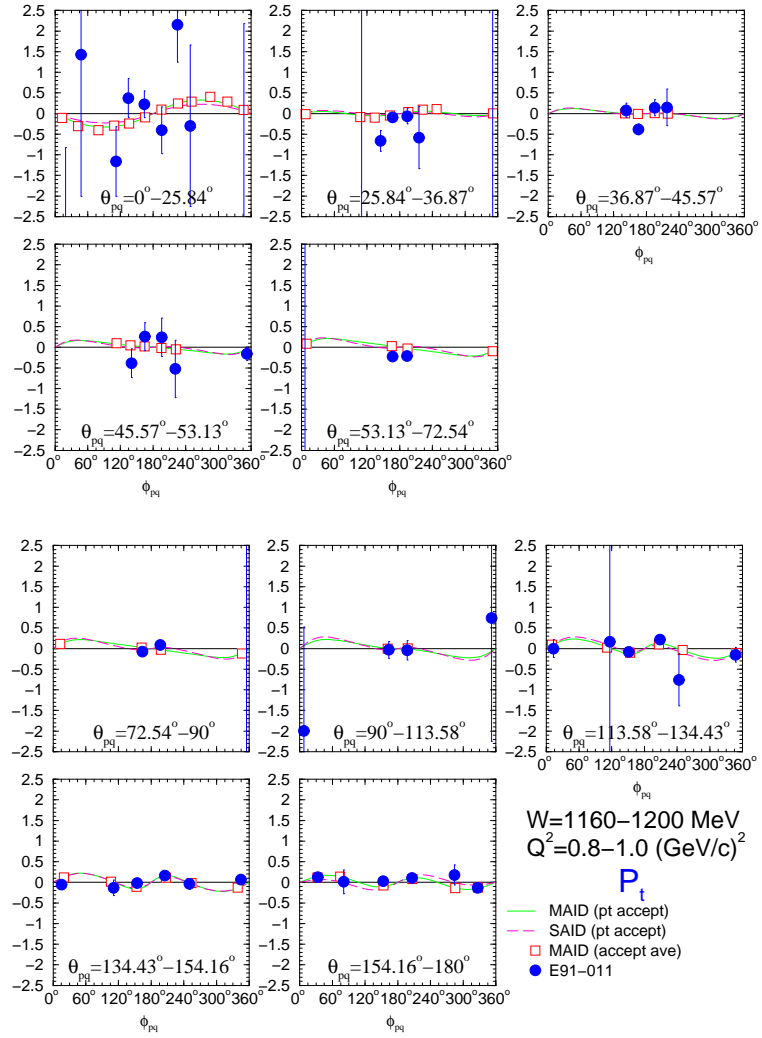
FIGURE C.0.6. Optimizations of hadron arm momentum versus energy deposited, hadron arm momentum versus  $\beta$ , and electron arm  $x_{rot}$  versus  $tc_{cor}$  for runs 3559 ( $\theta_{pq} = 135^\circ$ ) and 4034 ( $\theta_{pq} = 180^\circ$ ) using database *db\_ndelta\_6*.

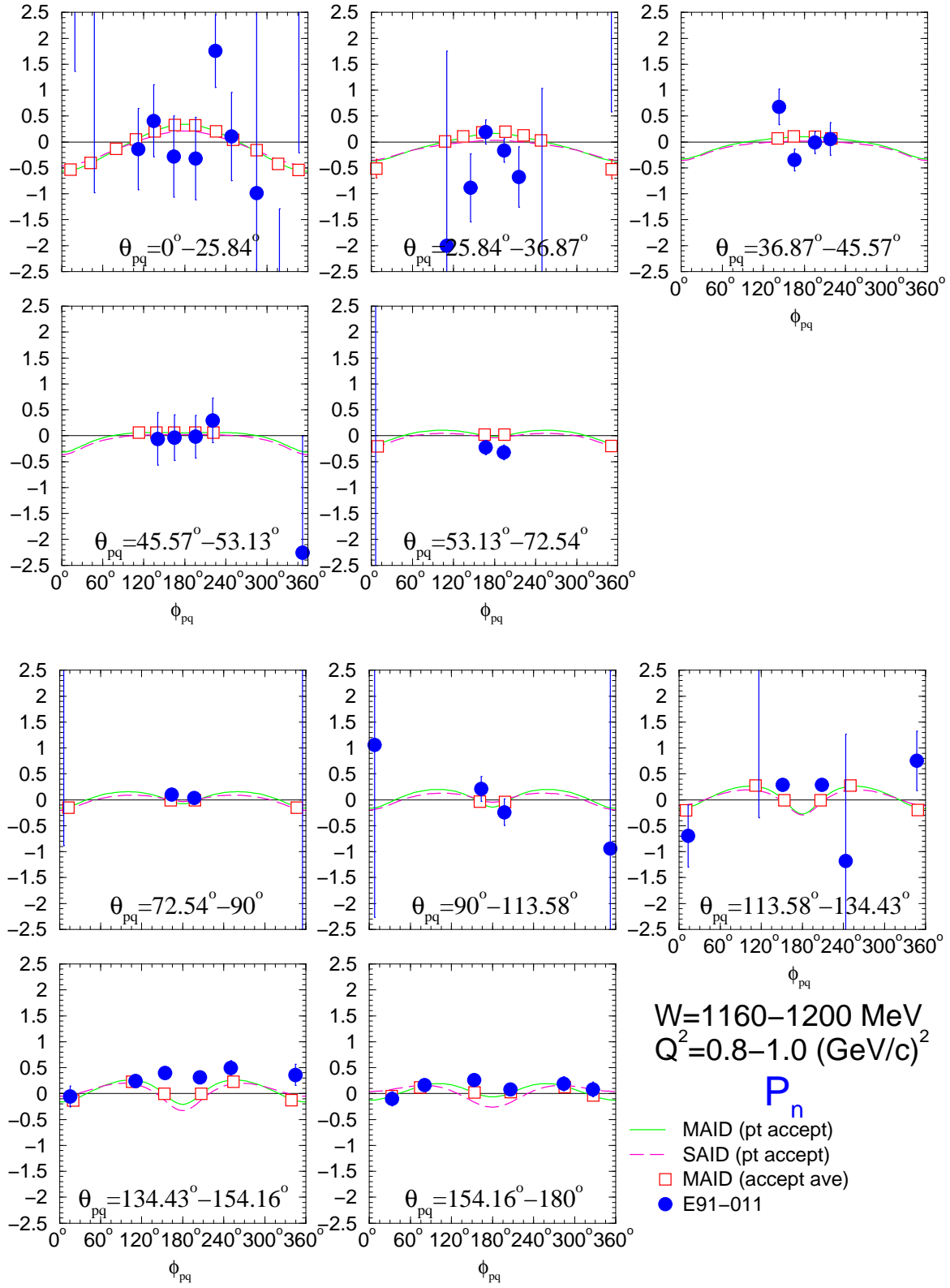


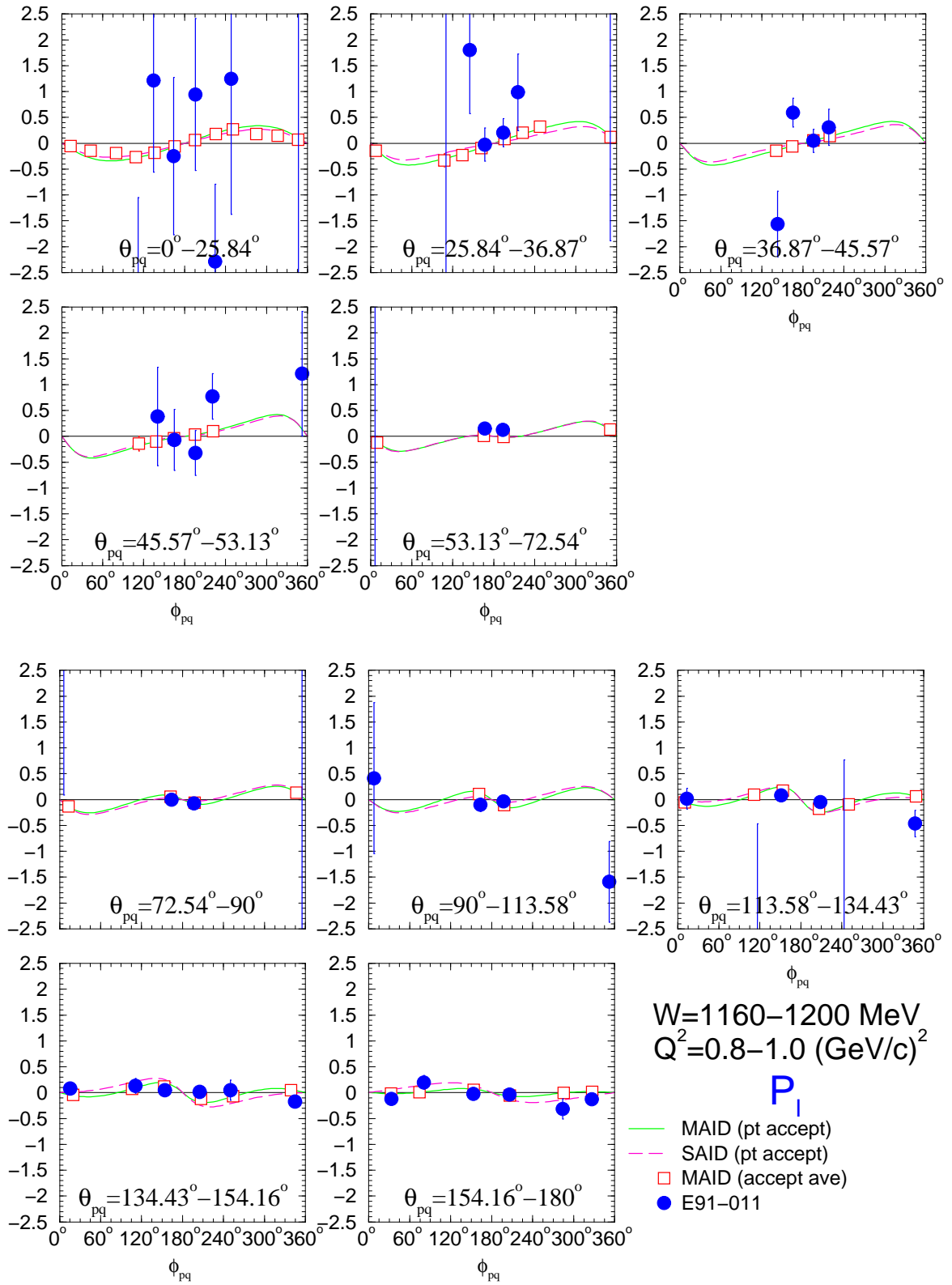
## APPENDIX D

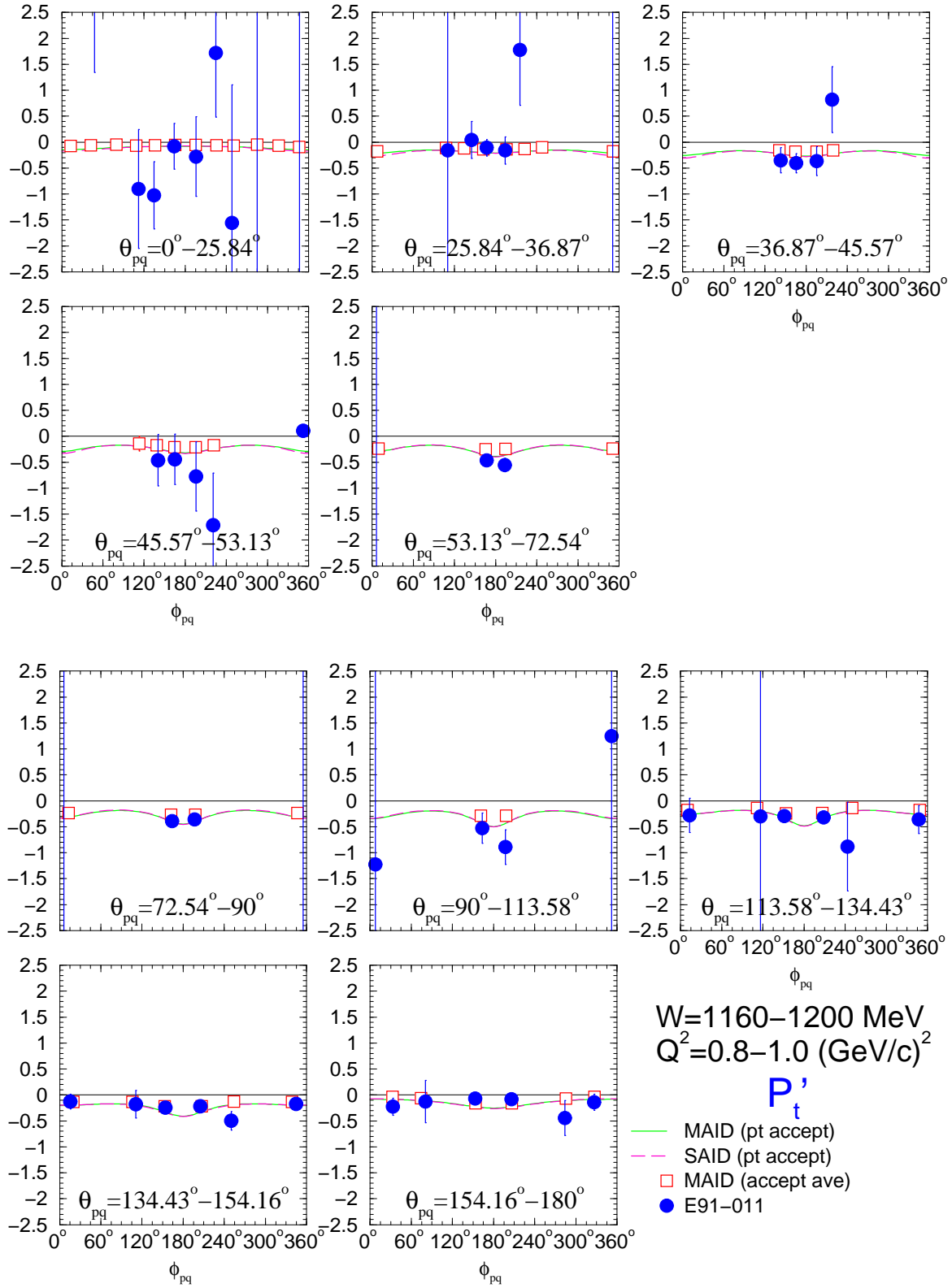
### RESULTS: TARGET POLARIZATIONS

**D.1.**  $W = 1160\text{--}1200\text{ MeV}, Q^2 = 0.8\text{--}1.0\text{ (GeV/c)}^2$

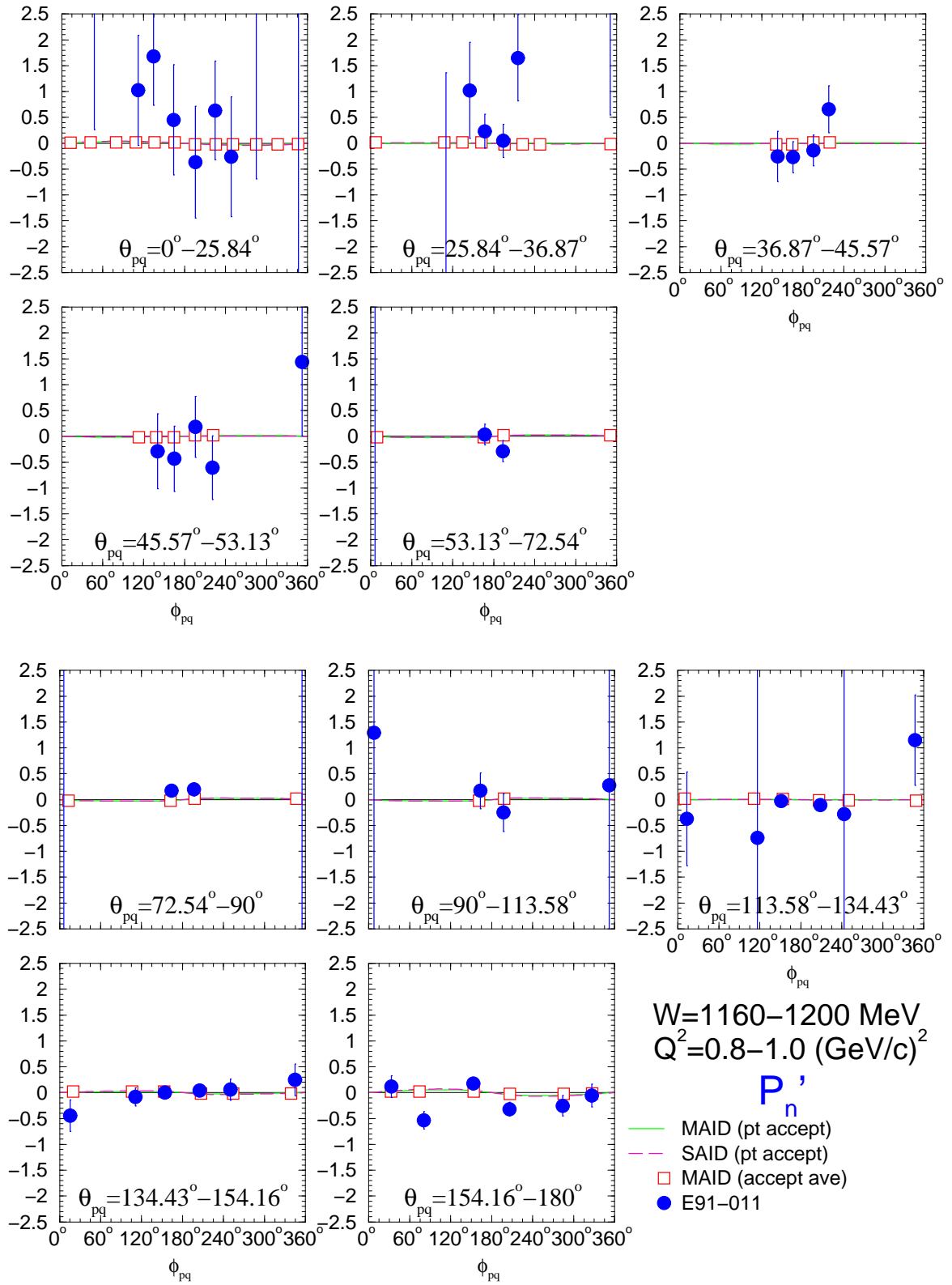


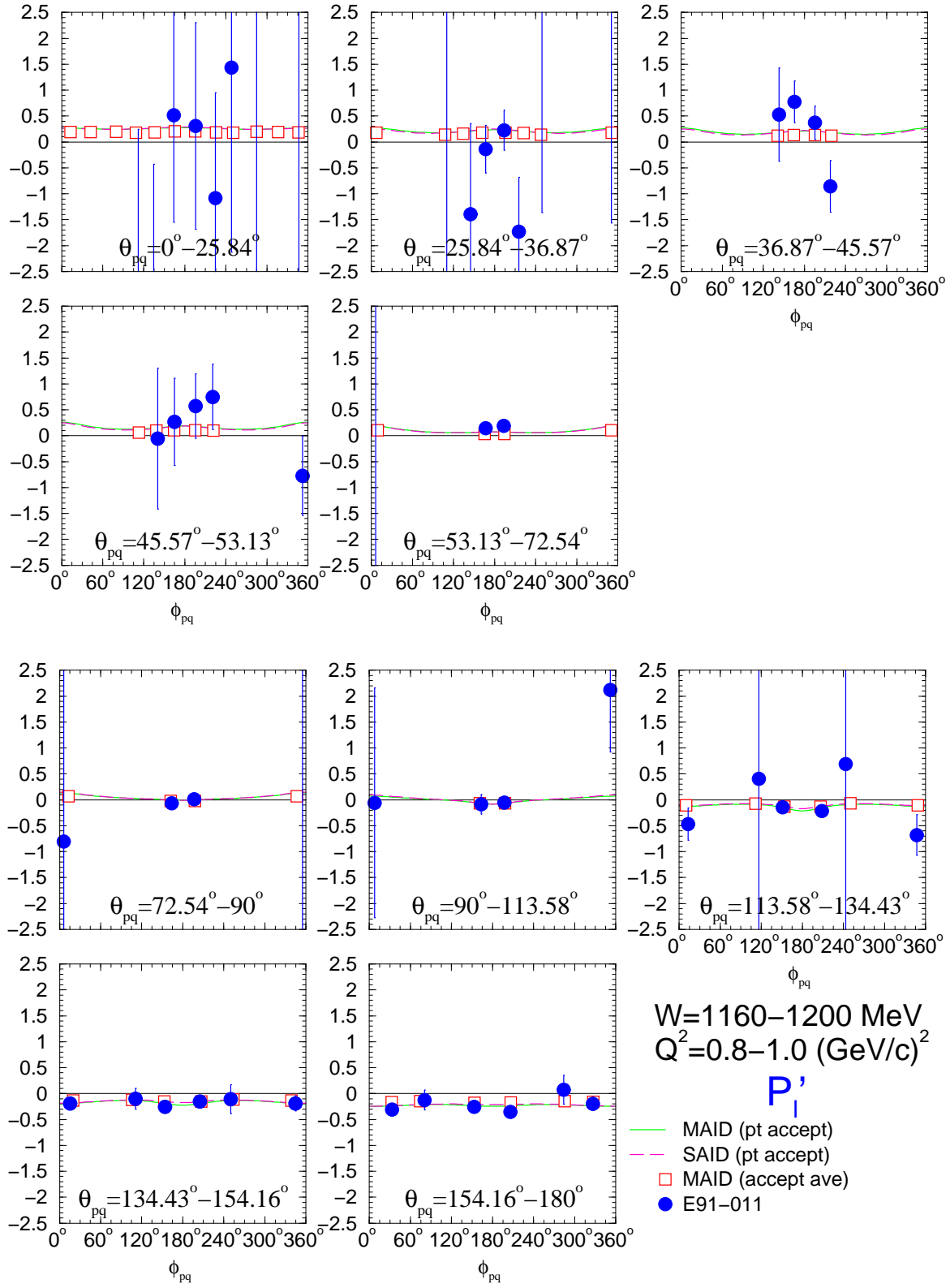




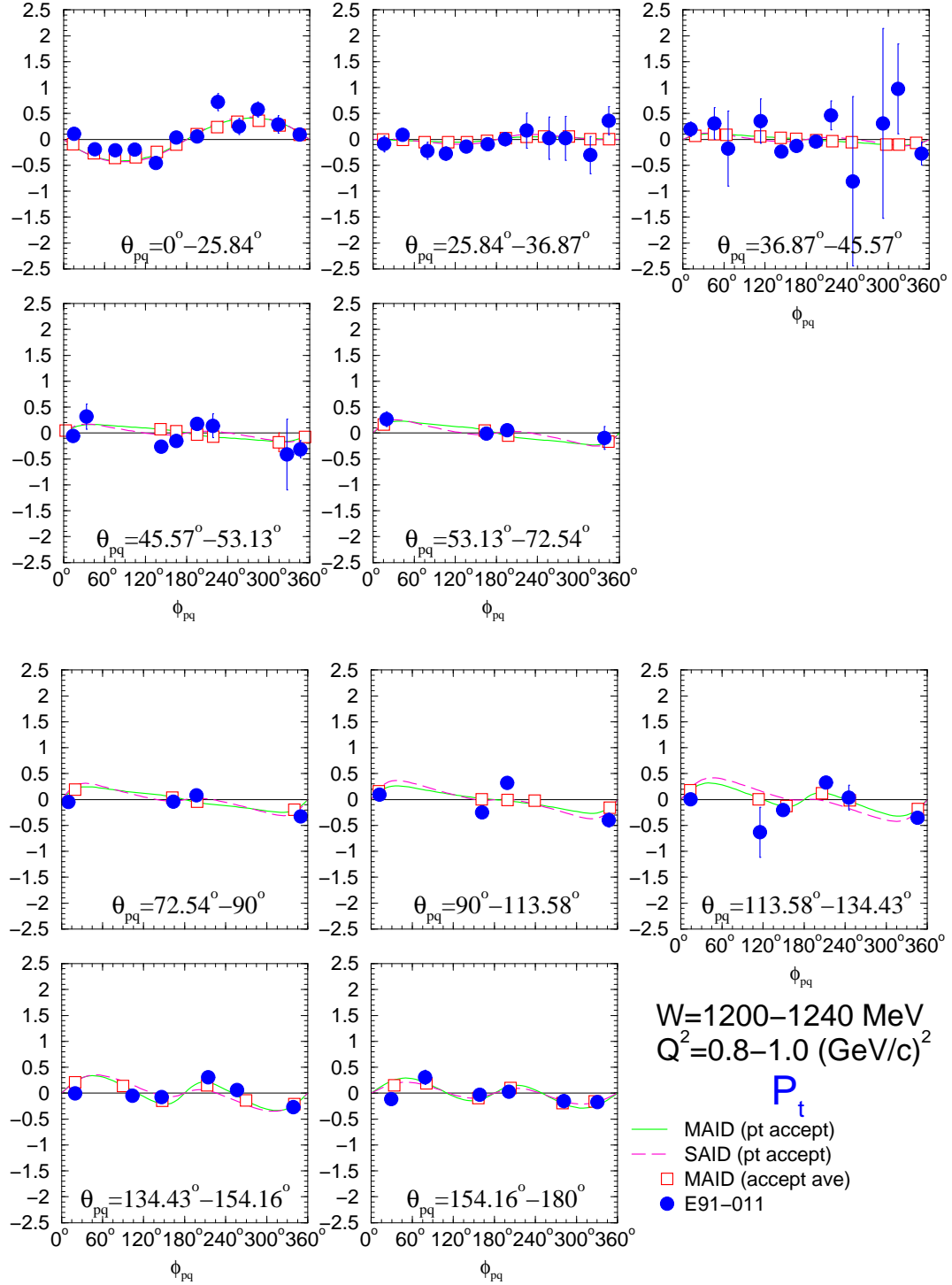


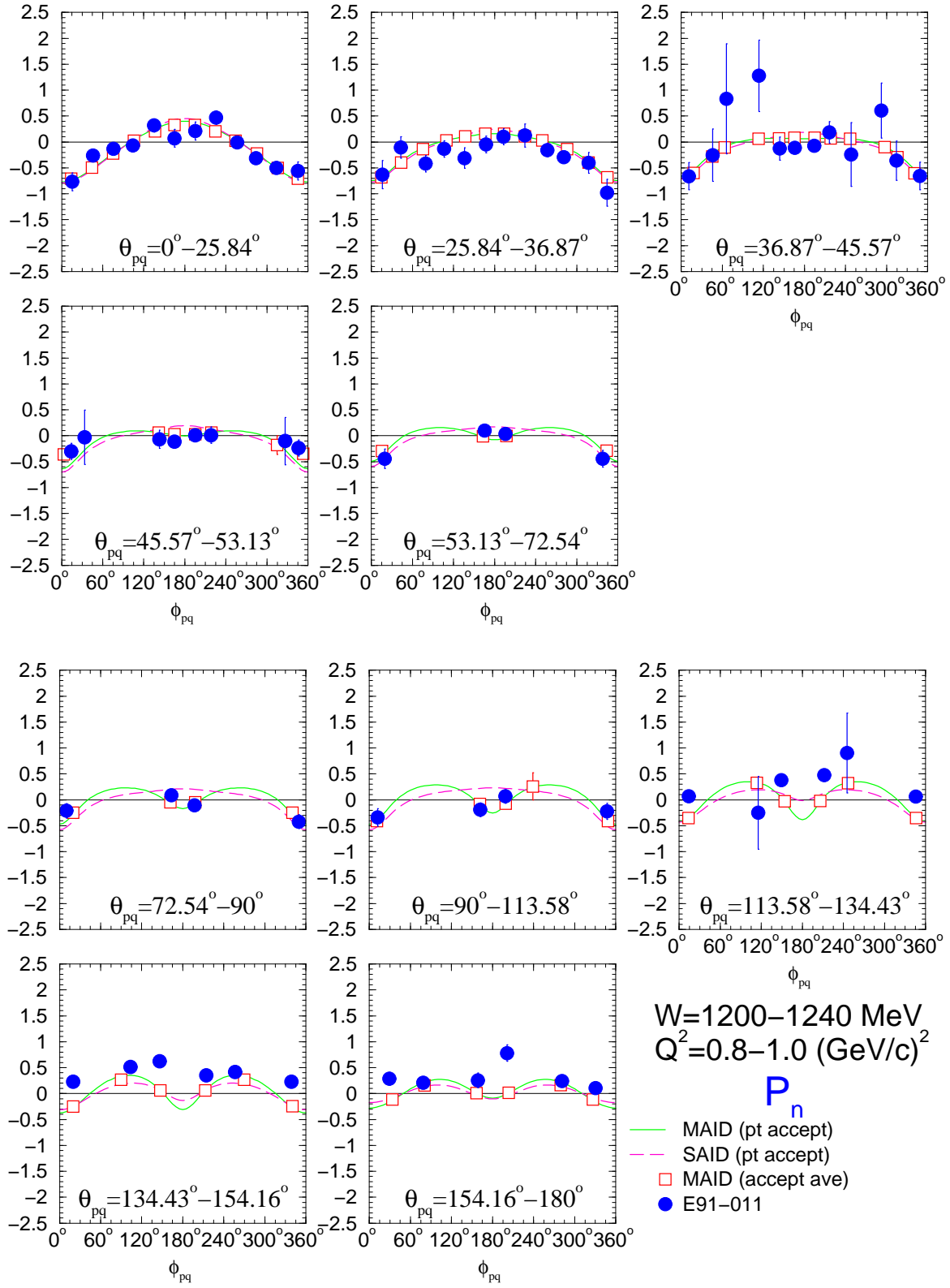


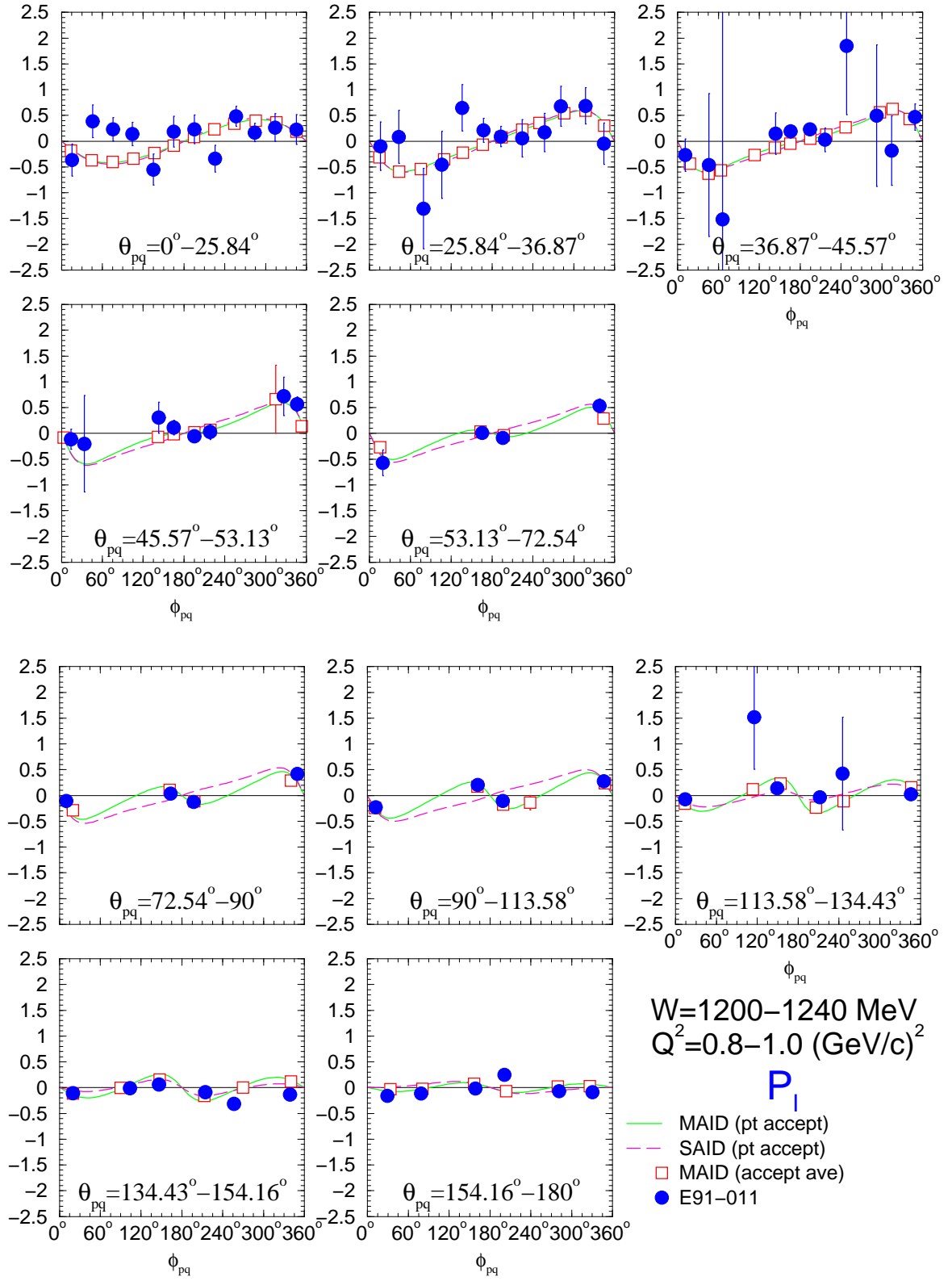


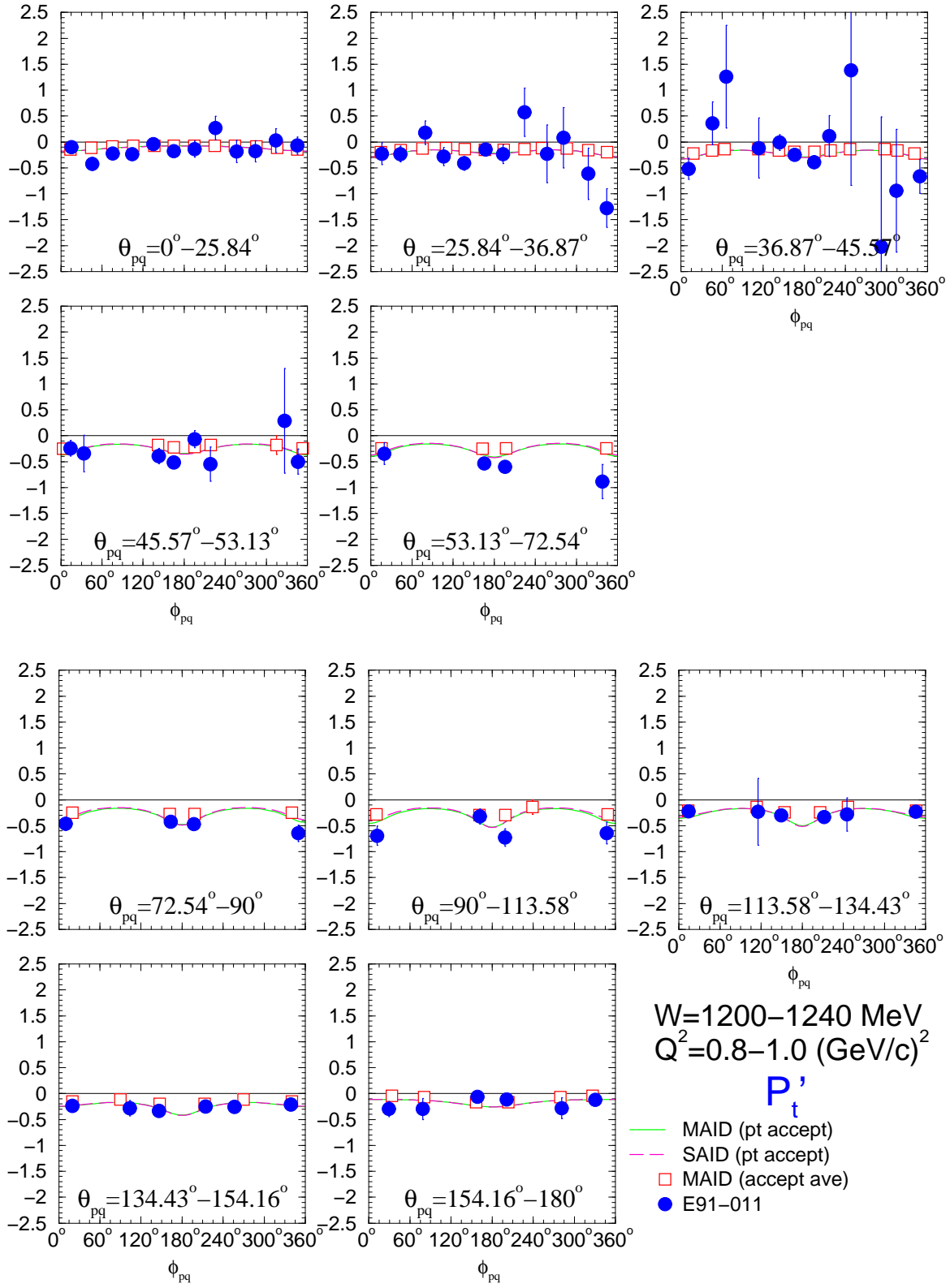


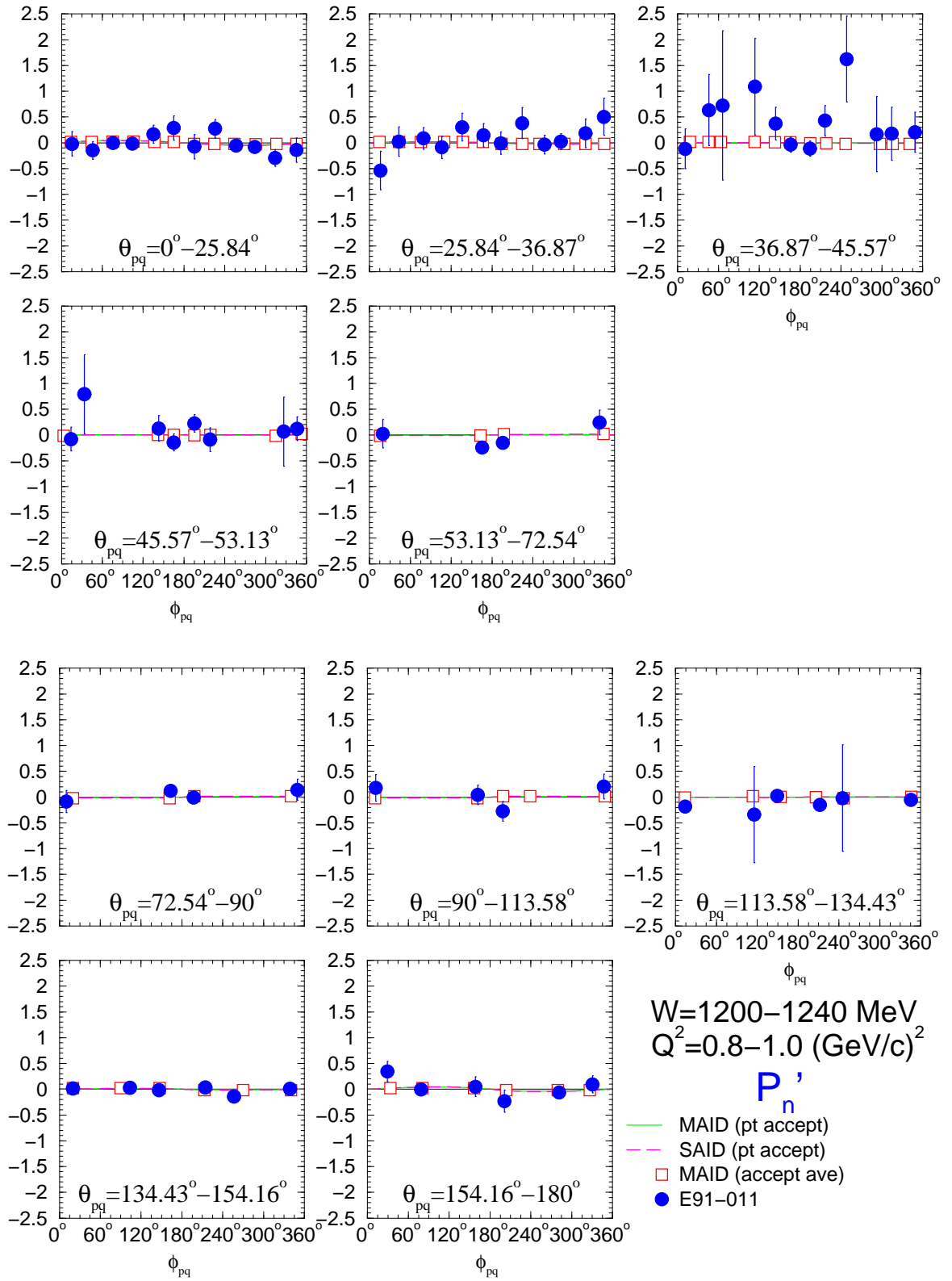
D.2.  $W = 1200\text{--}1240 \text{ MeV}, Q^2 = 0.8\text{--}1.0 \text{ (GeV/c)}^2$

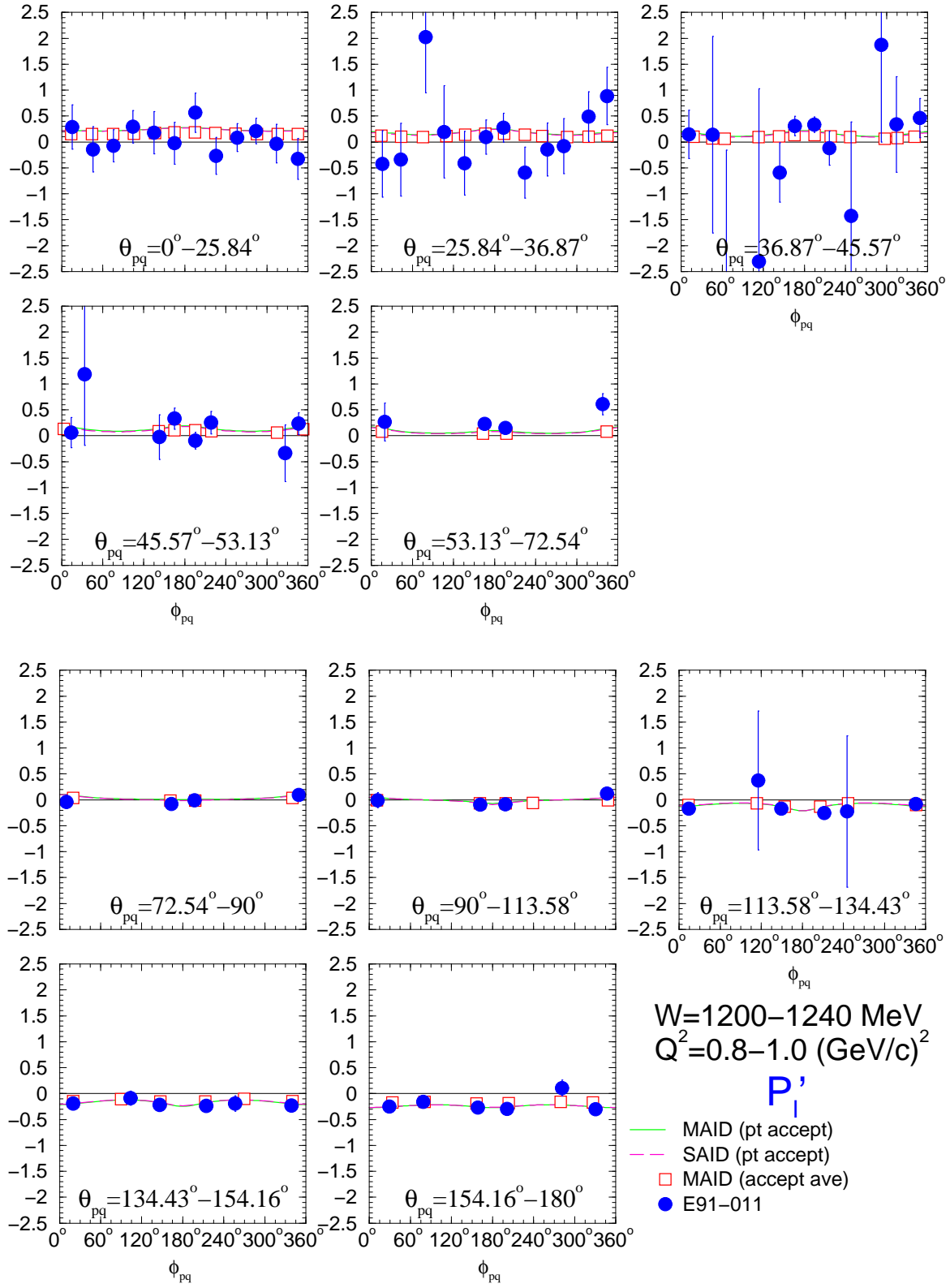






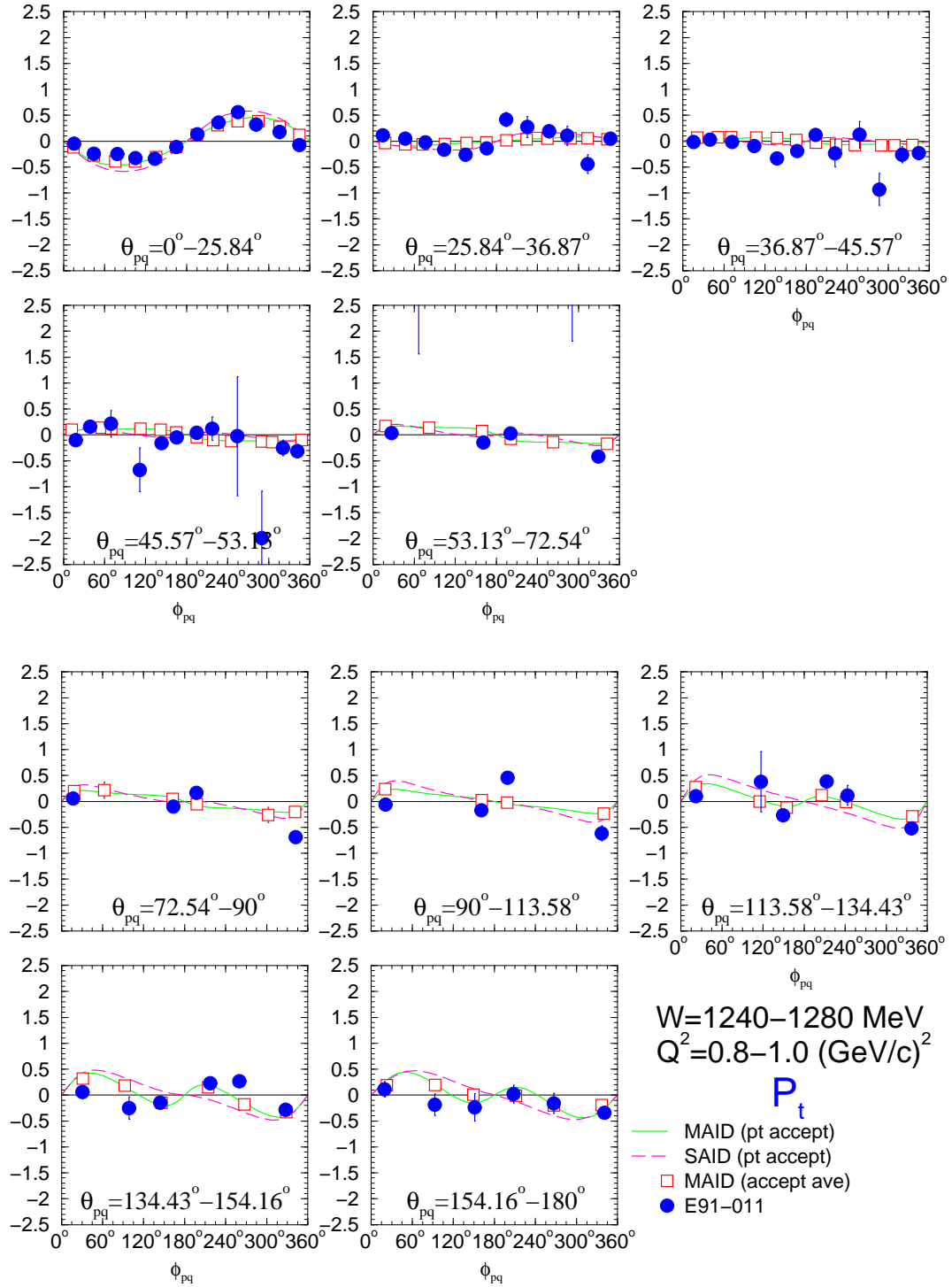


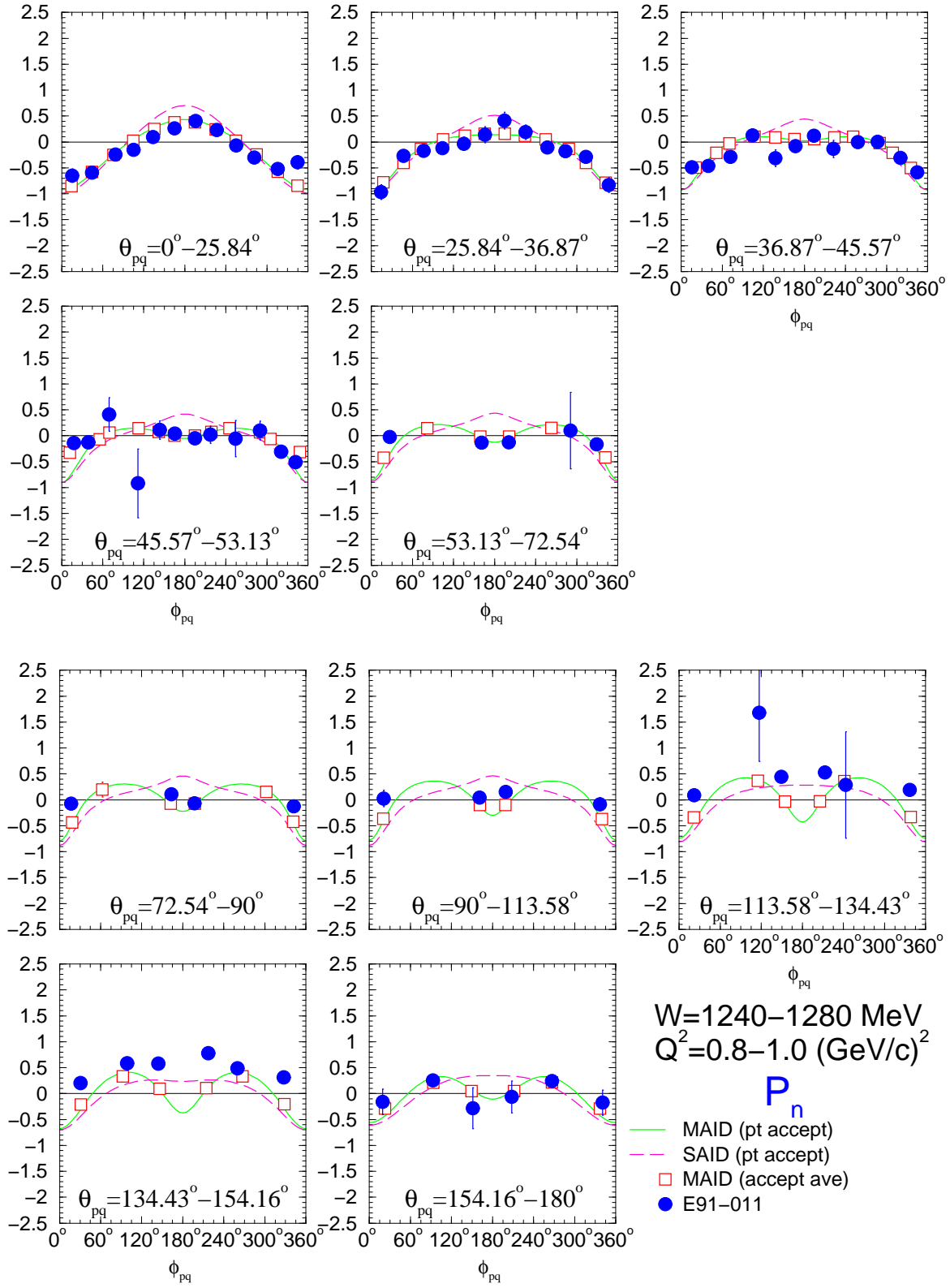


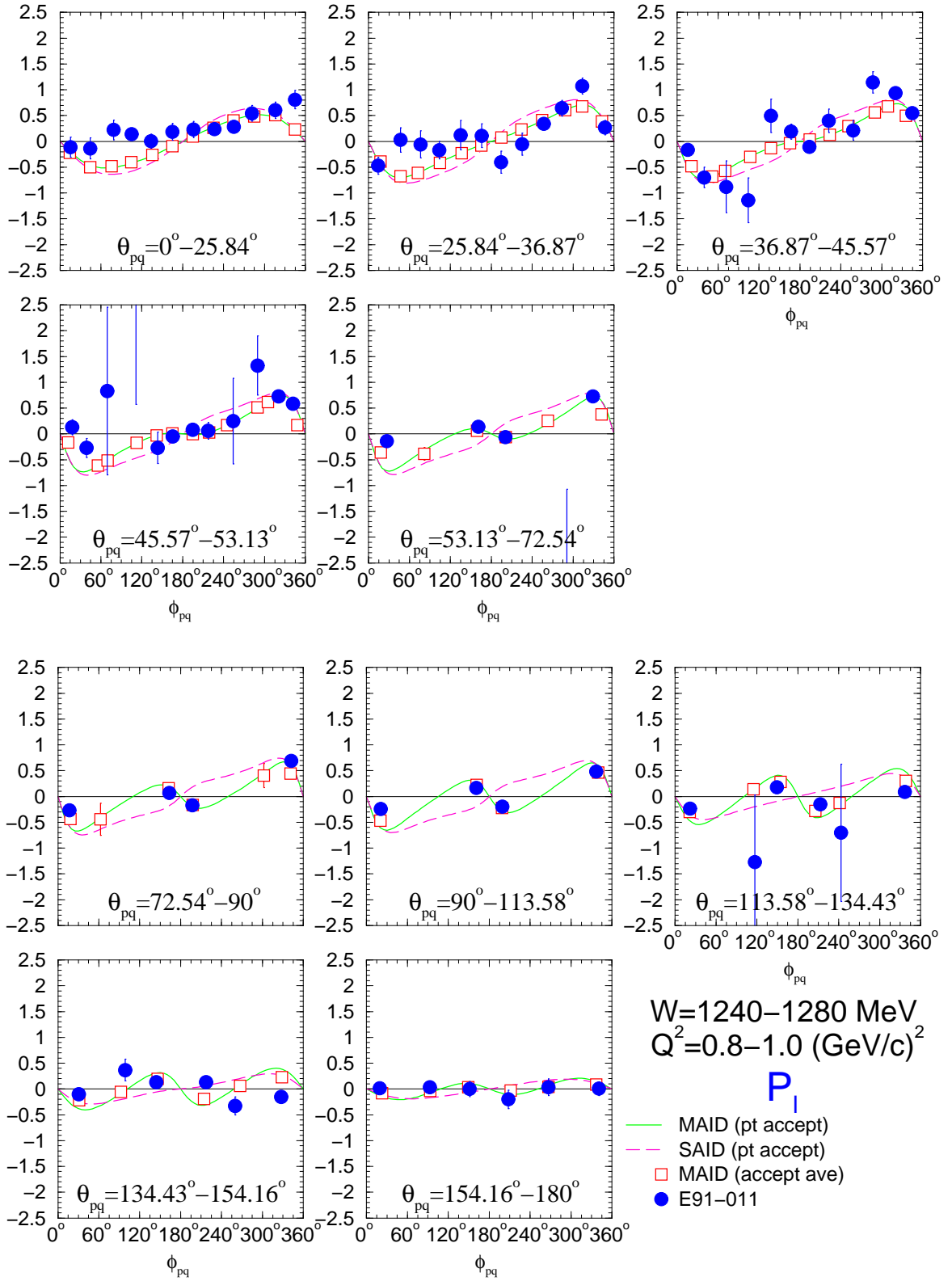


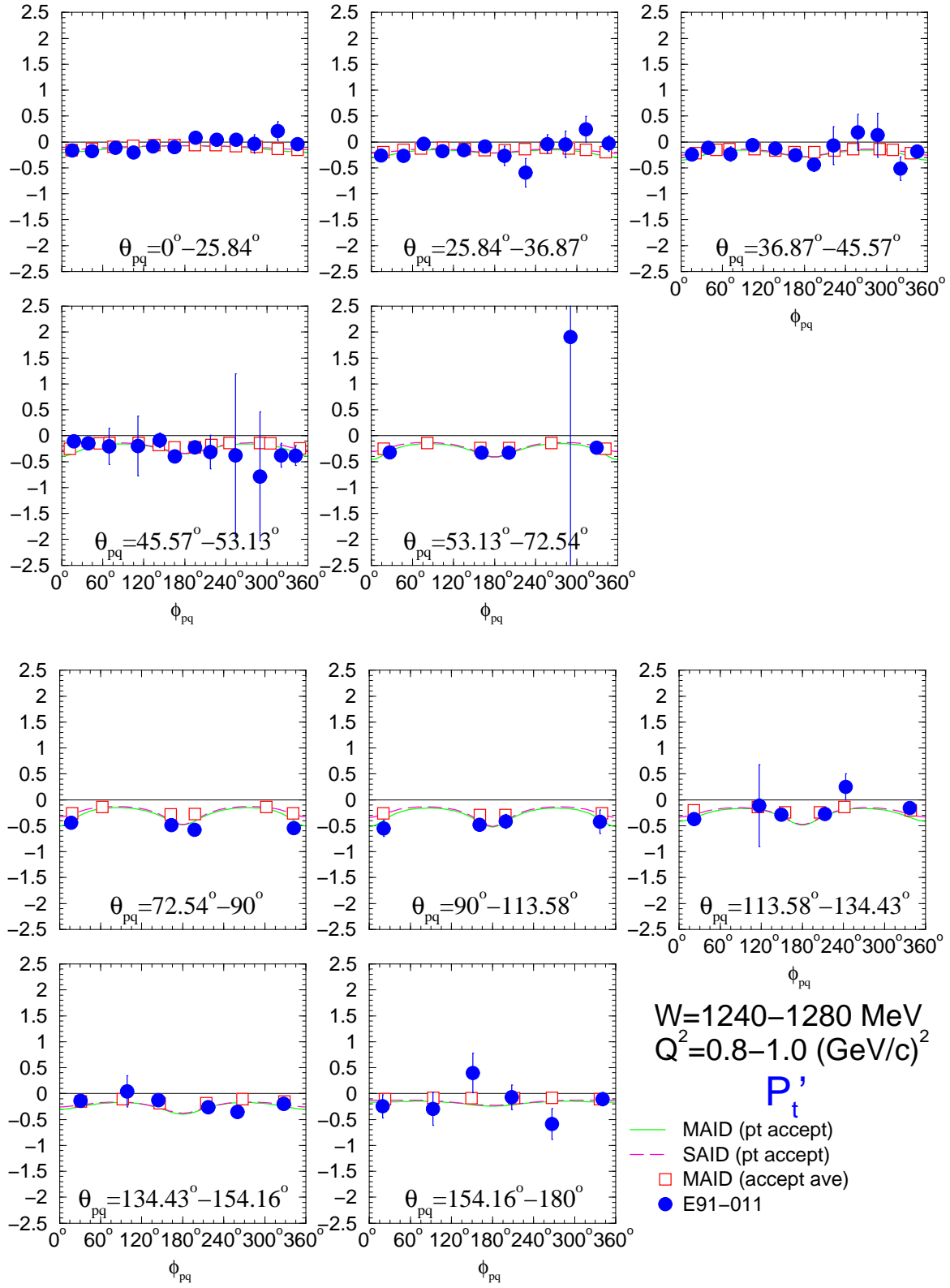


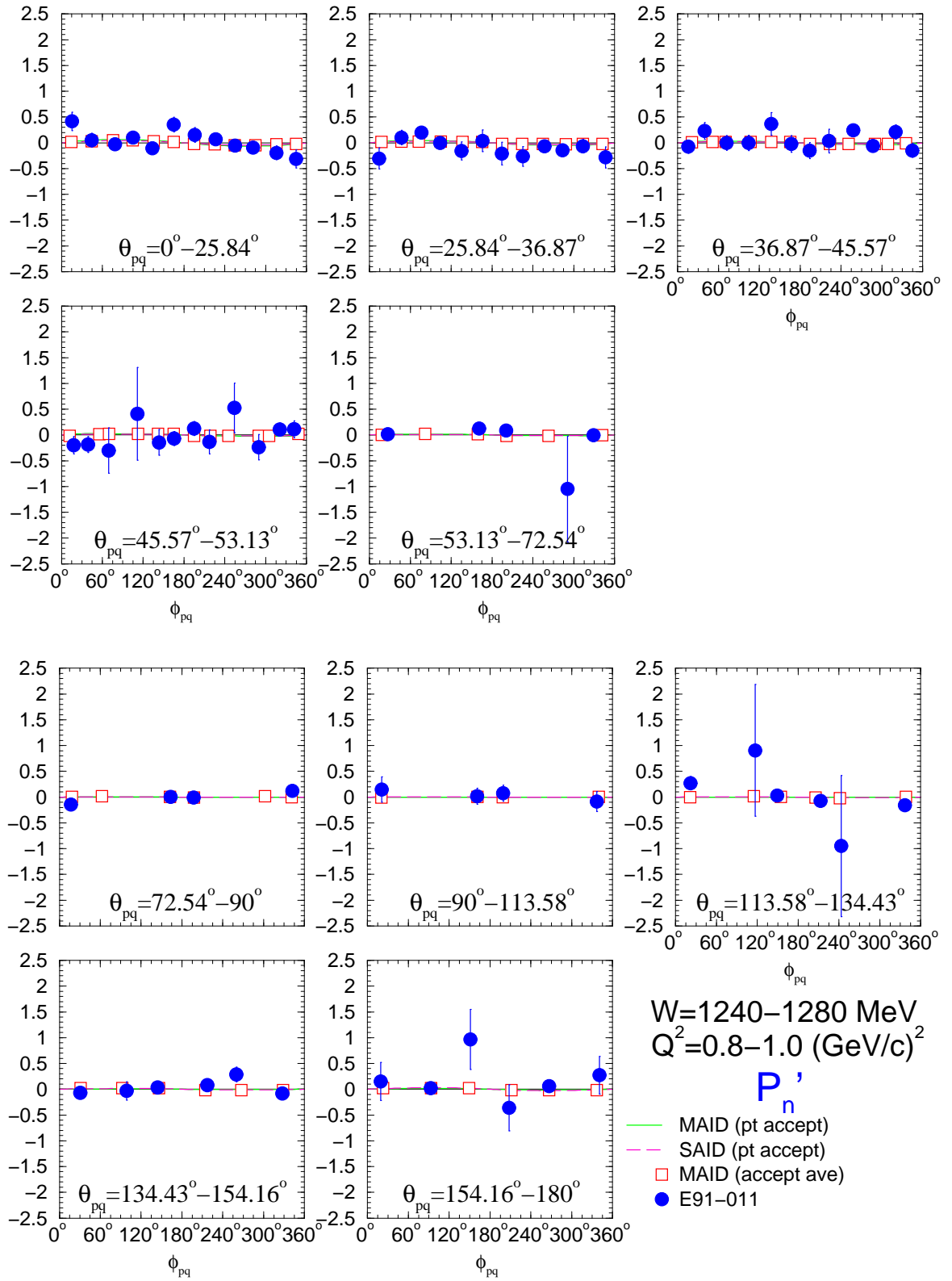
D.3.  $W = 1240\text{--}1280 \text{ MeV}, Q^2 = 0.8\text{--}1.0 \text{ (GeV/c)}^2$

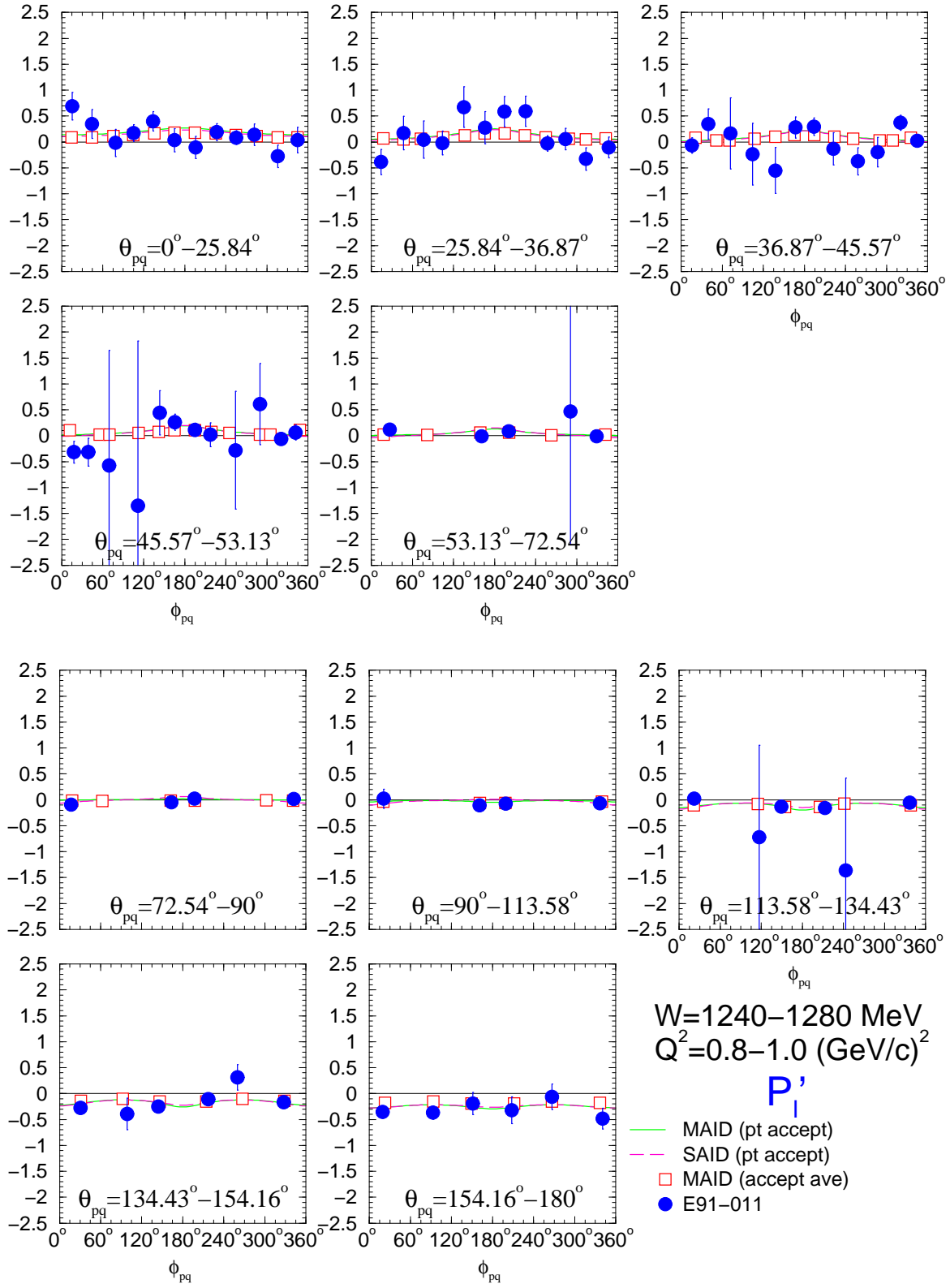




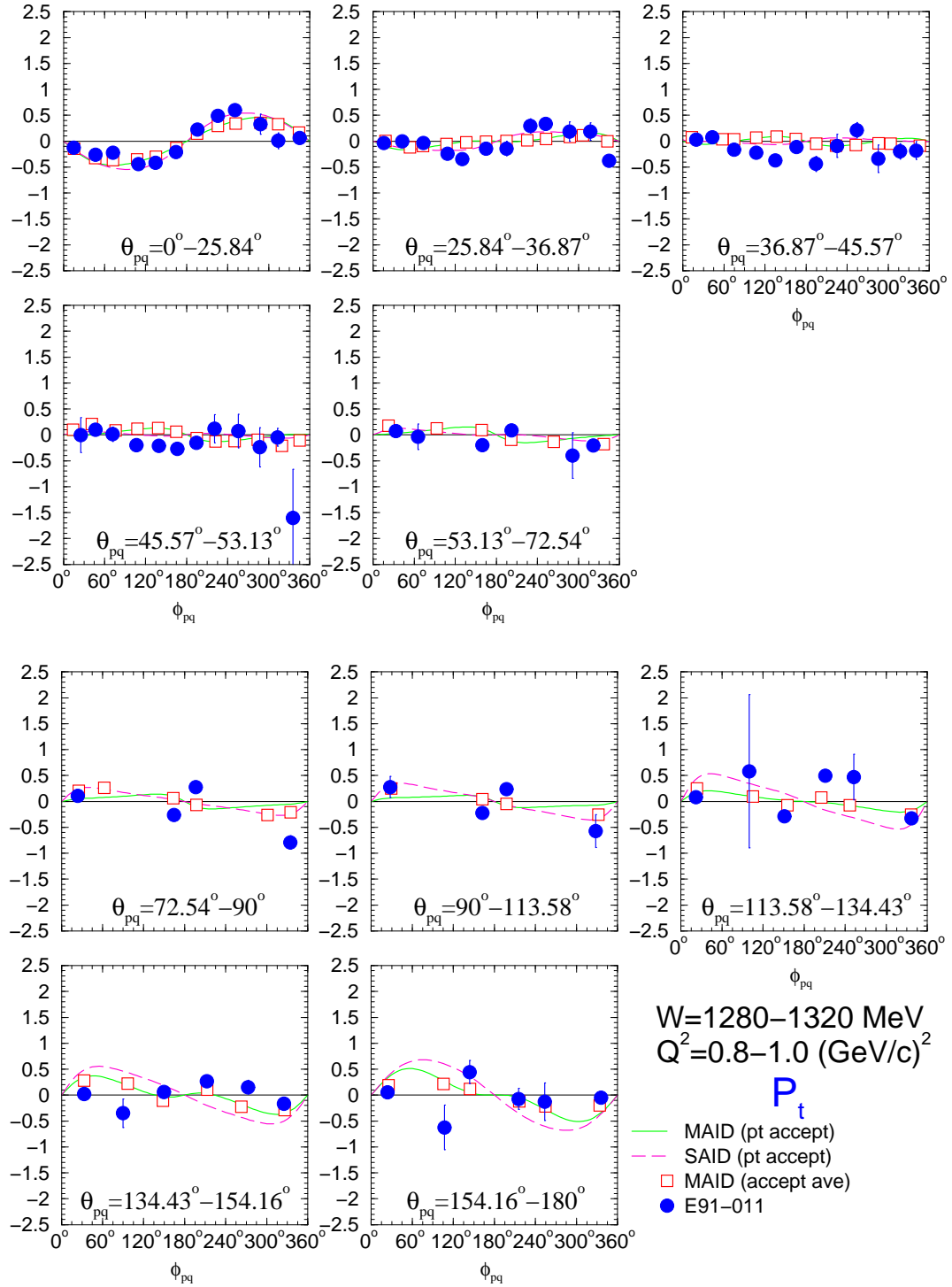


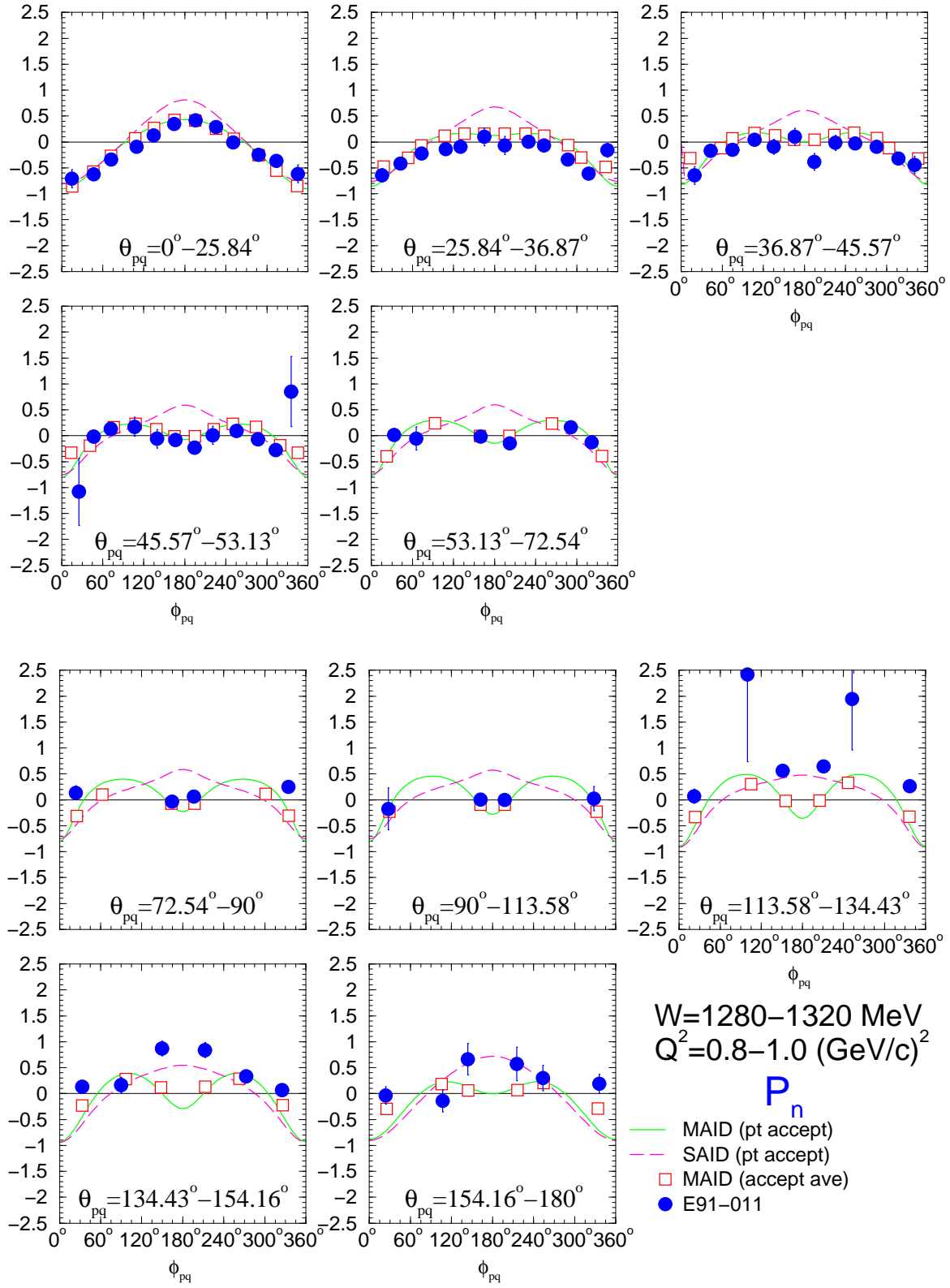




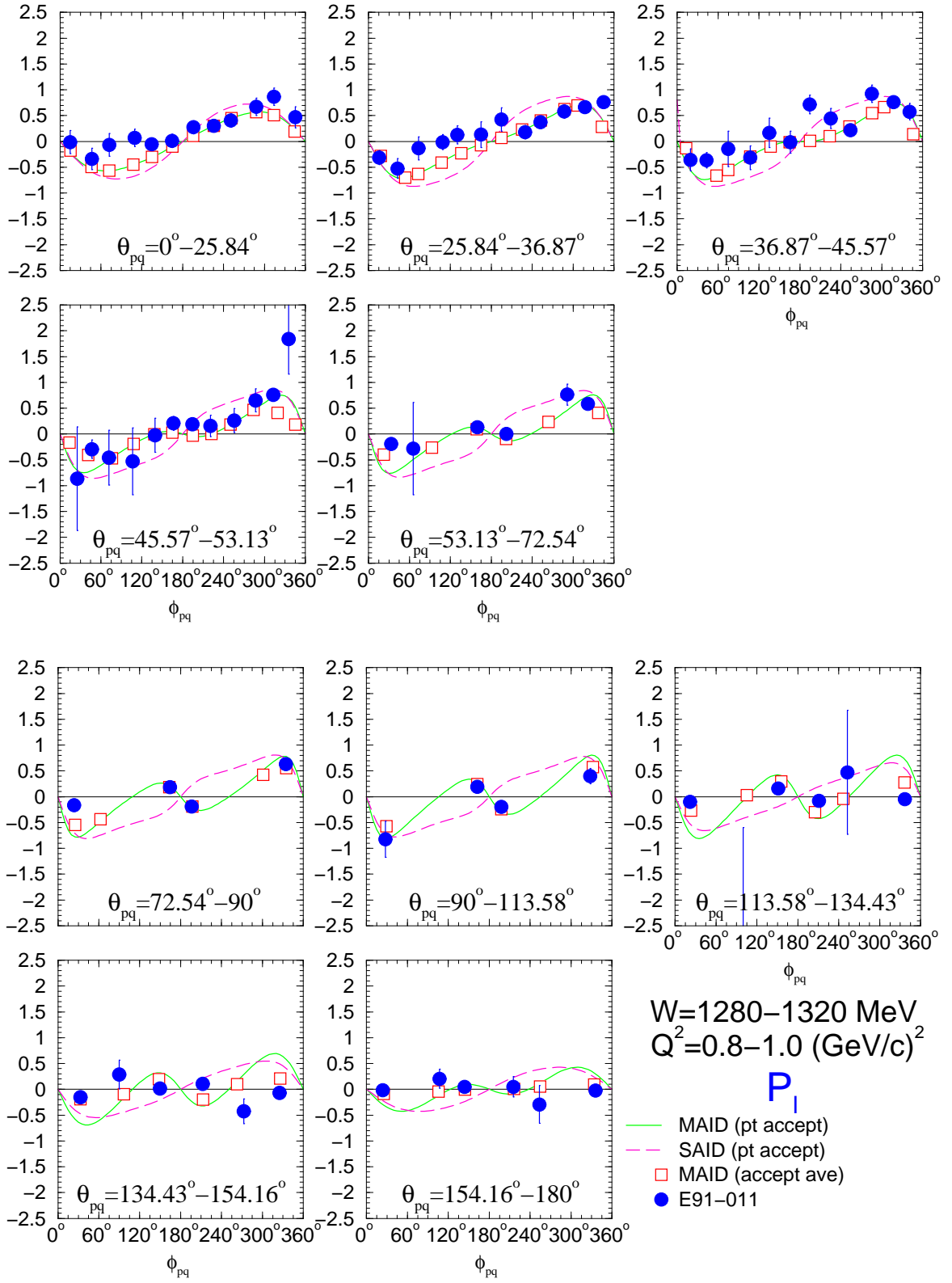


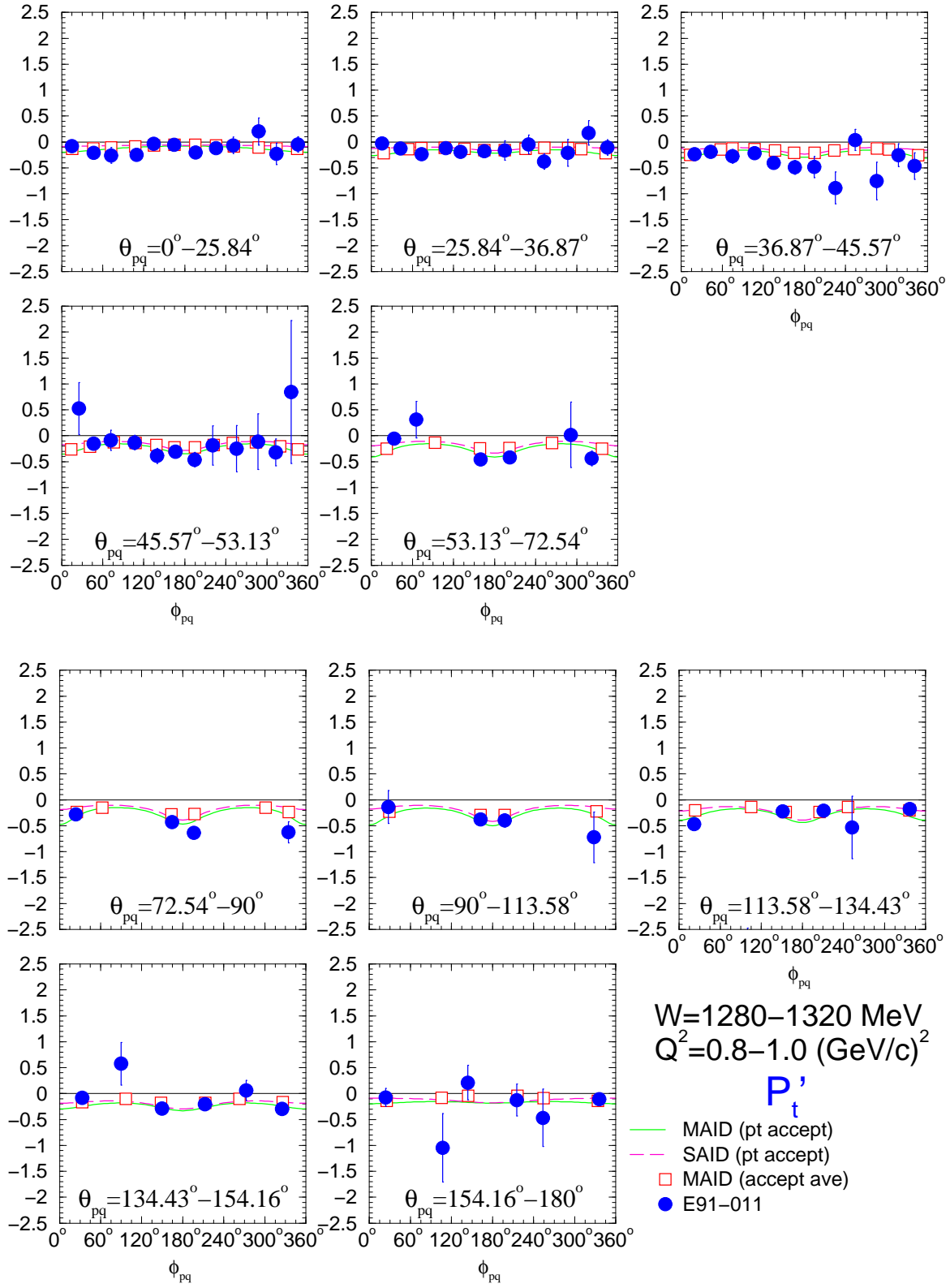
D.4.  $W = 1280\text{--}1320 \text{ MeV}, Q^2 = 0.8\text{--}1.0 \text{ (GeV/c)}^2$

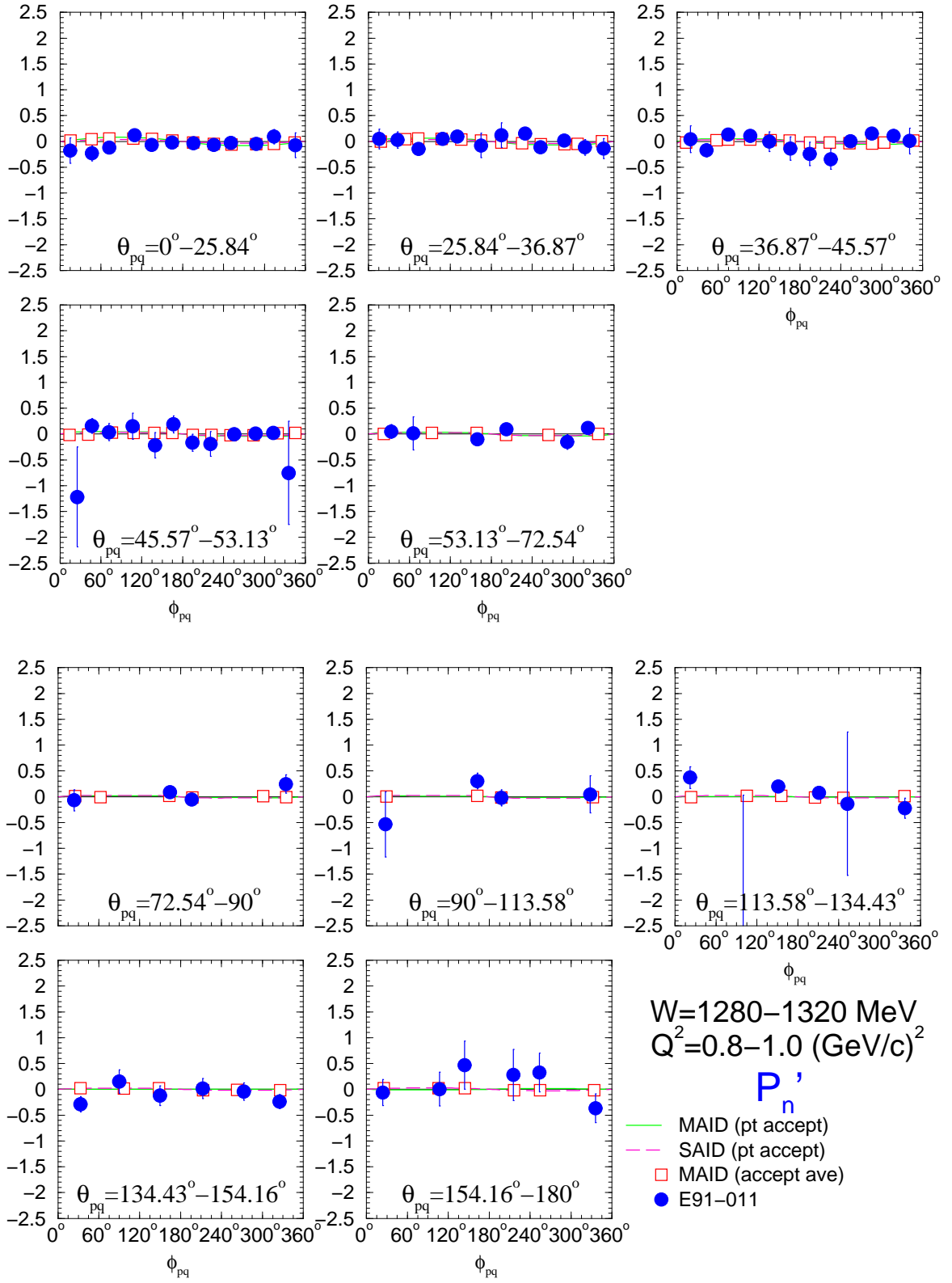


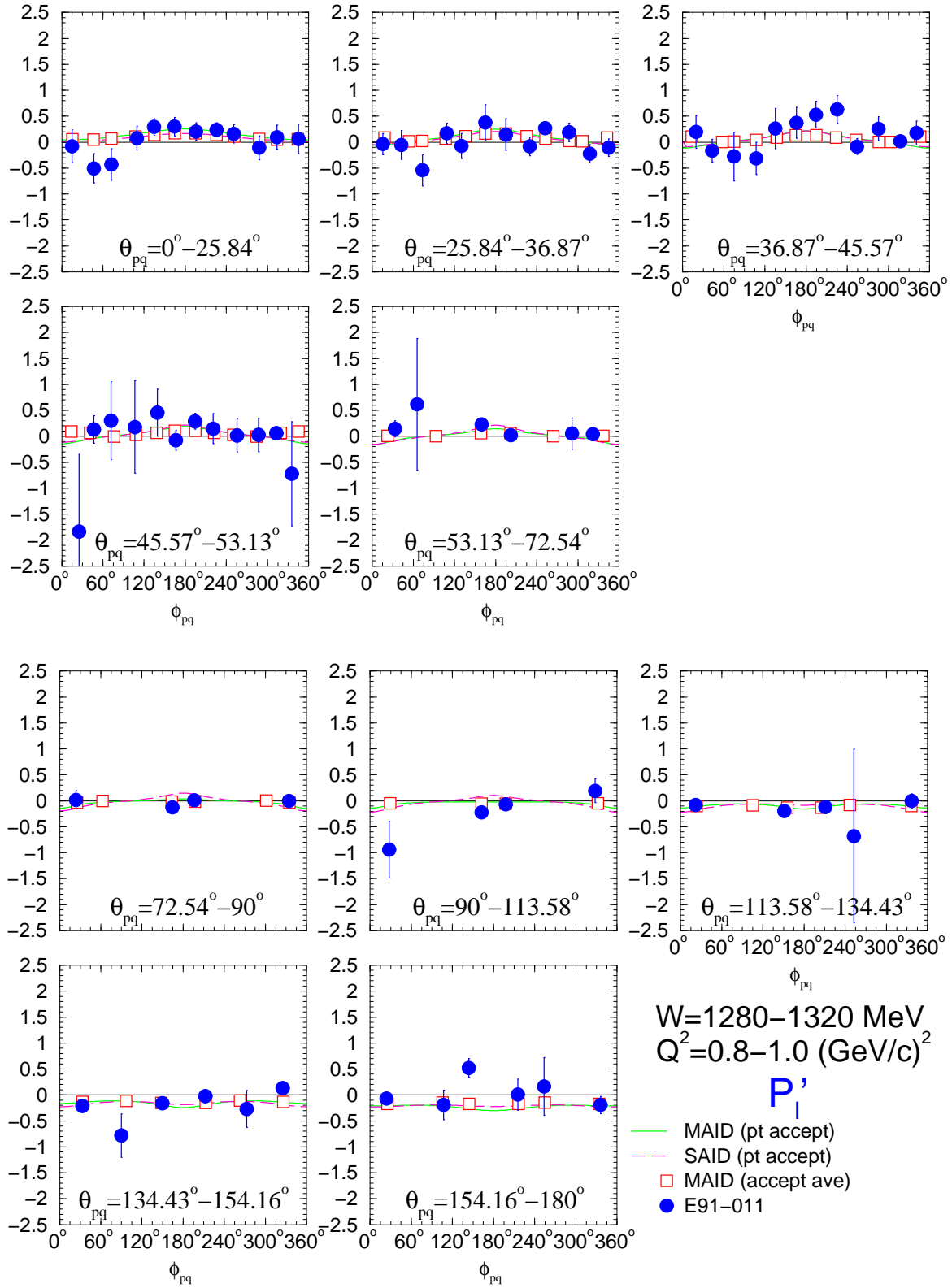




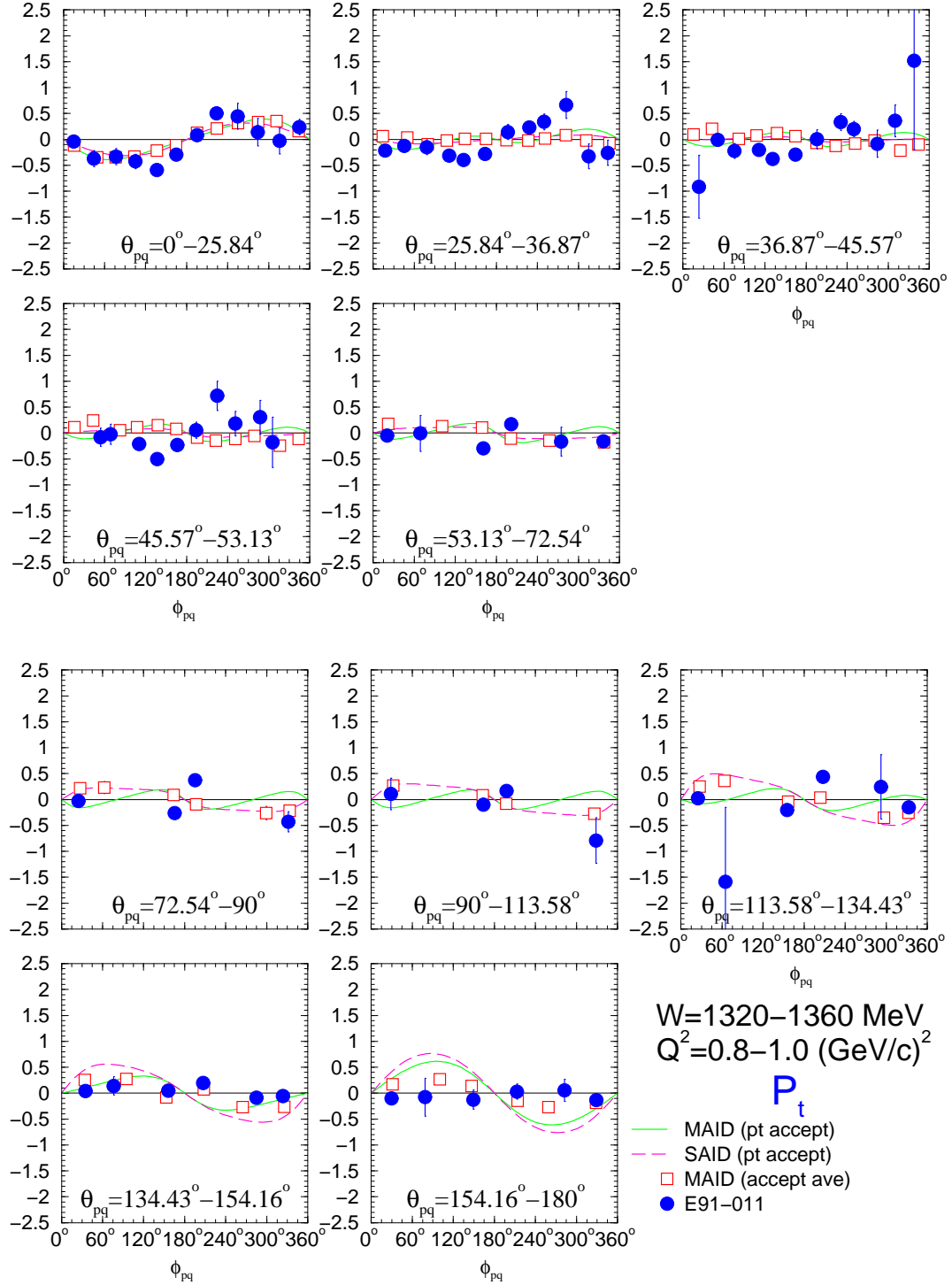


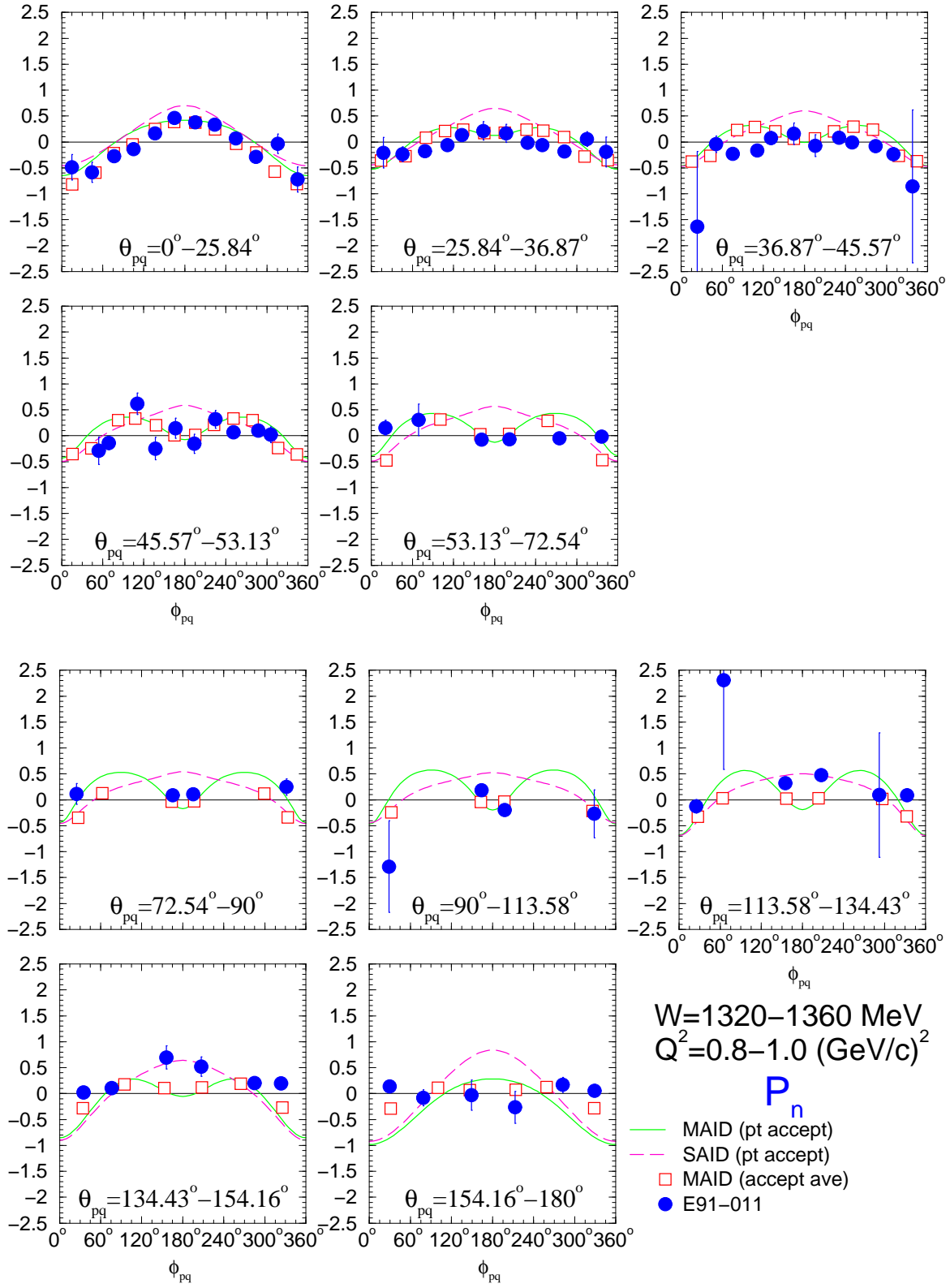


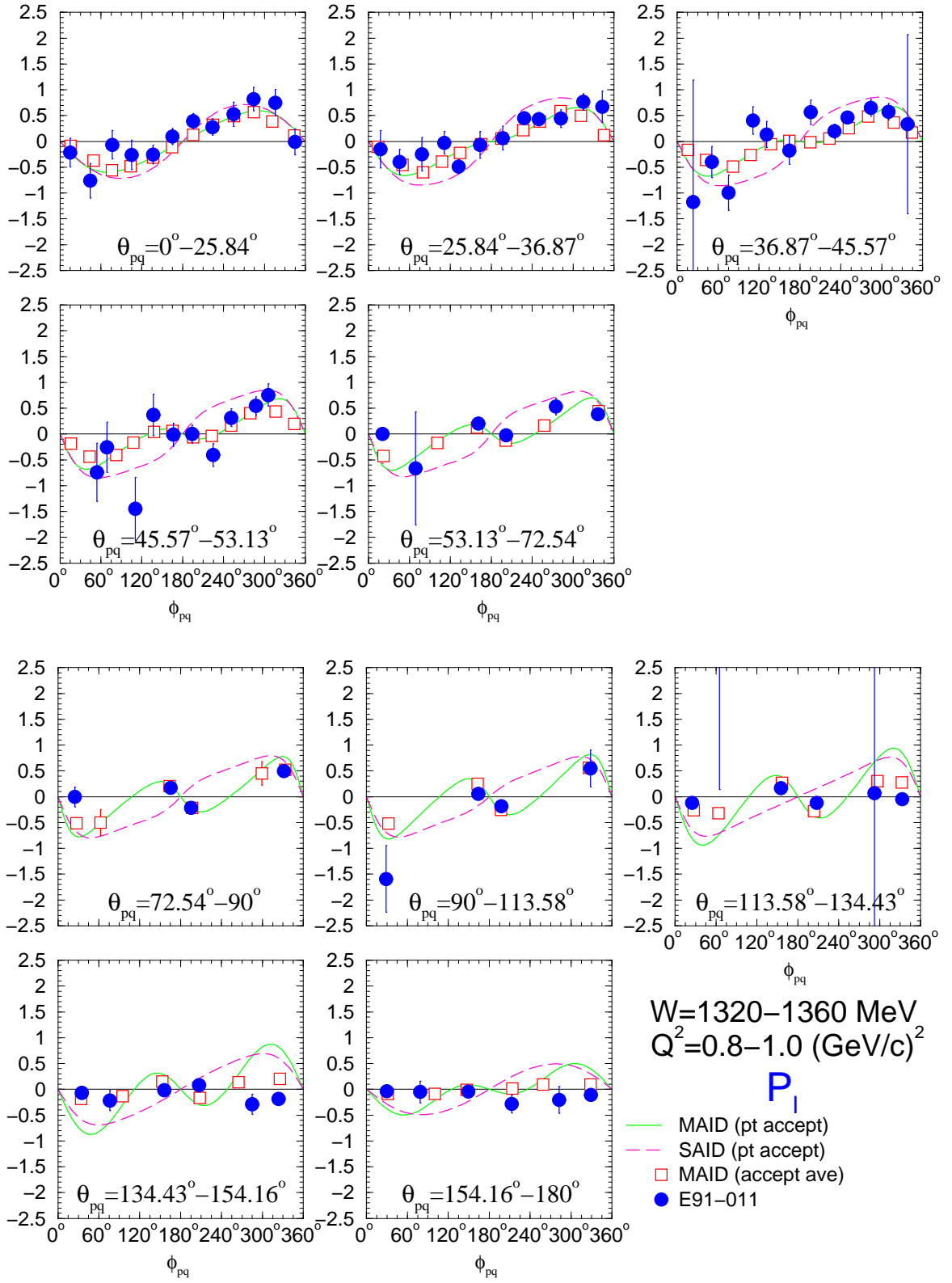


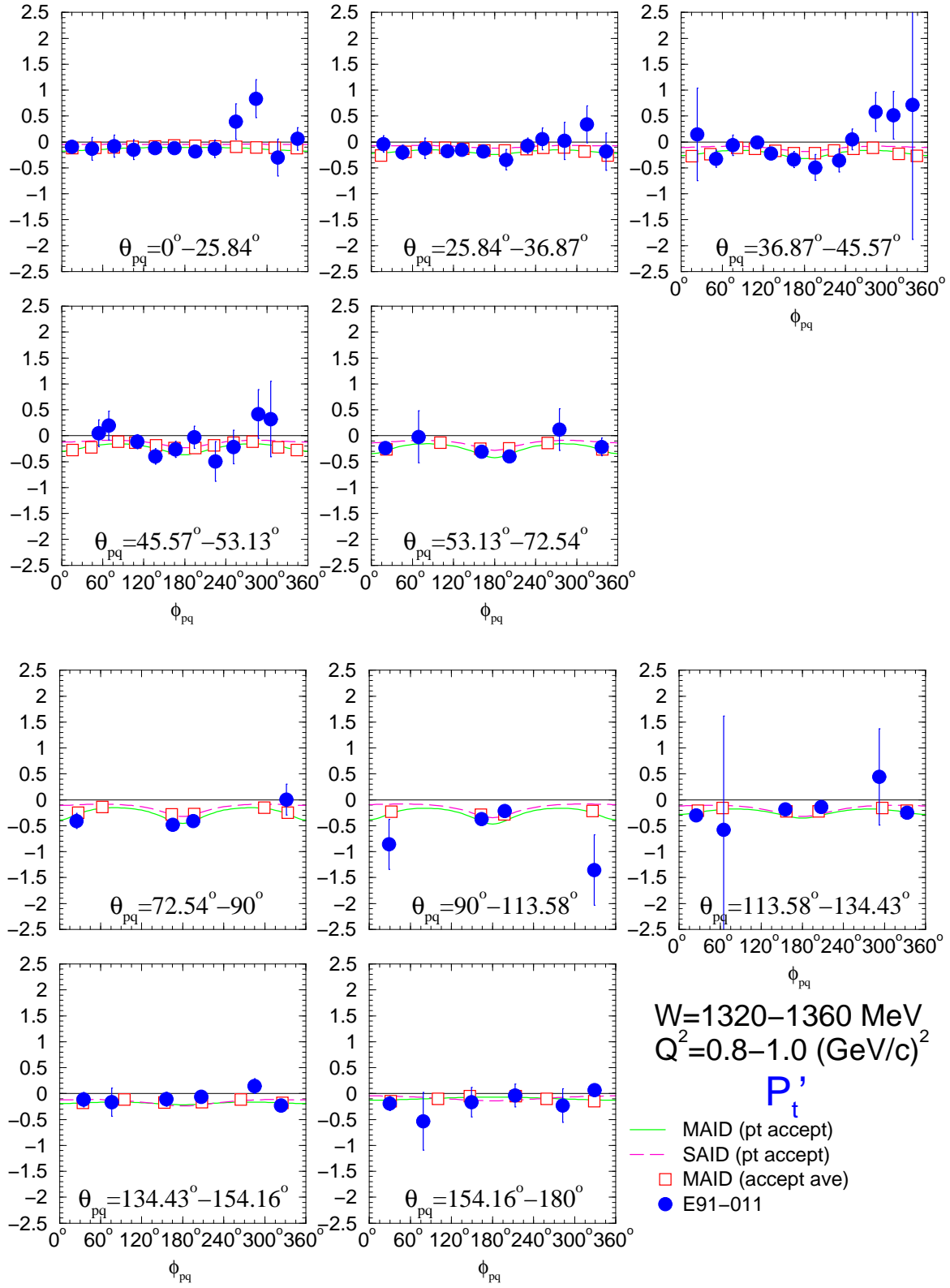


D.5.  $W = 1320\text{--}1360\text{ MeV}, Q^2 = 0.8\text{--}1.0\text{ (GeV/c)}^2$

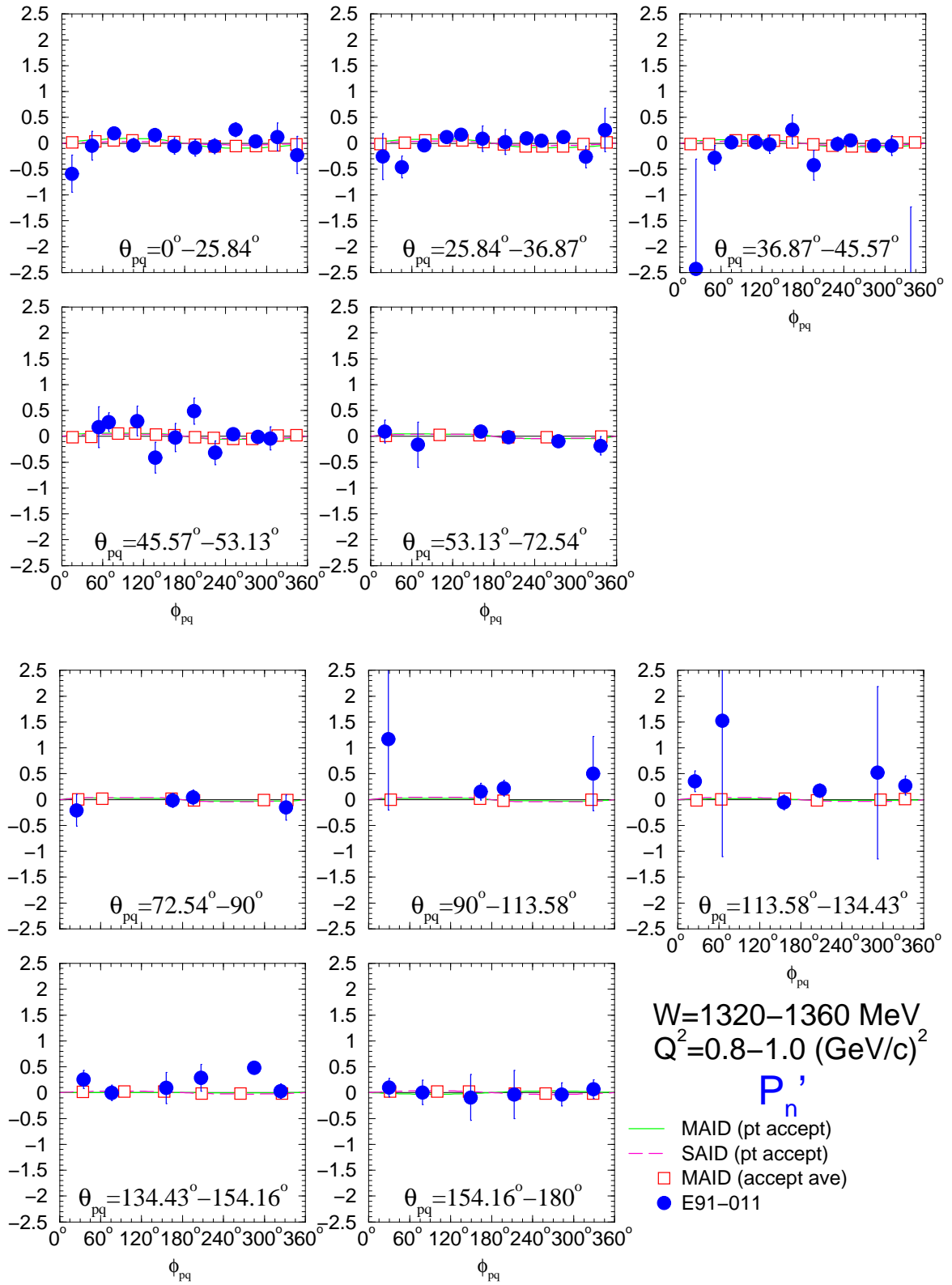


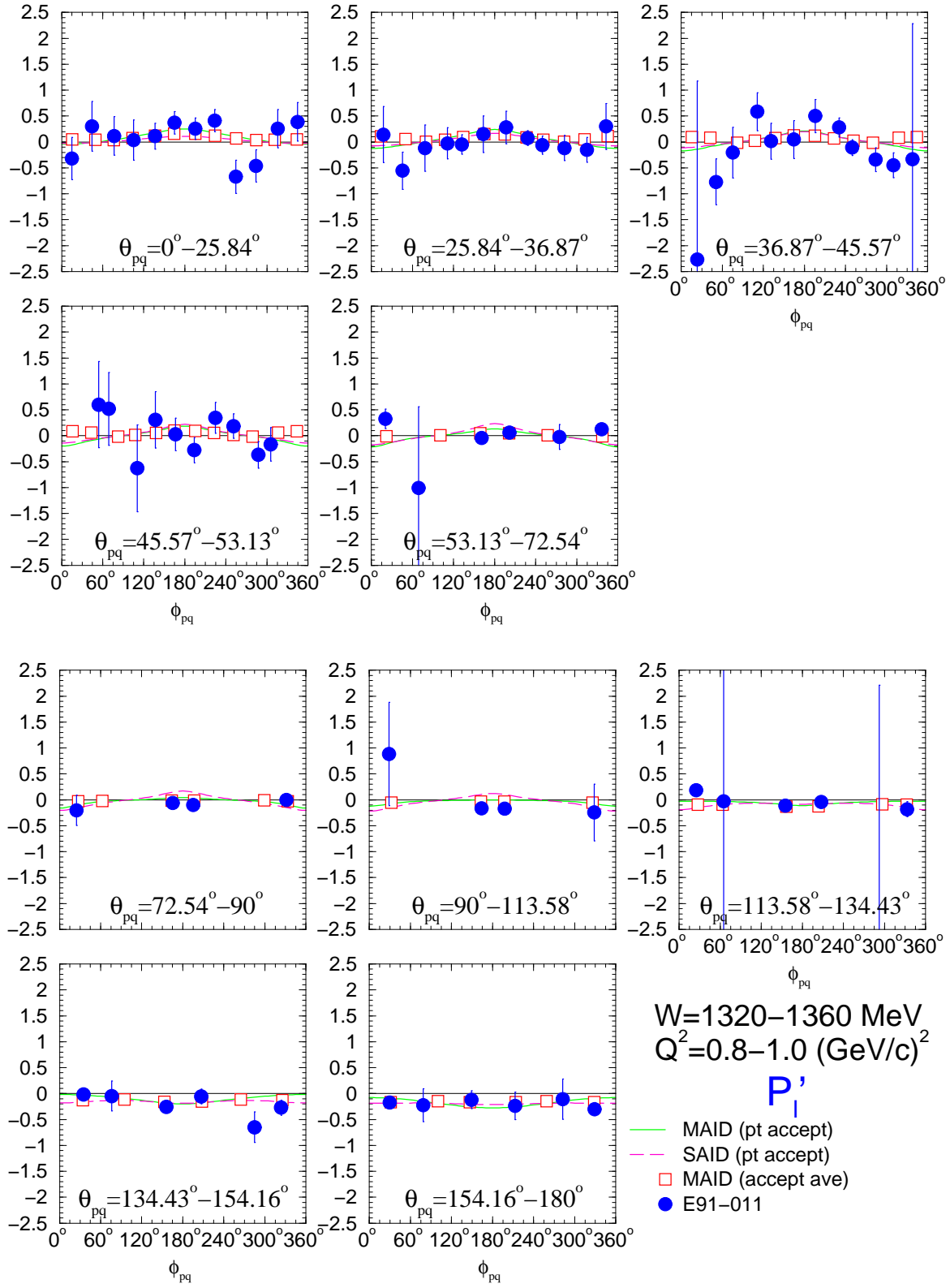




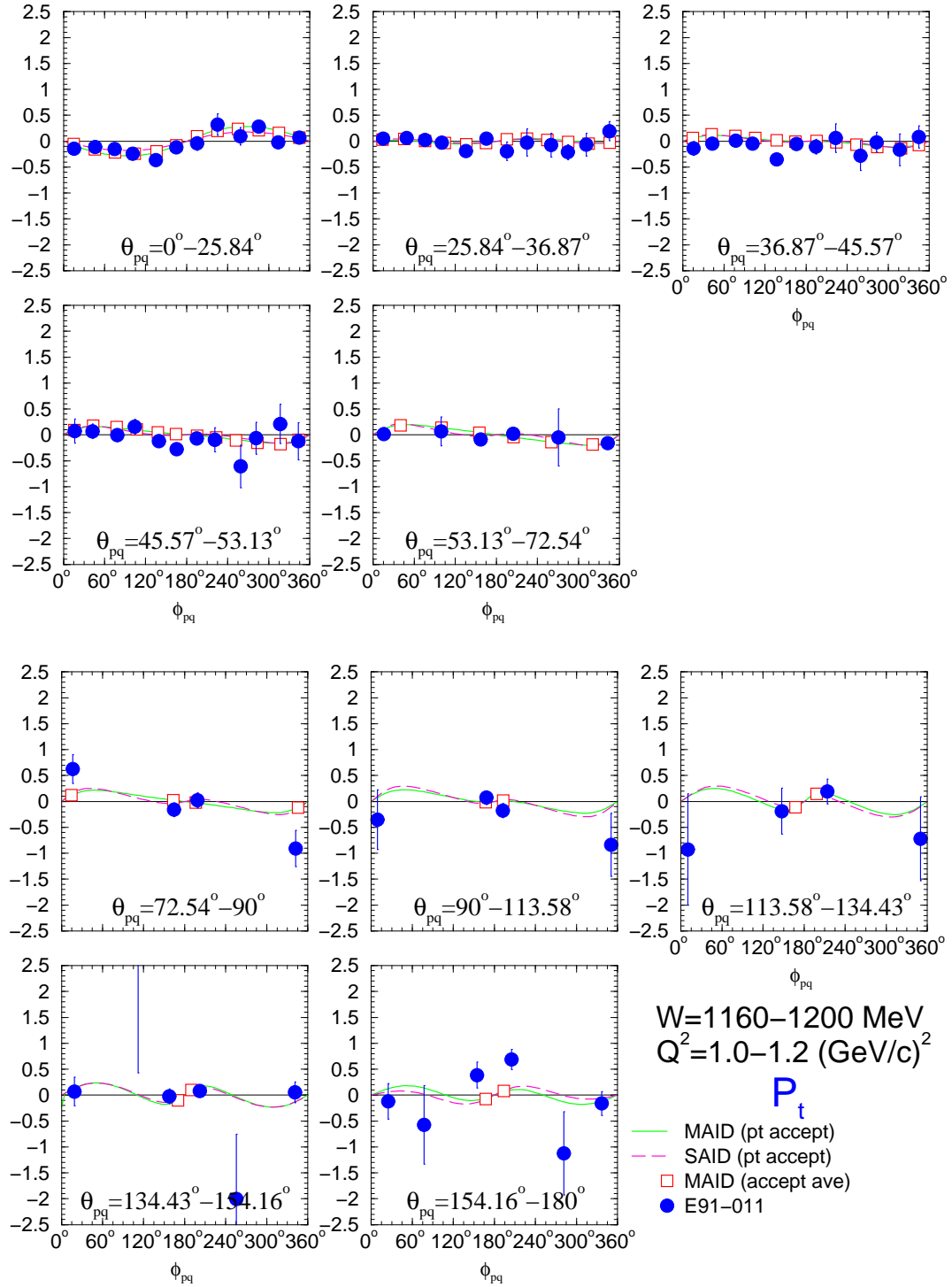


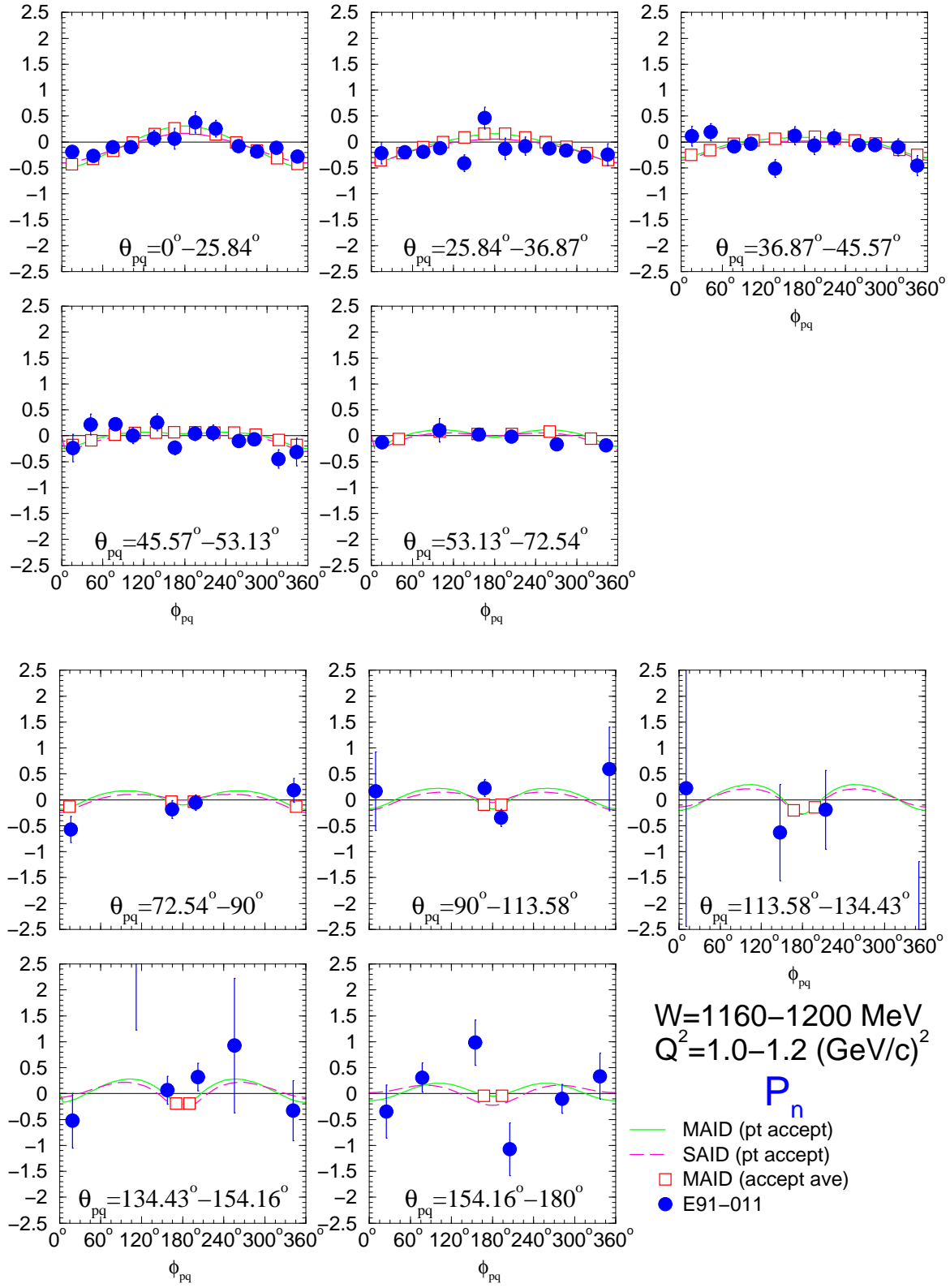


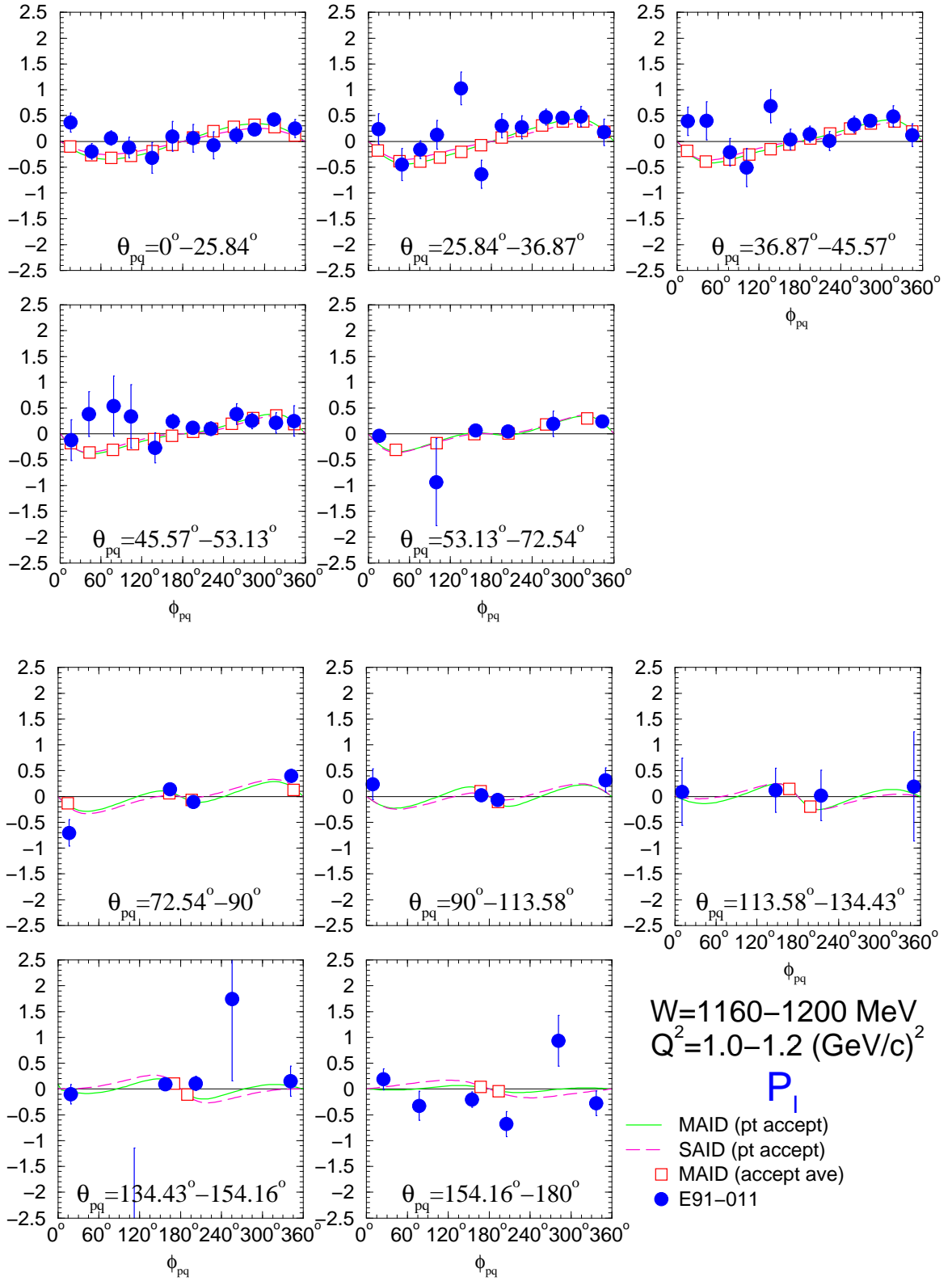


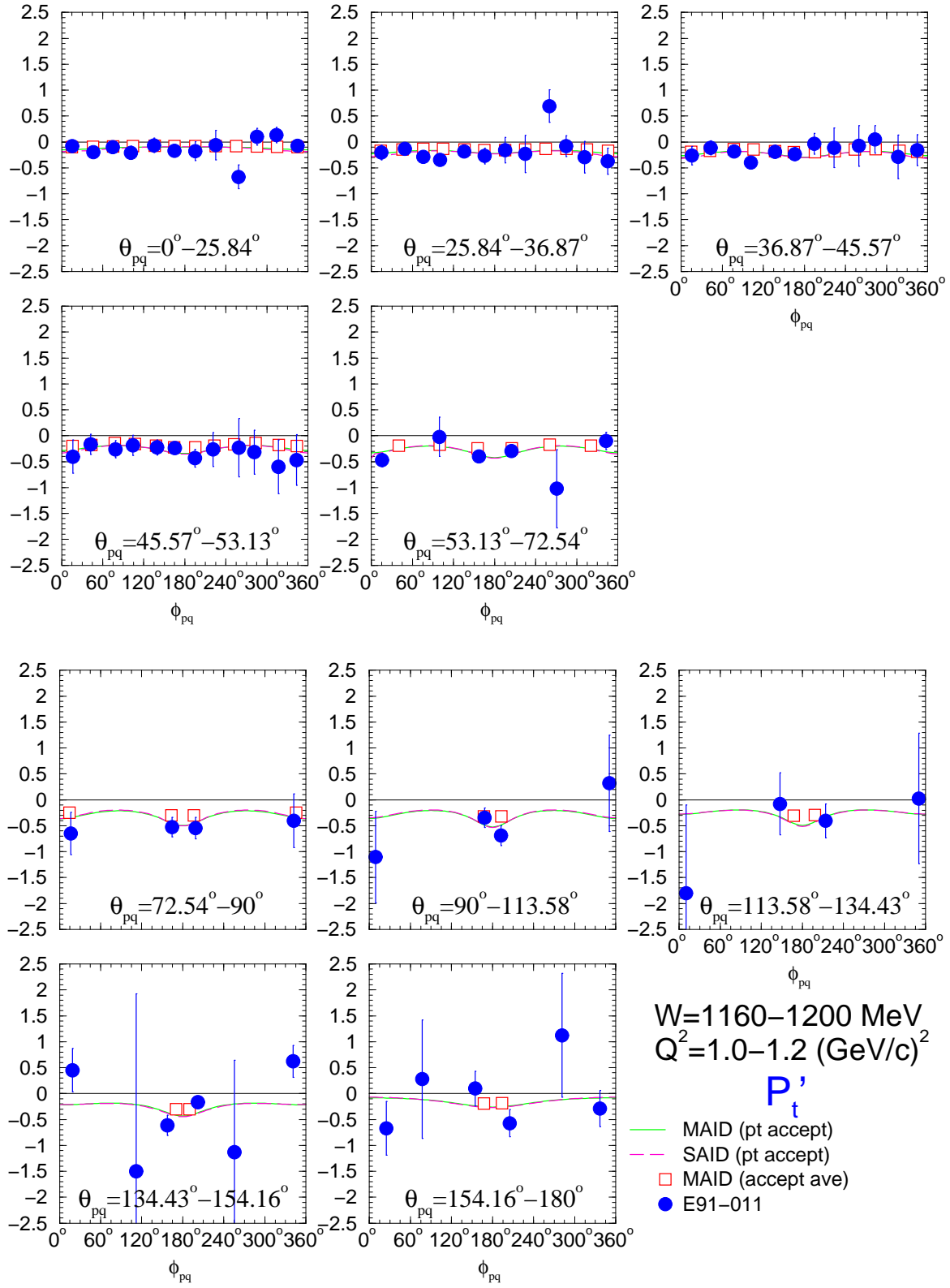


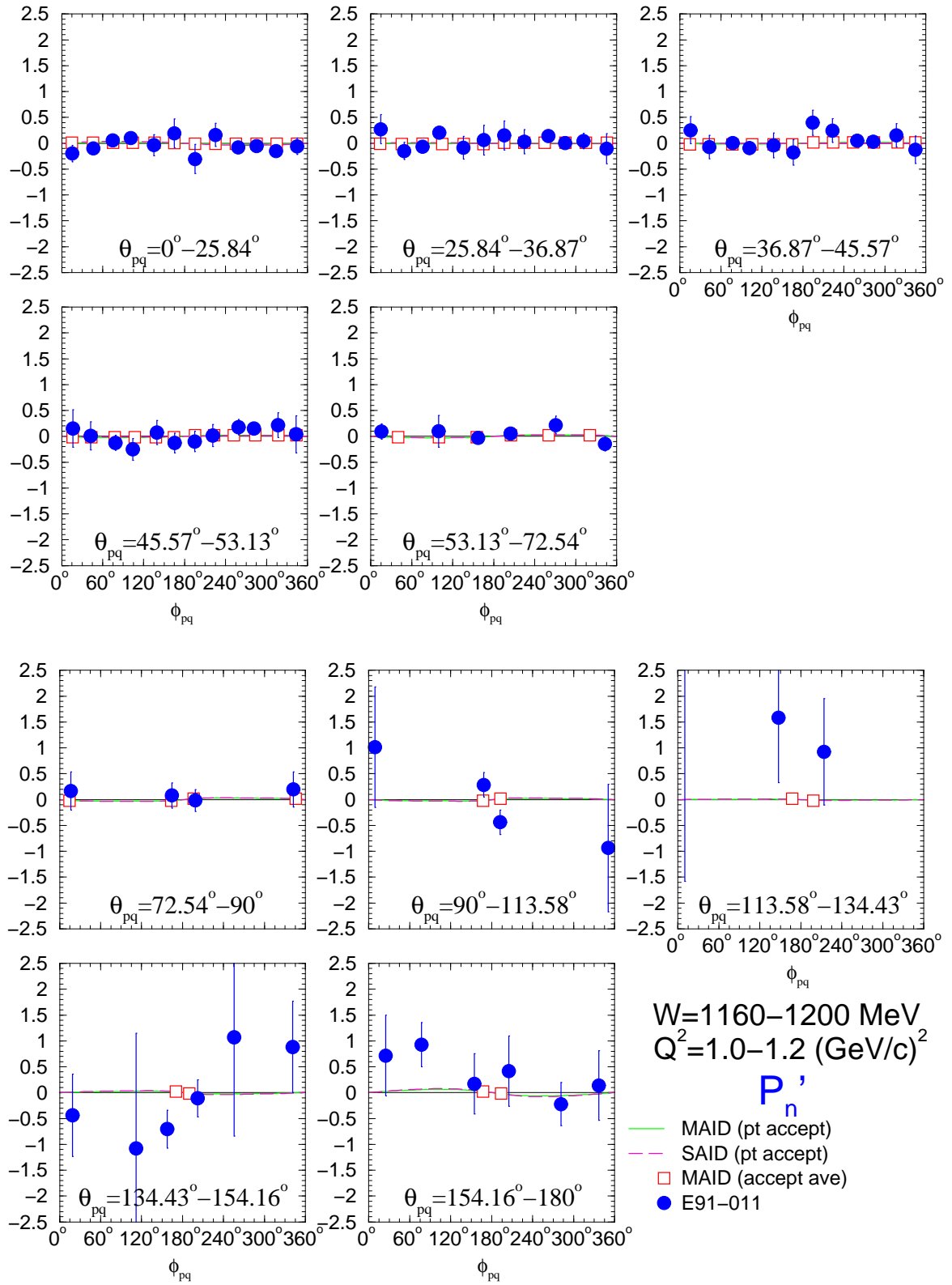
D.6.  $W = 1160\text{--}1200 \text{ MeV}, Q^2 = 1.0\text{--}1.2 \text{ (GeV/c)}^2$

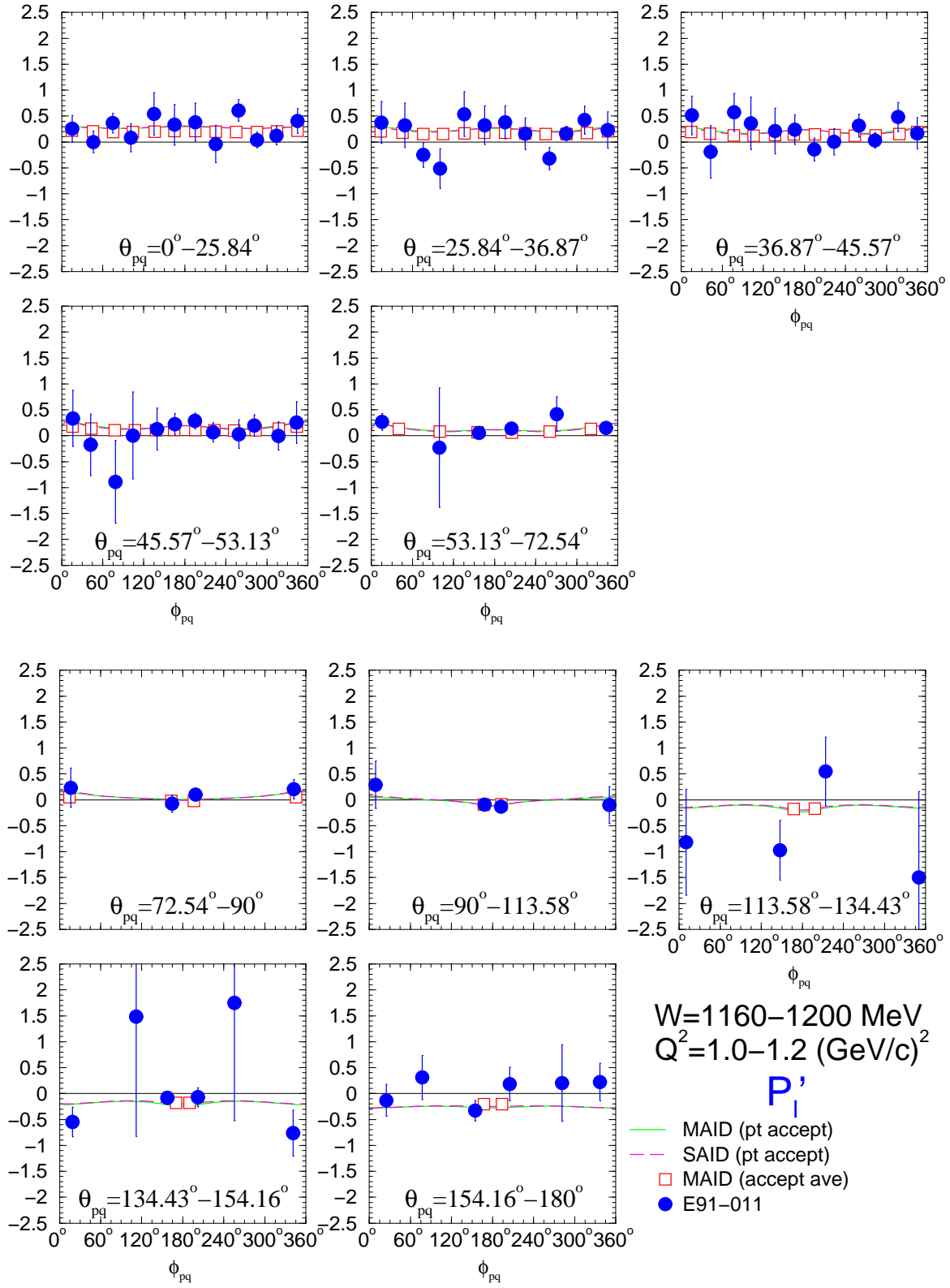






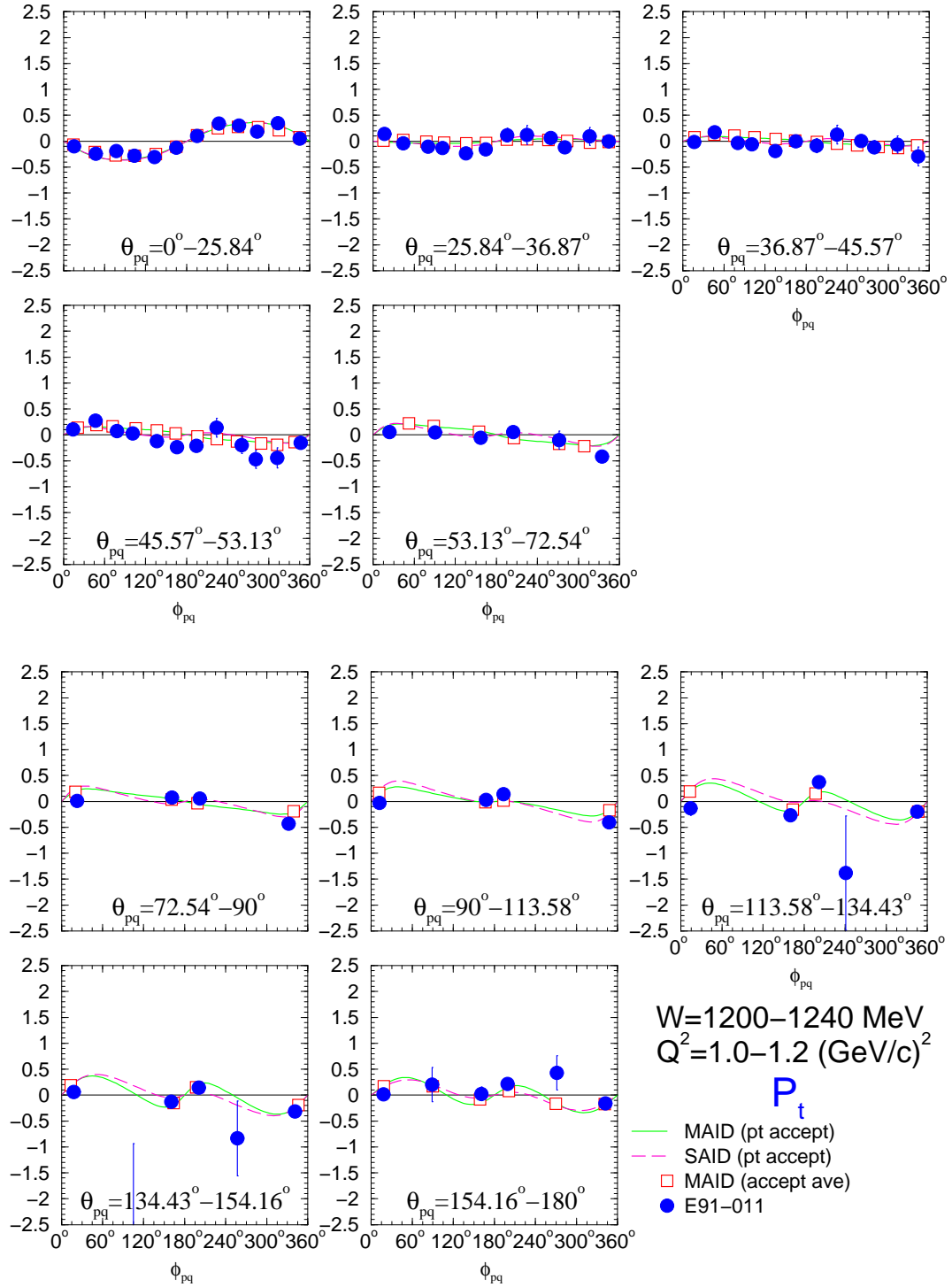


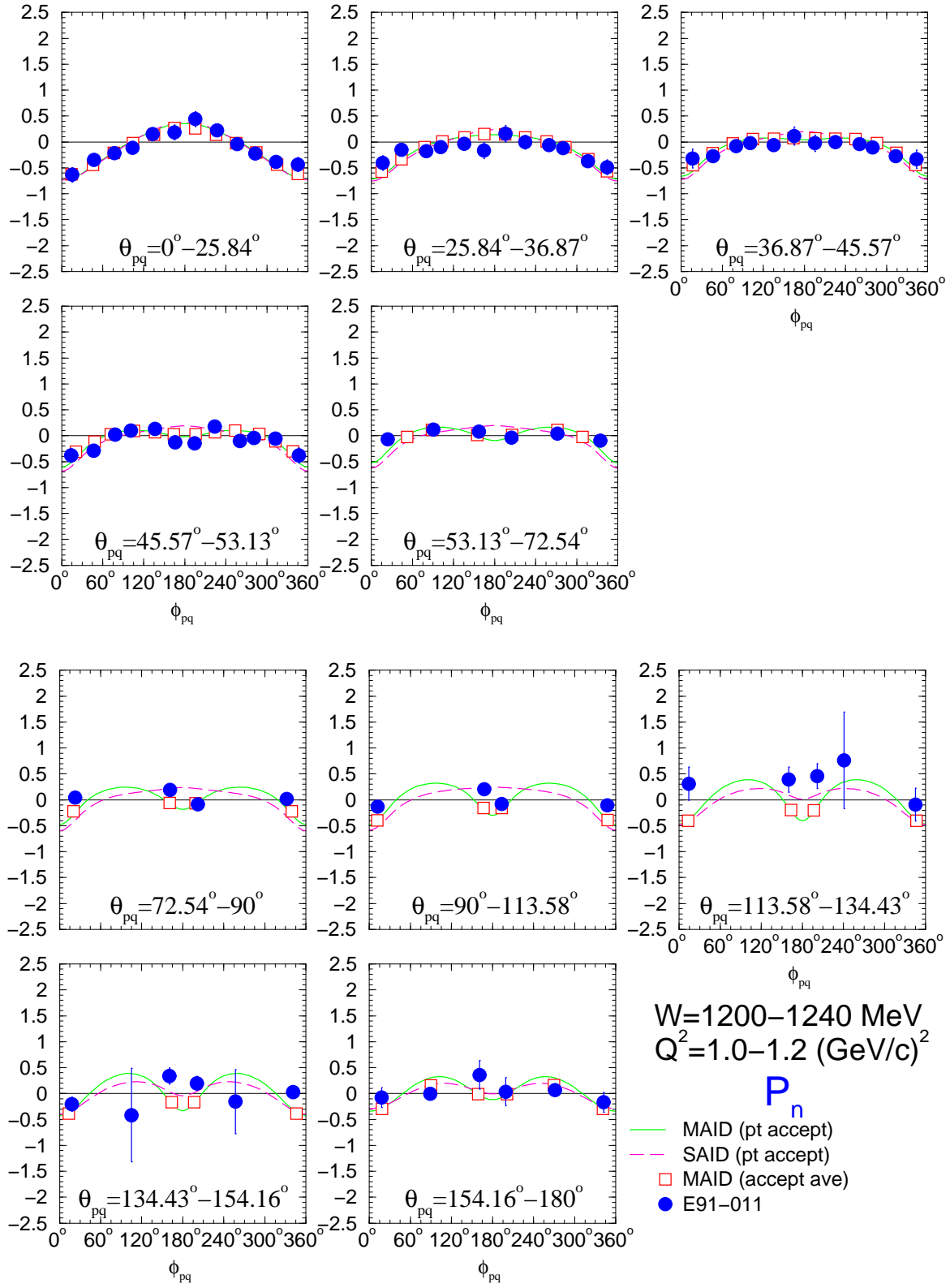


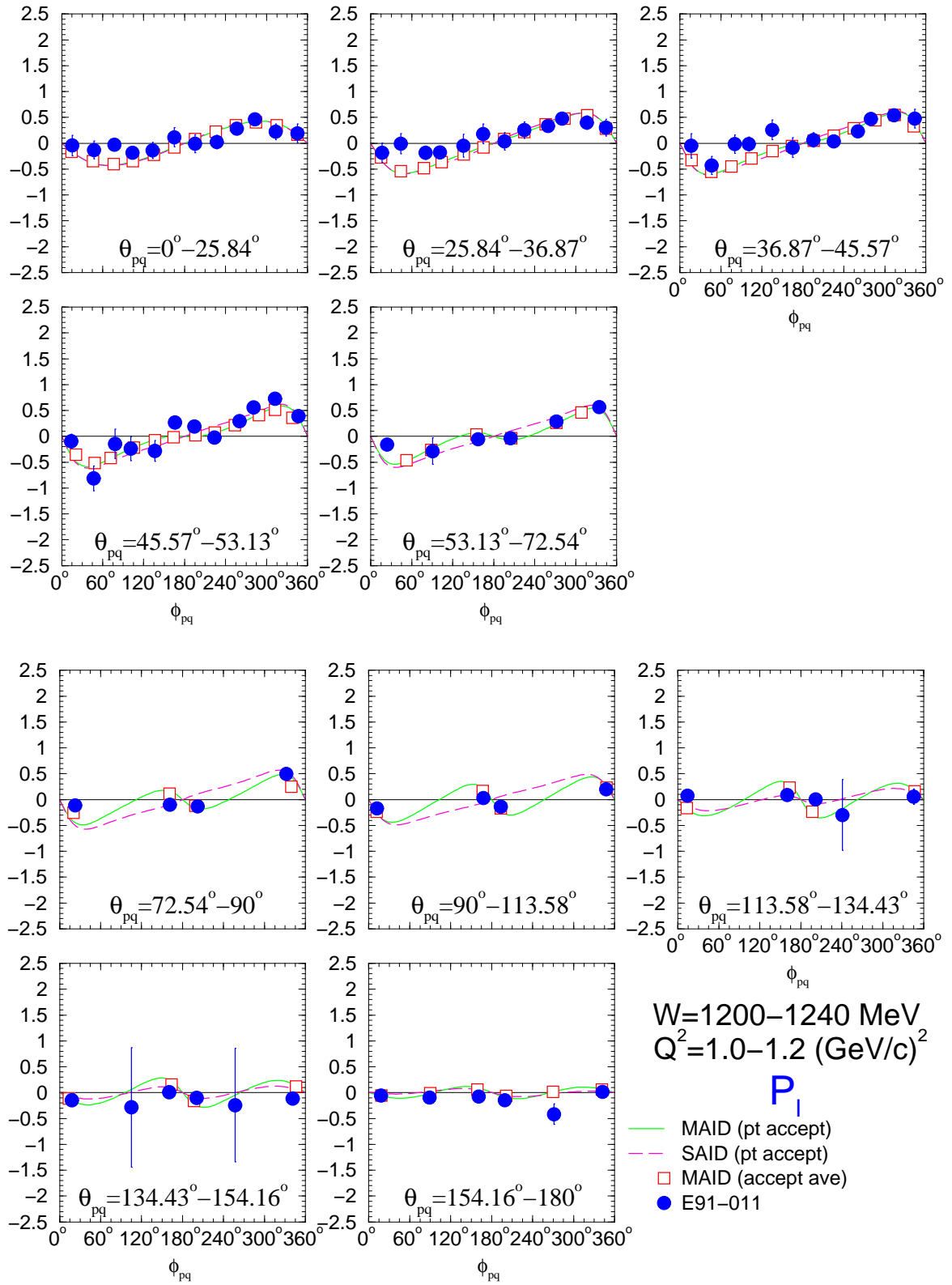


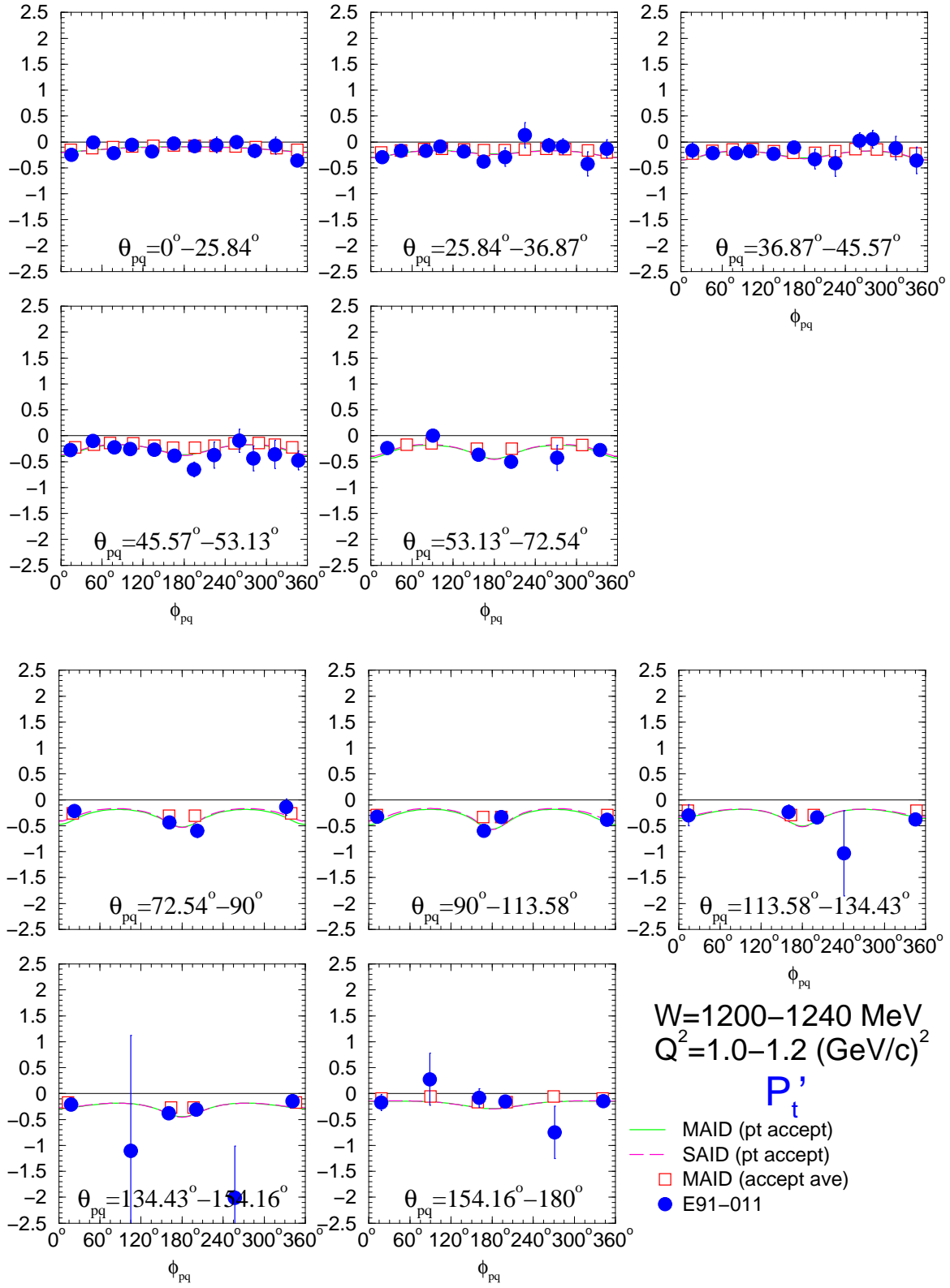


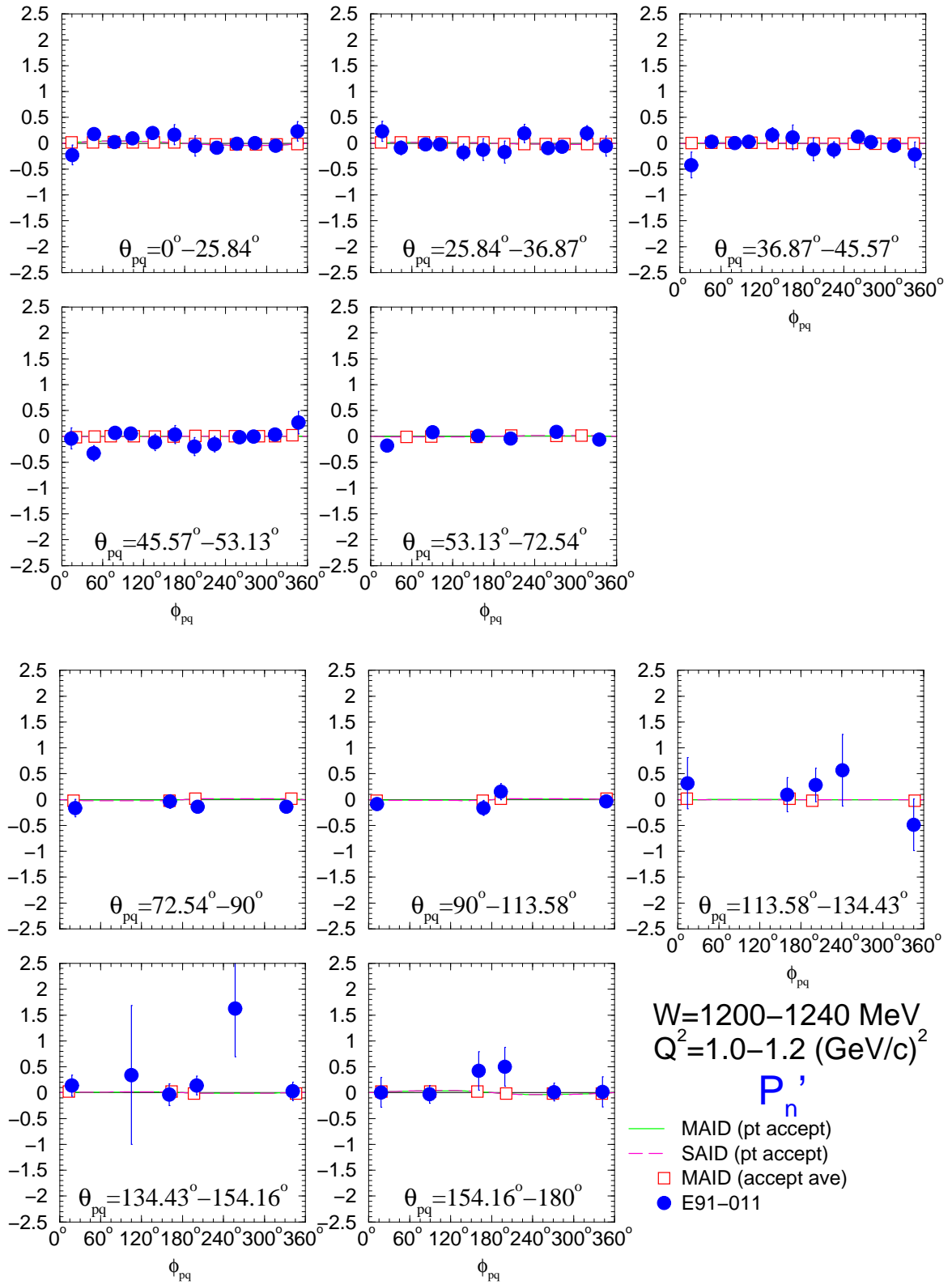
D.7.  $W = 1200\text{--}1240 \text{ MeV}, Q^2 = 1.0\text{--}1.2 \text{ (GeV/c)}^2$

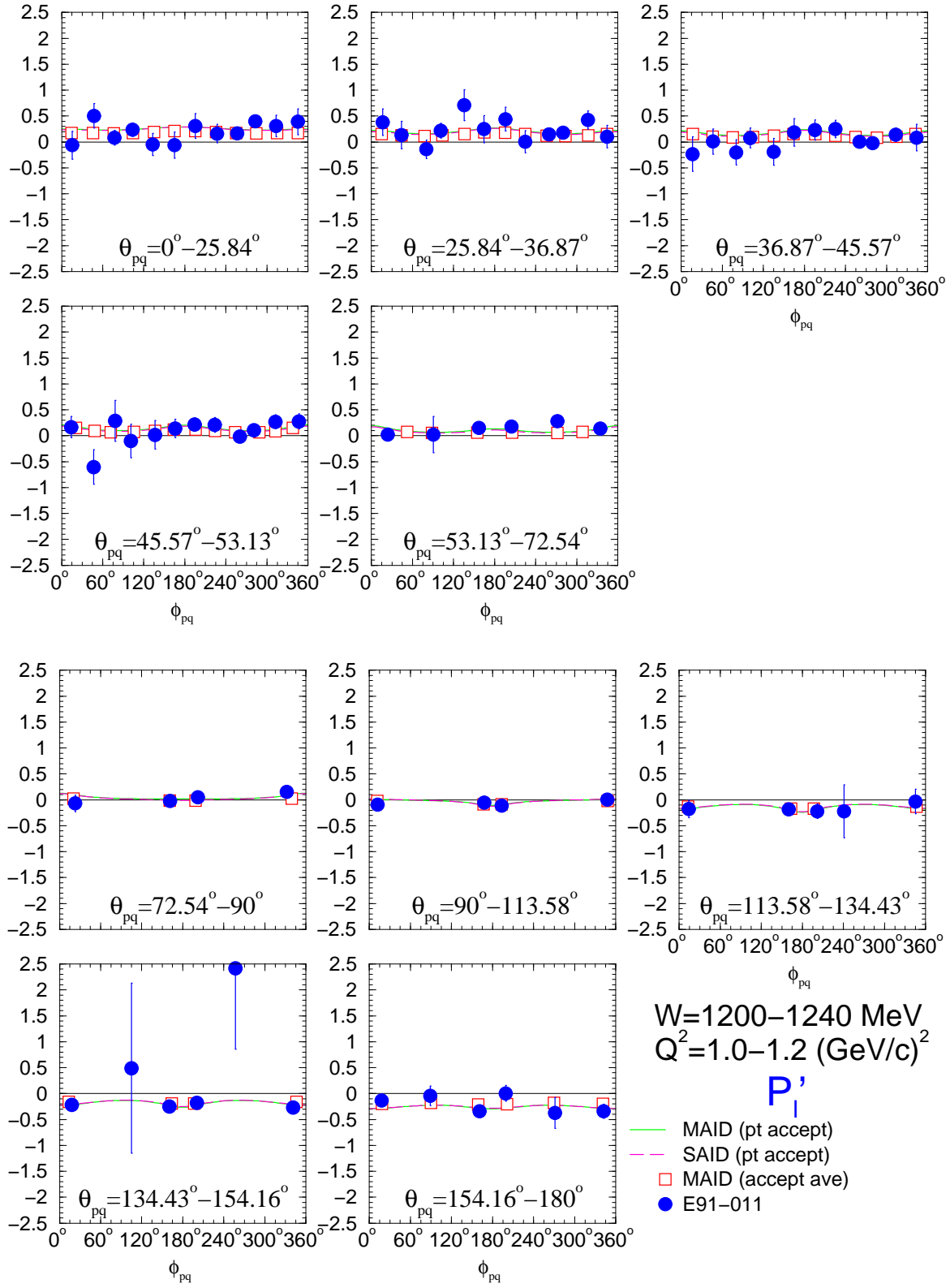




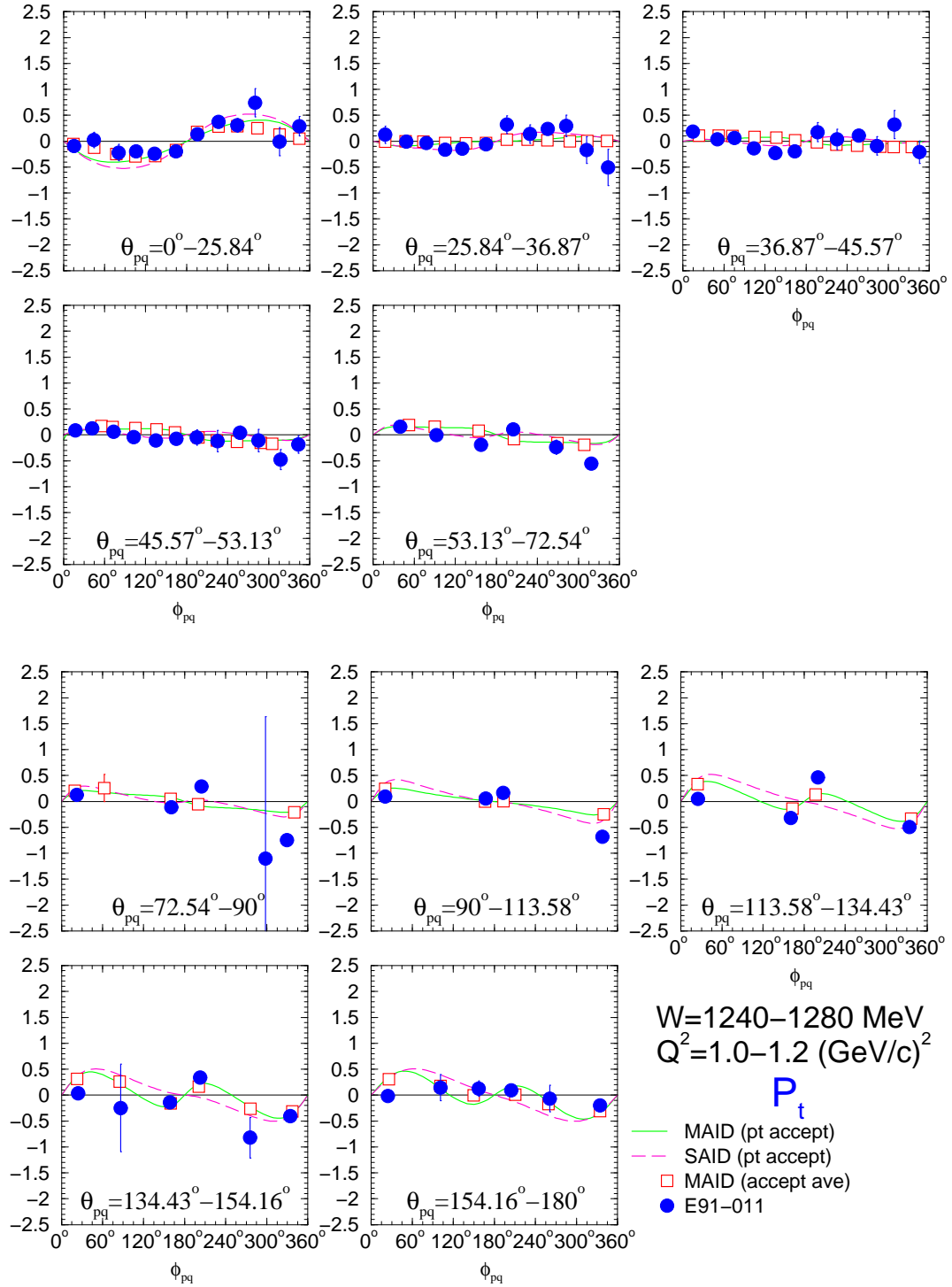


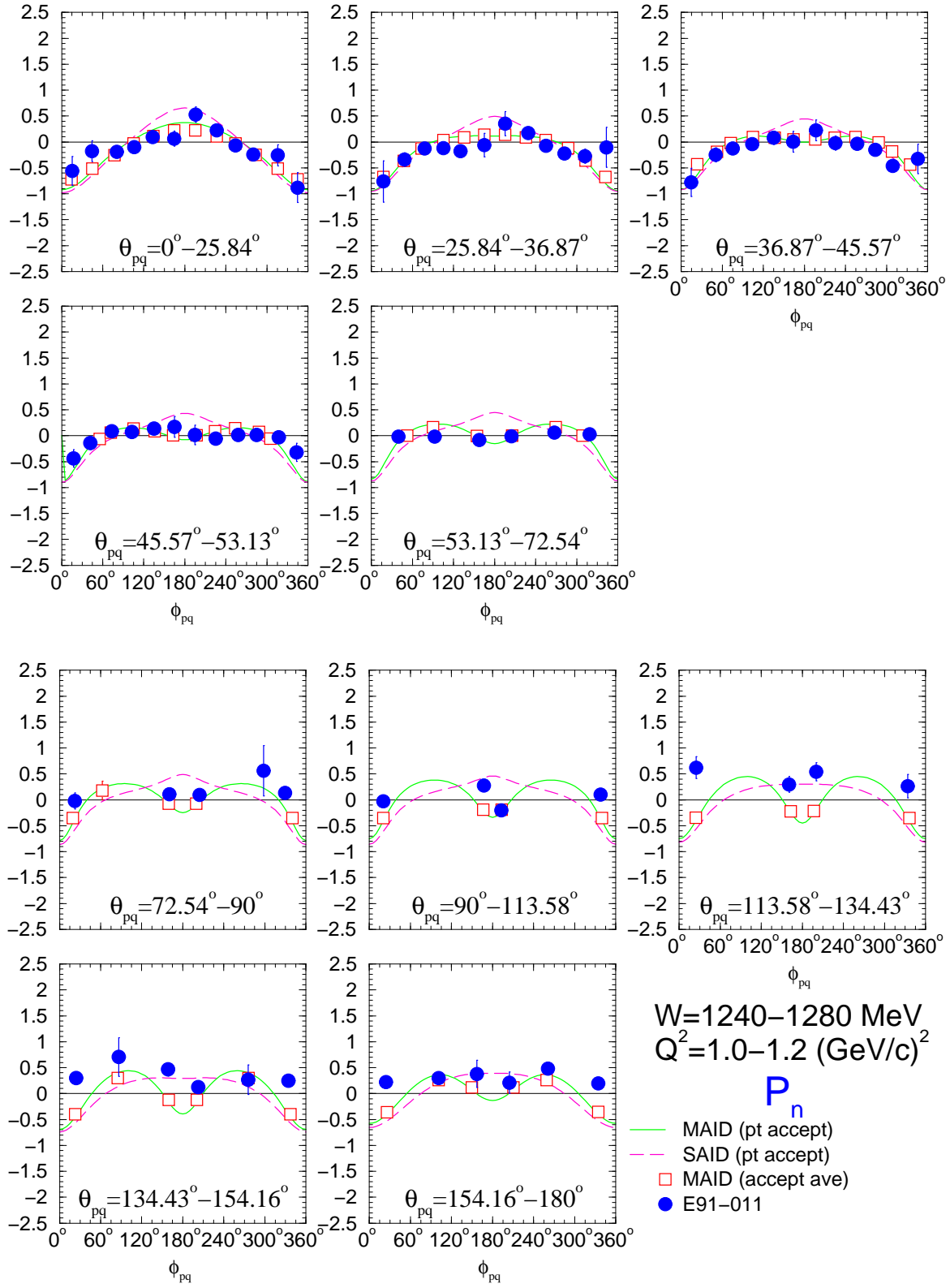




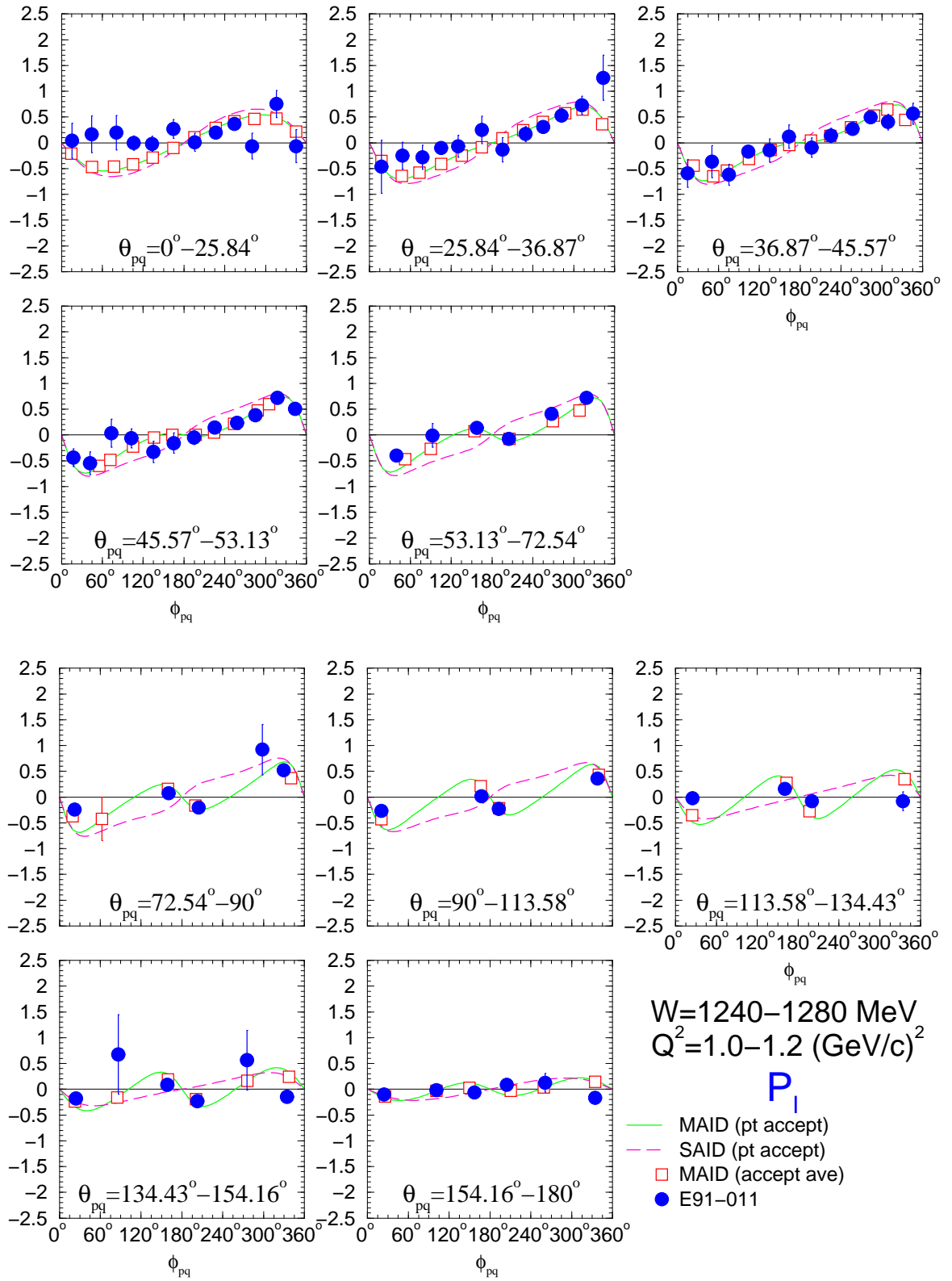


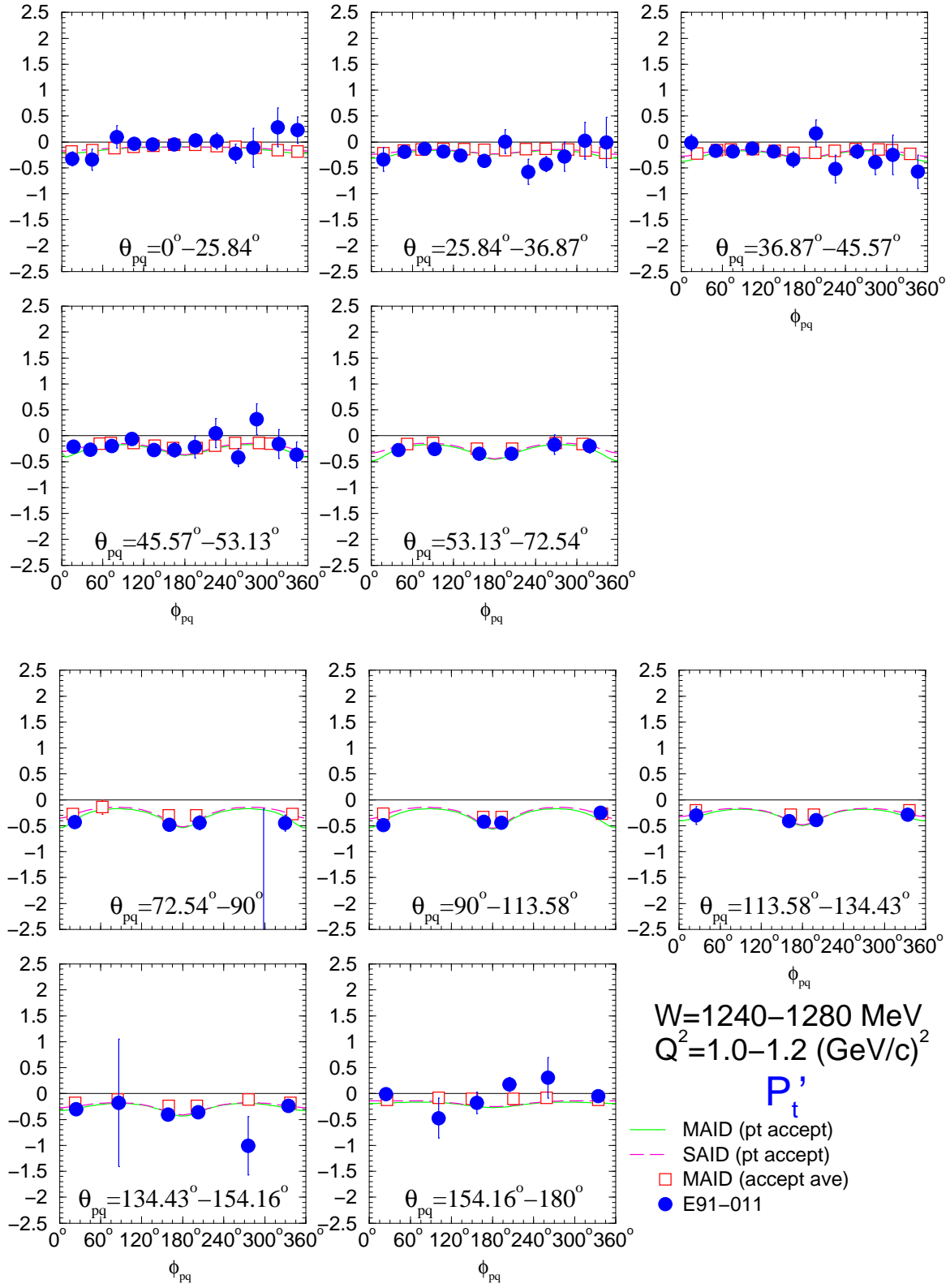
D.8.  $W = 1240\text{--}1280 \text{ MeV}, Q^2 = 1.0\text{--}1.2 \text{ (GeV/c)}^2$

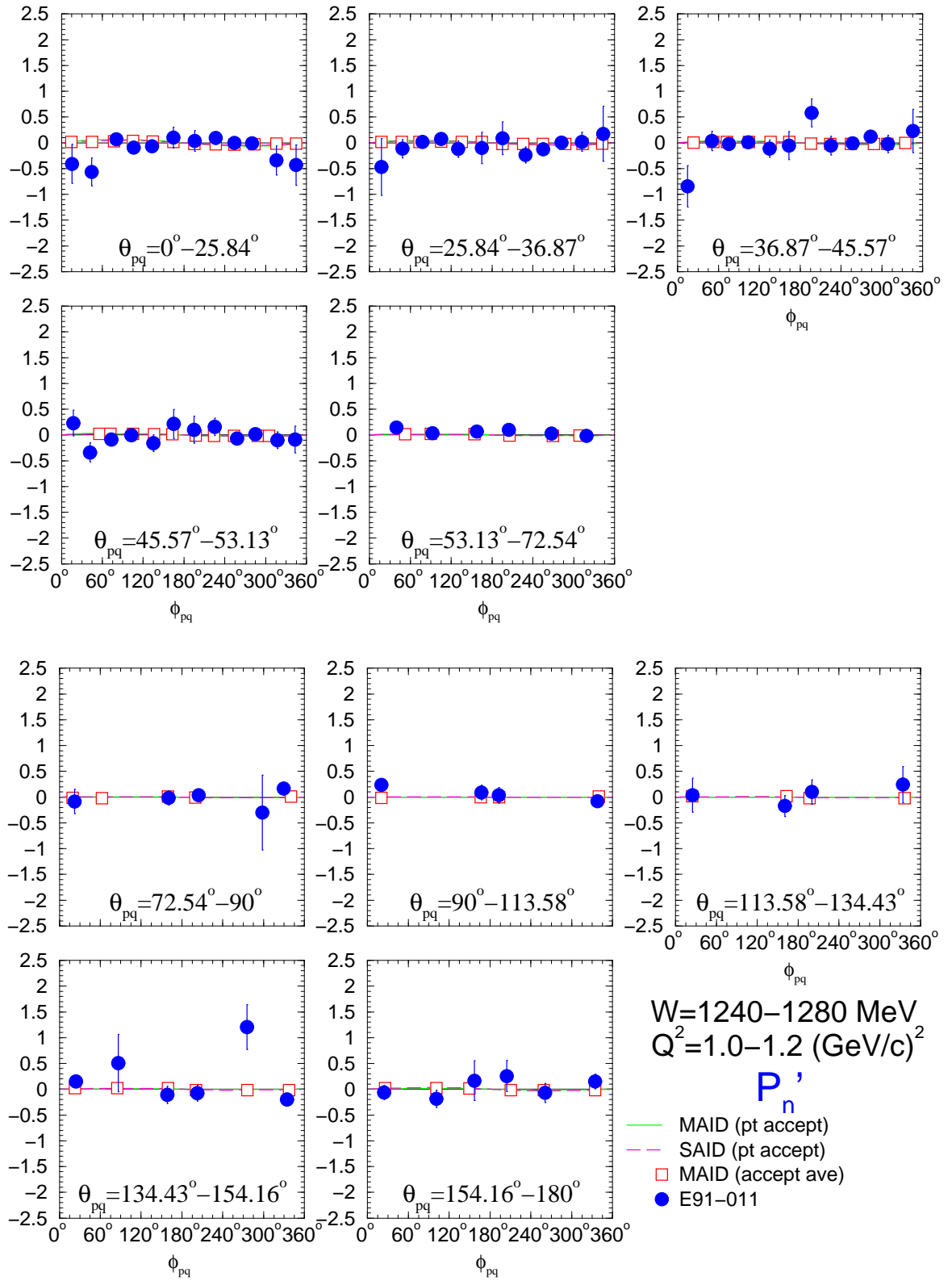


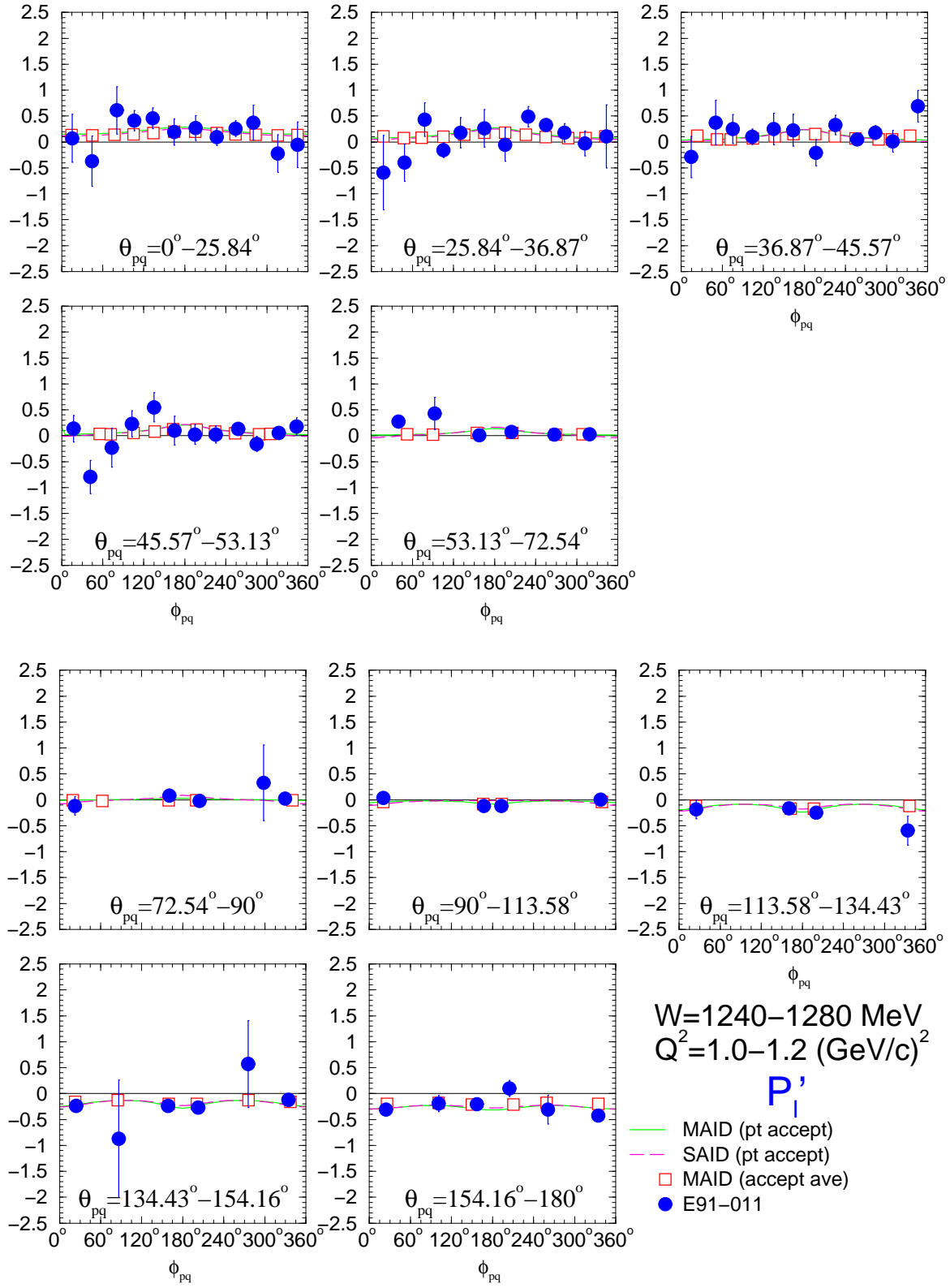




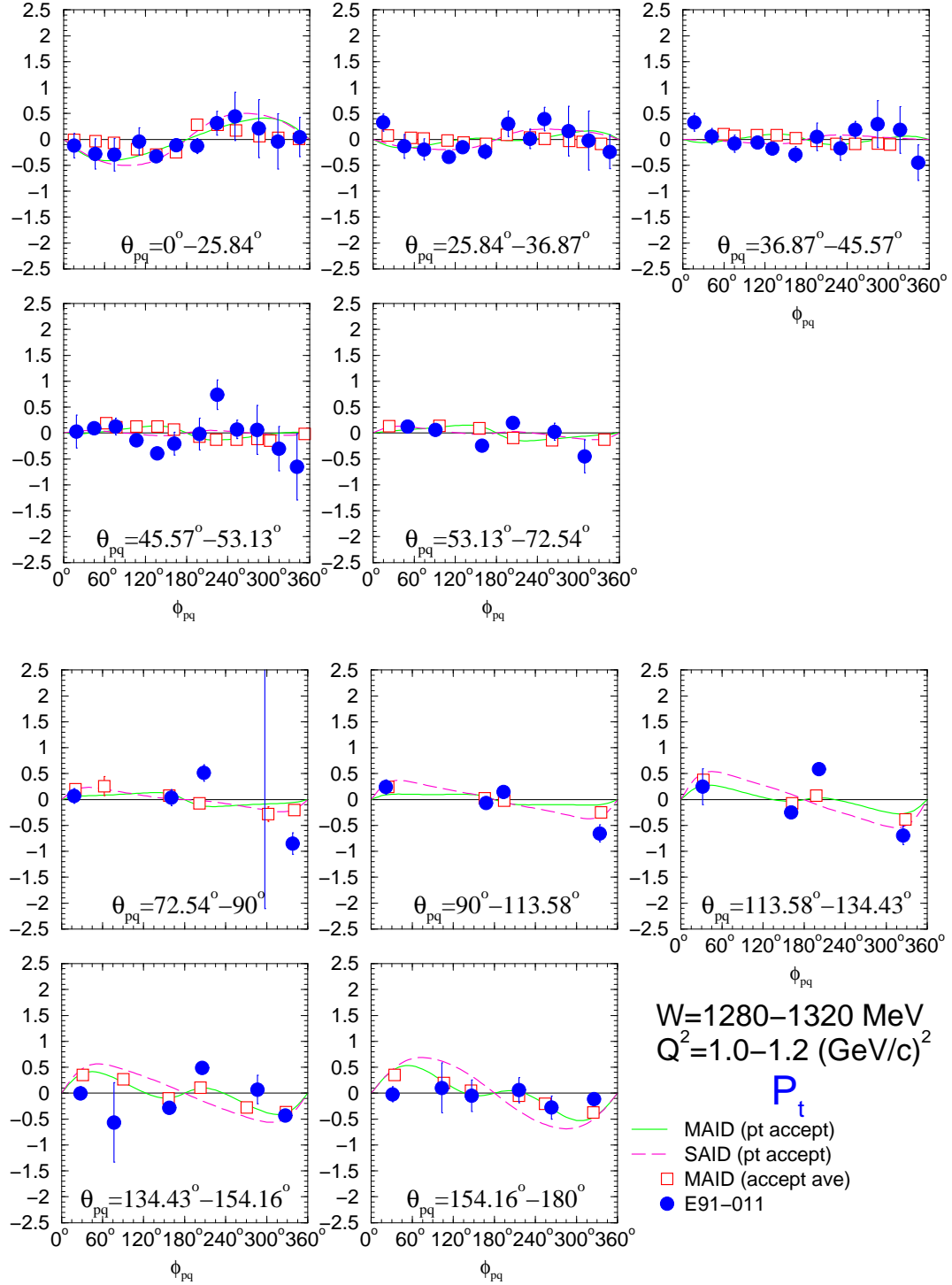


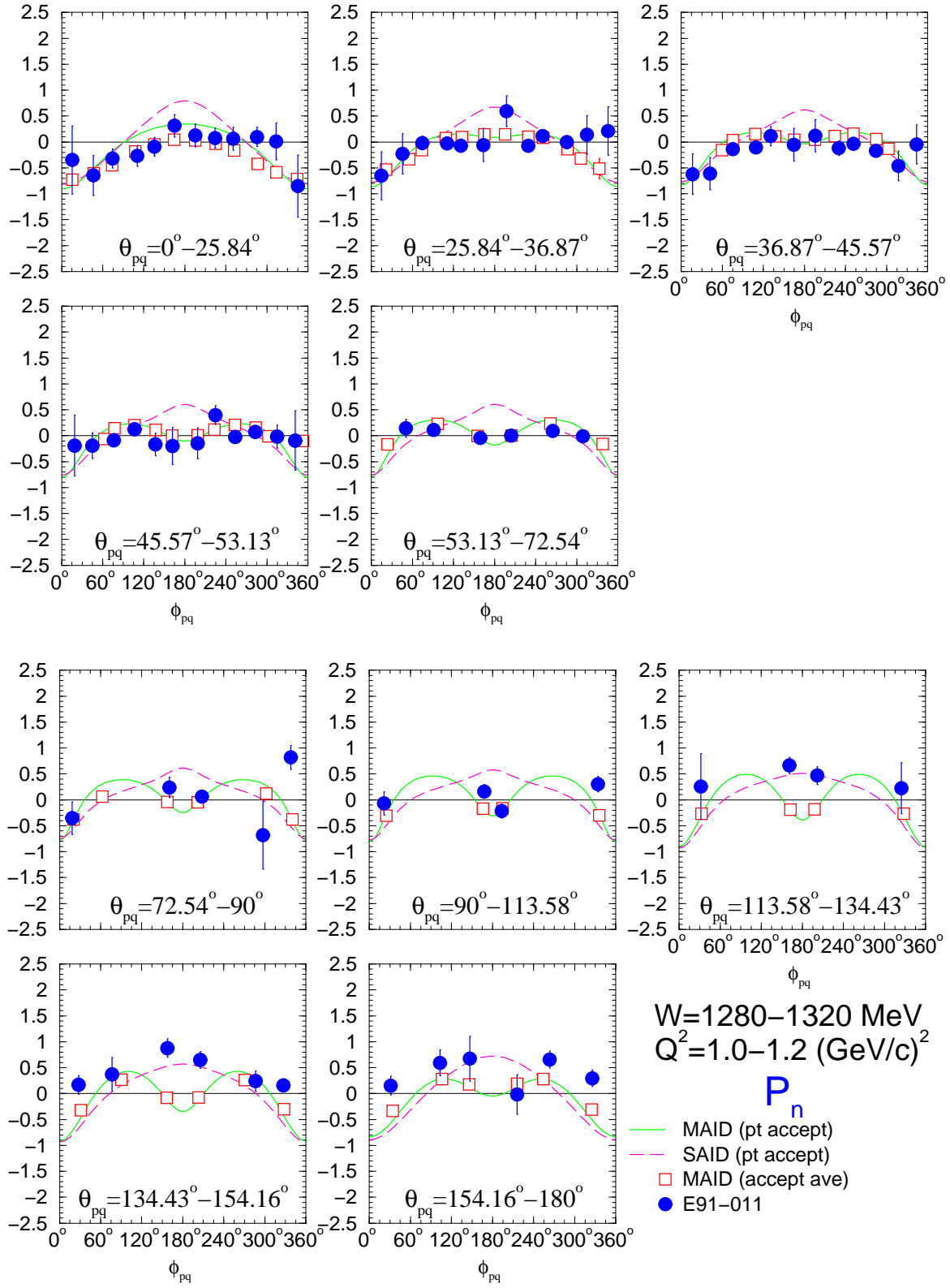


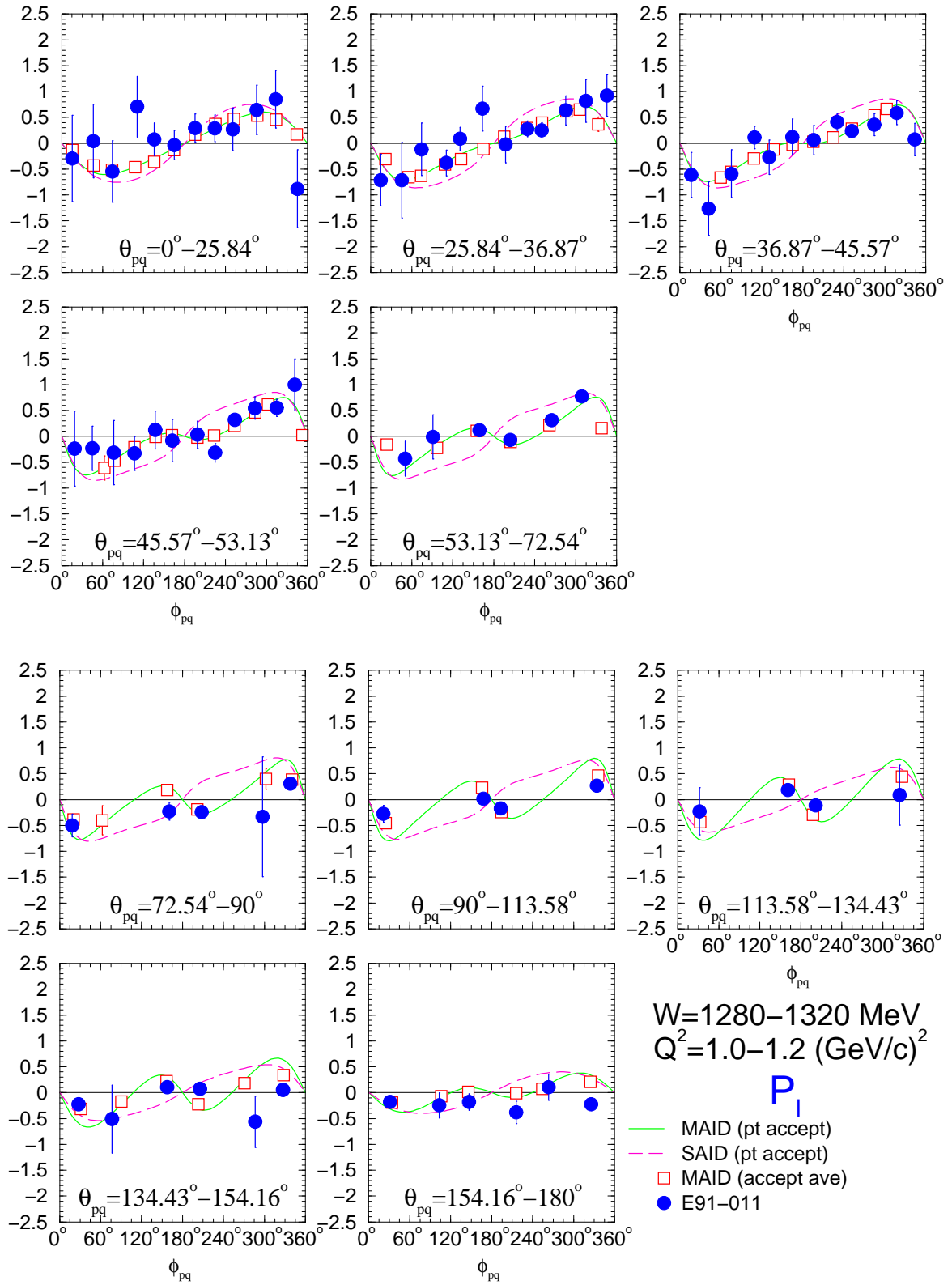


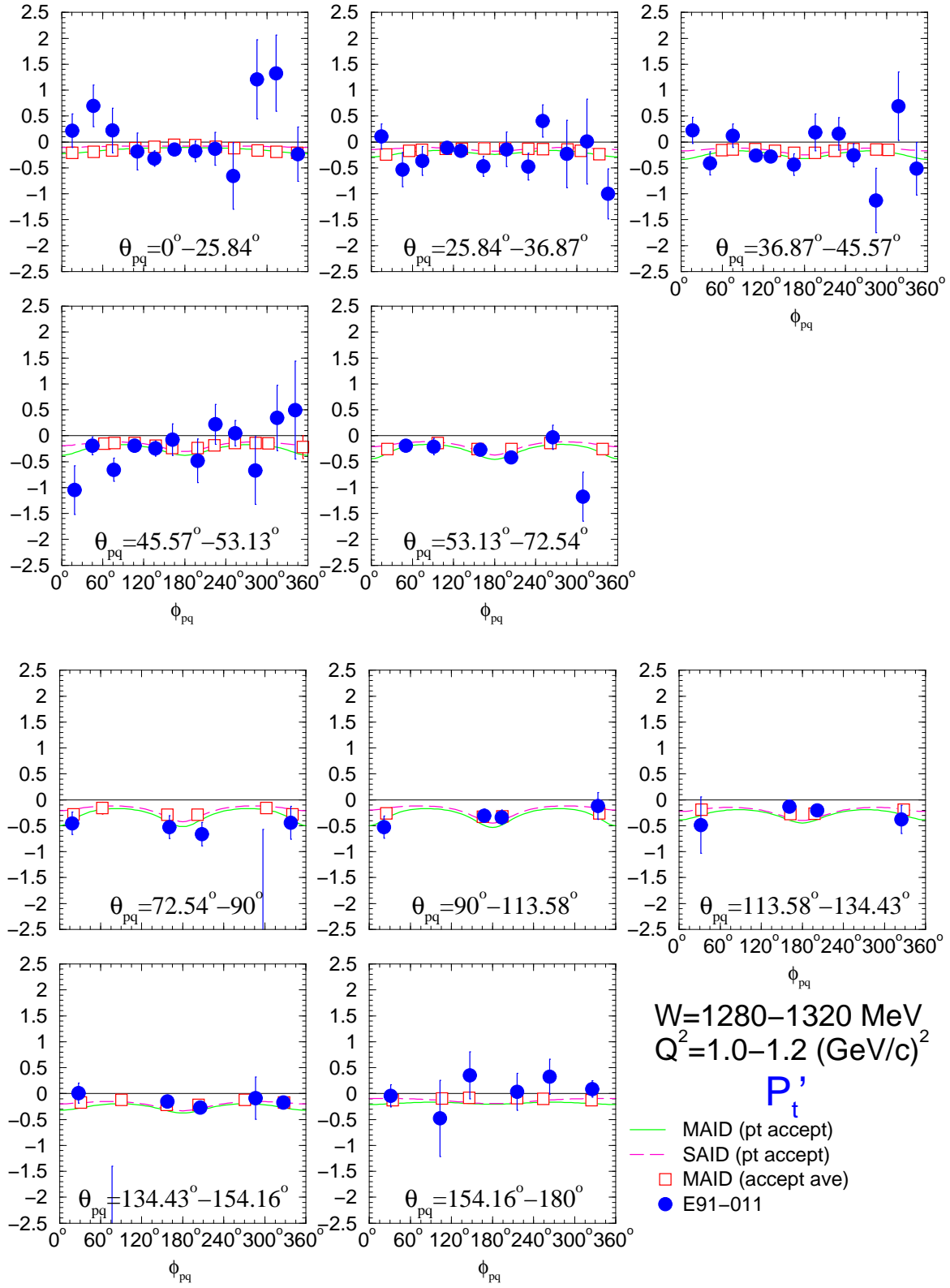


D.9.  $W = 1280\text{--}1320\text{ MeV}, Q^2 = 1.0\text{--}1.2\text{ (GeV/c)}^2$

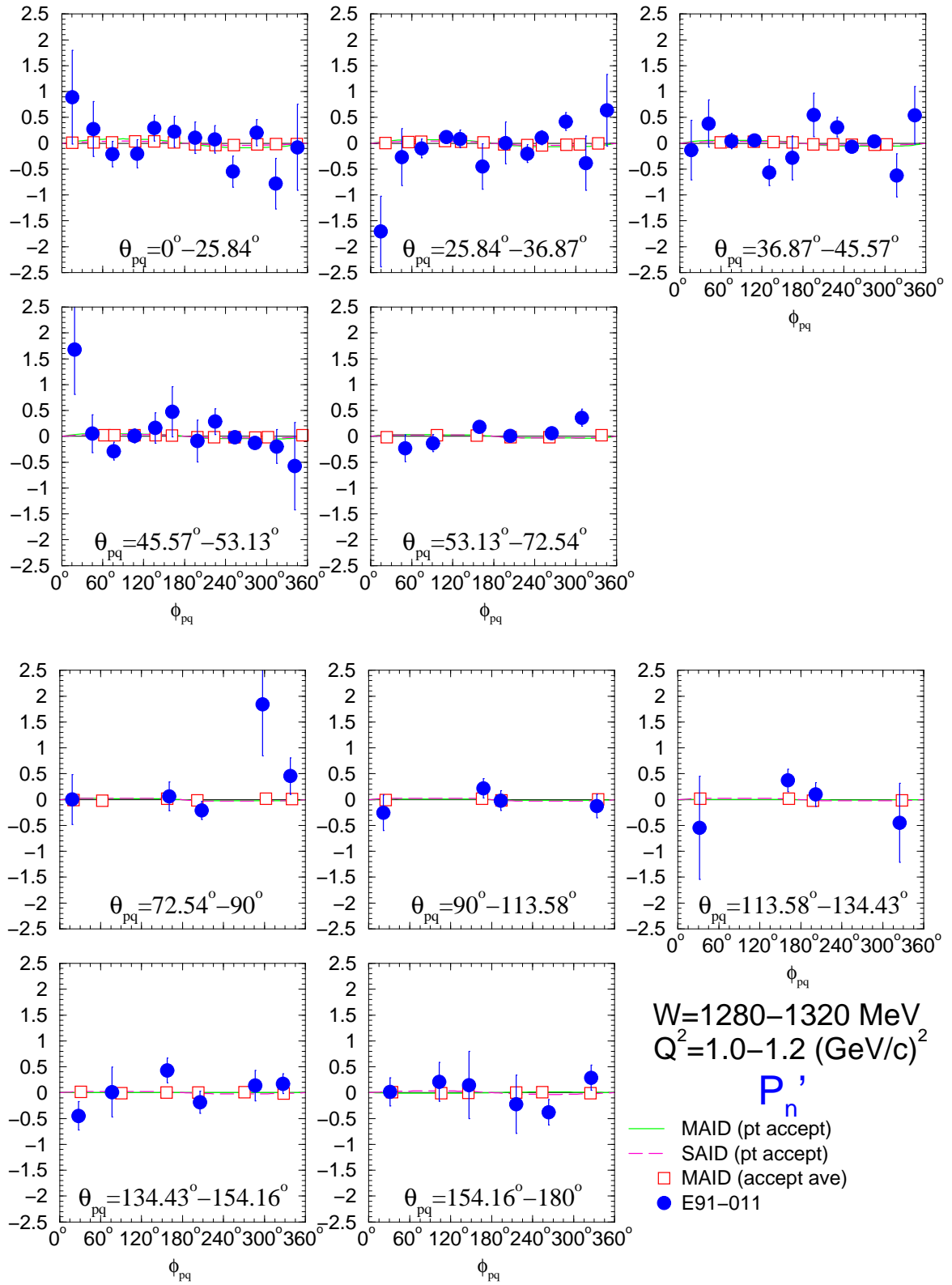


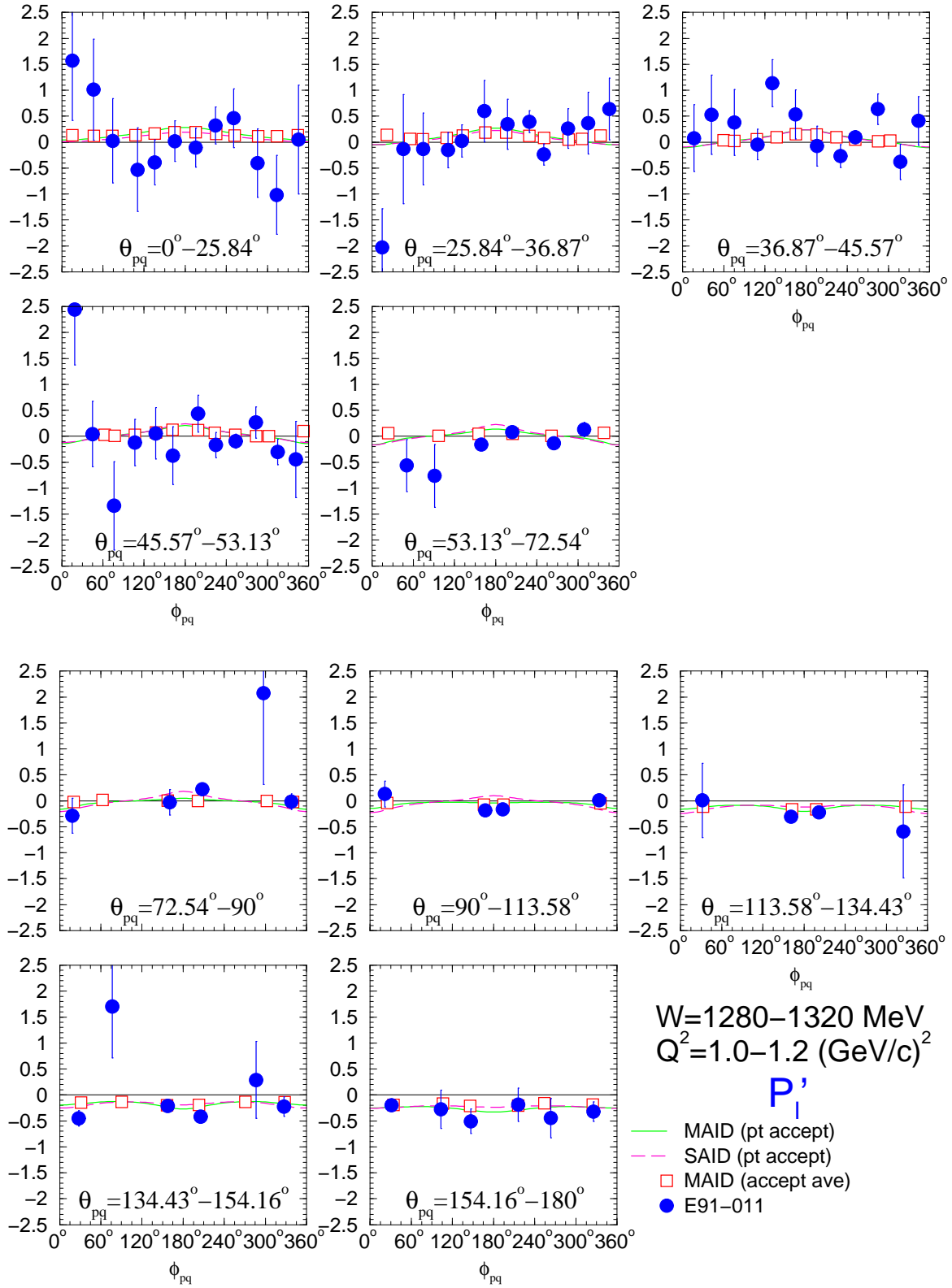




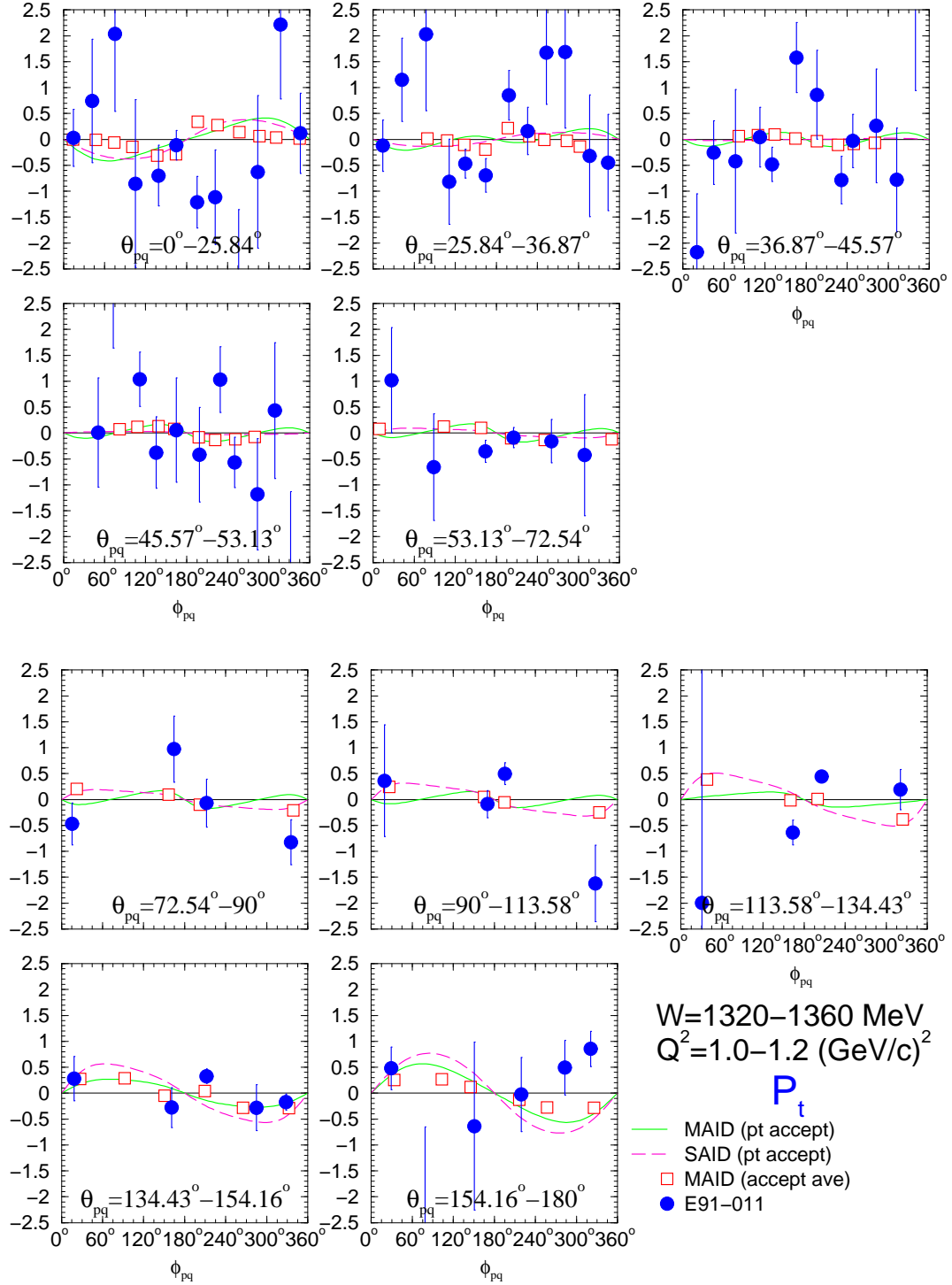


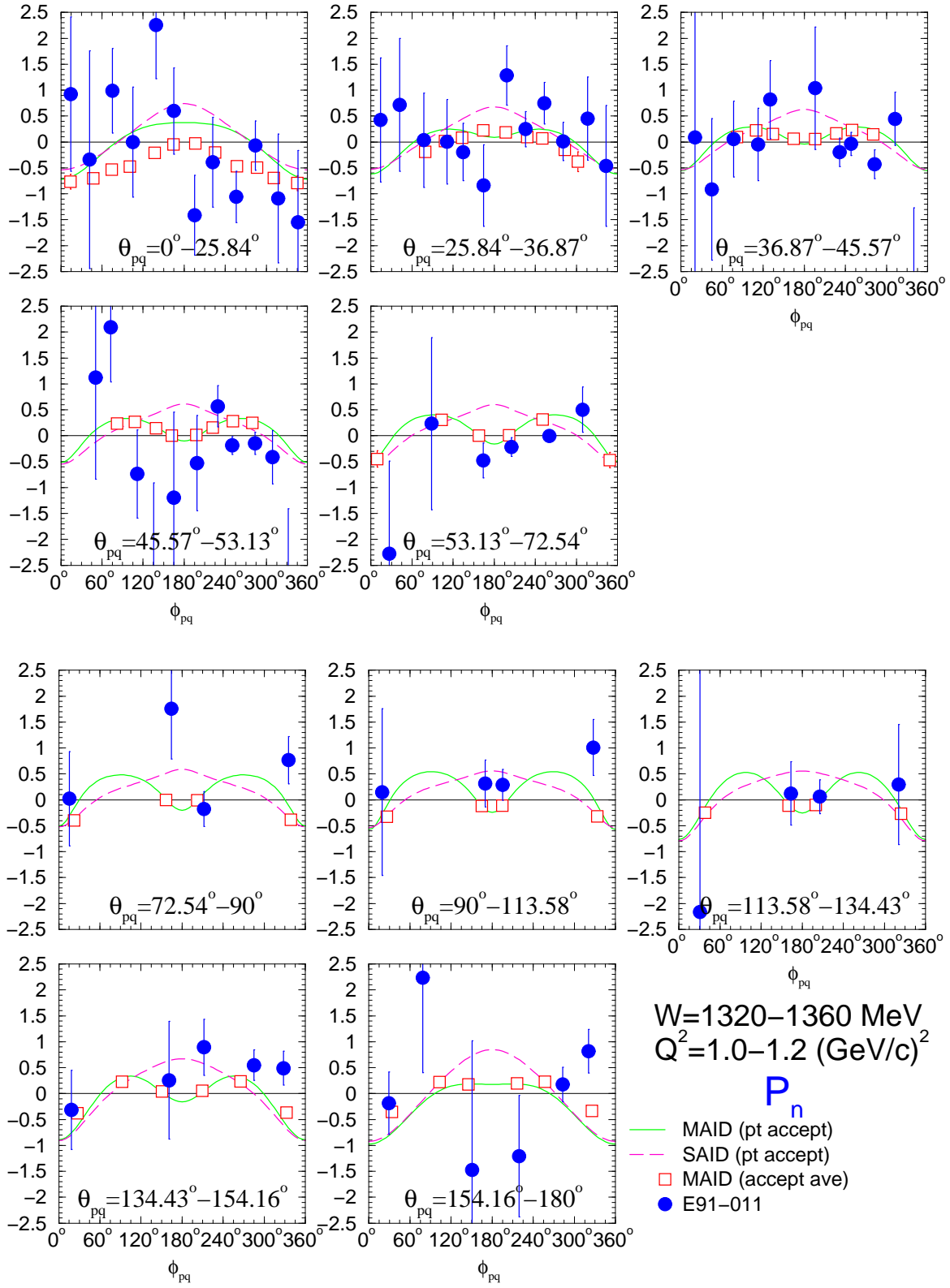


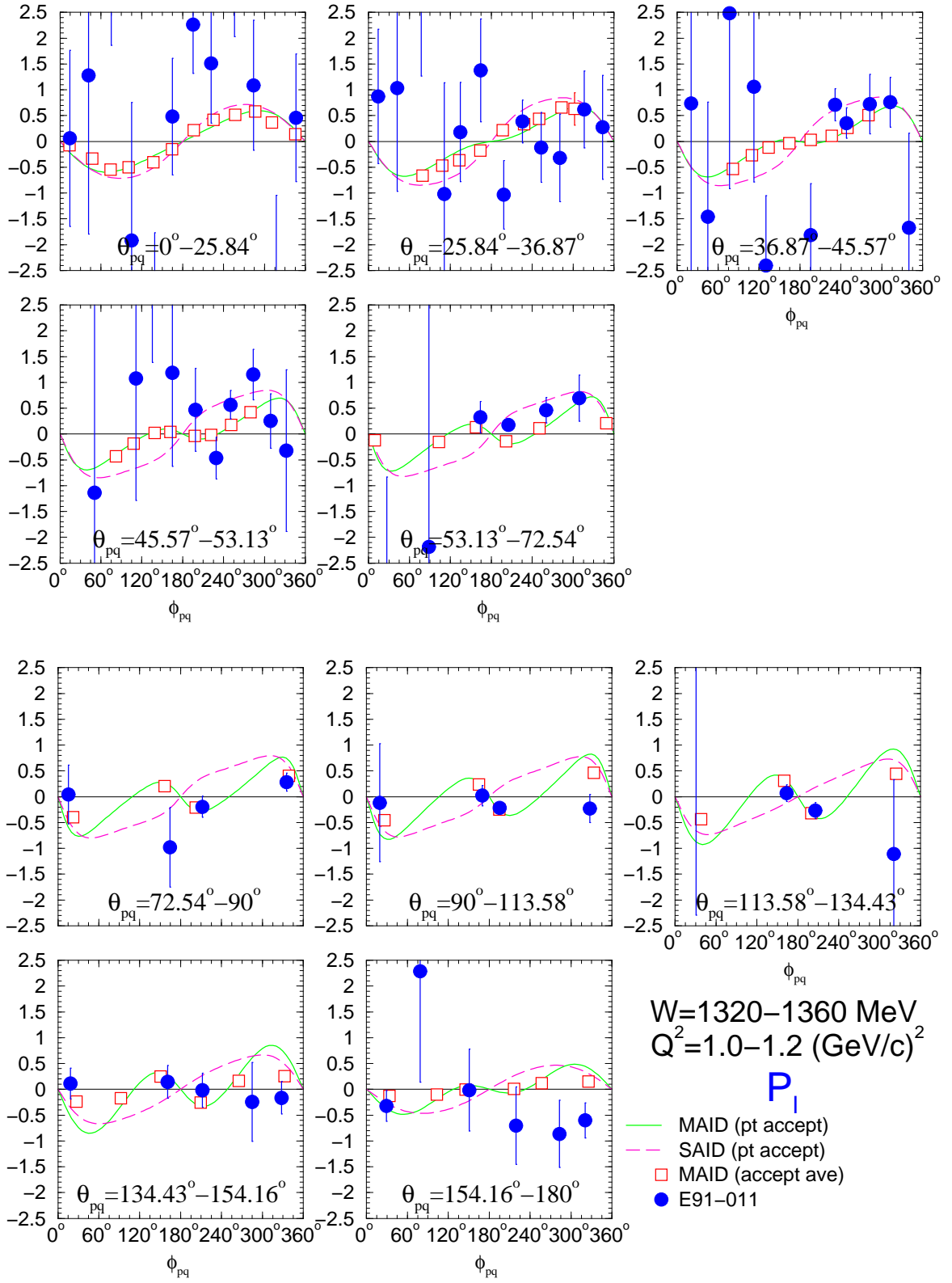


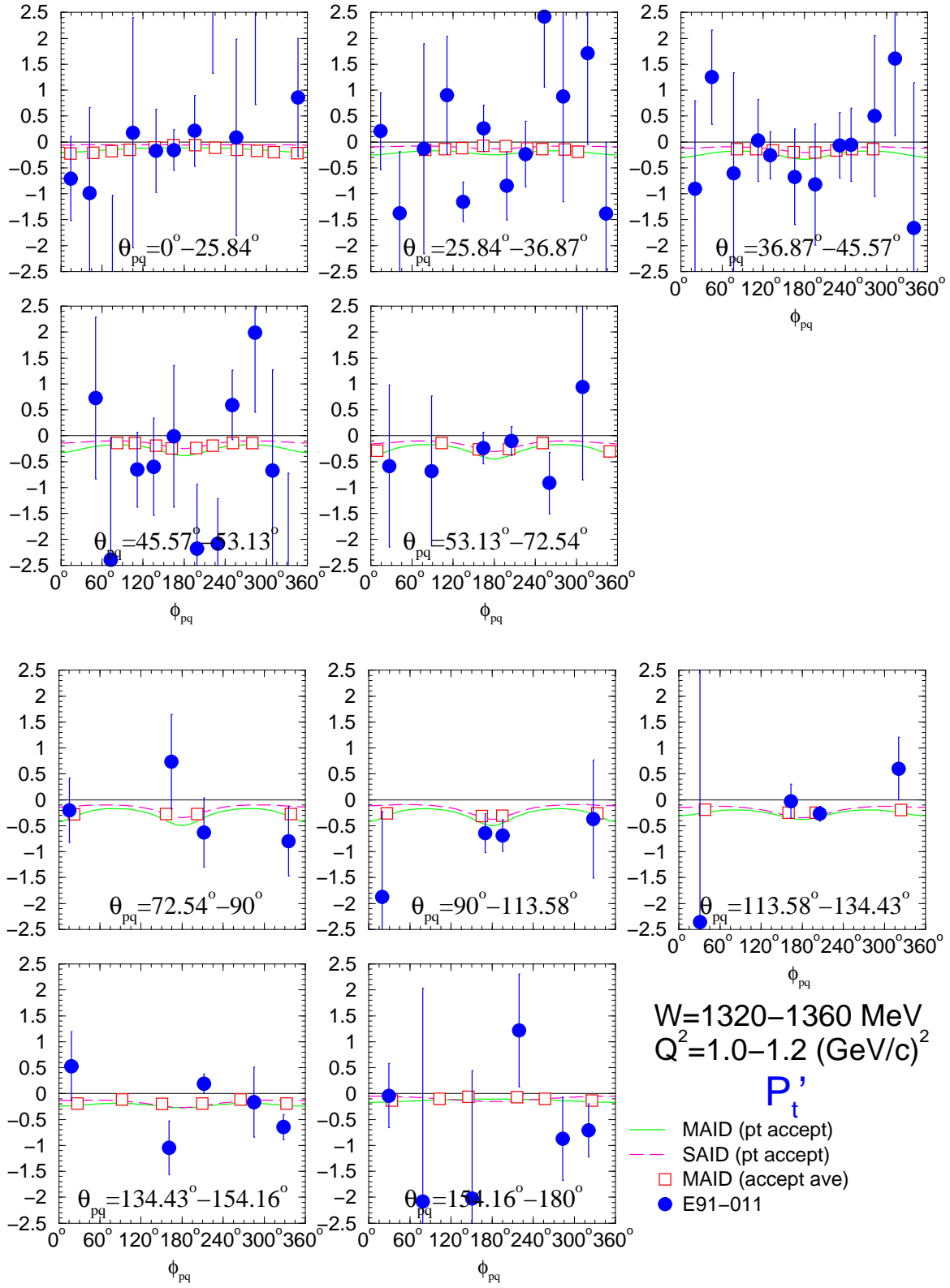


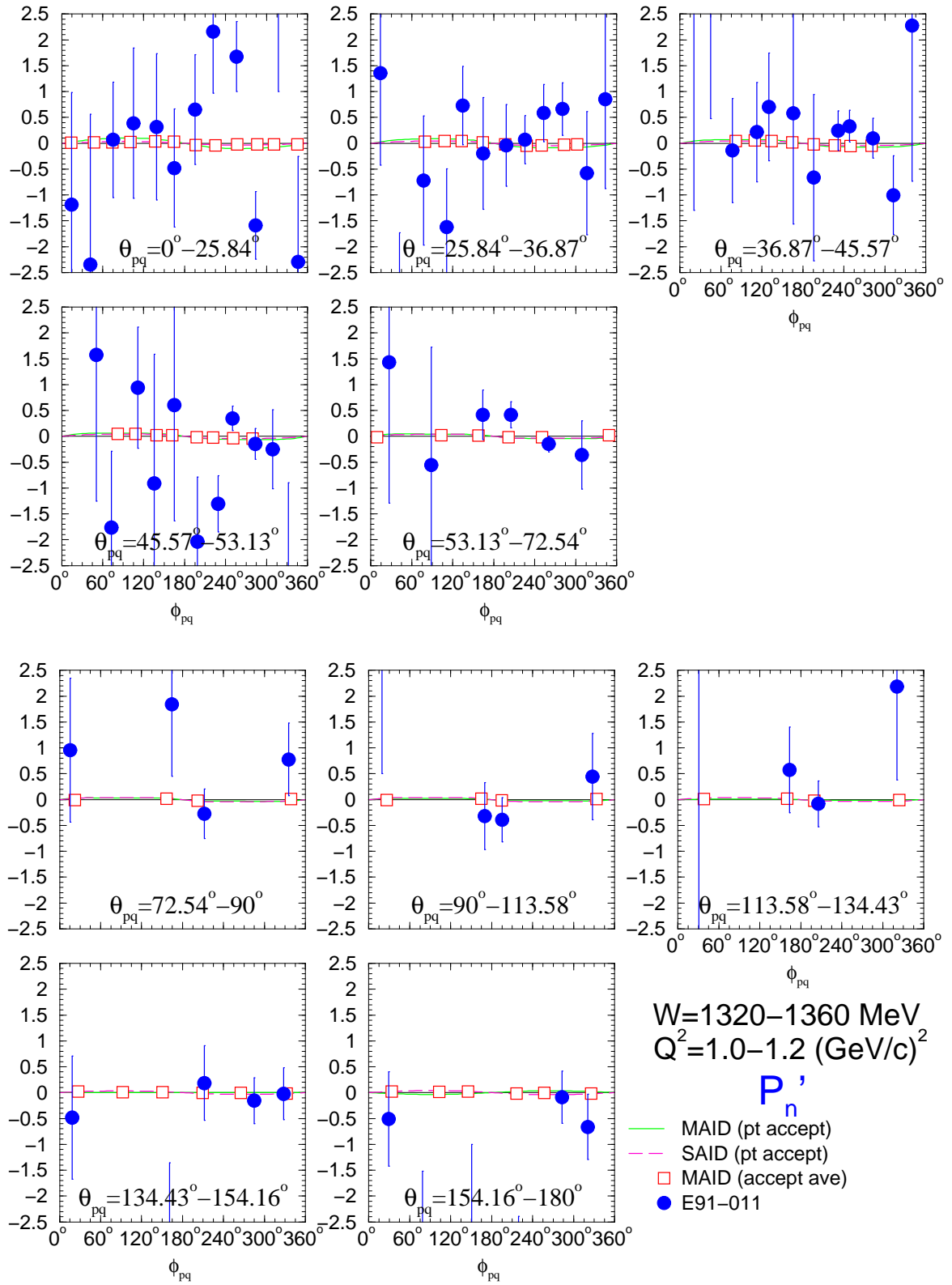
**D.10.  $W = 1320\text{--}1360\text{ MeV}$ ,  $Q^2 = 1.0\text{--}1.2\text{ (GeV/c)}^2$**

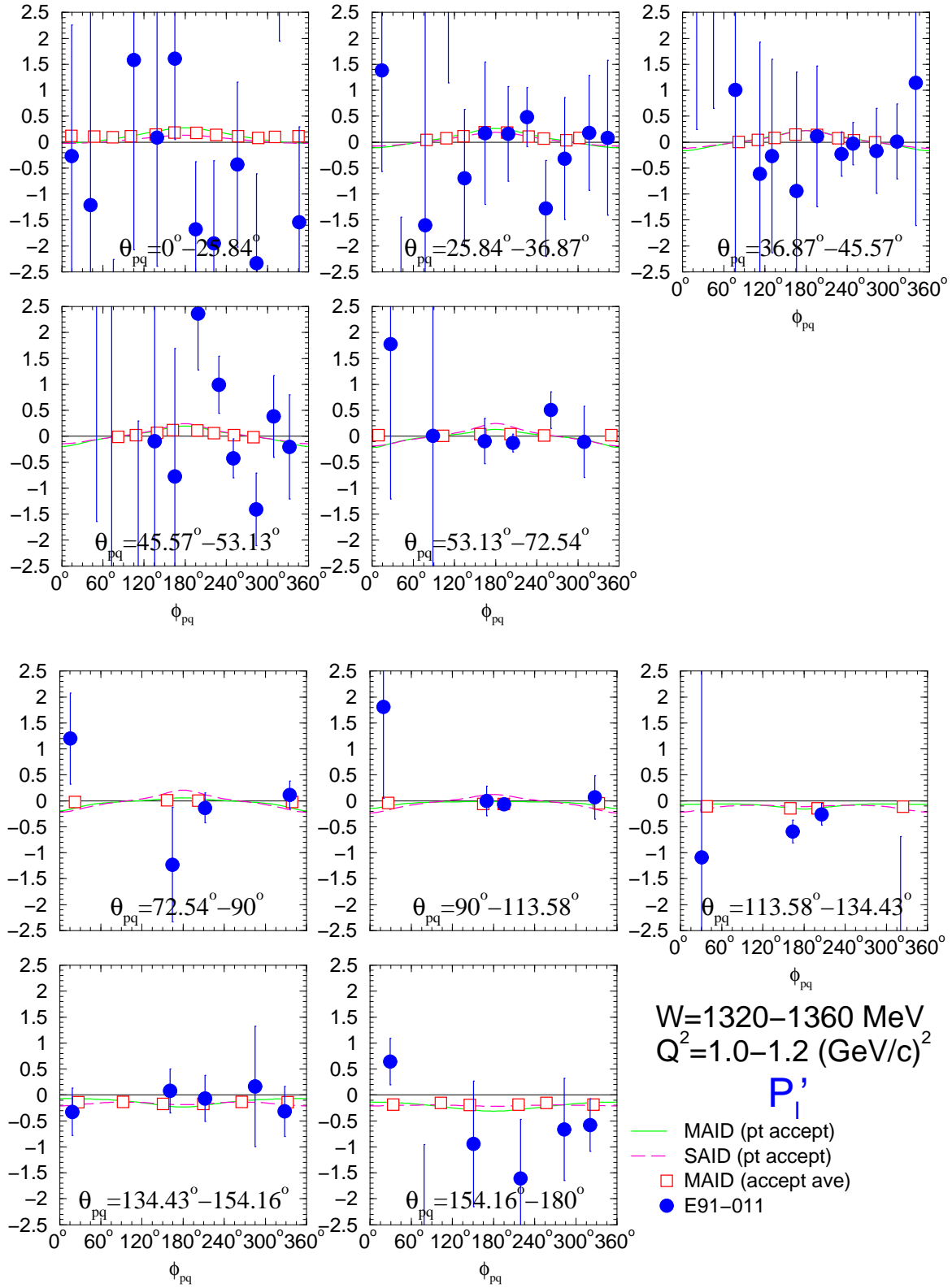










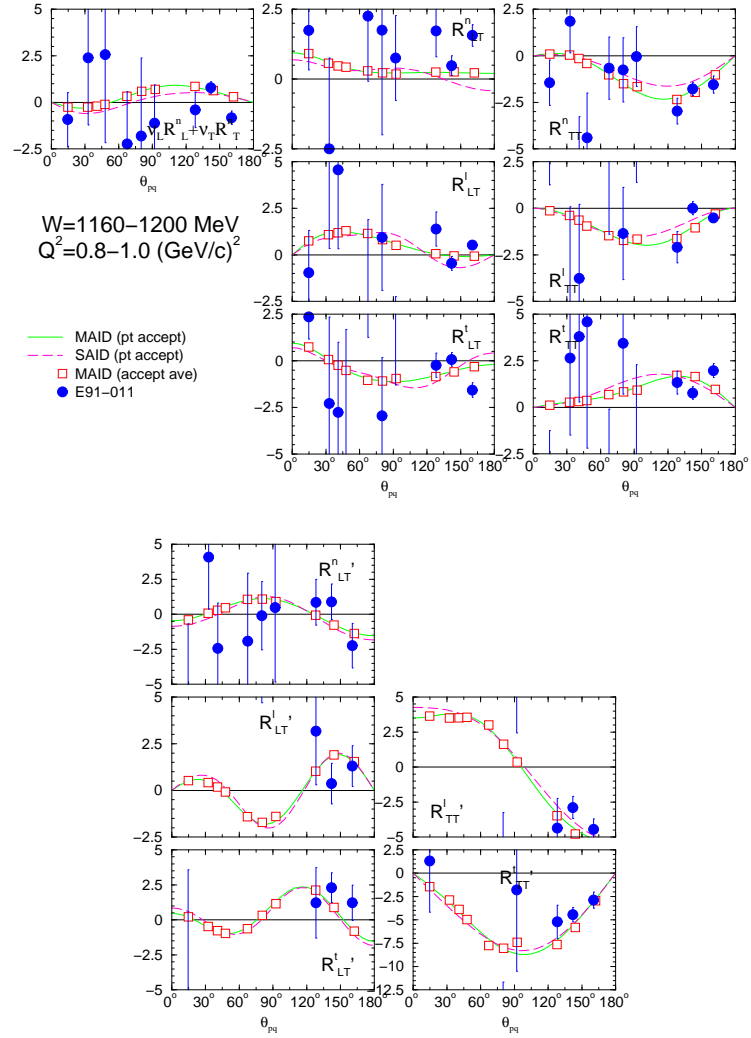




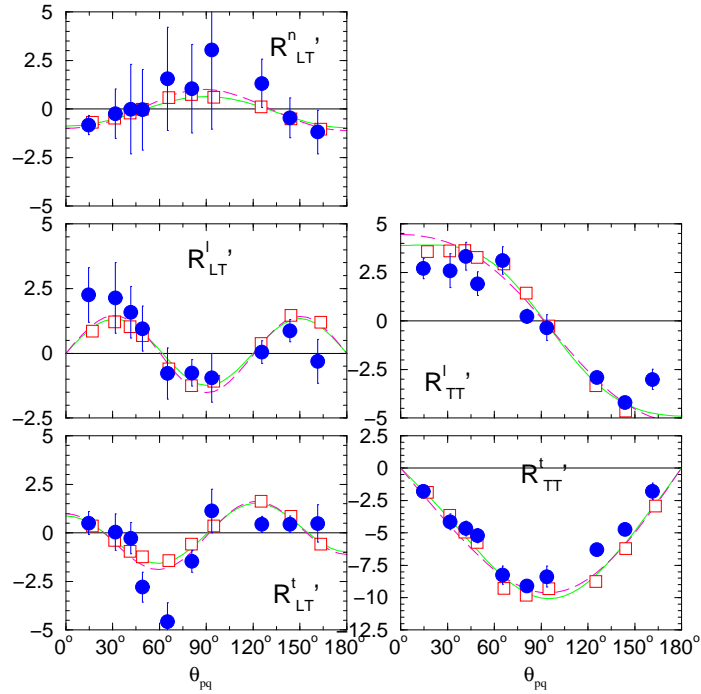
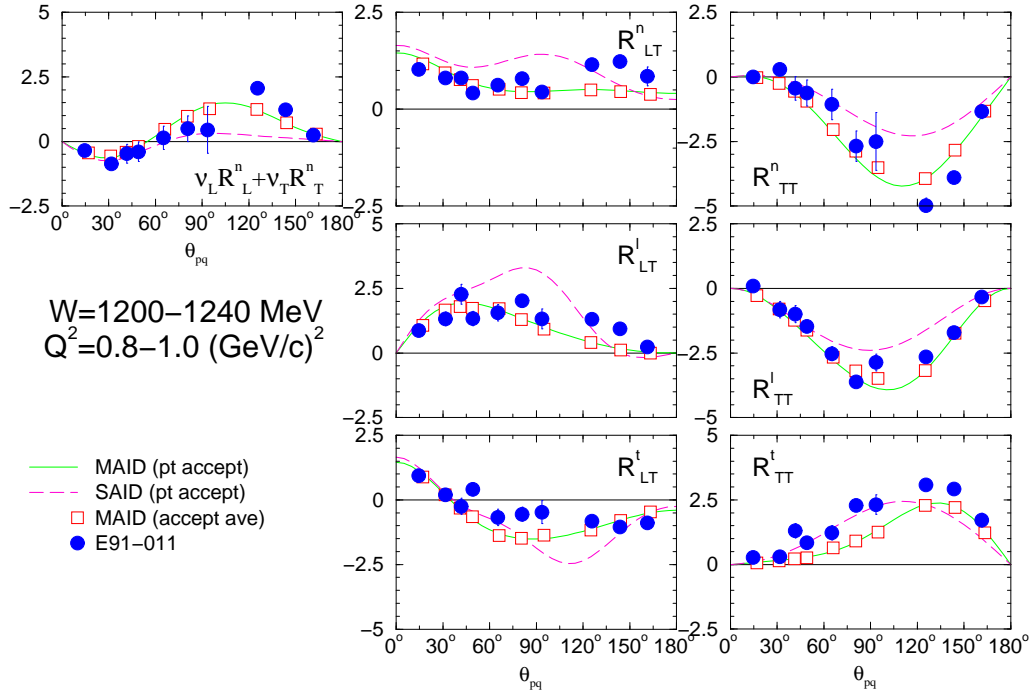
## APPENDIX E

### RESULTS: RESPONSE FUNCTIONS

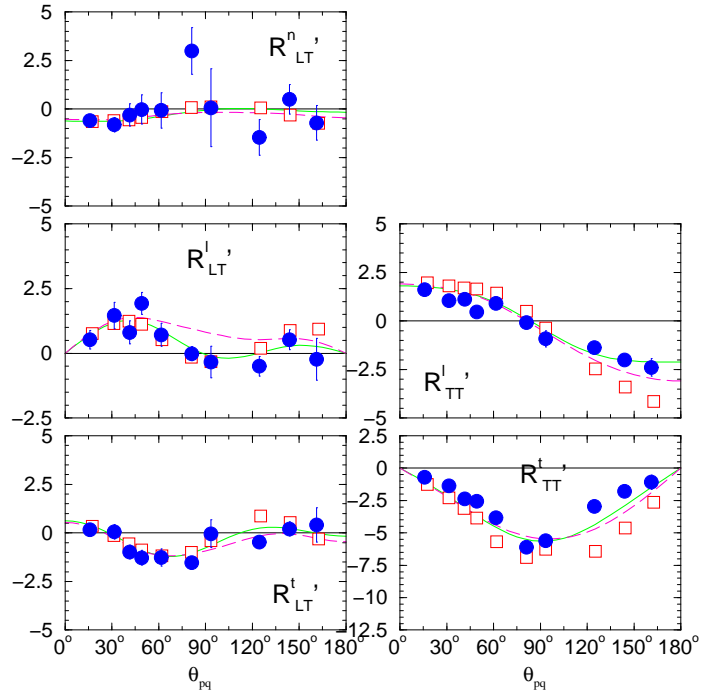
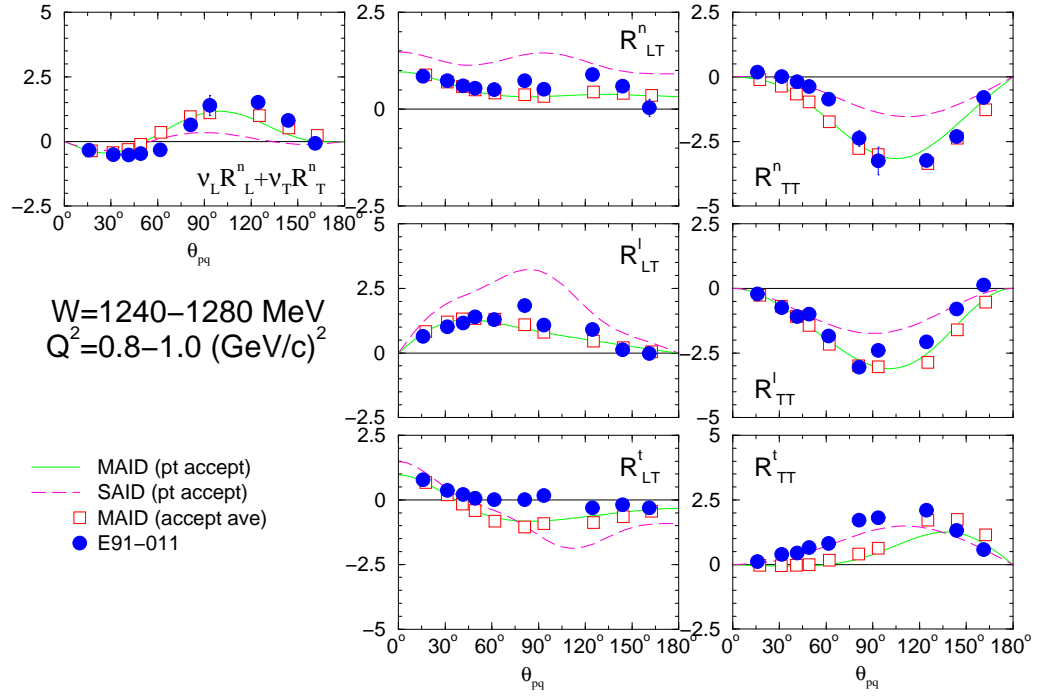
#### E.1. $W = 1160\text{--}1200\text{ MeV}$ , $Q^2 = 0.8\text{--}1.0\text{ (GeV/c)}^2$



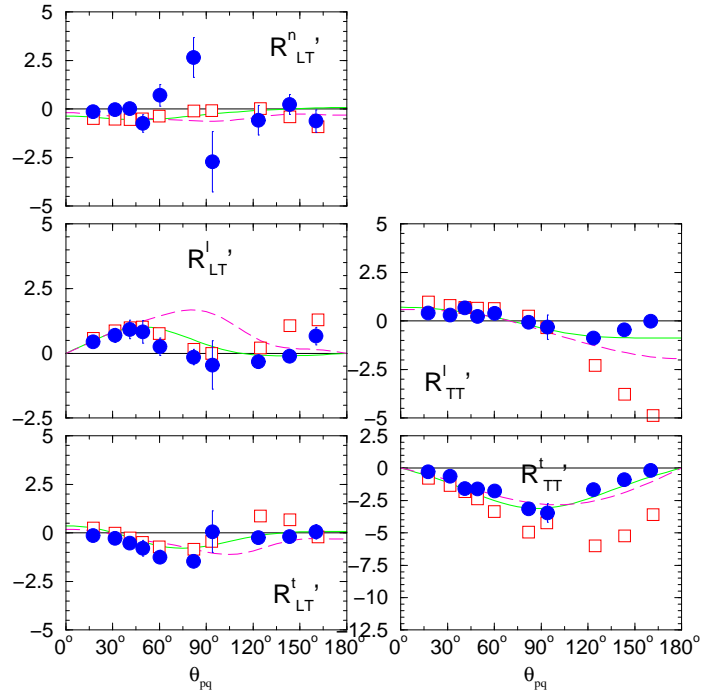
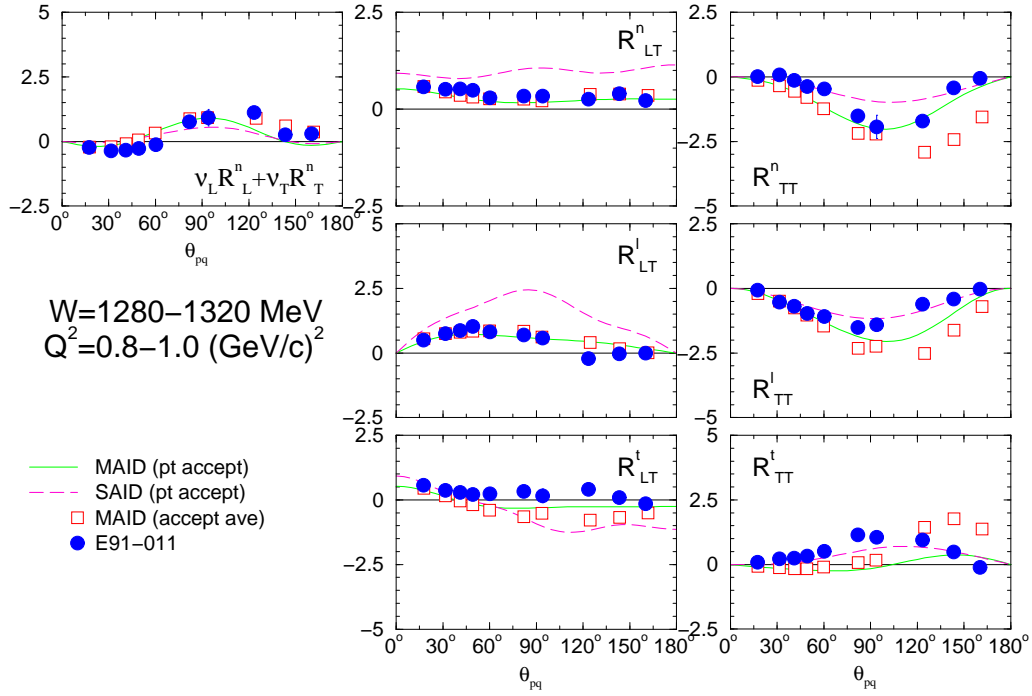
E.2.  $W = 1200\text{--}1240 \text{ MeV}, Q^2 = 0.8\text{--}1.0 \text{ (GeV/c)}^2$



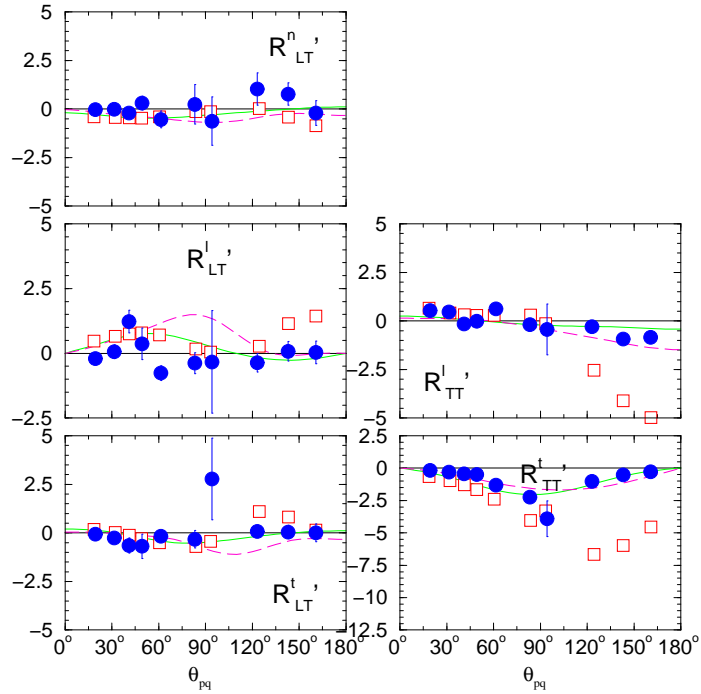
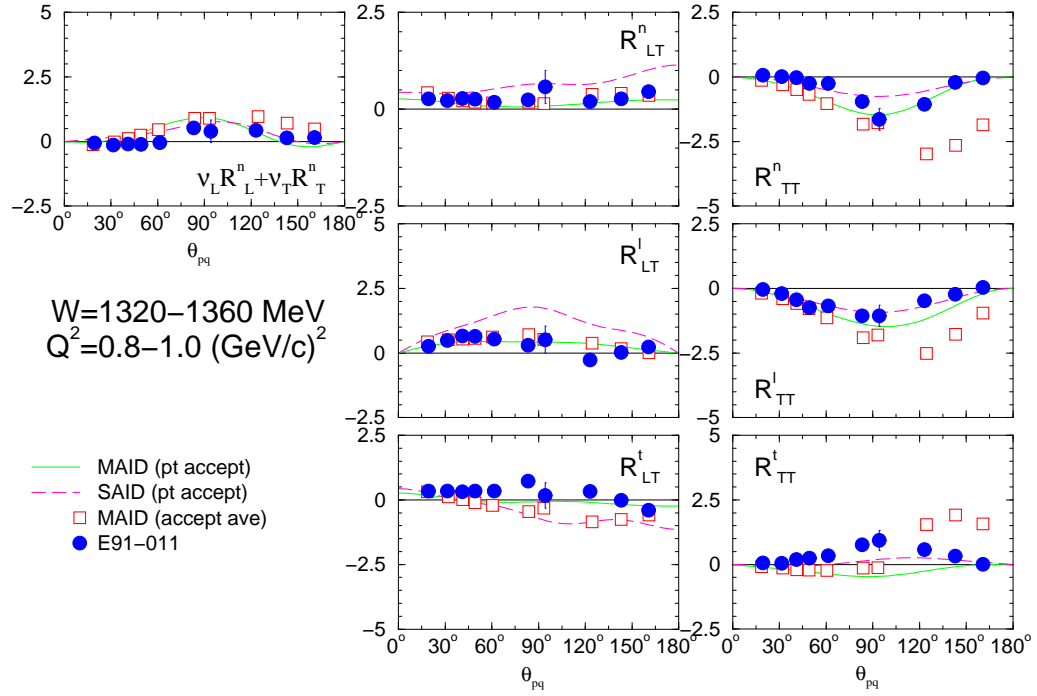
E.3.  $W = 1240\text{--}1280 \text{ MeV}, Q^2 = 0.8\text{--}1.0 \text{ (GeV/c)}^2$



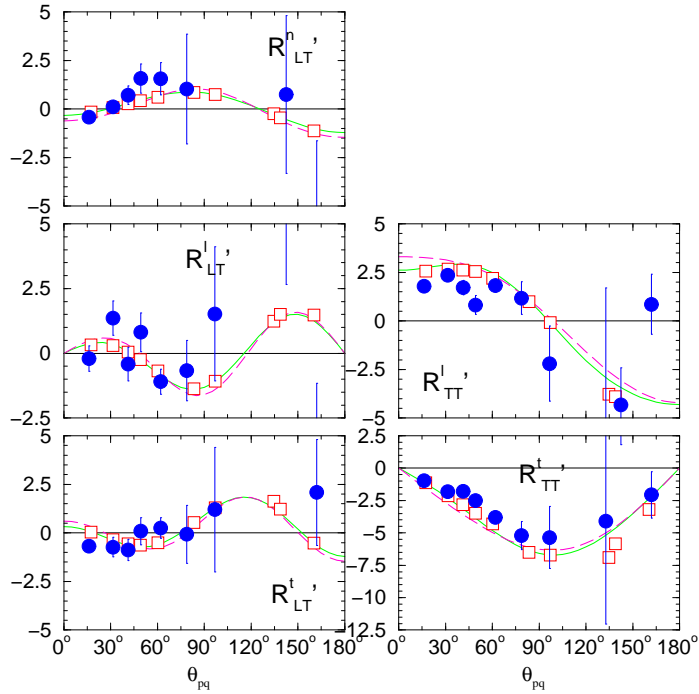
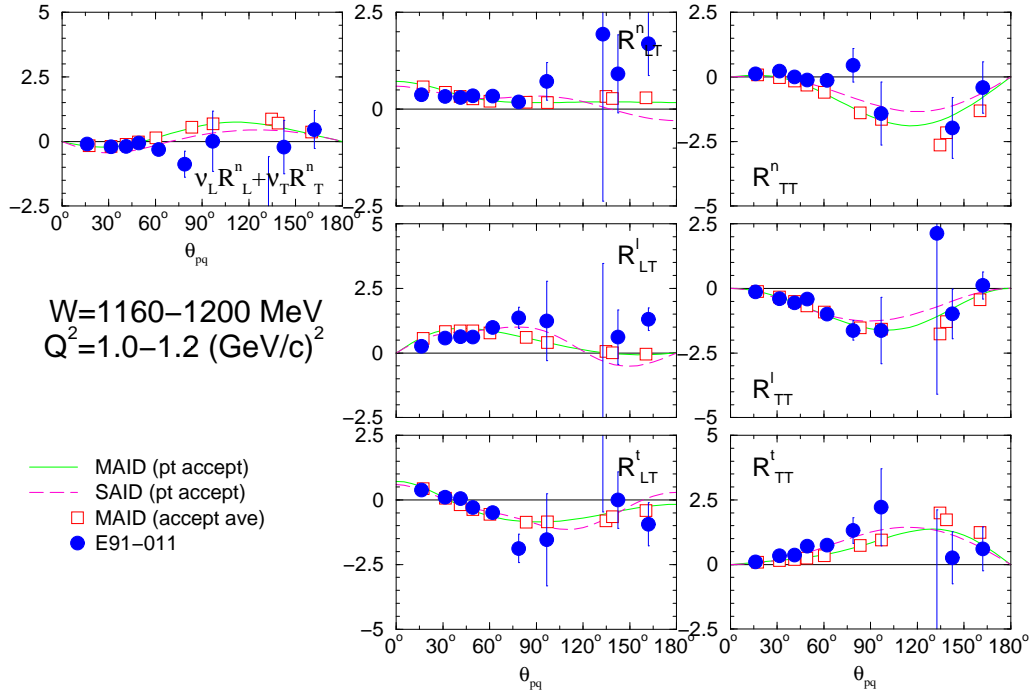
E.4.  $W = 1280\text{--}1320 \text{ MeV}, Q^2 = 0.8\text{--}1.0 \text{ (GeV/c)}^2$



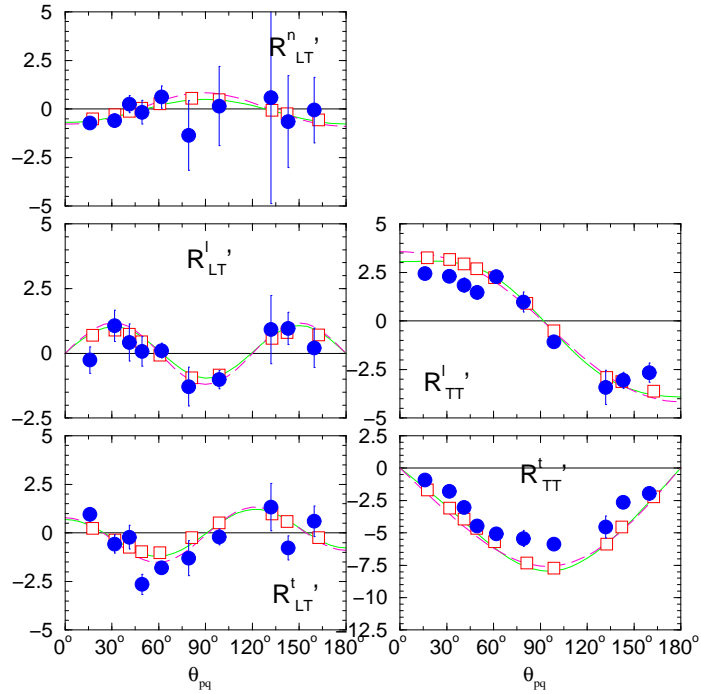
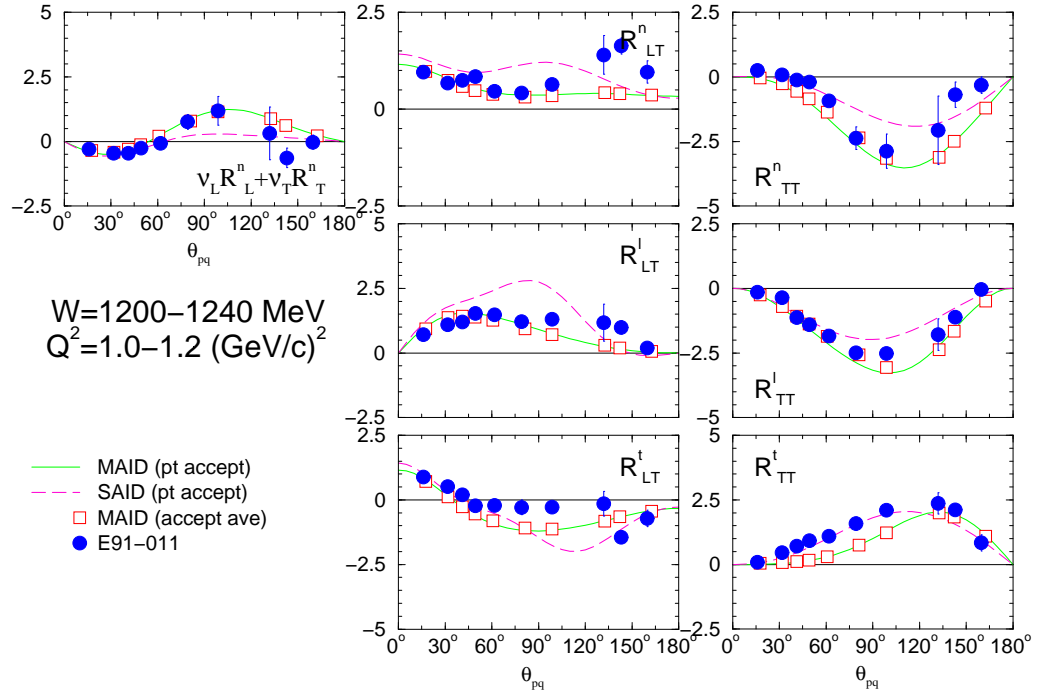
E.5.  $W = 1320\text{--}1360 \text{ MeV}, Q^2 = 0.8\text{--}1.0 \text{ (GeV/c)}^2$



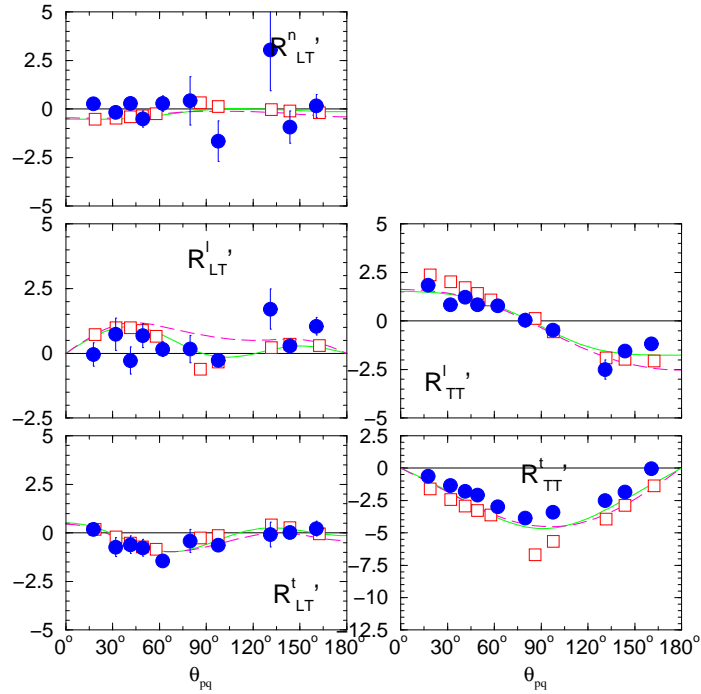
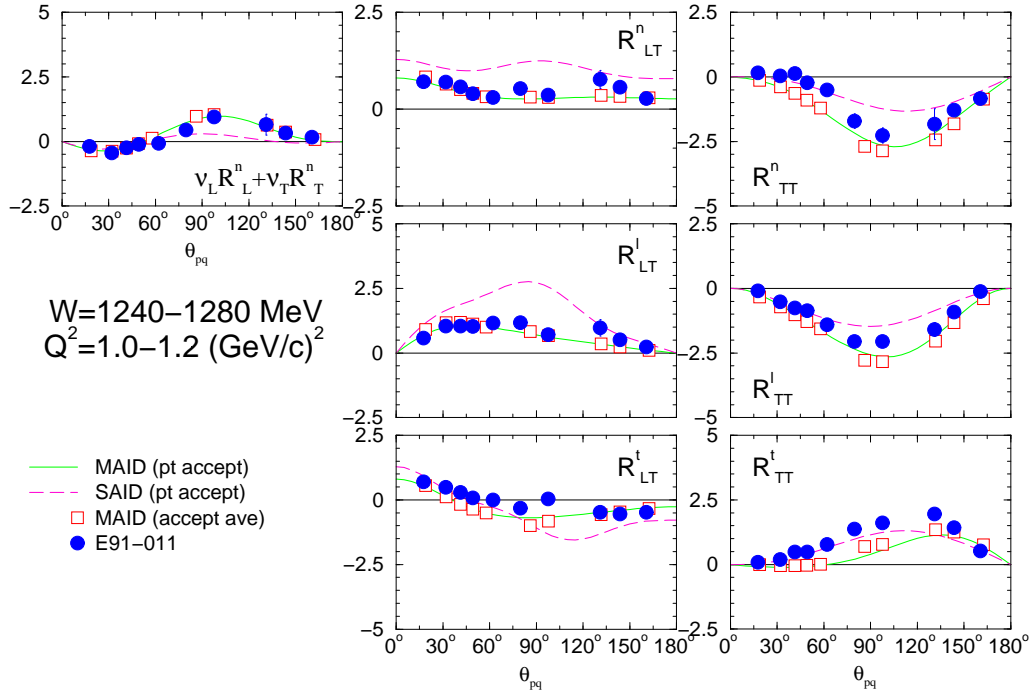
E.6.  $W = 1160\text{--}1200 \text{ MeV}, Q^2 = 1.0\text{--}1.2 \text{ (GeV/c)}^2$



E.7.  $W = 1200-1240 \text{ MeV}, Q^2 = 1.0-1.2 \text{ (GeV/c)}^2$

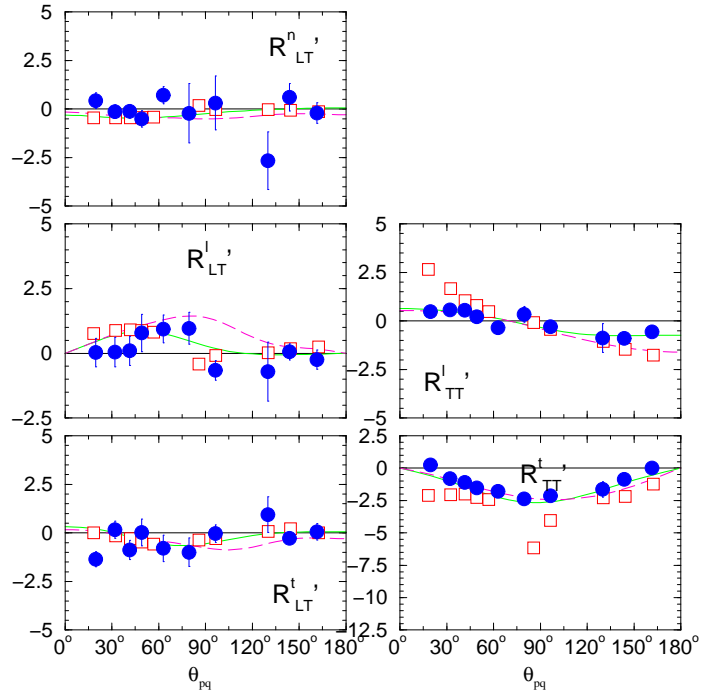
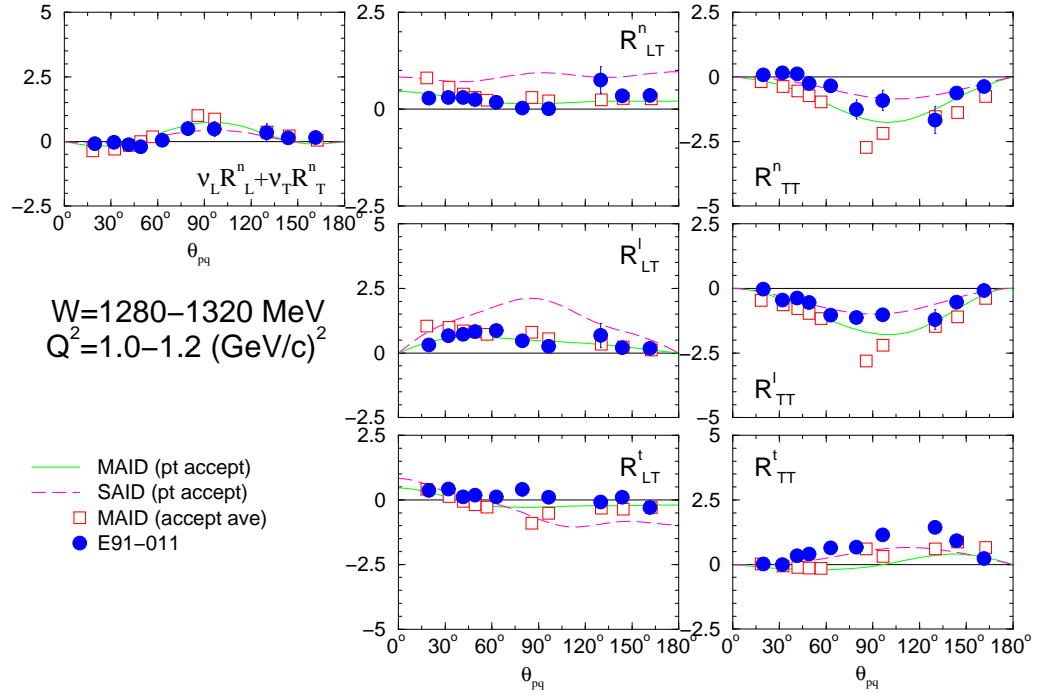


E.8.  $W = 1240\text{--}1280 \text{ MeV}, Q^2 = 1.0\text{--}1.2 \text{ (GeV/c)}^2$

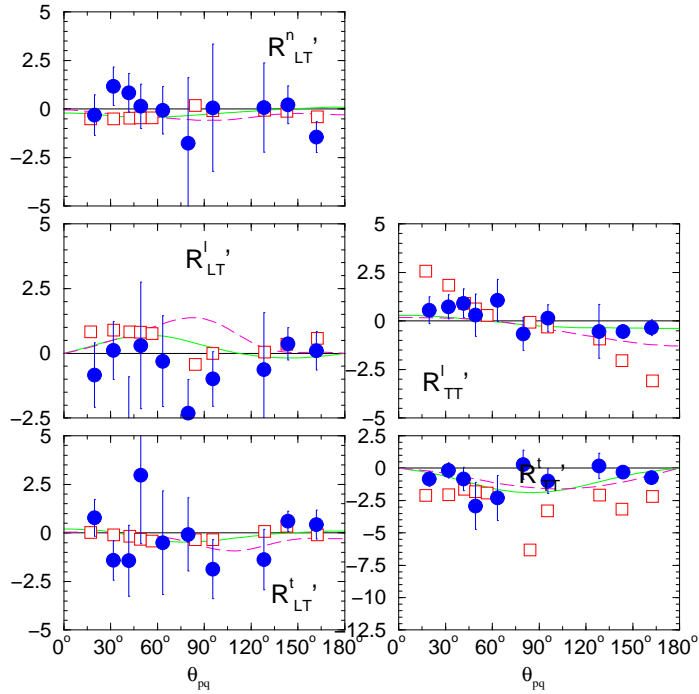
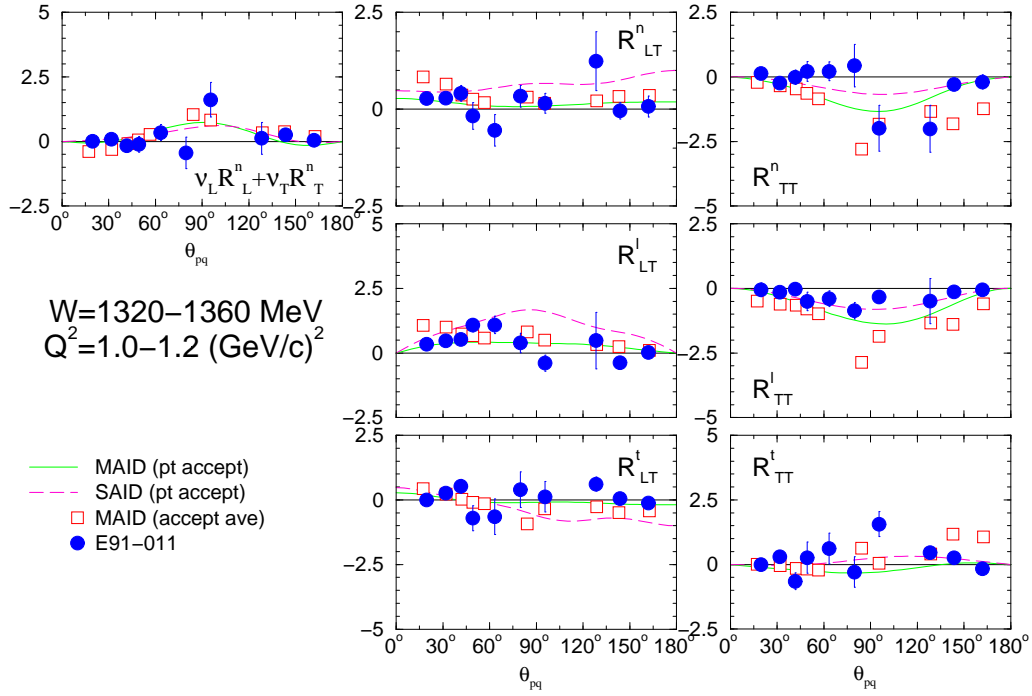




E.9.  $W = 1280\text{--}1320 \text{ MeV}, Q^2 = 1.0\text{--}1.2 \text{ (GeV/c)}^2$



E.10.  $W = 1320\text{--}1360\text{ MeV}$ ,  $Q^2 = 1.0\text{--}1.2\text{ (GeV/c)}^2$



## APPENDIX F

### **“ $N \rightarrow \Delta$ ” INTERNAL REPORT ON SCINTILLATOR EFFICIENCIES<sup>1</sup>**

This report will explain the steps taken in determining the scintillator efficiencies for the “ $N \rightarrow \Delta$ ” experiment.

Type 1 triggers (T1) are electron arm singles events and the electron arm main trigger; type 2 triggers (T2) are also electron singles events, but with a looser trigger; type 3 triggers (T3) are hadron arm singles events and the hadron arm main trigger; type 4 triggers (T4) are also hadron singles events, but with a looser trigger; and, type 5 triggers (T5) are the coincidence between T1s and T3s. Runs where T1, T2, T3, T4 triggers were not prescaled were used in determining efficiencies for the S1 and S2 scintillator planes.

In creating the T1 or T3 triggers, the left and right side of each of the six scintillator paddles in each scintillator plane is first AND'd to determine if a particular paddle fired. Next, the six scintillator paddles of each scintillator plane are OR'd together to determine if the scintillator fired. Then, if one paddle of each of the S1 and S2 planes fired, a T1 or T3 trigger is made. For our purposes, only electron and hadron singles events with S1·S2·SRAY were counted as T1 and T3 type triggers, respectively. The SRAY refers to the fact that both the S1 and S2 scintillator planes fired, but the paddle numbers differed by at most one paddle. For example, if S1 paddle 2 fired, then only events where S2 paddles 1, 2, or 3 fired cause a T1 or T3 trigger. This increases the probability that a real particle hit the scintillator.

#### **F.1. Electron Arm Scintillator Efficiencies**

The following formulae were used to determine the efficiencies of the electron arm S1 and S2 scintillator planes:

$$\text{S1 efficiency} = \frac{\text{T1} \cdot \text{cerenkov} \cdot \text{S1} \cdot \text{S2} \cdot 1 \text{ track}}{\text{T1} \cdot \text{cerenkov} \cdot \text{S1} \cdot \text{S2} \cdot 1 \text{ track} + \text{T2} \cdot \text{cerenkov} \cdot \text{S2} \cdot 1 \text{ track}}, \quad (\text{F.1.1})$$

<sup>1</sup>Scintillator efficiency was important for the cross section analysis, not for the polarization analysis discussed in this thesis. This study was, however, a task performed by this author.

$$\text{S2 efficiency} = \frac{T1 \cdot \text{cerenkov} \cdot S1 \cdot S2 \cdot 1 \text{ track}}{T1 \cdot \text{cerenkov} \cdot S1 \cdot S2 \cdot 1 \text{ track} + T2 \cdot \text{cerenkov} \cdot S1 \cdot 1 \text{ track}}, \quad (\text{F.1.2})$$

where the numerators are single track T1 events with a hit in the Čerenkov and at least one paddle of each of the S1 and S2 scintillators firing. The denominators for Eqns. (F.1.1) and (F.1.2) correspond to single track T1 events with a hit in the Čerenkov and at least one paddle of each of the S1 and S2 scintillators firing *plus* single track T2 events with a hit in the Čerenkov and at least one paddle of the S2 or S1 scintillator, respectively, firing.

## F.2. Hadron Arm Scintillator Efficiencies

**F.2.1. May 19 to June 5: S0 Scintillator.** For the first run period a third scintillator, S0, was in place in the hadron arm. For this period, the following formulae were used in determining the S1 and S2 scintillator efficiencies:

$$\text{S1 efficiency} = \frac{T3 \cdot S0 \cdot S1 \cdot S2 \cdot 1 \text{ track}}{T3 \cdot S0 \cdot S1 \cdot S2 \cdot 1 \text{ track} + T4 \cdot S0 \cdot S2 \cdot 1 \text{ track}}, \quad (\text{F.2.1})$$

$$\text{S2 efficiency} = \frac{T3 \cdot S0 \cdot S1 \cdot S2 \cdot 1 \text{ track}}{T3 \cdot S0 \cdot S1 \cdot S2 \cdot 1 \text{ track} + T4 \cdot S0 \cdot S1 \cdot 1 \text{ track}}, \quad (\text{F.2.2})$$

where the numerators are single track T3 events with at least one paddle of each of the S0, S1, and S2 scintillator planes firing. The denominators of for Eqns. (F.2.1) and (F.2.2) correspond to single track T3 events with a hit in at least one paddle of each of the S0, S1, and S2 scintillator planes *plus* single track T4 events with a hit in at least one paddle of the S0 and S2, or S0 and S1 scintillator planes, respectively.

**F.2.2. June 8 to August 1: Aerogel Čerenkov.** After the first run period the S0 scintillator was taken out of the hadron arm detector stack and an aerogel Čerenkov used in its place. For this period, scintillator efficiencies were calculated using the following formulae:

$$\text{S1 efficiency} = \frac{T3 \cdot S1 \cdot S2 \cdot \text{geom} \cdot 1 \text{ track} \cdot ! \text{aero}}{T3 \cdot S1 \cdot S2 \cdot \text{geom} \cdot 1 \text{ track} \cdot ! \text{aero} + T4 \cdot S2 \cdot \text{geom} \cdot 1 \text{ track} \cdot ! \text{aero}} \quad (\text{F.2.3})$$

$$\text{S2 efficiency} = \frac{T3 \cdot S1 \cdot S2 \cdot \text{geom} \cdot 1 \text{ track} \cdot ! \text{aero}}{T3 \cdot S1 \cdot S2 \cdot \text{geom} \cdot 1 \text{ track} \cdot ! \text{aero} + T4 \cdot S1 \cdot \text{geom} \cdot 1 \text{ track} \cdot ! \text{aero}} \quad (\text{F.2.4})$$

where the numerators are single track T3 events with some  $x$  and  $y$  position (geom) (maximum and minimum values are listed in Tab. F.1) with at least one paddle of each of the S1 and S2 scintillators firing, but not the aerogel. The denominators of Eqns. (F.2.3) and (F.2.4) correspond to single track T3 events with some  $x$  and  $y$  position firing at least one

paddle of the S1 and S2 scintillator planes but not triggering the aerogel *plus* single track T4 events with some  $x$  and  $y$  position with a hit in at least one paddle of the S2 or S1 scintillator, respectively, firing but not triggering the aerogel.

TABLE F.1. Hadron arm scintillator  $x$  and  $y$  geometry cuts.

detector geometry	minimum (m)	maximum (m)
S1 x	-1.1	0.85
S1 y	-1.25	1.05
S2 x	-0.18	0.18
S2 y	-0.32	0.32

### F.3. Relative Error

The relative error for each efficiency was calculated using:

$$\text{relative error} = \left( \frac{1}{N} + \frac{1}{N_t} \right)^{\frac{1}{2}}, \quad (\text{F.3.1})$$

where the scintillator efficiency is  $\text{efficiency} = N/N_t$ .

### F.4. Results

Values for the electron and hadron arm efficiencies are listed in Tabs. F.2 and F.3<sup>2</sup> and shown in Fig. F.4.1(a) and (b). For the hadron arm, the  $\times$ 's represent efficiencies determined using the S0 scintillator while the  $*$ 's represent efficiencies determined using the aerogel Čerenkov.

---

<sup>2</sup>Recall: Hadron efficiencies determined between May 19 and June 5 were done so using an S0 scintillator, and those determined from June 8 to August 1 were done so using an aerogel Čerenkov.

TABLE F.2. Electron arm S1 and S2 scintillator efficiencies.

run	date	$\theta_{cm}$	electron S1 (%)	electron S2 (%)
1220	May 22	0°	99.5±0.4	99.8±0.4
1400	May 28	-50°	99.2±0.4	99.5±0.4
1428	May 29	-90°	99.2±0.4	99.6±0.4
1568	May 31	135°	99.2±0.8	99.5±0.8
1668	June 1	-135°	99.2±0.4	99.5±0.4
1700	June 2	155°	99.5±0.7	99.7±0.7
2271	June 19	-90°	99.2±0.4	99.5±0.4
2437	June 22	-50°	99.2±0.4	99.5±0.4
2504	June 24	0°	99.1±0.4	99.5±0.4
2633	June 29	25°	99.6±0.5	99.8±0.5
2842	July 12	50°	99.6±0.5	99.7±0.5
3050	July 17	90°	99.6±0.6	99.8±0.6
3317	July 21	135°	99.6±0.9	99.8±0.9
3650	July 25	155°	99.6±0.8	99.8±0.8
3941	July 29	180°	99.3±0.7	99.5±0.7

TABLE F.3. Hadron arm S1 and S2 scintillator efficiencies.

run	date	$\theta_{cm}$	hadron S1 (%)	hadron S2 (%)
1220	May 22	0°	100.0±1.0	97.8±1.0
1400	May 28	-50°	99.9±1.6	96.8±1.6
1428	May 29	-90°	100.0±1.3	98.0±1.3
1568	May 31	135°	99.8±0.4	98.4±0.4
1668	June 1	-135°	99.9±0.7	98.4±0.7
1700	June 2	155°	100.0±0.4	98.4±0.4
2271	June 19	-90°	98.6±2.0	95.7±2.0
2437	June 22	-50°	98.5±2.5	95.3±2.5
2504	June 24	0°	98.2±1.5	96.2±1.5
2633	June 29	25°	99.1±0.9	97.2±0.9
2842	July 12	50°	99.3±0.6	97.7±0.6
3050	July 17	90°	98.6±0.6	95.5±0.6
3317	July 21	135°	98.7±0.7	95.2±0.7
3650	July 25	155°	99.1±0.7	95.9±0.6
3941	July 29	180°	98.8±0.5	96.9±0.5

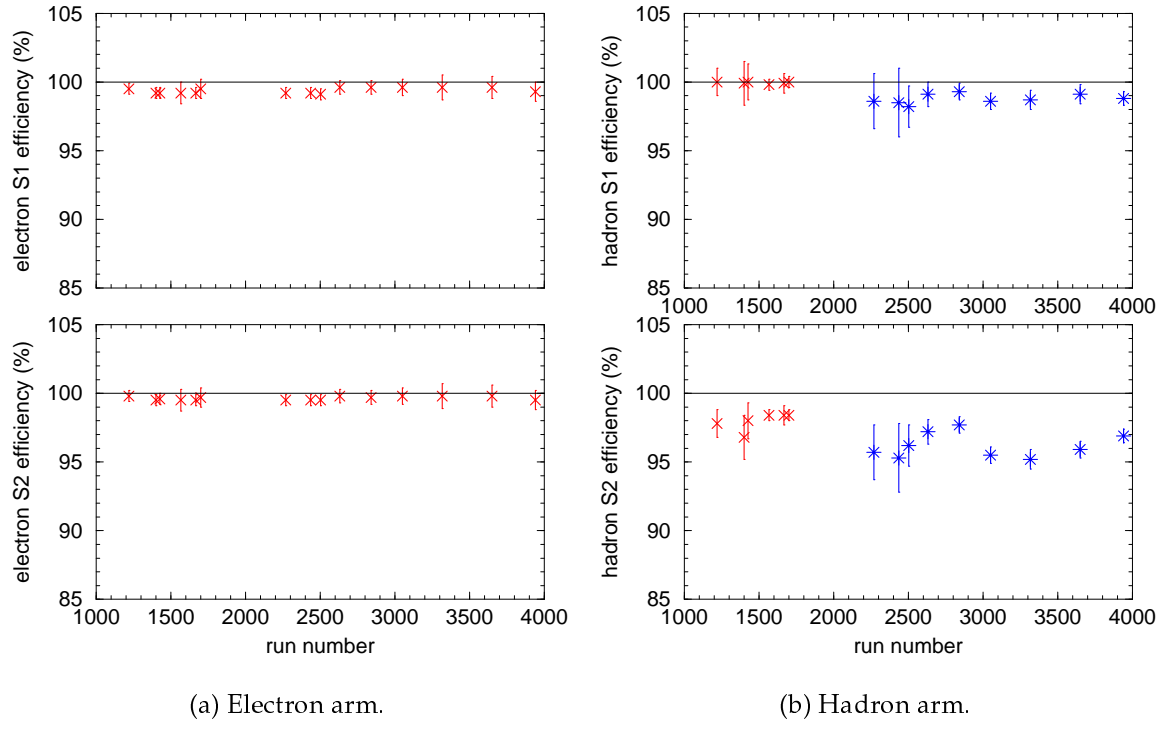


FIGURE F.4.1. Electron and hadron arm S1 and S2 scintillator efficiencies.





## BIBLIOGRAPHY

- [1] E. Rutherford, *Philosophical Magazine* **6:21**, 669 (1911).
- [2] J. Chadwick, *Proceedings of the Royal Society* **A136**, 692 (1932).
- [3] J. I. Friedman and H. W. Kendall, *Ann. Rev. Nucl. Part. Sci.* **22**, 203 (1972).
- [4] A. J. Buchmann and E. M. Henley, *Phys. Rev.* **C63**, 63 (2000).
- [5] J. D. Bjorken and S. D. Drell, *Relativistic Quantum Mechanics*, McGraw-Hill, New York (1964).
- [6] N. Dombey, *Rev. Mod. Phys.* **41**, 236 (1969).
- [7] A. Picklesimer and J. W. Van Orden, *Phys. Rev.* **C35**, 266 (1987).
- [8] C. Giusti and F. D. Pacati, *Nucl. Phys.* **A504**, 685 (1989).
- [9] J. J. Kelly, *Preliminary Fit Strategy for Angular Distribution*, July 2002 (unpublished).
- [10] Z. Chai, Ph.D. thesis, Massachusetts Institute of Technology (2003) (to be published).
- [11] J. D. Jackson, *Classical Electrodynamics*, John Wiley and Sons, New York (1975).
- [12] A. S. Raskin and T. W. Donnelly, *Ann. Phys.* **191**, 78 (1989).
- [13] J. J. Kelly, *Recoil-Polarization Response Functions for Electroproduction of Pseudoscalar Mesons*. <http://www.physics.umd.edu/enp/jjkelly/EPIPROD/epiprod.html>. Unpublished. (2000).
- [14] K. Joo *et al.*, *Phys. Rev. Lett.* **88**, 122001 (2002).
- [15] H. Schmieden, *Eur. Phys. J.*, **A1**, 427 (1998).
- [16] Th. Pospischil *et al.*, *Phys. Rev. Lett.* **86**, 2959 (2001).
- [17] R. Beck *et al.*, *Phys. Rev. Lett.* **78**, 606 (1997).

- [18] D. Griffith, *Introduction to Elementary Particle Physics*, John Wiley & Sons, New York (1987).
- [19] S. Wong, *Introductory Nuclear Physics*, Prentice-Hall, New Jersey (1990).
- [20] S. J. Brodsky and G. P. Lepage, *Nucl. Phys.* **A383**, 247c (1981).
- [21] N. Isgur and C. H. Llewellyn Smith, *Phys. Rev. Lett.* **52**, 1080 (1984).
- [22] N. Isgur and C. H. Llewellyn Smith, *Nucl. Phys.* **B317**, 526 (1989).
- [23] W. Heisenberg, *Z. Phys.* **77**, 1 (1932).
- [24] D. E. Groom, *et al.*, *Eur. Phys. Jour.* **C15**, 1 (2000).
- [25] H. L. Anderson, E. Fermi, E. A. Long, and D. E. Nagle, *Phys. Rev.* **85**, 936 (1952).
- [26] K. A. Brueckner, *Phys. Rev.* **86**, 106 (1952).
- [27] H. Ströher, *Acta Phys. Pol.* **B31**, 2333 (2000).
- [28] W. Albrecht *et al.*, *Nucl. Phys.* **B25**, 1 (1970).
- [29] W. Albrecht *et al.*, *Nucl. Phys.* **B27**, 615 (1971).
- [30] J. C. Alder *et al.*, *Nucl. Phys.* **B46**, 573 (1972).
- [31] R. Siddle *et al.*, *Nucl. Phys.* **B35**, 93 (1971).
- [32] C. Mistretta *et al.*, *Phys. Rev.* **184**, 1487 (1969).
- [33] N. Isgur, G. Karl, and R. Koniuk, *Phys. Rev.* **D25**, 2394 (1982).
- [34] S. Capstick and G. Karl, *Phys. Rev.* **D41**, 2767 (1990).
- [35] A. J. Buchmann, E. Hernández, and A. Faessler, *Phys. Rev.* **C55**, 448 (1997).
- [36] T. Sato and T. S. Lee, *Phys. Rev.* **C54**, 2660 (1996).
- [37] T. Sato and T. S. Lee, *Phys. Rev.* **C63**, 055201 (2001).
- [38] C. Mertz *et al.*, *Phys. Rev. Lett.* **86**, 2963 (2001).
- [39] G. Blanpied *et al.*, *Phys. Rev. Lett.* **79**, 4337 (1997)

- [40] F. Kalleicher *et al.*, *Z. Phys.* **A359**, 201 (1997).
- [41] V. V. Frolov *et al.*, *Phys. Rev. Lett.* **82**, 45 (1999).
- [42] R. M. Davidson, N. C. Mukhopadhyay, R. Whitman, *Phys. Rev. Lett.* **56**, 804 (1986).
- [43] D. Drechsel *et al.*, *Nucl. Phys.* **A645**, 145 (1999).
- [44] R. A. Arndt, I. I. Strakovsky, R. L. Workman, *Phys. Rev.* **C53**, 430 (1996).
- [45] B. D. Anderson *et al.*, *Basic Instrumentation for Hall A of Jefferson Lab.* <http://www.jlab.org/~kees/NIM.ps>. To be published. (2002).
- [46] J. Berthot and P. Vernin, *Nucl. Phys. News* **9**, 12 (1990).
- [47] D. Marchand, *Mesure absolue de l'énergie du faisceau d'électrons de CEBAF par une méthode magnétique*. PhD thesis, Université Blaise Pascal, Aubière, France (1997).
- [48] S. Escoffier, *Mesure de la polarisation du faisceau d'électrons de TJNAF par diffusion Compton pour les expériences N-Delta et GepII*. PhD thesis, Paris XI, France (2001).
- [49] R. Suleiman, *Hall A Cryogenic and Dummy Targets Information*. Jefferson Lab. Tech. Note JLab-TN-98-007 (1998).
- [50] A. Deur, *Temperature Analysis for the Hall A Cryotarget*. Jefferson Lab. Tech. Note JLab-TN-98-046 (1998).
- [51] K. G. Fissum *et al.*, *Nucl. Instr. Meth. in Phys. Res.* **A449**, 505 (2000).
- [52] K. G. Fissum *et al.*, *Nucl. Instr. Meth. in Phys. Res.* **A474**, 108 (2001).
- [53] Mauro Iodice *et al.*, *Nucl. Instr. Meth. in Phys. Res.* **A411**, 223 (1998).
- [54] <http://hallaweb.jlab.org/equipment/detectors/detectors.html>
- [55] <http://hallaweb.jlab.org/equipment/detectors/aero.html>
- [56] <http://hallaweb.jlab.org/equipment/detectors/fpp.html>
- [57] B. Bonin *et al.*, *Nucl. Instr. Meth. in Phys. Res.* **A288**, 379 (1990).
- [58] N. E. Cheung *et al.*, *Nucl. Instr. Meth. in Phys. Res.* **A363**, 561 (1995).

- [59] N. Liyanage, *Optics Calibration of the Hall A High Resolution Spectrometers using the C Optimizer*. Jefferson Lab. Tech. Note JLAB-TN-02-012 (2002).
- [60] K. Wijesooriya, *First ( $\vec{e}, e' \vec{p}$ ) Measurement of Polarization Transfer in a Complex Nucleus:  $^{16}\text{O}$* . PhD thesis, The College of William and Mary (1999).
- [61] R. D. Ransome *et al.*, *Nucl. Instr. Meth. in Phys. Res.* **201**, 315 (1982).
- [62] M. W. McNaughton *et al.*, *Nucl. Instr. Meth. in Phys. Res.* **A241**, 435 (1985).
- [63] O. Gayou *et al.*, *Phys. Rev. Lett.* **88**, 092301 (2002).
- [64] S. Dieterich, *Polarization Transfer in the Reaction  $^4\text{He} (\vec{e}, e' \vec{p}) ^3\text{H}$  in the Quasielastic Scattering Region*. PhD thesis, Rutgers (2002).
- [65] K. Makino and M. Berz. *Nucl. Instr. Meth. in Phys. Res.* **A427**, 338 (1999).
- [66] D. Basset *et al.*, *Nucl. Instr. Meth. in Phys. Res.* **166**, 515 (1979).
- [67] B. Milbrath *et al.*, *Phys. Rev. Lett.* **80**, 452 (1998).
- [68] B. Milbrath *et al.*, *Phys. Rev. Lett.* **82**, 2221(E) (1999).
- [69] M. K. Jones *et al.*, *Phys. Rev. Lett.* **84**, 1398 (2000).
- [70] O. Gayou, K. Wijesooriya *et al.*, *Phys. Rev.* **C64**, 038202 (2001).
- [71] S. Dieterich *et al.*, *Phys. Lett.* **B500**, 47 (2001).
- [72] L. Andivahis *et al.*, *Phys. Rev.* **D50**, 5491 (1994).
- [73] J. Litt *et al.*, *Phys. Lett.* **B31**, 40 (1970).
- [74] W. Bartel *et al.*, *Nucl. Phys.* **B58**, 429 (1973).
- [75] Ch. Berger *et al.*, *Phys. Lett.* **B35**, 87 (1971).
- [76] L. E. Price *et al.*, *Phys. Rev.* **D4**, 45 (1971).
- [77] J. A. Templon, C. E. Vellidis, R. E. J. Florizone, A. J. Sarty, *Phys. Rev.* **C61**, 014607 (2000).
- [78] <http://www.physics.odu.edu/~ulmer/mceep/mceep.html>

## **BIOGRAPHICAL SKETCH**

Rikki Erin Marie Roché was born on April 22, 1973 in Lexington, Kentucky. She graduated from Bethlehem High School in Bardstown, Kentucky in 1991. She did her undergraduate studies at Eastern Kentucky University in Richmond, Kentucky, on a University Regents Scholarship where she graduated as an Honors Scholar with a Bachelors of Science in Physics and minors in both Mathematics and Chemistry in 1996. She was accepted the same year in the Physics graduate program at Florida State University in Tallahassee, Florida. She received a Masters of Science degree in 1998 and the University's Women in Physics Fellowship beginning the next year. She defended her PhD dissertation on April 4, 2003. She then accepted a Postdoctoral Associate position at Old Dominion University in Norfolk, Virginia.